Analysis of Alterations in Matrix Quality at Nanoscale in Metabolic Bone Diseases using Synchrotron X-ray Diffraction

Malintha P. **Angelo Karunaratne** M. A.

A thesis submitted in fulfilment of the requirements for the degree of Doctor of Philosophy, University of London

School of Engineering and Materials Science

Abstract

Bone diseases such as osteoporosis and rickets cause significant reduction in bone quantity and quality, leading to mechanical abnormalities. While the reduction of bone quantity can be assessed using clinical tools like DXA and pQCT, there is little quantitative knowledge of how altered bone quality in diseased bone increases fracture risk. There is a clear need to develop high-resolution diagnostic techniques to close the gap between onset of fracture relevant changes and diagnosis. Here, a functional imaging technique (*in situ* synchrotron X-ray imaging with micromechanics) was developed to measure alterations in fibrillar deformation mechanisms in rickets, glucocorticoid-induced osteoporosis (GIOP), and premature ageing. During applied loading, percentage shifts in Bragg peak positions arising from the meridional collagen stagger, measured from the small angle X-ray scattering (SAXS) patterns, give fibrillar level strain as a function of applied stress in real time. To link nanostructural changes to altered fracture risk and deformability, well defined animal (mouse) models created via N-ethylnitrosurea mutagenesis were used. The fibril modulus, maximum fibril strain and fibril-to-tissue strain ratio were determined, complemented by quantitative backscattered scanning electron microscopy and microcomputed tomography to measure microscale mineralisation. A significant reduction of fibril modulus and enhancement of maximum fibril strain was found in rickets and GIOP mice. A significantly larger fibril strain/tissue strain ratio was found in GIOP mice compared to wild-type mice, indicative of a lowered mechanical competence at the bone matrix level. The effects of altered *in vivo* muscular force distributions on the skeletal system in rickets were measured using position resolved scanning SAXS. Increase of mineral nanoplatelet alignment is observed in wild-type mice near zones of large in-vivo muscle force but not in rachitic mice. These results demonstrate the ability of synchrotron-based *in situ* X-ray nanomechanical imaging to identify functional alterations in nanoscale bone quality in metabolic bone diseases.

Acknowledgements

First and foremost, I would like to express my sincere gratitude to my primary supervisor Dr. Himadri Gupta for his guidance, care and encouragement throughout the three year period of my PhD. Without his unstinting support and enthusiasm for this project, I would never have achieved what I have been able to do. I am eternally grateful. I would also like to thank my co-supervisors Prof. Nick Terrill and Dr. Jen Hiller for taking me under their wing during the course of my time in Diamond Light Source Ltd (DLS), U.K. I would like to give a heartfelt thanks to Dr. Andy Bushby for use of his lab space in the Queens Building basement where I managed to concentrate fully on my research. I am very grateful to Prof. Rajesh Thakker (Nuffield Department of Medicine, University of Oxford) and Dr. Chris Esapa (Medical Research Council, Harwell) both for a very fruitful and rewarding scientific collaboration and for providing the critical murine bone samples used in my experiments.

A huge thank you to Prof. Alan Boyde in all his guidance and the time spent with me on scanning electron microscope and to Mo Arora for the training and the help she provided me on sample preparation. I would like to thank Dr. Asa Barber for scientific discussions related to my thesis, as well as his PhD students Fei Hang and Ines Jimenez. I would like to thank all the technical staff in the School of Engineering and Materials Science, QMUL for their kind help on instrument training, especially Tony, Doug, Denis, Chris, Jun, Dany, and Mike. The financial and administration team in the School office, who helped me immensely with claims and other administrative work, and Dr. Zofia Zuklinska at the Nano-Vision Centre and Dr. Nima Rohpoor at IRC for their excellent training on SEM and Raman spectroscopy are also gratefully acknowledged.

My PhD journey would never be an enjoyable one without some very special friends. Especially I would like to mention Priyanka, Mudaza and Zeynab who worked with me since I started my higher education at Queen Mary. Many thanks given for the practical and useful discussion with my research team members Jasmin, Andrew and Yankai.

Without my parents this achievement would be a dream forever. My deepest gratitude and sincere thanking goes to Amma (Mother) Renuka and Thaththa (Father) Nimal for sacrificing your happiness and supporting me in realizing my dream. Then I thank my younger sisters Angeleena and Angela, for looking after amma and thaththa while I am in U.K. This achievement would never have been possible without the support and wishes of loved ones, my two aunts (Loku nanda and Podi Nanda), in-laws (Ranjan and Chrishani) and my three bother-in-laws (Sachila, Rajitha and Feron).

Last but not least, my wonderful daughter who always puts a smile on my face. Riyana, you are my strength. Above all there has been one person who has supported me throughout, and has sacrificed so much over the past three years to allow me to focus on my studies, conferences and writing papers and thank you for your patience, support and love in helping me to achieve this. My wife Romanie, without you this holds no value.

To the most inspiring people in my life, my parents (Nimal and Renuka) and my amazing wife (Romanie) and daughter (Riyana), this thesis is dedicated to you

Publications, Presentations and Prizes

From the work presented in this thesis, the following papers were published or presented at scientific meetings:

Publications

- A Karunaratne, CT Esapa, J Hiller, A Boyde, R Head, JHD Bassett, NJ Terrill, GR Williams, MA Brown, P Croucher, SDM Brown, RD Cox, AH Barber, RV Thakker, HS Gupta. *Significant deterioration in nanomechanical quality occurs through incomplete extrafibrillar mineralisation in Rachitic bone: evidence from in-situ synchrotron X-ray scattering and backscattered electron imaging*. *2012*, J Bone Miner Res. 2012 27(4):876-90.

- A Karunaratne J Hiller, CT Esapa, NJ Terrill, AH Barber, RV Thakker, HS Gupta. *Hypophosphatemic rickets is associated with disruption of muscle stress-mediated mineral orientation at the nanoscale in the flat scapular bones of rachitic mice with development. 2012*, Bone. 2012 51(3):553-62

- A Karunaratne J Hiller, CT Esapa, NJ Terrill, AH Barber, RV Thakker, HS Gupta Disruption in fibrillar level fracture mechanisms in rachitic mice bone: measured using in-situ cantilever bending with microfocus SAXD, 2012 (In press - Bone)

- A Karunaratne, GR Davis, J Hiller, Liz Bentley, CT Esapa, NJ Terrill, SDM Brown, RD Cox, RV Thakker, HS Gupta. *Functional link between material level structural alterations in steroid induced osteoporotic bone and its increased fragility*, 2012 (prepared for publication in either *PNAS* or *JBMR*)

Oral presentations

- A Karunaratne et al. *In-vitro functional Imaging technique to investigate the nanostructural and mechanical behaviour in the mineralised matrix of metabolic bone diseases.* Oral presentation at Material Research Society Fall meeting 2012, Boston, USA. November 25-30/2012

- A Karunaratne et al. *investigating the nano-structural and mechanical behaviour in the mineralized matrix of metabolic bone disease phenotypes using synchrotron X-ray diffraction,* Invited Key note oral presentation at Small Angle Scattering (SAS2012), Sydney, Australia

- A Karunaratne et al. *Hypophosphatemic rickets is associated with disruption of muscle stress-mediated mineral orientation at the nanoscale in the flat scapular bones of rachitic mice with development. Oral presentation at European Society of Biomechanics annual meeting 2012 at Lisbon, Portugal, Jun 30 – Jul 04/2012*

- A Karunaratne et al. *Functional link between material level structural alterations in steroid induced osteoporotic bone and its increased fragility.* Oral presentation at Material Research Society spring meeting 2012, San Francisco, USA. April 8-13/2012

Poster presentations

- A Karunaratne et al. *Mechanical tester for I22 - in-situ mechanical testing with synchrotron microfocus SAXS on biological tissues, Poster presented at the Science Away Day, Science Division, Diamond Light Source Ltd, Oxford, UK 11/06/2012.*

- A Karunaratne et al. *Disruption in fibrillar level fracture mechanisms in rachitic mice bone: measured using in-situ cantilever bending with microfocus SAXD,* Poster presented at the European Society of Calcified Tissues, 39th Congress 2012. Stockholm, Sweden, 19-23/05/2012.

- A Karunaratne et al. *Nano-scale deformation mechanisms in a mouse model of rickets using in-situ tensile testing and Synchrotron SAXS*. Poster presented at the Synchrotron User Meeting at Diamond Light Source, Harwell, UK. September 08-09/2011.

- A Karunaratne et al. *Rickets induces significant deterioration in nanomechanical quality through incomplete extrafibrillar mineralisation: evidence from in-situ synchrotron X-ray scattering and backscattered electron imaging*. Poster presented at the Bone Research Society/British Orthopaedic Research Society Joint Meeting, Cambridge, UK. June 27-29/2011.

- A Karunaratne et al. *Nano-scale deformation mechanisms in a mouse model of rickets using in-situ tensile testing and Synchrotron SAXS*. Poster presentation at the *S4SAS workshop* 2010, University of Cardiff, Cardiff, August 2010

.

Prizes

- **Best poster prize –** The poster title: *Mechanical tester for I22 - in-situ mechanical testing with synchrotron microfocus SAXS on biological tissues*. Poster presented at the Science Away Day, Science Division, Diamond Light Source Ltd, UK. Jun 11/2012

- **Material Research Society Travel Award for the best abstracts –** The abstract title: *Functional link between material level structural alterations in steroid induced osteoporotic bone and its increased fragility***.** Oral presentation at **Spring Meeting** 2012. April 8-13/2012

- **European Society of Biomechanics Travel Award for the best abstracts -** The abstract title "Hypophosphatemic rickets is associated with disruption of mineral orientation at the nanoscale in the flat scapular bones of rachitic mice with development" submitted to European Society of Biomechanics annual meeting 2012. Jun 30 – Jul 04/2012

- **Best poster prize –** The Poster title: *Rickets induces significant deterioration in nanomechanical quality through incomplete extrafibrillar mineralisation: evidence from in-situ synchrotron X-ray scattering and backscattered electron imaging.* Poster presented at the Bone Research Society/British Orthopaedic Research Society Joint Meeting, Cambridge, UK. Jun 27-29/2011

- **ASBMR Young Investigator Travel Award for the best abstracts -** The abstract title In-situ synchrotron SAXS Combined with Micromechanical Testing to serve as an In-Vitro Nanomechanical Functional Imaging Technique to Measure the Bone Quality Degradation in Metabolic Bone Diseases submitted to the American Society of Bone and Mineral Research annual meeting 2011. Sep 16-20/2011

Follow-up funding

- **A knowledge transfer-type *Impact-QM* award from QMUL -** I was offered these funds to involve in the integration of the in situ mechanical testing capacities into the beamline I22, including activities such as writing manuals to enable a wider user base to access the technique. The award is to run for a period of up to 6 months following the award will further enable Diamond to benefit from the research.

- **Travel Grant for PhD students and Postdocs**, Oct 2011 & Feb 2012 Awards are available to contribute to the travel costs of staff members and postgraduate research students attending conferences. I was awarded this grant in the second and third years of my PhD to attend international conferences.

List of Abbreviations

SEM	Scanning Electron Microscopy
TEM	Transmission Electron Microscopy
MCF	Mineralised Collagen Fibril
AGE	Advanced Glycation End products
SAXS	Small Angle X-ray Scattering
WAXD	Wide Angle X-ray Scattering
SAXD	Small Angle X-ray Diffraction
BMU	Basic Multicellular Unit
AFM	Atomic force microscopic
Hcp	hexagonal close packed
BSE	Backscattered Scanning Electron
qBSE	quantitative Backscattered Scanning Electron
microCT	Micro-Computed Tomography
DXA	Dual-energy X-ray Absorptiometry
BMD	Bone Mineral Density
GIOP	Glucocorticoid-Induced Osteoporosis
XLHR	X-linked dominant hypophosphatemic rickets
Phex	Phosphate-regulating gene with homologies to endopeptidases on the X-chromosome
FGF23	Fibroblast Growth Factor 23
pQCT	peripheral Quantitative Computing Tomography
Hpr	hypophosphataemia
BMDD	Bone mineralisation density distribution

FWHM	Full Width at Half Maximum
HA	Hydroxyapatite
PMMA	Poly-Methyl-Methacrylate
FEA	Finite Element Analysis
ENU	Ethyl-nitrosurea
SAMP6	Senscence-Accelerated Mice
Crh	Corticotrophin releasing hormone
ABS	Acrylonitrile Butadiene Styrene
Ca wt. %	Calcium weight percentage
LAC	Linear attenuation coefficient (μ)

Table of Contents

Table of Figures

Table of tables

Table of equations

$$\sigma = \frac{6FLy}{bd^3}$$ Equation 4.4 151

$$\varepsilon = \frac{6FL}{Ebd^2} * y$$ Equation 4.5 151

$$\sigma_{corr} = \sigma_{nom} \frac{1}{1 - porosity}$$ Equation 4.6 162

$$Mineral_{conc} = \frac{\mu - \mu_o}{\mu_p - \mu_o} \rho_s$$ Equation 4.7 164

$$\varepsilon_1 = \frac{F}{\pi\left(b/2\right)^2} \times \frac{1}{E_f}$$ Equation 5.1 178

$$\varepsilon_2 = \frac{F}{\left[\pi\left(d^2 + db\right)E_m + \frac{\pi b^2}{4} E_f\right]}$$ Equation 5.2 179

$$\varepsilon_f = \frac{4F}{\pi b^2 E_f}\left[\left(1 - \frac{l}{L}\right) + \frac{l}{L} \bullet \frac{1}{1 + \frac{4\left(d^2 + db\right)}{b^2}\frac{E_m}{E_f}}\right]$$ Equation 5.3 180

$$\varepsilon_{f,u} = \frac{4F}{\pi b^2 E_f}$$ Equation 5.4 180

$$\varepsilon_{f,0} = \frac{4F}{\pi b^2 E_f}\left[\frac{1}{1 + \frac{4\left(d^2 + db\right)}{b^2}\frac{E_m}{E_f}}\right]$$ Equation 5.5 180

$$\frac{\varepsilon_f}{\varepsilon_{f,0}} = \frac{l}{L} \times -1\left(\frac{4\left(d^2 + db\right)}{b^2}\frac{E_m}{E_f}\right) + \left(1 + \frac{4\left(d^2 + db\right)}{b^2} \times \frac{E_m}{E_f}\right)$$ Equation 5.6 181

$$= 1 - \frac{b^2}{b^2 + 4bd + 4d^2} = \phi_{TM,0}\left(1 - f_{IF}\right)$$ Equation 5.7 183

$$= \frac{\frac{l}{L}}{\frac{b^2}{4\left(bd + d^2\right)} + \frac{l}{L}}$$ Equation 5.8 184

$$E_f = E_m \Phi_m + E_c\left(1 - \Phi_m\right)$$ Equation 6.1 209

$$\frac{1}{E_f} = \frac{1}{E_m}\Phi_m + \frac{1}{E_c}\left(1 - \Phi_m\right)$$ Equation 6.2 209

$$\frac{1}{E} = \frac{4\left(1 - \Phi_m\right)}{\mu_p {\Phi_m}^2 \rho^2} + \frac{1}{\Phi_m E_m}$$ Equation 6.3 210

Chapter 1

Structure and Mechanics of Bone

1 Structure and Mechanics of Bone

Bone is a hierarchical biological composite (1). It is one of the three main classes of mineralised tissue found in vertebrates with the other two being cartilage and enamel (2). Bone is also an organ that forms the skeleton of the human body. Bone exhibits a hierarchical structure which is optimised for its mechanical performance (3). Besides its role in mechanical support, it is also the main mineral storage source of the body, storing calcium and phosphate ions and releasing them according to the physiological needs of the body. Compositionally, it is made up of three major components; 65% mineral, 25% organic materials and 10% water (4, 5). The mineral platelets are carbonate-substituted hydroxyapatite (dahllite (1)) embedded in an organic extracellular matrix, while type I collagen is the main component of the organic phase (4). The compositional profile varies with species, anatomical locations, developmental stages, environmental factors, and dietary habits. Although water content in the bone is very small percentage, it provides a huge contribution to the toughness of the bone by acting as a plasticizer (6). Non-collagenous proteins comprise 10% to 15% of the organic matrix, and are (in contrast to collagen) amorphous, hydrated and with little secondary structure. They may play a role in bone formation as well as, perhaps less obviously, in fracture due to their adhesive behaviour at the interface between the collagen fibrils (7).

1.1 Hierarchical structure of bone

Bone can be resolved into several levels of organisation from molecular to macroscopic level. While various authors have proposed slightly different categorisations of this hierarchical structure (**Figure 1.1**), all start with molecular level components at the smallest level and end with the different types of (macroscopic) whole bones (1, 8).

Level 1 – Molecular level

There are three main components in the molecular level of bone material: nanosized mineral platelets, type I collagen and water. Also, a phase of noncollagenous proteins generally comprising less than 10 % of the total protein content is present. Structurally, Type I collagen is distinguished, at the molecular level, by the repeating motif of Gly-X-

Y (Gly: glycine, and X, Y either proline or hydroxyproline). Three peptide chains (1000 amino acids long) wound together in a triple helix (tropocollagen molecules) and they are connected by intermolecular cross links (1, 9). Type I collagen provides the flexibility to the bone, while the mineral phase is the only inorganic part of the mature bone, primarily composed of calcium and phosphate and conferring stiffness to bone. Water can be found in bone in two modes: some of it is bound to other molecules and some of it is free (10). Since all three major components of bone have different mechanical properties, bone tissue can be classified as a composite material.

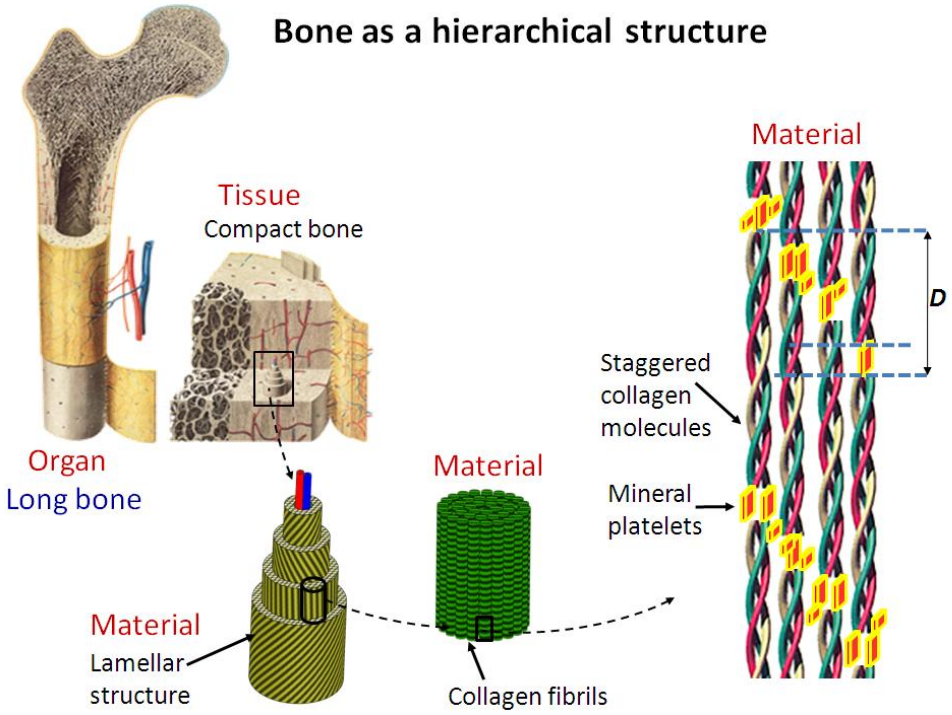

Figure 1.1: Different levels of hierarchy in bone

Level 2 – Mineralised collagen fibril

Each collagen fibril is made up of staggered oriented tropocollagen molecules. This level of bone will be discussed in more detail in section 1.2.

Level 3 – Collagen fibre

Mineralised collagen fibrils (MCFs) pack together to form fibres with diameter of 1 – 5 μm (11). They assemble in parallel arrays along their fibrillar long axis. One fibril bundle

(collagen fibre) merges with neighbouring collagen fibre instead of spreading out each other. Mineralised turkey tendons are good model systems to replicate the fibril bundles seen in bone. Turkey tendons are made up of type I collagen fibril arrays which are mineralising from one end. Mineral particle alignment in adjacent fibrils was studied using turkey tendon and it was observed that mineral layers in adjacent fibrils are highly ordered which proves neighbouring MCFs are ordered as arrays to form a fibril bundle (12). Parallel fibred bone (bovine periosteum) also consists of arrays of mineralised fibrils arranged along the long axis of the bone. However mineral content in parallel fibred bone is significantly higher (65 wt %) compared the mineralised tendons. A previous study has shown that these structures also are mechanically anisotropic; they exhibits different hardness values in all three directions relative to the fibril (parallel, transverse and radial) (13). Thus, the anisotropy of these structures is quite high, with highest modulus in tension and compression in the direction parallel to the fibrillar orientation.

Level 4 – Fibril arrays

The organisation of MCF arrays to form the next level in the hierarchy is more complex. There are four different ways that collagen fibres may be ordered into a higher structure (1) which is illustrated in **Figure 1.2**

Arrays of parallel fibrils (**Figure 1.2A**) are first laid down with the fibrils more or less parallel to the bone long axis. Combination of initially deposited parallel fibred bone and newly formed lamellar bone is referred to as fibrolamellar bone (or plexiform bone). Their anisotropic nature is very important as they can be orientated to one direction to optimise the mechanical adaptation. The elastic modulus of fibrolamellar bone is approximately 12 GPa along the long axis for the bone (14)

Woven bone (Figure 1.2B) consists of fibril bundles with different diameters (5 to 30 μm) loosely packed to form a poorly organised structure. Inorganic preparation of these samples illustrated that minerals are clustered to form spherical shapes with no alignment with fibrils. Woven bone is very common in the mammalian embryonic skeleton and in the fracture sites during healing process. These woven bones are not well adapted for

mechanical load bearing (1) when compared to lamellar bone. Therefore during the postnatal development woven bone is replaced by other well organised bone types such as lamellar bone. Compared to other bone structure, woven bone has higher rate of mineralisation and also it was observed that noncollagenous proteins are abundant within these structures (15).

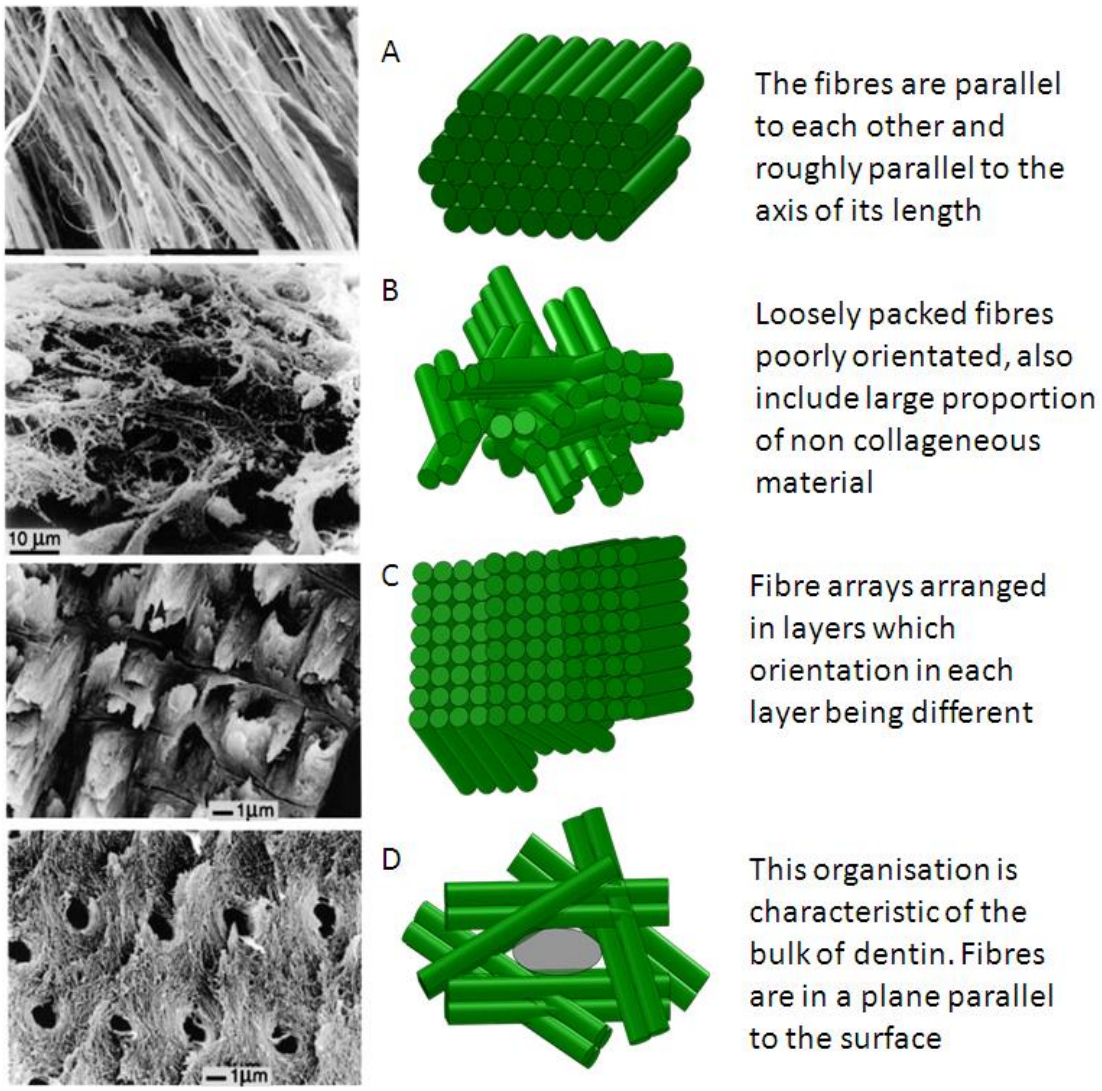

Figure 1.2: Four of the most common fibre array patterns of organisation. SEM images were adapted from (1). A. Array of parallel fibres B. Woven fibre structure C. Plywood structure D. Radial fibril arrays

Plywood patterns (Figure 1.2C) are present in lamellar bone. Marie Madeline Giraud Guille is the first person who explicitly described the lamellar structures as twisted plywood in bone (16, 17), following on earlier suggestions by Bouligand (18). Weiner et

al (19) carried out extensive scanning electron microscopy (SEM) studies on the lamellar bone of rat femurs. These authors found that the arrangement of the lamellae is twisted internally and that there is a change of angle approximately 30° from one fibre array relative to the adjacent array. Based on this data, they proposed a model in which a lamellar unit (3 – 4 μm) is composed of five sub layers (1). The five successive sub layers progressively rotate by 0°, 30°, 90°, 120° and 150°. Experiments performed with different animal models for lamellar bone showed that some of the sub layers are thicker than other layers within the same lamellar unit. These authors proposed a further refinement of the model, where collagen fibres in adjacent sub layers are not only oriented in the different planes but are also rotated around their own axis. Therefore this arrangement is called rotated plywood structure (17, 19-21). Further experiment showed that mineral crystals in first sub layer is parallel to the lamellar boundary and 4^{th} and 5^{th} sub layers in the same lamellar unit. However their progressive rotational angle is different to the fibrillar rotation, which introduces another degree of freedom to the structure of lamellar bone (20).

Rotated plywood like lamellar bone is very familiar in mammals especially with humans and they are folded into osteons or combined with parallel fibred bone to form fibrolamellar bone. Thus, an understanding of these single lamellar units are very crucial, however due to their complex structure and unavailability of bone specimens of the required size, it was difficult to perform mechanical testing directly at the lamellar level (1). Of the few studies that did consider this, microhardness experiments on rat tibia showed changes in mechanical properties at different orthogonal directions, indicating mechanical anisotropy of circumferential lamellar bone (22, 23). Further studies showed that the circumferential lamella found in baboon bone is anisotropic with respect to the deformation (bending modulus) and fracture (bending strength, fracture strain and work of fracture) mechanisms (24). However, the anisotropy of the plywood lamellar bone in humans is much higher compared to rat lamellar bone or baboon circumferential lamellar. Higher anisotropy observed in plywood-like lamellar bone, compared to its basic structure (parallel lamellar bone) implies bone tissue tends toward isotropic properties at higher levels of its hierarchy, in order to adapt to different modes of loading conditions such as tensile, compressive, torsional and bending loads (25).

Radial fibril arrays (Figure 1.2D) are mainly found in the inner layer of teeth which is comprised of dentinal tissue. Collagen fibrils are orthogonally oriented (to the tubule axis) in a plane which is parallel to the dentin surface. Intrafibrillar mineral particles are oriented along the long axis of the collagen fibril (26). Extrafibrillar mineral particles are randomly orientated and transmission electron microscopy (TEM) studies revealed that most of the mineral particles are not aligned between the adjacent collagen fibrils (1).

At this Level 4 (fibril arrays), it can be concluded that, fibrils and mineral particles are organised to various patterns in order to optimise for different mechanical environments. A complete understanding of structure-function relationships is not yet fully revealed at this (lamellar) length scale, due to the lack of experimental tools, advanced sample preparation techniques and inaccessibility of large enough samples which consist of a particular pattern of bone type.

Level 5: Cortical bone

At the next higher length scale in the hierarchy (10-100 μm), bone found principally in the central (diaphyseal) region of long bones is known as compact or cortical bone. Compact bone is comprised of concentric lamellar structures called osteons or Haversian systems. These osteons can be divided into two categories: primary osteons and secondary osteons, depending on the time (primary and secondary mineralisation) of their formation. Some species (mice) contain only primary osteons as they do not go through a bone remodelling phase. Each osteon has a diameter ~ 200 μm, consisting of a central channel (Haversian canal) approximately 50 μm in diameter, which house blood vessels and thin nerve filaments. These canals normally run parallel to the surface and along the long axis of the bone. Other canals, oriented obliquely or transversely to osteons, are known as Volkmann canals and connect the vessels in the osteon to the vessels in the periosteum and the medullary cavity (27). Osteocytes (bone cells) reside, inside ovoid spaces connected by a network of fine channels known as canaliculi. The mechanical properties were compared between planar lamellar bone and osteonal bone sections of the same animal and it was revealed that flexural modulus and work of fractures (**Figure 1.3**) values were similar for the specimens obtained parallel to the long axis of the bone. However there was a larger difference in inelastic regime of stress strain

curves between two types of bone specimens. These researchers suggested that due to the cylindrical nature of lamellar in secondary osteons, the plywood-twisting asymmetrical effects have been cancelled in the lamellar bone (24).

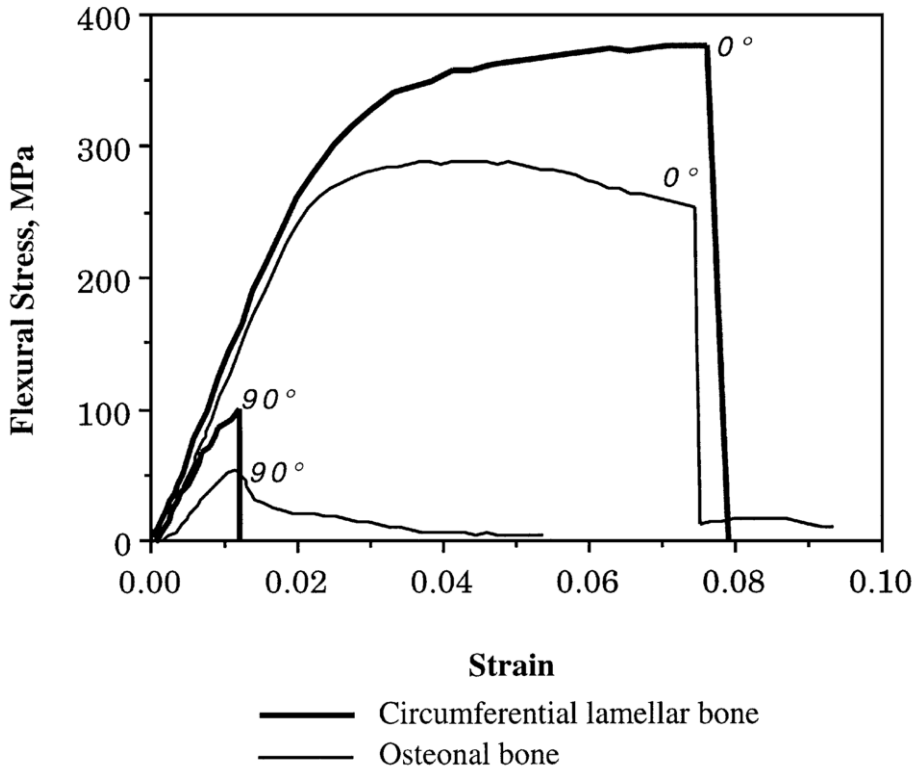

Figure 1.3: Flexural stress was plotted against strain for circumferential lamellar bone and osteonal bone of baboon tibia. Specimens were obtained from tibia parallel to long axis (0°) and perpendicular to the long axis (adapted from (1)).

Level 6: Trabecular bone

Epiphyses of long bones, vertebral bodies and flat bones contain a type of tissue known as spongy bone. Spongy bone is, at the coarsest level, a meshwork of plates and rods which hosts the red bone marrow. The individual rods and plates (trabeculae) are themselves made up of the lamellae described in the previous section. The average dimensions of a trabeculum are ~ 50 to 300 μm in diameter. The porosity of spongy bone is approximately 10 times higher than cortical bone (28, 29).

Level 7: Whole bones

Whole bones are classified according to their shape, ranging from long bones (tibia, femur), short bones (phalanges and carpal bones), to flat bones (scapula, ilium) and irregularly shaped bones (vertebrae).

1.2 The mineralised collagen fibril

The basic building block of the bone, the mineralised collagen fibril (MCF) is typically 50 – 200 nm in diameter. Since MCFs tends to merge with neighbouring fibrils, their exact length are not known (15). The MCF is a composite of collagen molecules and mineral platelets (30). The collagen in bone is Type I, comprised of tropocollagen molecules (~300 nm in length) which, in turn are composed of 3 polypeptide chains (length more than 1400 amino acids). The three chains (two α1 and one α2) are wound together in a triple helical structure, in which the repeated sequence of three amino acids (Gly-X-Y, where X and Y are proline and hydroxyproline) form hydrogen bonds with each other (7). These structures consist of three domains: $-NH_2$, -COOH (non triple helical domains) terminals and the triple helical terminal (9, 31). The triple helices form a hierarchical arrangement up to micro fibrils (1-4 nm) and finally the collagen fibril. Internal to the collagen fibril, the axial arrangement of tropocollagen molecules shows a staggered arrangement (**Figure 1.4**). This staggered model of collagen fibril arrangement was first introduced by Hodge and Petruska (32). In their model, collagen fibril consists of gap zones and overlap zones in two dimensions, as the starting point of one molecule is shifted by 40 nm relative to the end point of the next molecule. In the adjacent row, molecules are shifted by 67 nm, resulting in a 27 nm of overlap when the electron density is projected onto a single axis. Since many tropocollagen molecules are stacked side by side, this gap-overlap structure gives collagen fibrils a unique, internal period denoted by D ~ 65 – 67 nm. There are several factors influencing the banding periodicity such as age, species, pathology and state (dry or wet) of the bone. In order to explain the three dimensional fibrillar packing, Hulmes et al described a radial packing model in which he claims procollagen molecules (two α1 and one α2 chains) control the stages from tropocollagen molecule intracellular assembly to fibril diameter up to the suprafibrillar ordering of micrometer length scale (33). Electron microscopy of a transverse section of tendon fibrils revealed 4 nm of radial distance between two tropocollagen concentric

layers. This observation was combined with a concentric model of fibrillar packing leading to a predominant liquid like order with some degree of long range molecular ordering on a quasi-hexagonal lattice in the cross section of fibrils (33, 34).

Inter- and intra-molecular covalent cross-links in collagen fibrils play a vital role in stabilizing the periodic structures in MCFs (35). Also crosslinks provide tensile strength and viscoelastic properties to bone tissue (36). In human cortical bone, initiation of cross links occurs in two forms: enzymatic cross links and non enzymatic cross links. Enzymatic cross links (dihydroxylysinonorleucine and hydroxylysinonorleucine) occur intrafibrillarly at specific locations of collagen fibril (bind 2 tropocollagen molecules end-to-end along the fibril length) and subsequently these immature cross links turn into mature, more complex, multivalent interfibrillar cross links (37). Glucose mediated reactions regulate the production of non enzymatic cross links (advanced glycation end products (AGE)). At the present there are 7 naturally occurring different collagen cross links (37, 38).

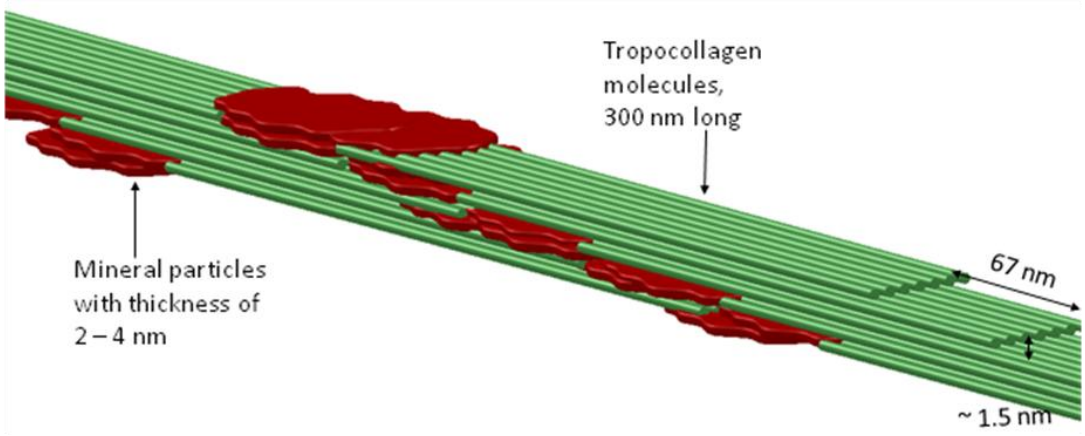

Figure 1.4: Tropocollagen arrangement in the collagen fibril. The tropocollagen molecules are arranged in a staggered orientation with 67 nm spacing. Mineral crystal nucleation occurs at the gap regions of collagen fibrils

Bone mineral acts both as an ion storage site and to provide structural stability to the bone by reinforcing collagen fibrils (39, 40). Plate-shaped bone apatite crystals (~50 nm×25 nm×2 nm) are among the smallest biologically produced crystals known (1, 8). The unit cell of hydroxyapatite ($Ca_{10}(PO_4)_6(OH)_2$) is a right rhombic prism where the space group and dimensions are, respectively $P6_3/m$ and a = 9.432 Å, c = 6.881 Å as

determined from three dimensional single crystal X-ray diffraction data (41). Mineral particle thickness was measured using small angle X-ray scattering (SAXS) and it was revealed that mineral particles from mineralised tendons and mature bones are around 1.5 nm and up to 4 nm respectively (42). Mineral crystals found in bone are plate shaped at the nanoscale despite dahllite having hexagonal close-packed crystal structure at the atomic crystallographic level.

There are larger interfacial spacings between collagen molecules and the mineral particles and noncollagenous proteins. These interfaces play a vital role in bone mechanical properties which have been studied in recent research (see **Chapter 1, section 2.4**). Noncollagenous proteins are well known for their role in regulating the mineralisation process (43). However recent studies have found that noncollagenous proteins may act as adhesive material on the surface of the collagen fibrils (44). They resist the interfibrillar breakage by attaching adjacent fibrils together with sacrificial bonds (45).

1.3 Bone cells – Cellular structure

1.3.1 Osteoblasts

Osteoblasts are derived from mesenchymal cells and they are bone forming cells. Osteoblasts synthesize and secrete collagen and some of the carbohydrate complexes which make up osteoid or matrix (3). Osteoblasts are usually connected to their neighbouring cells by thin cytoplasmic processes. These cells appear cuboidal during active growth and have a diameter of 15 – 20 μm (46). Some osteoblasts become inactive and eventually form bone lining cells, whereas others get encapsulated in the matrix and become osteocytes (**Figure 1.5**) (47).

1.3.2 Osteocytes

The formation of osteocytes occurs from osteoblasts that have been entrapped in osteoid and/or mineralised bone matrix (48). The cytoplasmic processes connect osteocytes with other osteocytes and bone lining cells which form the canalicular network for intercommunication between them. Osteocytes are most frequent cell type (90-95%) in

the bone tissue (49). The lacunae/canalicular system creates an extensive molecular exchange through its large surface area which contributes to the bone mineral homeostasis (50, 51). Osteocytes are thought to activate osteoblasts and osteoclasts via mechanosensation of external mechanical loading through their canalicular network, stimulating the bone remodelling (52).

1.3.3 Bone lining cells

Bone lining cells are formed once osteoblasts activity has been aborted. The osteoblasts flatten and elongate, attaching themselves to the bone surface in a thin continuous layer. Bone lining cells act as a membrane and control the transfer of ions between the bone and the interstitial fluid (3).

1.3.4 Osteoclasts

Osteoclasts (**Figure 1.5**) are responsible for bone resorption. They are larger than other bone cells and contain multiple nuclei in each cell (49). Osteoclasts could arise from precursor cells; haematopoietic macrophage and monocyte stem cell line circulating in the blood (53). Bone resorption cells release proteases and acids which dissolve the matrix and bone mineral respectively (54).

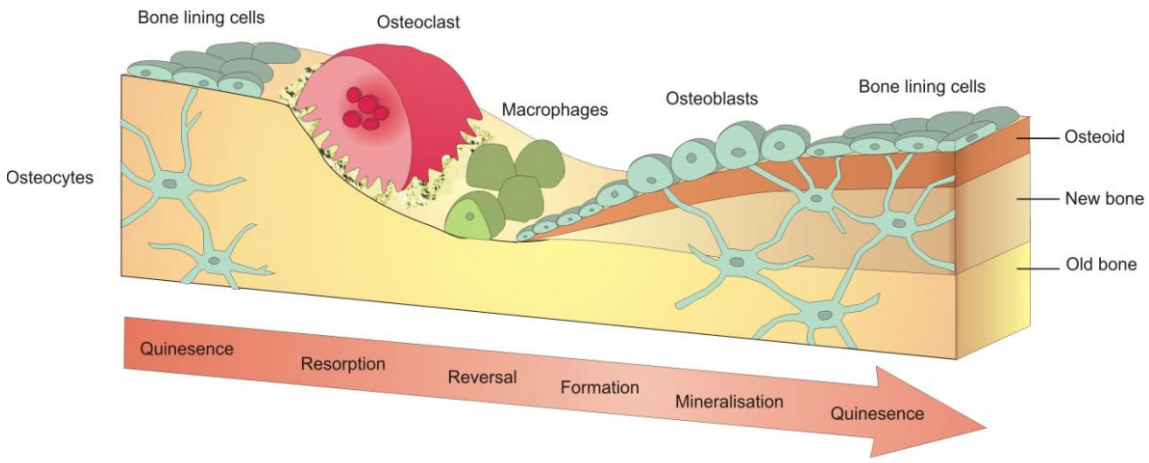

Figure 1.5: Cellular activity on bone surface: Bone resorption by osteoclasts and formation by osteoblasts

1.4 Bone modelling

Bone modelling is the process that takes place during new bone formation without prior bone resorption. This process may alter the shape of the bone, in which bone may be added or removed from periosteal or endosteal surfaces. Therefore changes in periosteal and endosteal remodelling around the bone are non-uniform with age (55). For example tibia acquires its mid-diaphysis curvature with development, by resorbing bone in the medial quadrant and forming more bone in the lateral quadrant (56, 57). Modelling occurs during the development phase of the skeleton in order to establish the skeleton's peak bone strength (47). In rodents both development and mature phases of the bone consist of modelling.

1.5 Bone remodelling

Remodelling occurs continuously on bone surfaces to maintain bone strength. During the remodelling process old bone is resorbed by osteoclasts and replaced by osteoblasts. Both osteoblast and osteoclasts are coupled biologically and work on an individual bone packet called basic multicellular unit (BMU) (1, 3). Cortical bone undergoes bone remodelling to produce Haversian systems, whereas bone remodelling in trabecular bone occurs on the surface of the trabeculae. The remodelling process is triggered by the microcrack formation and osteocytic apoptosis (58). The level of damage accumulation and the site where it occurrs is relayed through lining cells and surrounding osteocytes. Then, these cells release local factors that attract cells from the blood and bone marrow and subsequent cause osteoclastogenesis. Osteoclasts then resorb (**Figure 1.6**) the matrix and the microcrack followed by deposition of new lamellar bone by osteoblasts (1).

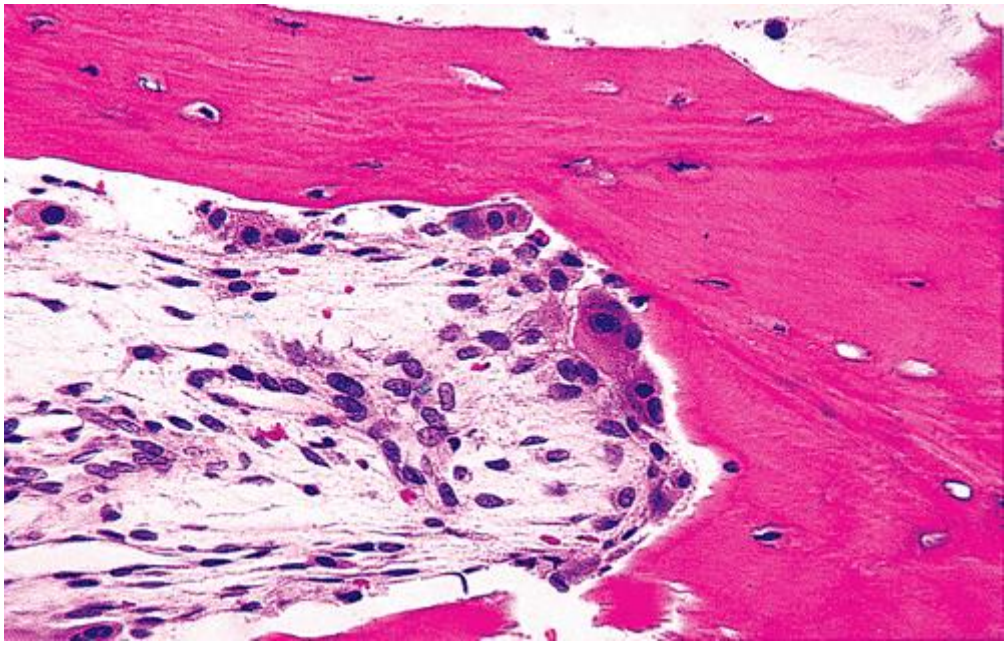

Figure 1.6: BMU of bone. Osteoclasts form the leading edge of the bone resorption (the cutting cone), and osteoblasts are secreting matrix and collagen in the newly created space (adapted from (46))

1.6 Bone mineralisation

The phenomenon and mechanisms underlying biomineralisation have been extensively studied with different techniques at the cellular and the molecular levels (7). It is accepted that biomineralisation is critically determined by physiological and biochemical processes (noncollageneous proteins and hormones) (59). However the mechanisms for initiation of mineralisation within the organic matrix are not completely understood. The key question which is not fully understood yet is how these mineral particles are delivered to the crystallization sites and in which chemical form. It has been suggested by several researchers (60-64) that the first deposited mineral in bone is not hydroxyapatite, but in a calcium phosphate precursor phase. Specifically, initially deposited amorphous calcium phosphate transforms into octacalcium phosphate and later changes into carbonated hydroxyapatite (dahllite) via hydrolysis, the mineral phase of mature bone. Presence of amorphous calcium phosphate in the newly forming bone was demonstrated by several studies (61, 64-66). It has been shown in the native mineralizing fin bone, amorphous calcium phosphate nanospheres are transported from cells to the collagen matrix, which then reinforce the collagen fibrils. However, the chemical

mechanisms transforming these precursor phases into crystalline platelets is not fully understood as yet (63).

The most widely accepted model of mineral reinforcement with preformed collagen matrix proposes the nucleation of mineral in the gap regions (**Figure 1.4**) of the collagen fibril (67). Atomic force microscopic (AFM) studies have found that with increasing time of mineralisation, crystals grow outside the fibrils compressing the triple helical molecules (68), and each collagen fibril is coated with mineral strongly adherent to the fibril surface through fusion with neighbouring crystals (69). SAXS measurements led by Fratzl and co-workers propose that during the early stages of mineralisation, thin mineral platelets fit into the gap zones, while subsequently platelets gain in thickness up to 3 nm, slightly compressing the micro fibrils surrounding them (70). Landis and co-workers (71) suggested that mineral particles replace water primarily inside the gap zones of the fibril, without a change in overall volume. As a consequence it was suggested that the collagen fibril consists of 60 % of gaps and 40 % of overlap zones. According to this suggestion it was speculated that the maximum mineral content that can be achieved inside the fibril is 43 % (72). Regardless of the precise mechanism, electron diffraction measurements show that the crystallographic *c*-axes ((002) in hexagonal close packed (*hcp*) structure) of the formed mineral crystals are parallel to the long axis of the collagen fibrils in bones (1, 73). The evolution in size of mineral particles with time has been studied using SAXS. It was found during the initial phase a strong increase in the mineral particle specific surface (surface per unit scattering volume) occurs, followed by a separate and distinct increase in particle thickness (8).

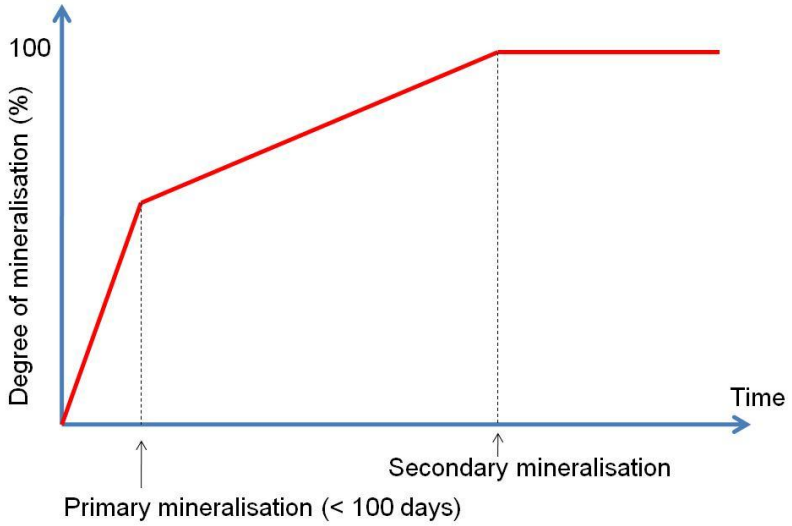

Figure 1.7: The different phases of mineralisation of bone tissue

At the micro-level, the mineral content of the bone can be measured by techniques such as quantitative backscattered scanning electron microscopy (qBSE) and energy dispersive X-ray analysis. The values obtained are within the range of 50 to 74 wt%, showing significant variation between different species, age and different locations in the same bone (74, 75). The degree of mineralisation can vary in humans between 0 to 43 vol% mineral content (76). Bone mineralisation is a two-phase process; a rapid primary mineralisation phase followed by a slower secondary mineralisation as shown in **Figure 1.7**. During the primary mineralisation phase, the collagenous matrix starts to get mineralised (up to 70 % of the final mineral content) over a period of several days. The remaining 30% of the final mineral content is filled by secondary mineralisation over a period of several years (77, 78). Due to this sequential process of mineralisation, at the micro-level bone material is made up of bone packets with different degrees of mineralisation depending on their local (tissue) age (as distinct from organism or organ age). qBSE and quantitative microcomputed tomography (microCT) can be used to measure the mineral content and the heterogeneity of the bone tissue mineralisation at the microscale level, and are being currently used in both basic and clinical bone research. A backscattered scanning electron (BSE) image of trabecular bone is shown in **Figure 1.8**, indicating different gray levels over the length scale of several tens of microns in the tissue. Darker gray area represent newly formed bone packets with lower average

mineral content (24.1 vol.%) compared to brighter areas, corresponding to older bone packets with higher mineral volume percentage (39.5 vol.%). The working principles of these techniques will be discussed in **Chapter 4**.

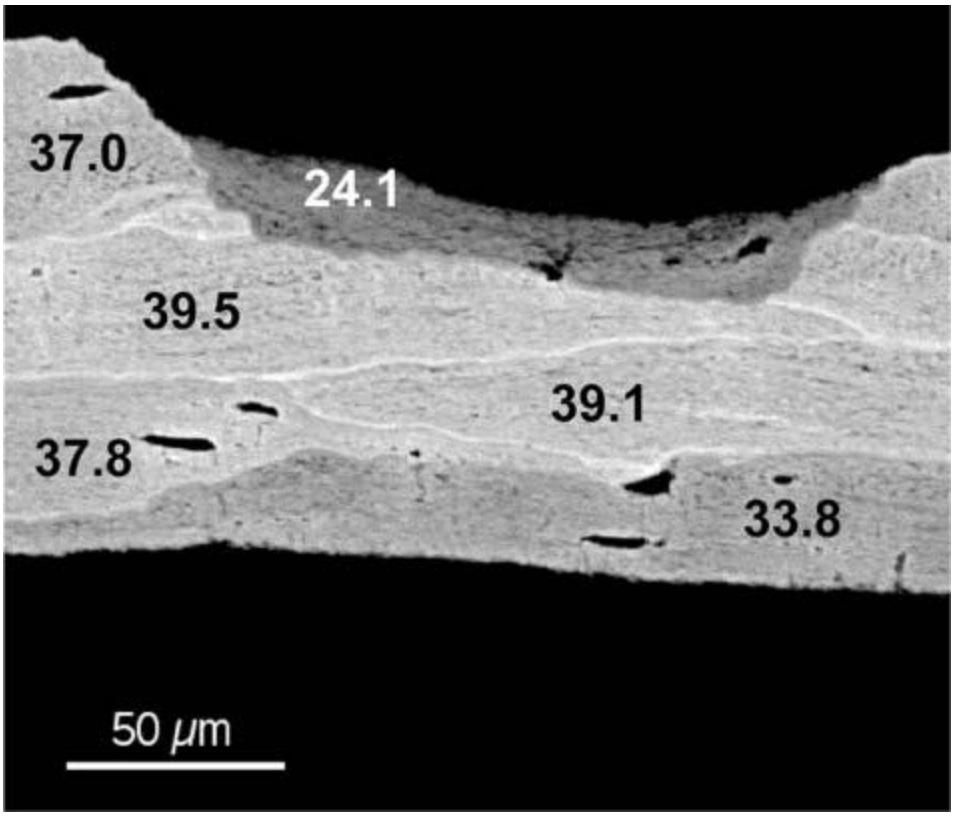

Figure 1.8: Backscattered scanning electron microscope image of trabecular bone showing different gray levels, which indicating bone packets with different mineral contents. Average mineral content at each individual bone packets is indicated by the mineral vol % shown numerically over the figure. (adapted from (8))

1.7 Deformation and fracture mechanisms of bone

1.7.1 Tissue level Deformation

As discussed in section 1.1, bone has a well-organized hierarchical structure. Each level of structural hierarchy plays an important role for the mechanical properties of bone. Considerable structural and mechanical experiments have been carried out to understand the structure-function relationship in bone at the macro- and microscale (5, 13, 14, 22, 24, 25, 79-83), and more recently, at the nano- and molecular scale (14, 82-87).

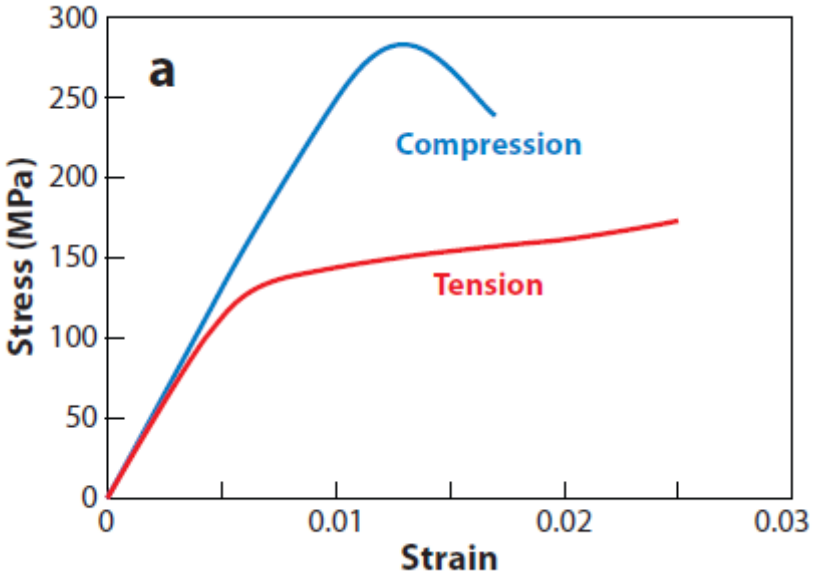

Figure 1.9: Typical stress strain curve for bone (adapted from(88))

Macromechanical experiments have shown that bone has higher compressive strength compared to tensile strength (89) (**Figure 1.9**). The most common mode of loading condition which, bones are subjected in physiologically is bending (90, 91). While bones subjected to bending forces are experiencing higher strain at the tensile zones, the maximum stress occurs in the compressive region (89). Under tensile loading bone exhibits a greater amount of inelastic strain (~ 2%) compared to compressive loading (~ 0.5%). Furthermore as previously noted that bone is a anisotropic tissue, both macroscopically (in terms of the shape of bones: long or flat) and microscopically (considering the oriented lamellae, fibrils and fibril bundles). It was observed that the stiffness of the lamellae along the fibril direction is 23 GPa, while in contrast, stiffness in direction transverse to the fibrils is only 16.5 GPa (92). At the microscale, trabecular bone exhibits a lower elastic modulus compared to interstitial bone of the diaphysis of cortical bone (1 vs. 20 GPa) (93). A similar behaviour (low modulus regions) was observed at the bone –cartilage interface with mineralisation gradient, which was proposed to have the function to allow transmission of loads from cartilage to bone without catastrophic failure. Gupta et al investigated the indentation modulus variation in lamellar bone in osteons (94). Using scanning nanoindentation, they found a variation of 24 to 27 GPa in modulus across the thin and thick sub-lamellae (with differing fibre

orientation) within a single lamella. In the interstitial bone region between two secondary osteons, the indentation modulus was significantly higher compared to osteonal lamellar bone. These researchers (94) also measured the mineral content using qBSE imaging, showing that mineral content positively correlated with the indentation modulus. They concluded that mineral content and fibre orientation significantly affect the modulus variation at the micro structural level in bone tissue (95). Several studies have used the fracture mechanics approach to understand propagation of cracks and micro damage formation, which provides insights on the bulk tissue behaviour (96-98). However, it was clear that the research so far on tissue-level mechanical properties have focused mostly on the strength, stiffness and fracture parameters, with the structural mechanisms underpinning these mechanical properties being relatively less investigated and understood.

1.7.2 Matrix-level deformation

The basic building block of bone matrix - the MCF - consists of Type I collagen molecules (tropocollagen) and carbonated apatite nanoparticles. This composite nature is crucial to their structural and physiological function. A second important factor at the nanoscale is the existence of interfaces both between mineral and collagen molecules (*intrafibrillar*) as well as between MCFs (*interfibrillar*), which play a critical role in load transfer from higher levels in the hierarchy to the smallest constituent elements (82). Macroscale failure strength and strain have been estimated by mathematical modelling for different modes of deformation (99), assuming that the interface between organic and inorganic phase is strong (100). However the chemical nature and the strength of these interfaces are not fully clear. MCFs in bone never exist in isolation, but merge with adjacent fibrils to form an array to make up the fibre (1, 3). Fibril arrangement inside the fibre may vary as well, increasing structural complexity and also influence mechanical properties of bone tissue (1). Due to the foregoing structural complexity, it is a challenge to probe the mechanics of collagen fibrils non-invasively and non-destructively in order to understand the nanoscale deformation mechanisms. Taking these difficulties into consideration, several research groups are currently attempting to understand the nanoscale deformation mechanisms, by techniques such as laser confocal microscopy

(101, 102), SEM (103) and AFM (69). These experimental studies were able to produce an in-depth view of bone ultrastructure, as well as to propose possible deformation mechanisms. A more recent approach, developed in this thesis, uses the structural resolving power of synchrotron X-rays combined with mechanical techniques to measure the deformation of MCFs *in situ* (14, 82, 104). These will be discussed in the following subsection.

1.7.3 Elastic deformation mechanisms

The structure and mechanical quality of the MCFs have been modelled mechanically by several researchers (82, 99, 105-109). Many of these model systems focused mainly on the mechanical properties of a single collagen fibril as a function of intrafibrillar mineral platelet parameters. For example, a three dimensional composite model was developed to determine the elastic properties of the single collagen fibril (105), and it has been proposed that shearing in the collagen phase between stiff mineral platelets inside a single collagen fibril was crucial to the high strength of the MCF (99). When mineral platelets are stacked in a laterally overlapped arrangement inside the fibrils, the difference between the tensile moduli in the mineral and collagen phases means that the stiff mineral particles are carrying predominantly tensile loads whereas the collagen phase transfers the load between mineral layers via shearing. It is easy to show (from force balance) that tensile stress in the mineral layer is equal to the product of mineral aspect ratio and shear stress in the collagen matrix (100). The high aspect ratio of the mineral platelets (~ 30 to 40 (110)) enabled a large contact area between the mineral and collagen phase, leading to the transmission of a large amount of force. Therefore balance of collagen strength, interfacial shear strength between collagen and mineral and strength of the mineral particles play a critical role in determining the ultimate modulus and strength of bone (99).

With the development of synchrotron facilities, several research groups performed *in situ* mechanical testing combined with synchrotron X-ray scattering to investigate deformation mechanisms in bone tissue at the supramolecular (nanoscale) level of the MCFs (82, 87, 111). Gupta et al measured the fibril, mineral and tissue deformation for a given external stress in real time. They used a customized tensile testing rig mounted on

a synchrotron beam line designed for simultaneous small- and wide-angle scattering and diffraction (SAXS/WAXD: **Figure 1.10**) to carry out *in situ* testing of fibrolamellar bone from the bovine periosteum (14, 82). The fibril strain was measured by tracking change in the D-periodicity (~65 nm) of the meridional banding patterns in collagen fibrils arising from the Hodge-Petruska model of intrafibrillar tropocollagen packing (32). The strain in the mineral phase was measured by percentage shifts in the wide angle diffraction spectrum. The tester was inclined to the X-ray beam at half the Bragg angle for the c-axis (002) *hcp* apatite reflection to ensure that strain measurements are only from mineral particles with c-axis along the loading direction. Tissue strain was measured by tracking movement of ink markers on the specimen surface.

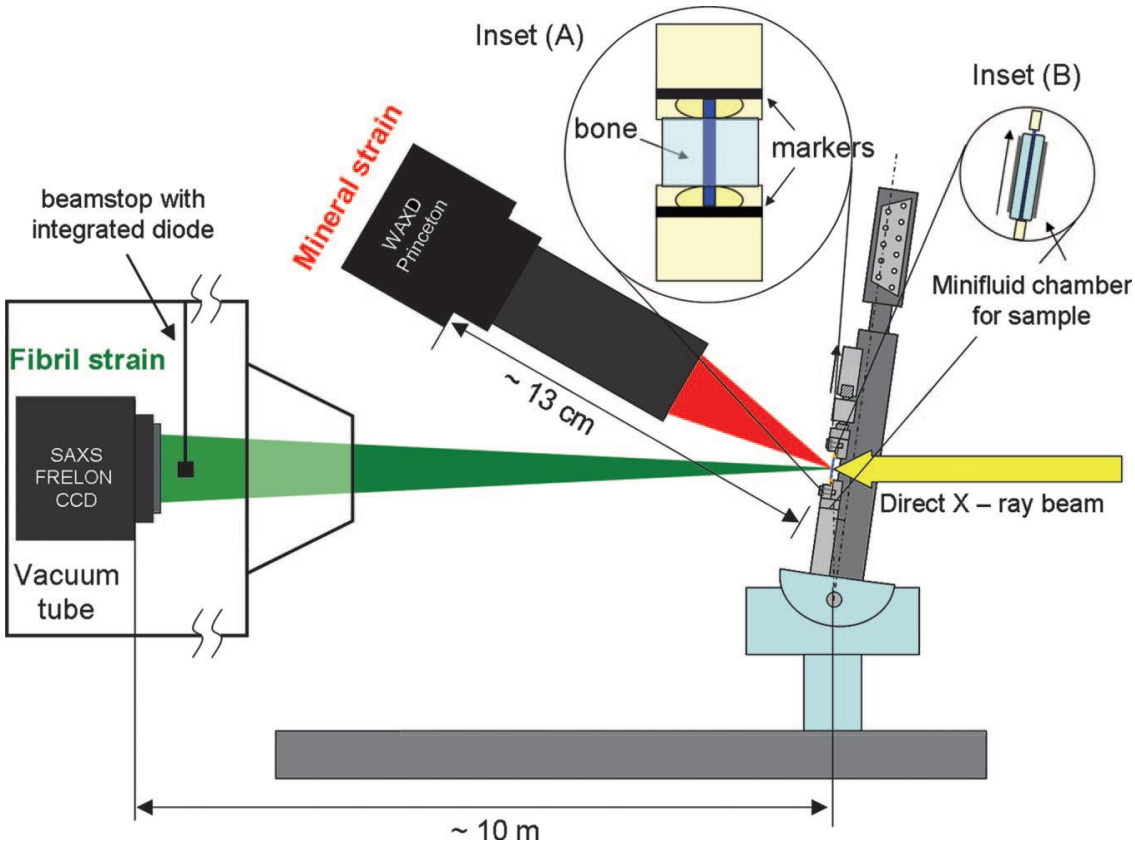

Figure 1.10: The schematic of microtensile testing combined with small and wide angle diffraction. (adapted from(14))

The key findings were that the tissue failed at an average tissue strain of 1.3 %, during which period the fibril strain increased from 0 % to 0.5 %, subsequently stabilizing at and beyond the yield point (tissue strain of 0.7 %). The levelling off of fibril strain to a constant, beyond the elastic/inelastic transition, led these researchers to speculate that

while tissue is strained beyond the yield point (plastic deformation), the MCFs are not. Further, fibrils did not return to a zero strain level beyond the yield point, indicating that they remained under stress. It was also observed that the fibril to tissue strain ratio increase with increasing tissue modulus in the elastic regime. The ratio is about ½ for less mineralised tissue (82) and increased to nearly 1 for increasing mineralisation. Since the primary means of increasing tissue modulus is via an increase in mineral content, this result suggests that at higher mineral content, the strain difference between fibril and tissue decreases. However, in this experiment modulus values were not varied in a controlled way but arose from the natural biological variance between samples. Based on these results, the influence of collagen hydration was modeled (82, 94). Lastly, a hierarchical staggered model based on combined measurements of fibril and mineral strain, in which both extrafibrillar and intrafibrillar shearing played a crucial role (107) was proposed. In this interpretation, MCF is considered as the stiff element as a whole, whereas the extrafibrillar noncollagenous matrix is introduced as the shear zone (82). Such a hierarchical scheme has a mechanical advantage in that the material becomes insensitive to cracks when the size of the mineral inclusions are below the scale of ~30-50 nm (110). The insensitivity arises from using the well-known Griffith's law to estimate the critical crack size required for a crack to propagate in a material (112). When the crack size drops below 30-50 nm, the theoretical stress exceeds the maximum possible breaking stress of the mineral, and cracks can no longer propagate. Finite element modelling has been used (106, 109), to estimate the mechanical properties of the MCF, and a continuum micromechanics model was also been developed to predict the ultrastructural stiffness of mineralised tissues based on isotropic hydroxyapatite crystal reinforced (cross linked) by unidirectional collagen molecules (113). Akkus et al predicted variation of the elastic stiffness tensor of MCFs with changing mineral volume fraction and mineral aspect ratio (106). Their model prediction was that the applied stress acting on mineral crystals was about 15 times greater than collagen stresses when fibrils were loaded longitudinally. The extrafibrillar mineral content also has a significant effect on the elastic deformation mechanisms. Molecular level modelling of the MCF has been used to generate stress-strain curves at different levels of mineralisation. **Figure 1.11** shows stress-strain curves for the MCF and for a non-MCF. In this modelling study, a

higher strength and greater energy dissipation under deformation was observed in mineralised fibril compared to the unmineralised fibril (114).

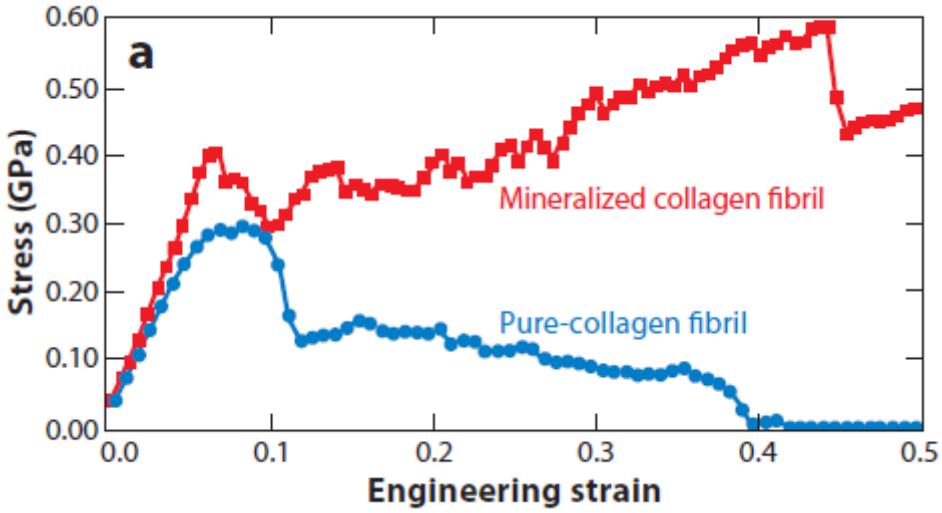

Figure 1.11: Computational (tensile testing) analysis of bone MCF vs. pure collagen fibril. Presence of mineral particles in collagen fibril leads to a significant difference on the deformation mechanisms (adapted from (114))

In a separate study Gupta et al, measured the tensile strains of collagen fibrils, mineral and tissue simultaneously (14). The strain ratio between the tissue strain and the strains of both collagen and apatite minerals obtained from this study is 12:5:2. Very interestingly, mineral strain also stabilizes at the elastic/ inelastic transition. In this hierarchical model stiff elements take up less strain than those at the higher levels of the hierarchy, as also proposed by Gao and co-workers (110) from theoretical considerations. Thus bone, as a composite, may sustain large deformation, despite containing a high volume fraction of stiff mineral particles at the nanoscale. These results are also consistent with measurements of fibrillar strain from partially mineralised turkey tendons (104) and parallel fibred bone (82). Another group used transmission high energy (80 KeV) synchrotron SAXS/WAXD combined with compressive loading on beagle fibulae and found substantial residual stresses ~ 100 – 200 MPa in bone, and inferred an increase in mineral crystallite size perpendicular to the load axis (111). These experimental results were further developed into 2D and 3D finite element models of the MCF (109). Using lab-based X-ray techniques, the mineral particle strain was found to be strongly dependent on the degree of alignment between load and fibre direction (115). Dong et al

measured the strain ratios between tissue level and nanostructural components at the compression (12:7:3.3) and it is slightly different compared with the ratios obtained from the tensile experiments (86). These differences in strain ratios could be due to the distinct experimental conditions (specimens obtained from different species and differing loading conditions: tensile - bovine and compressive - human). Despite the difference between strain ratios in tensile and compressive studies, in both experiments mineral particles has an average yield strain of 0.15% to 0.2%, whereas the estimated fracture strain of bulk microporous apatite is 0.1%. This enhanced strength of mineral particles in bone is most likely due the insensitivity of mineralised tissues (100, 110). Furthermore *in situ* compressive experiments showed relative deformation between collagen and mineral phases had very small correlation with the tissue level deformation prior to inelastic yielding. It was also found that collagen to mineral strain ratio is relatively consistent with the macroscopic strain in the elastic and the inelastic regime as shown in **Figure 1.12**. Thus there is no relative deformation existing between nanostructural components during compressive loading (86).

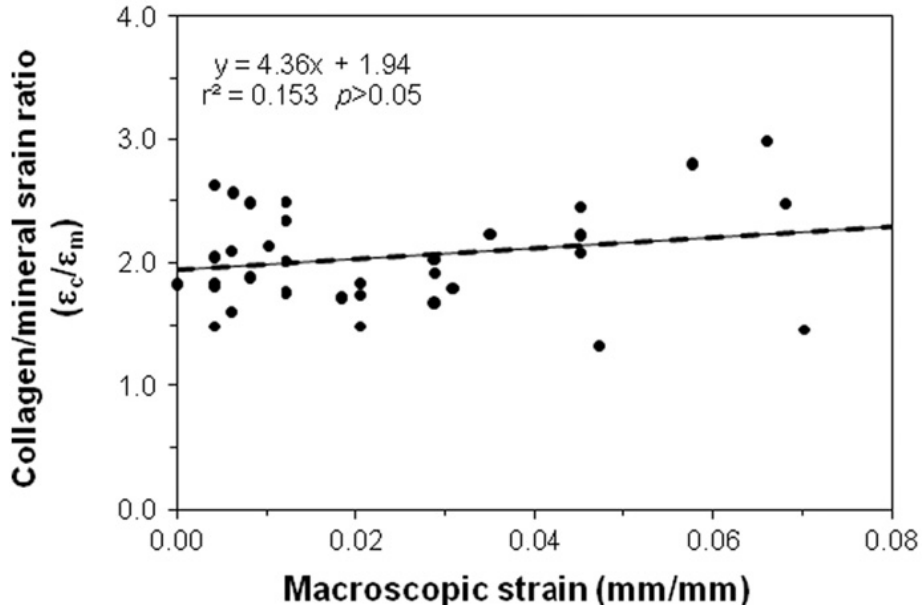

Figure 1.12: Collagen to mineral strain ratio plotted against tissue strain (adapted from (86))

Within the mineralised fibril, the organic matrix plays a vital role in transferring strain between mineral platelets. The shear transfer of load in the collagen phase occurs due to the greater elastic modulus in mineral (~100 GPa) compared to collagen (~1-2 GPa). The measured results of synchrotron X-ray experiments, with fibrillar to mineral ratios of 5:2

in tensile loading (14) and 7:3.3 in compressive loading (86), support this hypothesis. The suggested nanoscale deformation is shown schematically in **Figure 1.13**, where the stresses are transferred in zigzag manner and it is this multiscale shearing deformation mechanism between stiff and ductile components that prevents mineral platelets from being exposed to large stresses (14).

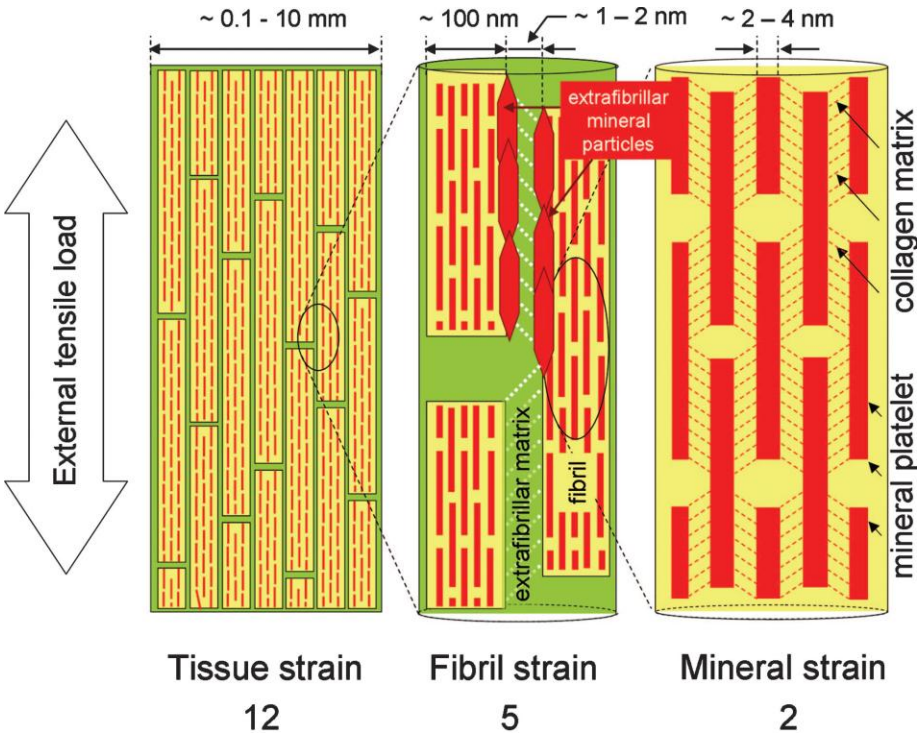

Figure 1.13: Schematic representation of nanoscale bone deformation in response to external tensile loading at three levels in the structural hierarchy. At the intrafibrillar level (right) mineral particles deform in tension and transfer load between adjacent mineral particles by shearing intrafibrillar matrix. At the collagen fibril bindle level, mineralised fibrils deform in tension and transfer stress between adjacent fibrils by shearing in the extrafibrillar matrix (adapted from (14))

1.7.4 Inelastic deformation mechanisms

1.7.4.1 Submicrometer length scale – Intrinsic toughening

Intrinsic toughening mechanisms in bone can be defined as the inherent resistance of the bone material to deformation and fracture, in other words the resistance to initiate cracks at the sub-micrometer length scale (116). The plasticity of the bone provides a major contribution to the intrinsic toughness by forming zones of plastically deformed material,

which absorb energy, around the incipient cracks (87). The permanent deformation in bone is the result of concurrent intrinsic toughening mechanisms, arising from different structures in the hierarchy at the micron-scale and below. It was reported, based on molecular simulations, that at the molecular level, breaking and reforming of hydrogen (H-) bonds during fibrillar stretching, provides one of the major deformation mechanisms in larger-plastic strains (without brittle fracture) of protein molecules, fibril and fibres (117). When applied forces are removed, these hydrogen bonds are reformed at strain levels of 10 % to 25 %, indicating that this mechanism is reversible (**Figure 1.14**). This reversible process mediates the deformation behaviour of collagen fibril and is hence believed to be important to dissipate energy. The force required to break H-bonds within the collagen molecules are strain-rate dependent (118, 119). Therefore at the molecular level, stretching and unwinding of collagen molecules provides the basic deformation mechanism.

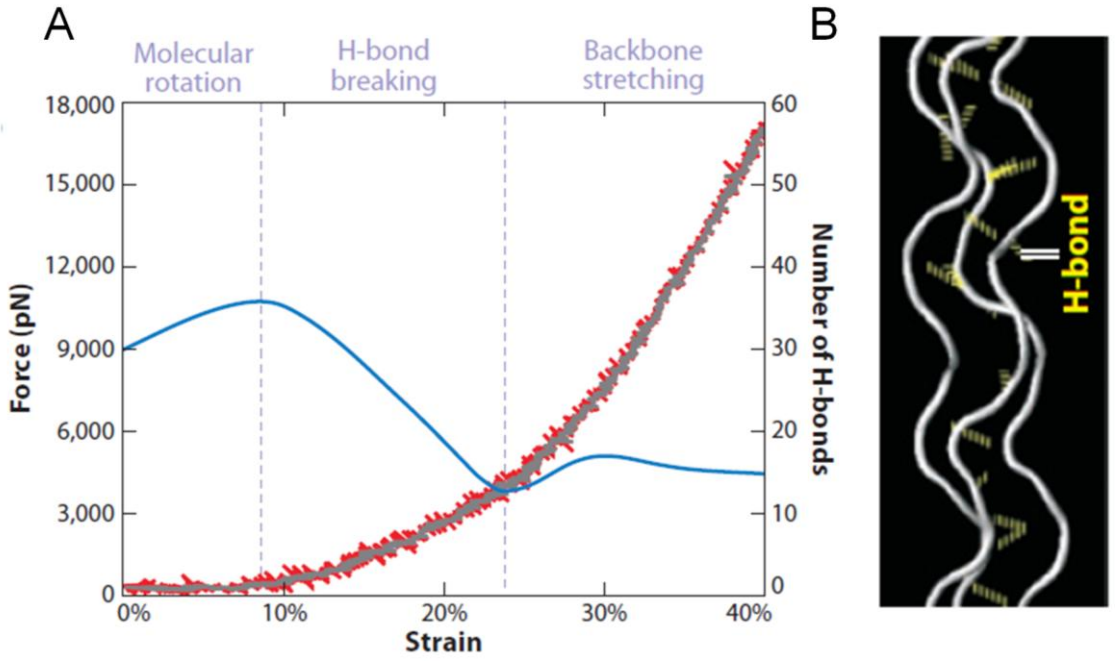

Figure 1.14: (A) Force – strain behaviour of tropocollagen molecules. Change in H-bonds with the molecular strain is also plotted in the same graph. Number of H-bonds decreases from 30 to 10 on going from strains of 10 % to 25%. Beyond 25% of strain, number of H-bonds stays constant and the backbone of the collagen molecule stretches. (B) **Schematic representation of H-bonds between tropocollagen molecules (adapted from (120))**

It was demonstrated, by molecular dynamics simulation and theoretical analysis, that adding mineral particles to collagen fibril leads to an increase in elastic modulus (4.6 to 6.2 GPa), yield strength and fracture toughness (114). Experimental studies have shown that the stiffness of the MCFs in mineralised turkey leg tendon enhances with increasing mineral content (104). It was speculated from the above simulation (114) that the slip between the tropocollagen molecules and mineral particle interface initiates the gliding between tropocollagen molecules and mineral particles beyond the yield point. In this intrinsic toughening mechanism, continuous glide or flow initiates between mineral particles and collagen molecules, to enable the dissipation of increased amount of energy by inelastic deformation compared to fibrils without mineral reinforcement (114). The mineralised fibrils are capable of preserving elevated failure stresses (0.6 GPa vs. 0.3 GPa for the pure collagen fibril) even after the yielding occurs (**Figure 1.11**) due to the additional frictional resistance (extrafibrillar mineral layer) to slip obtained by the mineral phase (114, 121). The analysis also showed that MCF starts its plastic deformation at 6.7 %, whereas pure collagen starts yielding at 5 %, indicating that MCF has greater energy dissipation under deformation compared to pure collagen. In the MCF, the formation of large localised plastic regions around the cracks increases the resistance to the fracture. These microcracks or localised yield regions (100) are of the order of hundred of micrometers in size (122).

The mechanisms of slip between collagen molecules and mineral platelets was also proposed by another research group (89) at the same length scale. These researchers observed appreciable stress and strain hysteresis during the loading and reloading tests of bovine bone with constant elastic modulus in the loading regime, and modelled this process at the nanoscale using a fibre-composite shear lag approach. In their model, the mineral/collagen irreversible slip causes the inelastic deformation of the bone tissue at macroscale. Due to the heterogeneity of shear stress along the mineral/collagen interface, the slip, in their model, initially occurs at the edges of the mineral inclusions. On unloading, incomplete reverse slip occurs at the fibrillar level. However, the model is solely at the smallest (MCF) level, and does not consider deformation mechanisms at higher length scales such as at the interfibrillar or lamellar level.

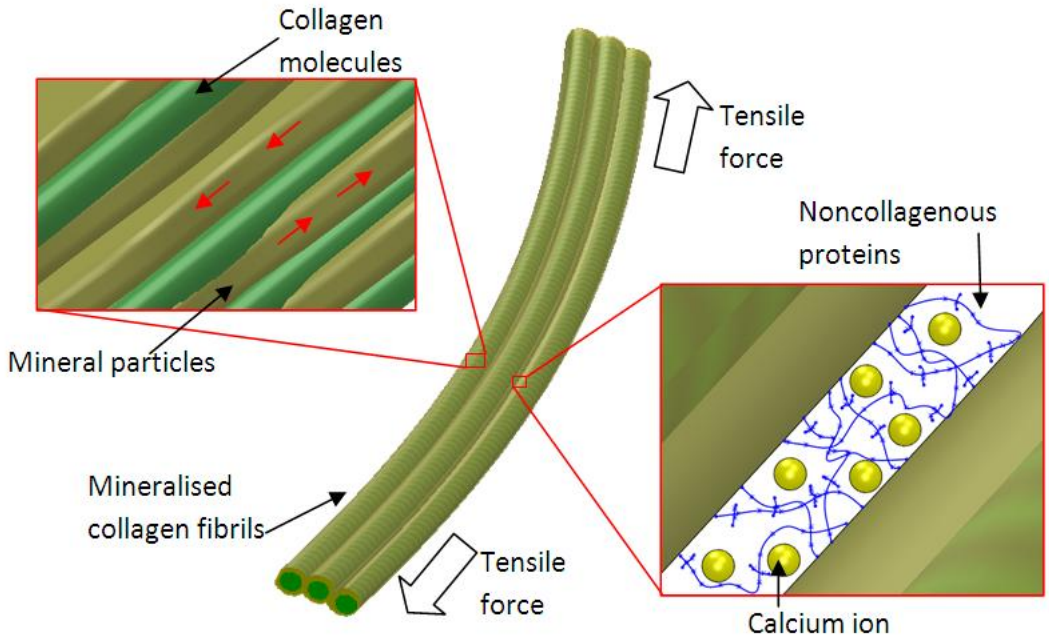

Figure 1.15: Intrafibrillar damage between mineral particles and tropocollagen molecules (top plane) and interfibrillar damage occurs between the mineralised fibril and the interfibrillar matrix (bottom plane)

At the next higher length scale (fibril arrays), the relative motion of MCF and the extrafibrillar matrix is believed to play a contributing factor to the plastic deformation. Gupta et al suggested, based on fibrillar-strain measurements as a function of stress using *in situ* SAXS, that beyond the yield point, externally applied stress exceeds the critical shear strength of the interface between the interfibrillar matrix and the fibrils, leading to irreversible interfibrillar sliding (82). This extrafibrillar matrix is believed to consists of noncollagenous proteins (osteopontin), proteoglycans (decorin) (123) and fused mineral particles (11). The noncollageneous proteins are macromolecules (phosphorylated protein polymers) in which sacrificial bonds have been suggested to act as a glue between collagen fibrils (45). As shown in **Figure 1.15**, sacrificial bonds have negatively charged phosphate groups that are capable of making stable ionic bonds with the divalent positive ions (Ca^{2+}) found on the surface of mineral particles. If the extrafibrillar matrix contains only these proteins, it is expected to be relatively weak and ductile. Under external loading, it is expected that it deforms by consecutive breakage of sacrificial bonds. Therefore fracture is resisted by frictional dissipation due to this breakage of sacrificial bonds and stretching of hidden lengths (124, 125). Using laser scanning

confocal microscopy, it has been shown that increased scattering of light (whitening) occurs in the plastically deformed bone specimens. These researchers suggest that whitening is due to the opening of interfaces between fibrils (126). Furthermore, the fused mineral particle layer in the extrafibrillar space increases the friction due to the fibrillar sliding and reduces the deformability. Using antler bone, Krauss et al showed an increasing heterogeneity in fibril strain beyond the elastic region due to the progressive decoupling between fibrils (127). Tai et al claims that in the inelastic regime, frictional stresses occurs due to the disruption of bonds between matrix and mineral particles (128).

Using thermal activation analysis and structural information from synchrotron data, it was suggested interfibrillar or intrafibrillar decohesion in the mineralised collage fibrils mediates bone inelasticity. This irreversible deformation in bone may be due to the ionic bonds breaking between collagen fibrils (in the extrafibrillar matrix) or between collagen and mineral platelets in the intrafibrillar space (129) and disruption of sacrificial bonds between collagen fibrils (123, 124). Dong et al observed that mineral and collagen fibril stretches until the yield region and subsequently the strains sharply decreased and then gradually stabilize at 0.3 % for the collagen and 0.15 % for the mineral. These researchers also suggested the most dominating factor in the bulk deformation of bone tissue in compression beyond the yield point is obliquely oriented mineral particles and collagen fibrils. According to the interfibrillar sliding model suggested by Gupta et al, when the tensile strain increases beyond the yield point, the damages begins to accumulate between the fibrils leads to appearance at larger length scale as cracks (130). These cracks were observed in the SAXS images in the form of streaks in the perpendicular direction to the crack path. It was suggested that combination of elastic stretching of collagen and sliding between the mineral and collagen accounts for hardening effect and the plastic behaviour of bone beyond yield point. An elastic behaviour of the collagen in the inelastic region is due to the set of complex interactions between mineral and collagen layers (82).

It can be concluded from these experimental studies, modelling and speculations of bone material, that the structure and function relationship in bone at the nanostructural level has been of wide and growing interest to the scientific community. It has become apparent that the bone mineral phase or collagen phase alone does not determine the mechanical properties of bone tissue. Therefore it is crucial to obtain mechanical information at the MCF-level, which is the basic structural unit of bone. In this regard, it was shown in the previous section that many experimental studies performed to investigate the link between structure and function of MCF are based on X-ray methods like SAXS and WAXD. Such a technique could be used to develop a clinical *in-vitro* diagnostic tool to examine the bone material level alterations due to the metabolic diseases, and this is the aim of the present thesis.

1.7.4.2 Micro to near millimetre length scale – Extrinsic toughening mechanisms

At a larger length scale in the range of micrometres to millimetres, additional structural mechanisms are activated in response to loading, which have an important role to play in determining ultimate fracture resistance. The toughness of bone is related to the capability of bone tissue to absorb energy during the failure, and this is quantified most frequently through the energy to fracture and fracture toughness (87, 131, 132). The energy to fracture per unit area is defined as the area under the stress-strain curve. For example Currey et al measured the energy to fracture of cortical bone of human femur by tensile testing to be 3400 J/m^2 (133). Fracture toughness of a material is assessed from the amount of energy dissipated due the formation of new surfaces in a steady-state condition (134). Ritchie and co-workers have extensively studied the fracture toughness of human bone using fracture mechanics approach (98, 131, 135-140). Recently these researchers investigate the fracture toughness of bone tissue under combination of three loading conditions: tension, shear and out of plane shear using symmetrical and asymmetrical notched four-point bending (140). These experiments showed that fracture toughness values for bone obtained from the above combined loading conditions are intermediate between those measured from pure tensile and shear loading experiments (140, 141). As a corollary, during physiological (mixed-mode) loading conditions, these

researchers pointed out that the resistance to fracture of bone will be dependent on the trajectory of the crack path, the resultant force of maximum crack driving force, and the weakest microstructural resistance force (142).

In a heterogeneous, anisotropic material like bone, cracks originating at the nanoscale are strongly influenced, by their extension behaviour, by structural features at the microscale. These include crack deflection, uncracked ligament bridging and microcracking, which act to inhibit the further propagation of the main crack. The crack path will, for example, be deflected at weak interfaces like cement lines around the osteons. Since most of the osteons are aligned along the long axis of the bone, these microstructural interfaces are easier to fracture along the bone axis than in the transverse direction. Due to this marked anisotropy in the bone fracture properties, toughness in the transverse orientation is considerably lower in shear than in tension (142).

Microcracks

It was suggested that plasticity mechanisms arising at the fibrillar level (ahead of the crack) serve to limit the microstructural damage by dissipating the energy and blunting the crack tip (139). Microcracks usually form at weak interfaces such as the cement lines or hypermineralised boundaries of the primary osteons (mice bone) and they are primarily along the long axis of the bone. The exact mechanisms of microcrack formation are not fully understood, however Parsamian and Norman speculated that fracture or separation of the hydroxyapatite crystals surrounding collagen fibres may causes the diffuse damage and microcracks in cortical bone (143). Since previous studies have also shown microcracks usually originate in the vicinity of macrocracks as shown in the **Figure 1.17,** it has been speculated that microcracks are responsible for the rising behaviour of resistance to fracture in bone (101, 144).

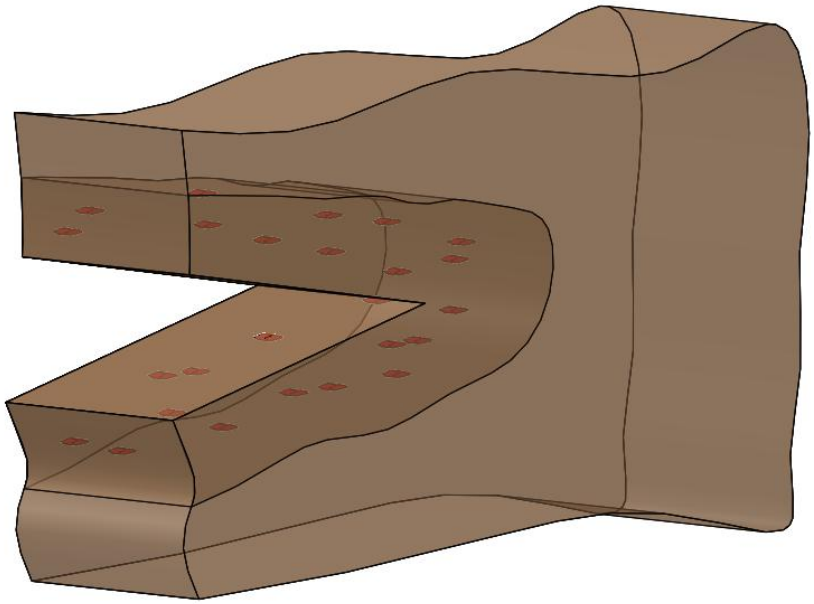

Figure 1.16: Microcrack formation around the macrocrack where the localised stresses are highest

Several researchers have been shown that repetitive mechanical loading has a significance influence on microcrack formation at the ultrastructural level. These discrete microcracks are easily visibly under bright-field light microscopy (145, 146). Microcrack accumulation in the extracellular matrix also triggers the remodelling process via cell (osteocytes) sensory mechanisms. During ageing and in metabolic bone diseases, the presence of abnormal remodelling (faster resorption) levels increases the microdamage accumulation which leads to fracture (147).

There are several experimental techniques which have been used to investigate microcracks, including SEM, laser scanning confocal microscopy, and optical microscopy. Out of the techniques most commonly used technique is confocl microscopy. Using bulk staining of bone samples optical microscopy was used to show that repetitive physiological loads are capable of creating two types of micro damage: microcracks and diffuse micro-damage. Microcracks are visible in 2D plane sections as clear linear cracks (**Figure 1.17A**), while diffuse microdamage is 3D in nature, appearing as a cloud (fine network of smaller cracks (148)) in 2D plane as shown in **Figure 1.17B**. Most microdamage is found in interstitial bone which may be due to the following reasons: 1) interstitial bone is formed prior to the osteons where no remodelling has

occurred, 2) older bone is more prone to damage due to the altered mineral and collagen and 3) interstitial bone contain more damage zones because it is subjected more fatigue loading compared to osteonal bone (149). Burr and Stafford developed criteria to identify microcracks in a stained bone sample. Microcracks (~ 300 µm) are larger than the osteocyte canaliculae and smaller than blood canals. They consist of sharp borders with less strained in the middle gap region (150). Structural elements like vascular canals and osteocyte lacunae can initiate microcracks by creating stress concentrations in the bone tissue. Furthermore bone tissue with higher mineral content is also associated with greater level of microcracks (151).

Bones that are subjected to different loading modes, appear to show different types of damage accumulation. For example compressive and tensile zones in bones subjected to bending forces accumulates linear microcracks and diffuse microdamage respectively (152). It has been claimed that microdamage accumulates more rapidly in the tension zone compared to the compression zone (96). The growth of the microcracks in the tensile zone is limited, whereas microcracks formed in the compressive zone are long and linear (**Figure 1.17A**). These small microcracks observed in the tensile zone produces a fine network of diffuse damage (**Figure 1.17B**) (96).

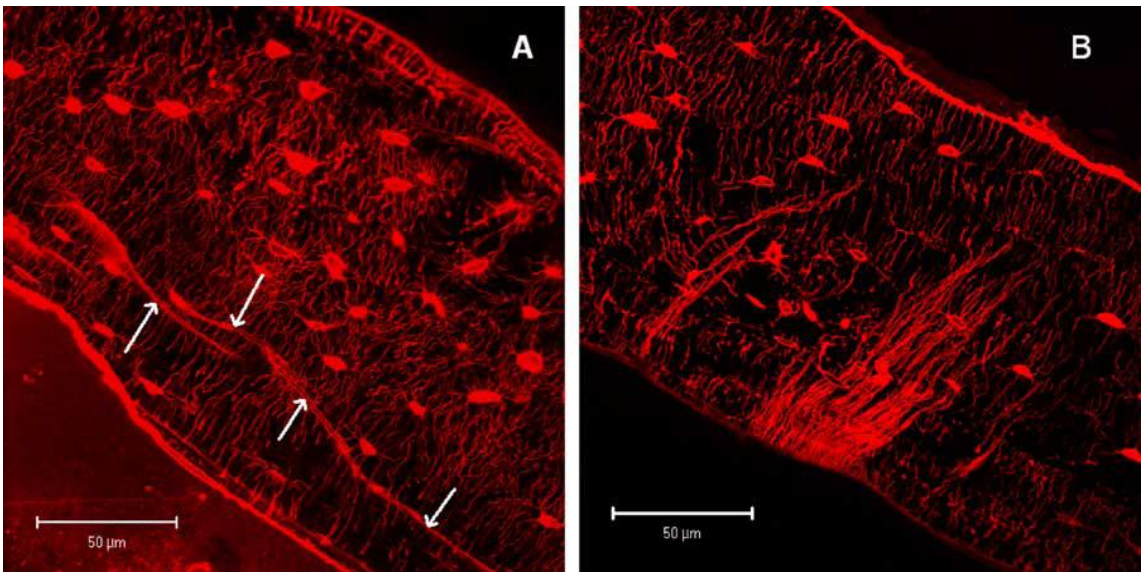

Figure 1.17: Microcracks developed at compressive (A) and tensile zones (B) after fatigue under four point bending testing (adapted from (147))

Due to the composite behaviour of the bone tissue, microdamage and mechanical properties in bone are generally known to be associated. The correlation between microdamage and alterations in mechanical properties depends on the type of microdamage and loading mode (uniaxial loading, bending and monotonic vs. fatigue loading). For example microdamage accumulation due to the fatigue loading coupled with progressive loss of stiffness has detrimental effect on bones mechanical properties (153). However under appropriate conditions, microdamage and crack formation may also have a beneficial effect on the mechanical properties. The increased energy absorbing ability of bone which can dissipate stresses by forming a network of microcracks will enhance the fracture resistance (154). The foregoing study proves that microdamage does have an effect on improving toughness in bone but up to a critical threshold of accumulation. The growth of cracks exceeding a critical crack length ultimately causes fracture of the whole bone (155).

Crack Deflection

In human cortical bone the cement lines surrounding each secondary osteons forms a mechanically weak interface parallel to the loading direction, as stated previously. Microcracks that originate perpendicular to the crack path can deflect the major crack to an indirect path. These indirect crack paths consist of rough surfaces. The deviation of the major crack path away from the maximum tensile stress plane and blunting of the crack tip reduces the stress intensity at the tip (138). Several other studies have shown that cracks may be deflected in other paths as well (132, 135, 156, 157). In a recent study using BSE on mouse bone it was revealed that blood canals play vital role in deflecting cracks (135). The interstitial bone between the secondary osteons (**Figure 1.19**) also has the ability to deflect cracks (157). It was also reported that osteonal lamellar boundaries within the Haversian systems also act as crack deflectors (132, 156).

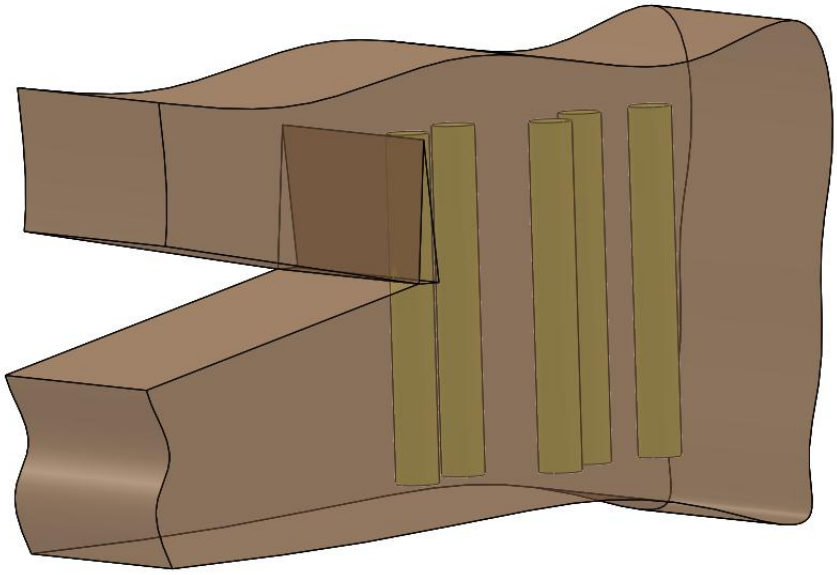

Figure 1.18: Crack deflection along the secondary osteonal boundary

The crack deflection and twisting along the osteonal boundary was observed in elk antler bone, one of the toughest material so far recorded (120). The experiments performed with antler bone showed that the crack twisting angle is approximately 90° from the main crack path, leading to an increase in fracture toughness by a factor of six or more compared to the propagation in the same plane (158).

Uncracked ligament bridging

The cracks propagating along the longitudinal orientation of the bone are roughly parallel to the microcracks in the cement line. These microcracks form ahead of the main crack tip and develop uncracked regions along the crack length that bridge the main crack as shown in **Figure 1.19**.

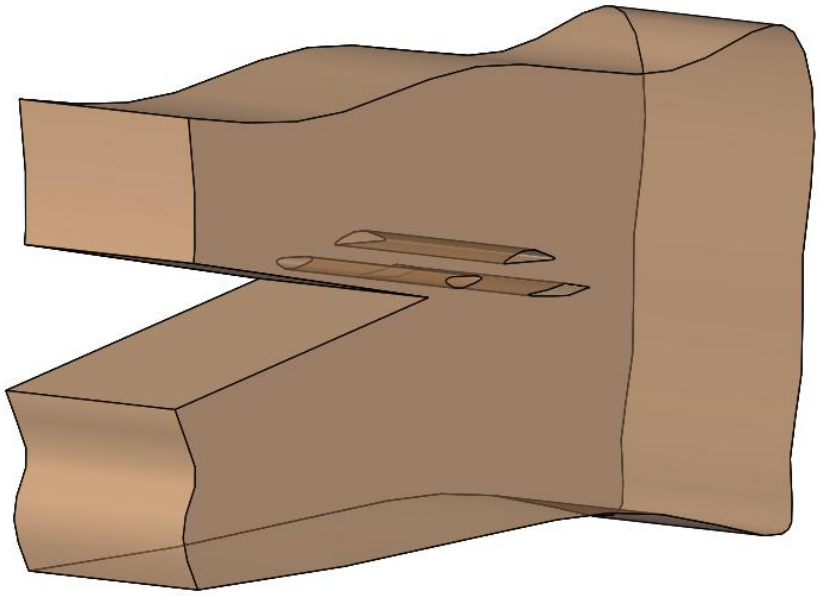

Figure 1.19: Uncracked ligament bridging act as a toughening mechanism in the longitudinal orientation of the bone tissue

Collagen-fibril bridging

At submicron meter length scale, collagen fibrils and fibres at the boundary of lamellar layers act as a bridge in the wake of the crack tip (**Figure 1.20**) to prevent it from opening the crack further. These collagen fibril bridging in single crack propagation does not increase the total fracture toughness of the bone, however the cumulative effect on several cracks increases the fracture resistance (97). Nalla and co-workers argued this is one of the most dominant mechanisms in resisting fracture (131).

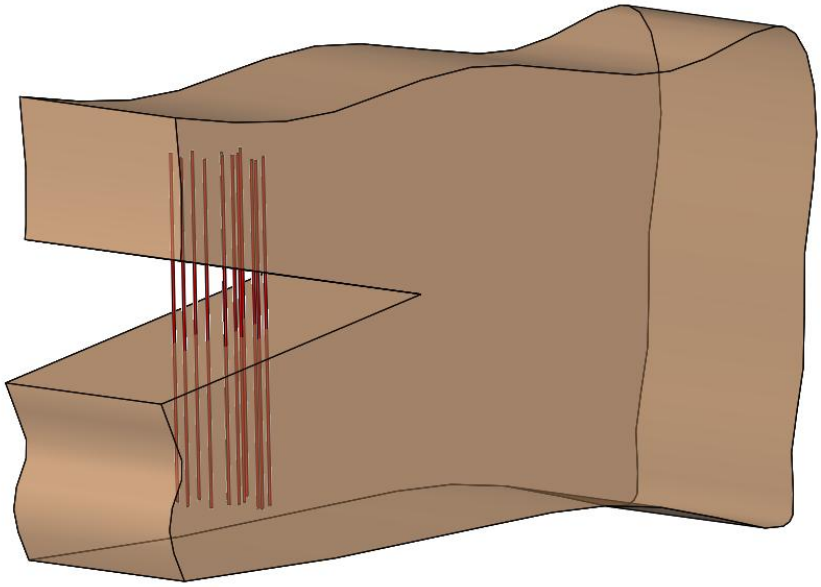

Figure 1.20: Crack bridging by collagen fibres at the wake of the crack tip to resist the fracture

It was shown by other studies that collagen fibril orientation differs across adjoining lamellae (1, 130), leading to variations in stiffness across bone lamellae. Due to this heterogeneity of modulus, when the crack develops in one lamella, the adjacent layer is capable of bridging the damage layer by sustaining the load. (130).

1.8 Bone diseases and their structural and mechanical pathologies

There are number of skeletal disorders that can impact the structural and mechanical properties of bone as a material. Reduction in mechanical and structural competence of the bone matrix by these diseases can often lead to fracture and severe patient pain, immobility and associated degeneration of other tissues like cartilage. Although fracture is most often the clinical manifestation of a disease, the ultimate cause lies often deeper in one or more of the hierarchical levels of the bone material, and is also intimately bound up with alterations in cellular and endocrinal activity. Bone diseases can be classified in various manners, one example of which is presented below (159).

- Endocrinopathies – hypercortisolism, hyperparathyroidism
- Deficiency states – rickets/osteomalasia, scurvy
- Drugs – glucocorticoids heparin, alcohol

- Hereditary diseases – *osteogenesis imperfecta*, homocystimuria

Bone diseases can be metabolic, congenital or an implication of other health issues such as cancer. The normal function of bone requires a precisely regulated supply of amino acids, calcium and phosphorus, hormones, vitamins and enzymes. Metabolic bone diseases can be defined as skeletal diseases arising due to the inadequacies in the supply or action of the mineral phase, the organic matrix, the cellular processes of remodelling and the endocrine, nutritional and other factors which regulate the mineral amount in the body, associated with abnormalities outside the skeleton (159). The main focus of this thesis is on disorders of bone matrix associated with several metabolic bone diseases, some examples are presented below:

1.8.1 Osteoporosis

Osteoporosis is defined as "a skeletal disorder characterised by compromised bone strength predisposing a person to an increased risk of fracture" (160). Bone strength is a combination of both bone quantity and bone quality. Bone mineral density (BMD) is the diagnostic criteria which is established by the World Health Organisation measured by the Dual-energy X-ray Absorptiometry (DXA) (161). There are two categories of osteoporosis, primary and secondary. In all types of osteoporosis, reduction in the amount of bone is a direct result of osteoclastic activity (resorption or bone removal) that cannot be matched by osteoblastic activity (bone formation) (162). The increase in the fragility of osteoporotic bone has also been speculated to be due to a reduction in collagen fibres and weaker collagen cross linking, caused by an increase in both synthesis and degradation of collagen as well as higher number of immature cross-links (163-165), but this has not been directly tested. Osteoporotic bone also undergoes a higher collagen turnover and a reduction in mineralisation compared to the age-matched non-osteoporotic bone. Previous studies have shown that mineral content in osteoporotic bone is reduced by 40% compared to healthy bone (166). There is no change in collagen concentration in osteoporotic bone; however the bone mineral in osteoporotic bone is more crystalline or mature than normal bone (162, 167, 168)

1.8.1.1 Primary Osteoporosis

Ageing, postmenopausal osteoporosis in women and idiopathic osteoporosis can be classified as primary osteoporosis (161, 169). Primary osteoporosis is more commonly seen in women. Post-menopausal osteoporosis is due to an increase in bone resorption and systemic calcium imbalance caused by menopause-induce estrogen deficiency (170) leads to lengthening the life span of the osteoclasts. Esteogen deficiency also decreases the amount of bone formation by suppression of osteoblasts activity. Elevated remodelling rate has a greater adverse effect on spongy bone compared to cortical bone due to its high surface area. A large amount of trabeculae bone is removed in each remodelling event resulting in loss of trabecular struts and connectivity (**Figure 1.21**) which is more detrimental to bone strength compared to trabacular thinning. Severe age-related and idiopathic osteoporosis typically occur in men (161) and is largely due to the trabecular thinning compared to the trabecular perforation .

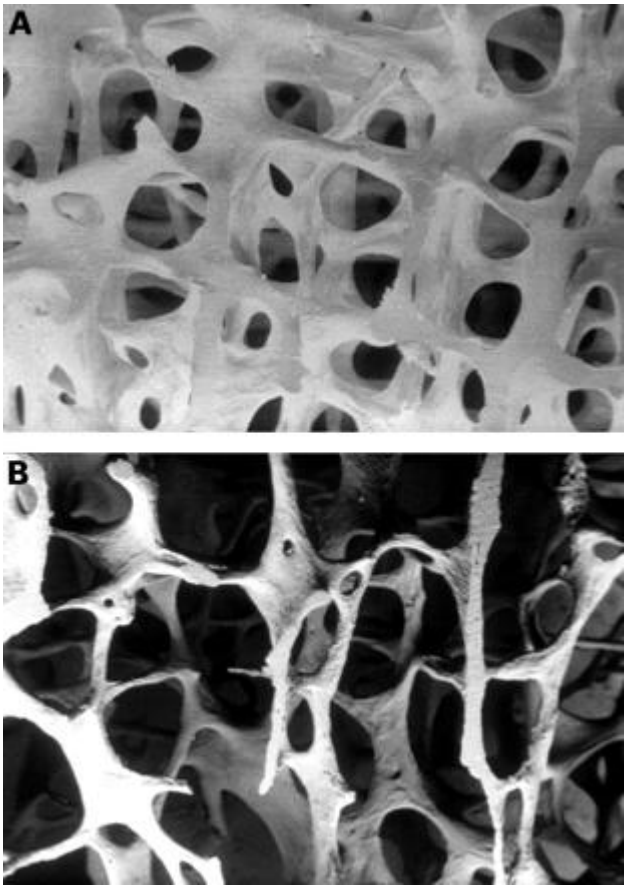

Figure 1.21: Scanning electron microscope image showing trabeculae architecture of healthy and osteoporotic bone with thinning and loss of struts (adapted from (171))

1.8.1.2 Secondary Osteoporosis

Secondary osteoporosis caused by excessive alcohol intake, medication (e.g. glucocorticoids), hypogonadism, hypercortisolism and hyperthyroidism (161). It is more commonly experienced by men and premenopausal women. 30 to 60 % of osteoporosis in men is due to hypogonadism, use of glcoorticoids and excessive alcohol intake. More than 50 % of osteoporosis in premenopausal women is caused by hypoestrogenemia, use of glucocorticoids, thyroid hormone excess and anticonvulsant therapy (160).

Glucocorticoid induced osteoporosis

The most common form of secondary osteoporosis is glucocorticoid-induced osteoporosis (GIOP), widespread mainly due to excessive alcohol intake and anti-inflammatory glucocorticoid treatments prescribed to an elderly patients suffering from

overactive immune system disorders such as asthma, autoimmune diseases, arthritis rheumatism, hyperthyroidism and hypercortisolism (172). There are several short term (high blood glucose levels, insomnia and euphoria) and long term side effects (Cushing's syndrome, glaucoma and cataracts) associate with this particular steroid therapy. Patients exposed to glucocorticoids have a higher fracture risk at a similar BMD level (~ 930 mg/cm^2) measured by DXA compared with non-users (173, 174). This indicates that bone quantity, as currently assessed by BMD, is not the overriding, or sole, factor in fracture risk. The foregoing statement is supported by data that suggests fracture risk strongly correlates with the dose of glucocorticoids given and the duration of their administration (172). Glucocorticoid dosage also has a positive relationship with osteocyte apoptosis (175) in the GIOP disease state, alluding to a potential link between osteocyte behaviour and fracture risk. Changes in osteoporotic bone cannot be diagnosed externally, however larger resorption cavities are observed internally and the bone tissue is reduced significantly causing trabecular thinning. Rapid reduction in trabeculae and gradual loss in cortical bone is result in mechanical failure leading to spontaneous fractures (49). Due to the elevated osteoclastic activity and suppression of osteoblasts (**Figure 1.22**) there is less bone to sustain the load. Therefore in the osteoporotic bone, microcrack and/or damage accumulation may directly lead to fracture upon exceeding the local stress concentration of the bone matrix (176).

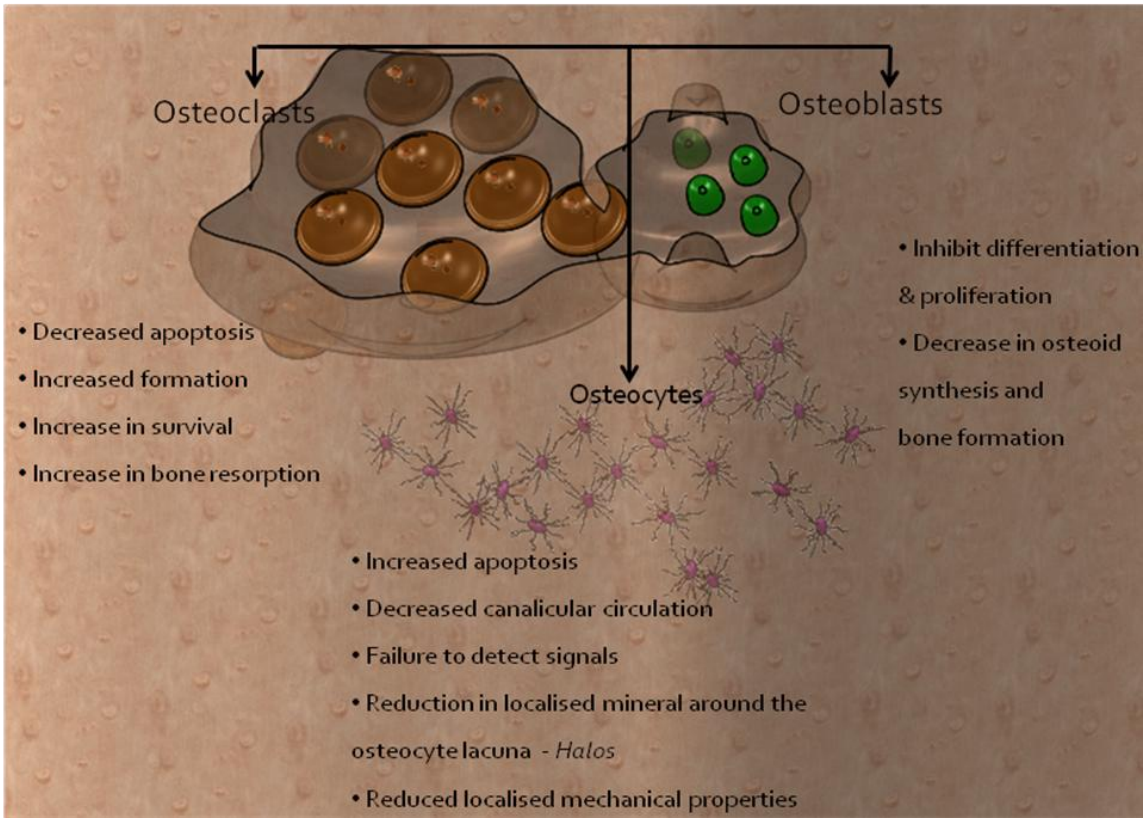

Figure 1.22: Direct effect of glucocorticoid treatment on the bone cells: osteoblasts, osteoclasts and osteoctytes (177-179)

Clinical evidence exists that the nanoscale structure in osteoporosis and related conditions is distinct from normal tissue. The increase in fracture risk in osteoporotic bone could be also due to the weaker cross linking between collagen fibres caused by an increase in both synthesis and degradation of collagen as well as higher number of immature cross-links (164, 165). An avian model of osteoporosis showed altered collagen cross-linking (180) exist in the osteoporotic bone matrix. Therefore, moving beyond BMD measurements by DXA, it is important to understand the nature of the nanostructural alterations, in order to diagnose the fracture risk more precisely.

1.8.2 Osteomalacia/ Rickets

Rickets and osteomalacia are disorders that result from decreased mineralisation and cause progressive deformities in the lower extremities, growth retardation and poor dental development. Decreased growth plate mineralisation or rickets is seen only in children because adults no longer have active growth plates. The decrease mineralisation

in remodelled bone is known as osteomalacia and can be found in all ages. Rickets and osteomalacia are usually divided into hypocalcemic and hypophosphatemic, based on which mineral (Ca or P) is deficient. X-linked dominant hypophosphatemic rickets (XLHR) can be considered as the most prevalent genetic of disorder form which is due to the deficiency in phosphorus. XLHR is caused by mutations in the *Phex* (phosphate-regulating gene with homologies to endopeptidases on the X-chromosome) gene (181). *Phex* gene encodes an endopeptide that resembles a protease responsible for degradation of phosphatonins. Phosphatonins are factors which down regulate the serum phosphate level. This is achieved by inhibition of renal phosphate reabsorption and reducing the activity of the 1α-hydroxylase enzyme leading to inappropriately normal levels of 1,25 (OH)2 vitamin D3 (182). The primary phosphatonin candidate is fibroblast growth factor 23 (FGF23) and increased levels of this factor has been observed in XLHR (183). These phosphatonins are mainly produce in the bone and act on the proximal renal tubular cells. Proximal renal tubular reabsorption of phosphate is regulated by changes in the activity, number, and intracellular location of the brush border membrane (184). These alterations in serum levels of phosphate-retaining enzymes critically affect the mineralisation process in the skeleton, by changing the amount of available phosphate for mineralisation. Phosphorus in serum moves in and out of bone as needed (approximately 3 mg/kg/day) (183), and its concentration is important in determining the rate of bone mineralisation. As describe before mutated *Phex* function causes decrease in extracellular P_i and Ca levels leading to impaired bone mineralisation. The impaired mineralisation caused by rickets and osteomalacia clearly alter the bone material quality and must thereby amend the remarkable mechanical properties of bone.

1.8.3 Ageing

With ageing the functionality of bone, including both mechanical and homeostatic functions (allowing locomotion and load bearing, protection of internal organs and storage for calcium homeostasis), become impaired (185). Understanding how changes in the structure of the bone matrix due to the ageing process which leads to increase the risk of fracture is clearly very important clinically. Human cortical bone from 34 to 99 years old age showed 40 % reduction in the crack initiation toughness, and complete loss of

crack growth toughness with increasing age (136). When considering age-related increases in fragility, it is important to remember that the components of the bone at different hierarchical levels are maintained in balance to resist the fracture by absorbing the energy from impact loads. Shifting the balance in mineral content to higher mineral concentration will generally yield stiffer but more brittle bone. Alterations to the collagen structure in bone is also an important factor to consider during ageing, because enhanced cross-linking contributes towards to brittleness and may also affect the morphology of the mineral phase indirectly.

It has been also shown in a previous study that older individuals have 10-fold increase in fracture risk compared to younger individuals but with the same BMD (186). Several studies have reported both cortical and trabecular bone becomes more brittle and weaker with age (187-189). At this structural level (1 μm to 100 μm) imbalance between micro crack initiation and removal of crack by remodelling process leads to an increase in damage accumulation which will contribute to lower strength and stiffness of the bone. Schaffler et al reported that accumulation of microcracks are highly abundant in human femoral cortical bone in individuals above the age of 40 years (190). Younger individuals develop increased amount of microcracks compared to older individuals due to their higher activity level as well as being subjected to repetitive loading for a greater duration of time (e.g. running, skipping or other athletic activities). However young people have greater physiological capability compared to older population to sustain with larger loads, because microdamage is continuously repaired with new bone in young adults (191). Furthermore, progressive Haversian remodelling occurs in human cortex with increasing age leads to a large density of osteons and cement lines, which provides the prime site for microcrack formation and smaller uncracked ligament bridges, leading to propagation of the crack (136, 137, 192).

The cause of initial stages of alterations at the ultrastructural level due to the ageing process is hypothesised to be either, debonding at the mineral-collagen interface, changes in the collagen and/or mineral platelet structure, abnormal cellular activity or the multiple effects of all four of the above. The apoptosis of osteocytes and their altered interaction with bone matrix was observed in klotho mice, a mouse model of early premature ageing

(193). *In situ* small angle X-ray diffraction (SAXD) studies showed that mechanical degradation at the mineralised collagen fibrillar length scale increased with ageing. For a given external tissue strain, the measured fibrillar strain was significantly less (25 %) in aged bone compared to young bone (87). In this study as well as others, it was found that enhanced amount of AGE cross links in aged bone compared to young bone (36, 194). The enzymatic cross-links connect the nonhelical termini (N- or C-) of one tropocollagen molecule to the helical region of an adjacent molecule. With increasing age, it is believed that these cross links connect both terminals of collagen molecule with the helical region of the adjoining molecule, thereby increase the overall stiffness of the collagen fibril. Several researchers reported strong positive correlation between non-enzymatic cross links and age in both cortical and trabecular bone (195, 196). These findings led to the suggestion that increase in AGE products stiffens the collagen fibrils by restricting the fibrillar sliding mechanism and reducing the capacity to deform for an applied external load. Formation of cross linking at fibrillar levels may also affect the higher structural levels, by forming microcracks in order to accommodate plastic deformation (87). Also it was reported that AGE cross-links can be removed only by osteoclastic activity, which would necessitate increased bone resorption and reduced bone mass, increasing fracture risk (196). Other factors such as collagen fibril orientation, functionality of noncollagenous proteins (197), extracellular bone matrix protein production (198) and site-specific expression of different proteins (i.e. osteopontin, osteonectin) (193), exhibit changes with increasing age, and may also play a contributory role in the deterioration in material properties.

Based on the X-ray diffraction studies on human bone mineral of different ages (0 to 95 years), crystal size, perfection and carbonate content were increased during 0 to 30 years, and then decreased thereafter (199). Increase in length (17-20 %) and width (5-9%) of crystal aggregates as a function of age was also observed using TEM and cryofractography studies performed on human lamellar bone (200). A few other studies have shown that increased in carbonate and hydroxyl content and reduction in acid phosphate content in bone mineral with age, using Raman (201) and infrared spectroscopy (29) and chemical analysis (202). A similar pattern of change in mineral parameters with animal age was observed with tissue age (old vs. new osteons) as well

(77, 162). The underlying mechanism for these alterations in mineral parameters has not been fully understood yet. The mineral particle mechanical properties was measured at different ages using synchrotron *in situ* WAXD combined with tensile testing and it was observed that no significant difference in mineral platelet deformation between young and aged bone (116), in contrast to this group's previous findings of a higher stiffness at the collagen fibril level.

1.9 Bone quantity vs. quality

The deformation and fracture of bone in health and disease depends on the volume of bone (bone quantity) and the quality of the bone matrix (bone quality). Bone quantity relates to the degree of bone loss or bone resorption and it is use to predict osteoporotic fracture risk in patients (203), whereas bone quality is not routinely use to predict clinical outcomes, largely because the parameters that may affect such macroscopic mechanical outcomes are not fully understood. Bone quality has been defined as "the material, architectural, and mechanical characteristics which in addition to bone strength" (204). Here and in the following, the techniques used to assess bone quantity and quality will be discussed.

Bone quality is determined by microstructural properties, that include the mineralisation distribution, cortical/trabecular microarchitecture, and molecular/supramolecular properties, that include the deformability of the ~200 nm diameter MCFs, types of non-collagenous proteins present, and collagen cross linking. Bone quality can be significantly altered by structural changes in the collagen and mineral. Suppression of bone remodelling can lead to increased tissue mineralisation and homogeneity, making it possible for microcracks to form (146). Mechanisms at the nanometre length scale, such as stiffening via collagen cross-linking (205), changes in collagen i.e. mutations in molecules (206) as well as amount of mineralisation in MCF (79) will alter the macroscopic deformation and fracture mechanisms of bone. Alterations to bone turnover rate due to the disease conditions or medications (207) cause changes in osteoclastic activity on trabecular surface, as well as likelihood of perforation and elimination of trabecular struts. Bone quality and the factors involved have a direct effect on ageing bone and those affected by metabolic bone diseases (208). Most of the diagnostic tools

available in clinical use measures only the bone quantity (bone mineral density, bone volume etc) to assess the disease state in patients. Some of the clinical tools and their limitations are discussed below.

1.10 Clinical diagnostic techniques

1.10.1 DXA

BMD assessment by DXA is currently the standard technique to determine fracture risk from patient bone-biopsies, which is accessible, non-invasive and quantitative (161). However, it has many limitations, namely its restriction to 2D imaging, resolution of only 0.1mm (209) and an inability to take into account changes in bone volume when calculating bone mineral density. BMD measures only total mineral content (quantity) and not the structure or mechanics of the bone matrix (bone quality) (210). BMD also cannot explain more than ~ 44% of the incidences of non-vertebral fracture in women and ~21% in men, as shown in a study on an ageing cohort (211). Attempts have been made to improve DXA output by using it synergistically with newer techniques such as applying statistical models of bone shape to create 3D reconstructions (212).

1.10.2 FRAX

BMD assessment from DXA is not a reliable measurement for patients at risk of osteoporosis because; it is not sensitive enough to predict the fracture accurately. There are many patients undiagnosed and untreated who are in risk of fracture due to the lower sensitivity of the DXA analysis. In order to improve the osteoporotic fracture assessment World Health Organisation developed an easily accessible tool called FRAX, including several risk factors such as age, prior fracture, parental history of hip fracture (203), low body weight or body mass index (213), use of glucocorticoids of 5 mg or more for 3 months or more, rheumatoid arthritis, current cigarette smoking, excessive alcohol intake of 3 units or more daily (3 medium glasses of wine or 3 half pints of beer), and secondary osteoporosis (214, 215). Even though it increases the sensitivity of detecting fracture risk in osteoporotic patients compared to DXA measurements, it has several limitations. It assumes body mass index and mortality are constant across different ethnic

groups in the world. Because FRAX is designed to give a binary response (start treatment or do not start treatment) it is not to be used to estimate the treatment efficacy (216).

1.10.3 Peripheral quantitative computing tomography (pQCT)

This technique is a relatively new technique, being an advancement of clinical computer tomography (217), and is capable of *in vivo* determination of the geometry, structural parameters and distal radial and tibial density. *In vivo* pQCT determines the structural and tissue properties of peripheral bone within a short time (2.8 minutes). In contrast to DXA measurements, this technique is able to predict the cortical bone strength by obtaining cortical thickness and geometry. The scans obtained from pQCT can be processed by finite element analysis to estimate the strain distribution and failure load by simulating the mechanical test. Peripheral QCT measurements are based only on the density (quantity) (218) and not the structure or mechanics of the bone matrix and the resolution is quite low (~ 1 mm), and hence cannot track the alterations at the ultrastructural and submicron level.

1.11 Limitations in current techniques

Diagnosing the onset of disrupted mineralisation parameters, especially early on during disease progression, is critical for timely therapeutic intervention. Alterations in bone mechanical competence may involve changes both in the volume of bone (quantity) as well as the type of tissue formed (quality). While the former can be assessed using clinical tools like DXA, plain radiography, microCT analysis and FRAX, the latter are much less understood. The strengths and limitations of the various techniques currently in use to assess bone functional competence are presented in **Table 1.1**. The above standard clinical techniques do not, however, provide information on the nano-structural components of the bone matrix, as they are spatially limited in resolution to approximately 1 μm. Disease-specific alterations in bone quality at the scale of the fibril may change the mineral/collagen arrangement, as has been reported in osteomalacia, rickets (79) and osteogenesis imperfecta (219) as discussed in detail in the foregoing literature review. Consequently, if there are intrinsic changes in nanoscale compressibility and extensibility at the fibrillar level, these may be dramatically

amplified in disease-induced changes in bone quality, and critically affect fracture risk (203).

Table 1.1: Comparison of *in situ* X-ray nano-mechanical imaging with other assays of bone functional competence

Technique	Hierarchical level diagnosed	*In situ* testing	In-vivo/in-vitro	Monitoring of treatment effect	Both structure & mechanics
DXA – BMD mineral density per area	Micro level – Cortical and trabecular bone (210)	No	In vivo	Poor – Fails to separate measures for trabecular and cortical bone (218)	No
qCT/mCT – BMD mineral density per volume	Micro level	Yes	In vivo	Yes - Separates cortical and trabecular bone (218)	No, developing
qBSE – BMD Distribution	Micro level	No	In vitro	Yes - only in 2D	No
In situ mechanical testing with SAXS/WAXD	Nanolevel – MCF	Yes	In vitro	Yes –Measures the changes to the material and functionality of the bone at nano level	Yes

1.12 Aims and scope of this study

As explained in section 1.1, bone is a complex hierarchically structured composite which at nanometer level can be described as MCFs through staggered assembly of tropocollagen molecules and mineral platelets. Bone quality changes occur initially at smaller length scales, dictated by rates of formation of new BMUs, at level of lamellae (~ 5 μm) and mineralised fibrils (~ 200 nm). The majority of studies on the structural and mechanical changes induced in metabolic bone diseases of the types given above (section 1.8) investigated separately the mechanical and structural aspects; i.e. the changes in macro-level mechanical properties and the mineral nanostructural parameters like crystal size, content and distribution were measured separately (for example, in rickets, see (79, 220, 221)). During early stages of bone diseases (osteoporosis and rickets), structural and mechanical alterations are far too small to be detected by current clinical techniques. Therefore it is still unclear quantitatively how deterioration in quality of bone nanostructure causes lowered mechanical behaviour and tissue level skeletal deformities. The approach of this thesis is to use mouse models of human diseases like osteoporosis, rickets created by the novel technique of ENU-mutagenesis, as test systems where the macro-level mechanical properties, altered mineralised nanostructure, and nanoscale deformation mechanisms occurring *in situ* are measured directly. To do this, synchrotron SAXD combined with micromechanical testing (14, 86) was used to measure the altered fibrillar deformation mechanisms. The high brilliance of synchrotron X-ray beams enables time-resolution of the order of seconds, enabling a series of scattering or diffraction spectra to be measured concurrently during macroscopic deformation. This approach thus measures directly the deformation of the MCFs at the nanoscale under different external physiological loading conditions, and may be considered a form of nanomechanical imaging.

1.12.1 Aims

1. Investigation of alterations to the nanostructural and mechanical properties of bone during metabolic disease conditions such as rickets and osteoporosis, and ageing using *in situ* mechanical testing combined synchrotron SAXD.

2. Using structural and mechanical data from nanomechanical imaging technique, to develop an assay linking ultrastructural changes to altered macro level mechanical properties (e.g. increased fracture risk in osteoporosis).

The study is motivated by the urgent need for developing high-resolution diagnostic technique for early detection of metabolic bone diseases and monitors the efficacy of the treatment methods (**Figure 1.23**). The fundamental long-term benefit in terms of relieving the burden of bone disease will be to establish nanoscale biomarkers from the tissue biopsies of patients at risk of fracture, months before deterioration would have progressed to the point of total failure in bone. Early detection and treatment also can reduce costs as well as reduce both patient pain and mobility and risks of secondary effects (cancer).

1.12.2 Objectives

- Design of a specialised *in situ* micromechanical testing machines for small-scale mouse bone testing. Special challenges involve design of miniature sample holders and *in situ* fluid chamber systems, to test irregular bone tissues in close to in-vivo states.

- Conduct synchrotron based *in situ* mechanical testing of the above tissue types with SAXD on mineralised tissues.

- Apply qBSE imaging techniques for static characterisation of the altered mineralisation density distributions in these disease types.

- Development of structural models for the MCF in cortical bone of mice to correlate them with macroscopic mechanical properties.

1.12.3 Report Outline

The research presented in this thesis is consists in the following format. **Chapter 2** describes the principles of the experimental methods used in this study. Development of micromechanical testing machines, general sample preparation techniques and experimental protocols used in the experiments are described in the **Chapter 3 and 4** respectively. In **Chapter 5** it was demonstrated how *in situ* synchrotron SAXD with

micromechanical testing can be used to quantitatively image metabolic bone disease-induced alterations in the fibrillar deformation mechanisms in bone matrix. This technique initially tested on a mouse model of hypophosphataemia (Hpr). Hpr is a well-established disease where the reduction of mechanical competence due to the reduced mineralisation is known, and hence the Hpr animal model serves to validate the technique. **Chapter 6** explains and discuss the use of high brilliance microfocus synchrotron SAXD (μSAXD) combined with *in situ* cantilever bending to measure the fibrillar strains at the zones of compression and tension developed in real time during macroscale deformation in the same mouse model used in **Chapter 5**. Furthermore, the Hpr mouse model was used to investigate muscle force mediated mineral particle orientation in scapula and alterations from defective bone mineralisation using synchrotron scanning SAXS in the **Chapter 7**. Understanding metabolic-disease induced alterations to mineral particle parameters and collagen fibril orientation in this spatially variable force-mediated environment in detail will inform the development of advanced nanoscopic clinical diagnostic methods and novel treatments for metabolic bone diseases. As reviewed in **Chapter 1 section 1.6.1**, the increase in fracture propensity in GIOP cannot be explained by reduction in bone quantity (BMD) alone, but must involve changes in the bone material as well. Increase in fracture risk in ageing is another growing problem in the UK and elsewhere in the western world due to a rapidly ageing population. **Chapter 8 and 9** discussed the change in the material level (fibrillar) fracture mechanisms in GIOP (an inherited mouse model for Cushing's disease that results in GIOP by endogenous production of steroids) and klotho (well-established transgenic mouse model of ageing) which lead to increased fragility using *in situ* synchrotron SAXD based nanomechanical assay. The overall conclusions, limitations of the technique and suggestions for future work are discussed in **Chapter 10**.

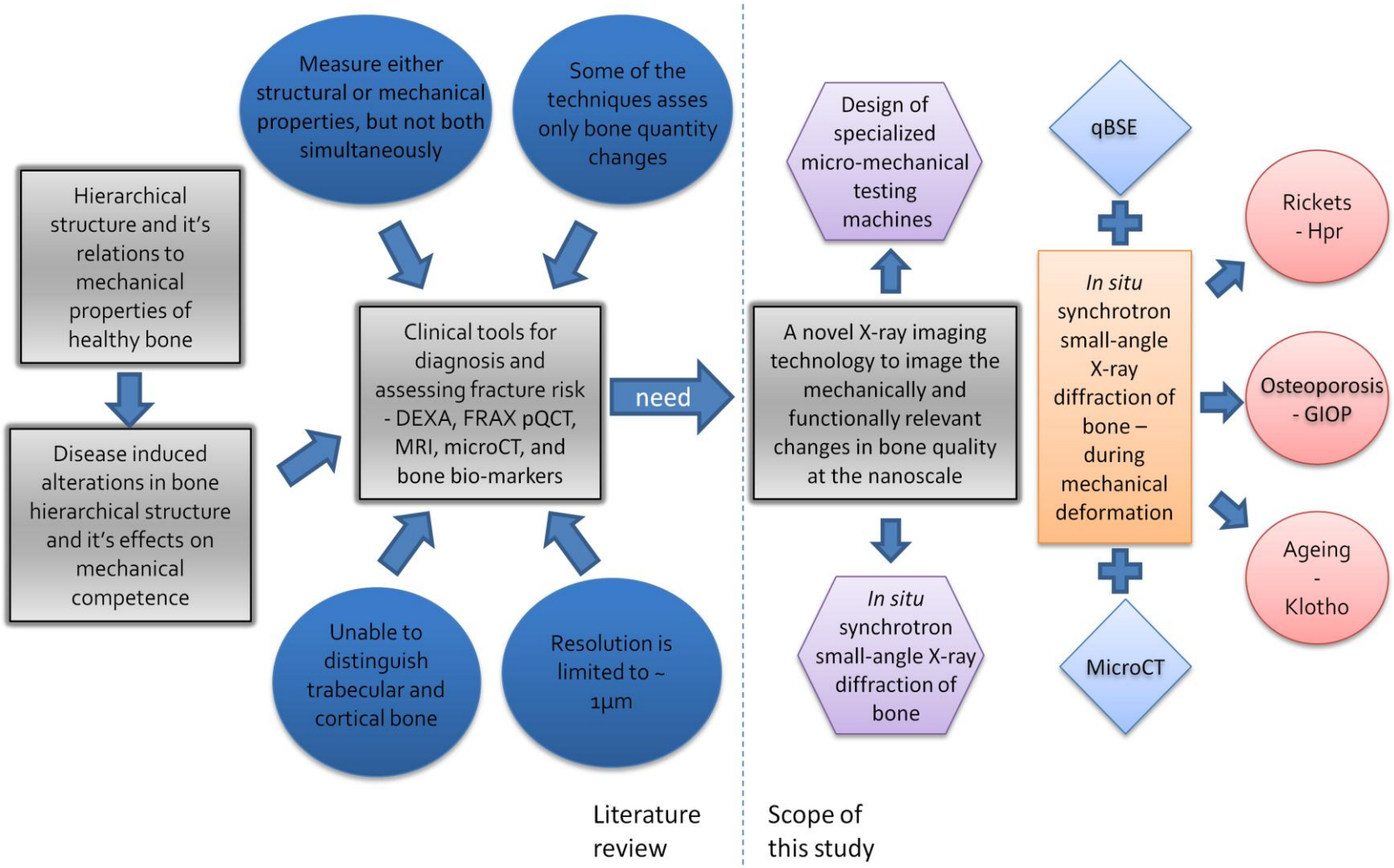

Figure 1.23: Project literature and scope of the study

Chapter 2

Introduction to Methodology

The contents of this chapter explains the technical aspects of the methods and experimental techniques used in this study

2 Introduction to Methodology

2.1 X-Ray Scattering and Diffraction

X-ray diffraction by crystals was discovered by Max von Laue and subsequently put to practical use by W.H. Bragg and W.L. Bragg to solve the crystal structure of a range of materials. X-rays are electromagnetic waves which have wavelengths broadly in the range of 0.01 nm to 10 nm (corresponding to energies in the range of 120 keV to 120 eV). The ability of a material to diffract or scatter X-rays from the primary beam depends on its atomic and/or molecular structure. Crystals are made up by periodic repetition of units, such as an atom or molecule (e.g. tropocollagen molecules packing in a collagen fibril), with spacing in the range of a few Angstroms. These interfaces and periodic arrangement of atoms or molecules create electron density fluctuations in the material. When X-rays are incident on such matter these periodic electron density profiles give rise to a characteristic spatial pattern of scattered light, provided that the wave length of the X-rays are of the same order of magnitude as the spacing between interfaces. The nature of the scattered X-ray pattern is sensitive to the nanometre scale structure, and thus provides indirectly ultrastructural information within the sample. X-ray scattering is therefore an appropriate tool for investigation of structures on length scales below 100 nm that are not accessible by light microscopy. It is complementary to TEM and AFM, which are capable of direct visualisation (quantitatively and non-destructively) of the ultrastructure (222-225), by providing indirect information in reciprocal space.

2.1.1 Theoretical background

Diffraction is essentially a scattering phenomenon. The diffracted beam can be defined as a beam composed of large number of scattered rays mutually reinforcing one another. Atoms or molecules in a crystal scatter incident X-rays in all directions, and scattered beams which in a given direction have similar phase reinforce each other constructively to form a diffracted beam. Scattering can be separated into three different modes –

- by randomly arranged atoms in space – scattering occurs in all directions – *diffuse scattering*

- by periodically arranged atoms in space (perfect crystal)
- scattering occurs in a few directions – *strong scattering* or diffraction, which satisfies Bragg's law

Therefore, diffraction is in fact a special case of scattering which depends on the organisation of the molecular structure of the sample. If the sample has an ordered molecular packing which leads to the reinforcement of scattering signal, one has diffraction. In contrast scattering generally implies interaction of photons with spatially unordered atoms or molecules (222, 226).

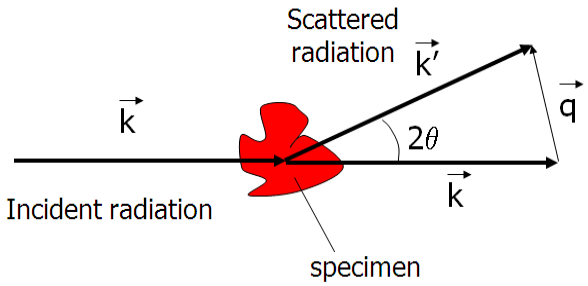

Figure 2.1: Elastic scattering vector can be defined relative to the incident beam and scattered beam. An X-ray beam is scattered in the specimen and the intensity of the scattered radiation as a function of 2θ with respect to the incident beam is detected

The scattering vector $\vec{q}$ is defined by $k_1 - k_0$, k_0 and k_1 being the wave vectors of the incoming and scattered beam respectively. In elastic scattering (**Figure 2.1**), the relationship between the scattering vector $\vec{q}$ and the scattering angle 2θ is given by:

$$\vec{q} = \frac{4\pi}{\lambda} \cdot \sin\frac{2\theta}{2} \quad (when\ \vec{k} = \vec{k}') \qquad \text{Equation 2.1}$$

where λ is the wavelength,

Bragg's law

In a crystalline structure, if atoms are perfectly ordered, sharp discrete peaks of X-ray intensity are visible in the diffraction pattern. In contrast, if atoms of the crystalline structure are randomly ordered, the intensity of the peaks is diminished and the width of the peaks increases

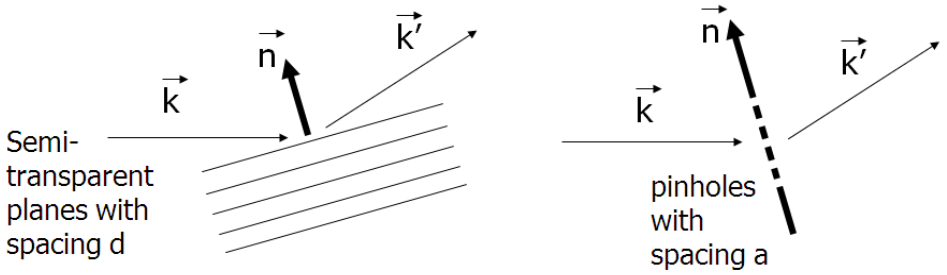

Figure 2.2: Bragg's law explains the origins of these discrete intense peaks, by considering the interaction of X-rays from different planes of crystals at specific angles

Bragg's law states the essential condition which must be met if diffraction is to occur. Bragg's law refers to the following equation:

$$2d_{hkl}.\sin\theta = m\lambda \quad \text{Equation 2.2}$$

The angle between the diffracted beam and the transmitted beam is 2θ. m is an integer, (hkl) are the Miller indices of the crystallographic plane and d_{hkl} is the interplanar spacing between planes. Since $\sin\theta$ cannot exceed 1, $m\lambda$ must be less than or equal to $2d$. For diffraction the smallest value of m is 1 (m = 0 cannot be observed as this corresponds to the beam being diffracted in the same direction as the incident beam), therefore the wavelength (λ) must be less than or equal to $2d$ at any diffraction angle 2θ.

Bragg's law can be written as follows:

$$\lambda = 2 \cdot \frac{d_{hkl}}{m} \cdot \sin\theta \quad \text{Equation 2.3}$$

The lattice planes are producing the reflection mirror planes with respect to the incident and scattered beam. In one dimensional space, the coordinate in reciprocal space, *q*, is inversely related to the coordinate in real space by the equation given below:

$$q = m\frac{2\pi}{d}n$$

$$q = \frac{2\pi}{d} \rightarrow (when\ m = n = 1) \quad \text{Equation 2.4}$$

The general case for three dimensions is explained in section 2.1.2.1.

2.1.2 Small angle X-ray scattering (SAXS) and diffraction (SAXD)

Scattering and diffraction patterns obtained by hierarchically structured materials can be divided into two regimes; WAXD (224) and SAXS (225). WAXD is associated with periodic (Bragg) reflections reflecting the underlying crystalline order **(Figure 2.3)**, while such regularity is not necessarily a component of the SAXS signal. The distinction between WAXD and SAXS also reflects the fact that in the wide angle (large Bragg angle) range, discrete Bragg reflections are found (for most materials). WAXD patterns recorded at large Bragg angles provide information on the crystal structure and degree of crystallinity of materials at the atomic level. In contrast, in the small angle (low Bragg angle) range, both scattering and diffraction are present. For example discrete Bragg reflections observed in the small angle regime where the intensity distribution reflect the electron density fluctuations at length scales of 1 – 100 nm, giving rise to small-angle X-ray diffraction

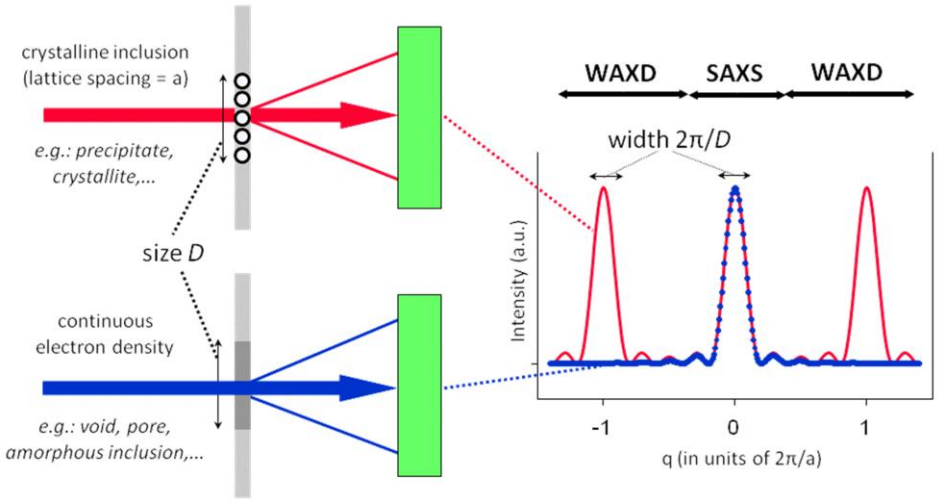

Figure 2.3: Principles of SAXS and WAXD. D is the size of the lattice. The Bragg peaks are widened if the lattice has a finite dimension of D. A single pinholes does not give Bragg reflections in itself, and its finite width D widens the primary peak (= 0th order Bragg reflection) to 2π / D. For wider pinhole with a larger zone of crystallite inclusion, the peak width will decrease as D increases.

SAXS was pioneered by André Guinier, who established and improved the method in the late 1930's (227), with theoretical underpinnings by Günther Porod (223). SAXS has more recently come to denote all X-ray scattering in the low wavevector ranges (< 5 nm^{-1}). As such, the SAXS signal is sensitive to structures in the range of 1 – 5 nm and above, making it is a very useful tool to characterise the statistically distributed structures of colloidal dimensions such as polymers (bulk polymers, semi crystalline polymers, polymer solutions), fibres, metals (alloys, non crystals), colloids (gels and sols), liquid crystals and biological materials (proteins, DNA, RNA, biological membranes and biological solid structures and tissues) (228, 229).

As both diffuse scattering and discrete diffraction peaks may both appear in the small angle regime (although diffuse scattering is dominant), different abbreviations were used to denote them in this thesis. Diffuse elastic scattering of the primary beam and diffraction below 5° (with incident X-rays generated by a Cu-K_α source (λ = 1.54 A)) are denoted as SAXS and SAXD, respectively. The measured scattering intensity $I(q)$ is related to the squared modulus of the Fourier transform of the electron density distribution $\rho(r)$ as follows:

$$I(q) = K\frac{d\Sigma}{d\Omega}(q) = \frac{K}{V}\left|\int_V \rho(r)\exp(iqr)d^3r\right|^2 \qquad \text{Equation 2.5}$$

Here, q is the scattering vector, defined as the difference between the wave vector of the incident beam and outgoing beam (**Figure 2.2**), V is the sample volume, K is a constant dependent on the instrumental setup and $\frac{d\Sigma}{d\Omega}(q)$ corresponds to the macroscopic differential scattering cross-section of the sample.

K constant can be determined by:

$$I(q) = K\frac{d\Sigma}{d\Omega}(q)$$

$$I(q) = K_1\, d\, t\frac{d\Sigma}{d\Omega}(q)$$

where d is sample thickness, t is specimen transmission and K_1 is instrumental related

$$I(q) = I_0 d\, t\varepsilon(q)\Delta\Omega\frac{d\Sigma}{d\Omega}(q)$$

$$K_1(x,y) = I_0\varepsilon(x,y)p^2/L^2 \qquad \text{Equation 2.6}$$

Here I_0 is the primary beam intensity (photon flux (φ) × beam cross section (A)), ε is detector efficiency, p is detector pixel size and L is detector to specimen distance.

2.1.2.1 SAXS - Three dimensions of reciprocal space

Information on the size of very small particles or their surface area per unit volume can be obtained from the amount and angular distribution of scattered intensity regardless of whether the object is crystalline or amorphous. Two constraints have to be valid for SAXS: (a) the measured length scales are much larger than the atomic length scale and (b) the system consists of two phases with different electron densities, separated by a boundary. For materials like polymers with a more diffuse boundary, information can be

gained by correlation function analysis, which can give information about the separate layers and the interface region (230).

In a two-dimensional scattering pattern (**Figure 2.4**) as obtained by an area detector, two-dimensional section of intensity ($I(q,\psi)$ in **Equation 2.5**) is perpendicular to the incident beam. Through the implicit dependence of ($I(q,\psi)$ on $\rho(r)$, the shape of the SAXS pattern depends on the shape and ordering of the particles embedded in the two-phase system. Thereby morphology of the sample can be determined by interpretation of the SAXS pattern.

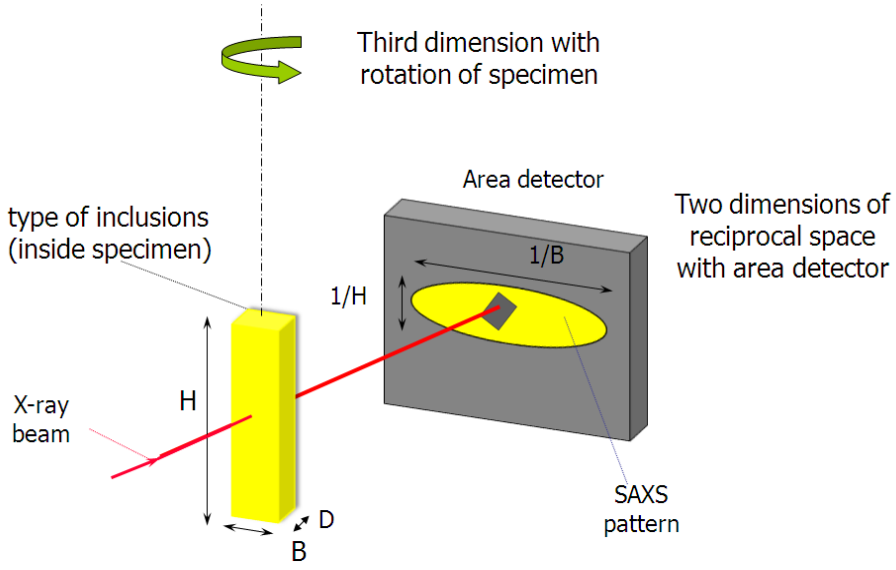

Figure 2.4: Correlation between real space and reciprocal space. Large dimensions in real space appear small in reciprocal space and vice versa

In analogy to Bragg's law, in SAXS the width of the scattering signal in reciprocal space is inversely proportional to the dimensions of the scattering object in real space (whereby small dimensions in real space appear large in reciprocal space and vice versa).

$$q_y \propto \frac{2\pi}{H}, \qquad q_x \propto \frac{2\pi}{B} \quad \text{Equation 2.7}$$

where H is the height and B is the width of the scattering object. This relationship can be generalised to the three-dimensional case by rotation of specimen (**Figure 2.4**). Specific

examples of physical parameters that can be calculated are described for the case of bone in the next **section 2.2.**

2.1.2.2 SAXD

SAXD is a special case of SAXS, and typically appears in long-periodic structures such as tropocollagen molecules in collagen fibrils, where the axial stacking generates a periodicity in electron density at the scale of tens of nanometres and greater (specifically for collagen with a period of 64-67 nm). By analyzing diffraction peak position, intensity and angular distribution, a great deal of nanostructural information on the collagen fibril can be obtained (226) which will be discussed in the following section.

2.2 Small angle scattering and diffraction analysis of bone

Bone is a heterogeneous material at the nanoscale, as described in **Chapter 1**. SAXS provides information on the size, orientation and shape of mineral platelets in bone (231), as can be expected from its description in the previous section. In bone, the two phases are taken to be collagen (30% organic components of which 95% is collagen) and mineral (70%), (61) with the electron density of mineral much larger than that of collagen. For physiologically wet bone, the collagen component can be considered as hydrated collagen. The strong SAXS scattering signal is due to the large difference in electron density between the mineral platelets and organic components of the mineralised fibril (MCF). A typical two-dimensional SAXS spectrum from mouse bone is shown in **Figure 2.5**.

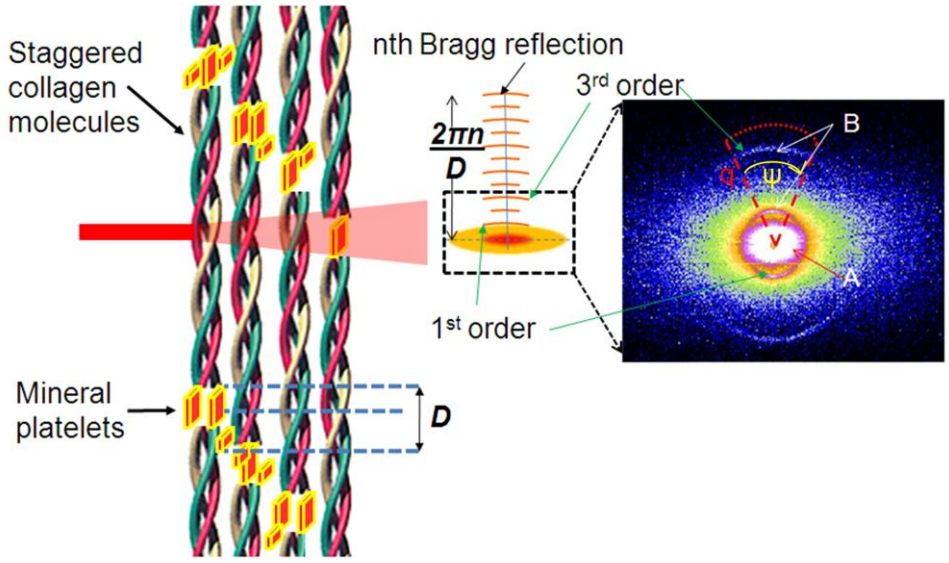

Figure 2.5: The staggered axial arrangement of tropocollagen molecules. By irradiating the fibril with X-rays a series of Bragg reflections with a period $2\pi / D$ appears in reciprocal space. The 2D scattering pattern of mice (4 weeks old male) bone exhibits the two main features: (A) diffuse scattering ellipse arising from the mineral particle and (B) diffraction arcs from the collagen fibrils showing the 1st and 3rd order reflections arising from the collagen D-period

As shown in **Figure 2.5** the 3-dimensional SAXS iso-intensity surfaces in reciprocal space are ellipsoidal in shape. This ellipsoidal intensity distribution is due to scattering from plate-like mineral crystals in the bone (42). A large number of plate-like mineral crystals, mutually parallel to each other (**Figure 2.6A**), generate a disk shaped SAXS pattern that is perpendicular to the long axis of the mineral crystal. Conversely, if mineral crystals are randomly oriented (**Figure 2.6C**), their SAXS pattern is less anisotropic as when anisotropic disks at different angles ψ are averaged a more isotropic and circular patterns arises. Therefore eccentricity, orientation and shape of the SAXS ellipse depend on the orientation and distribution of the mineral platelets in real space.

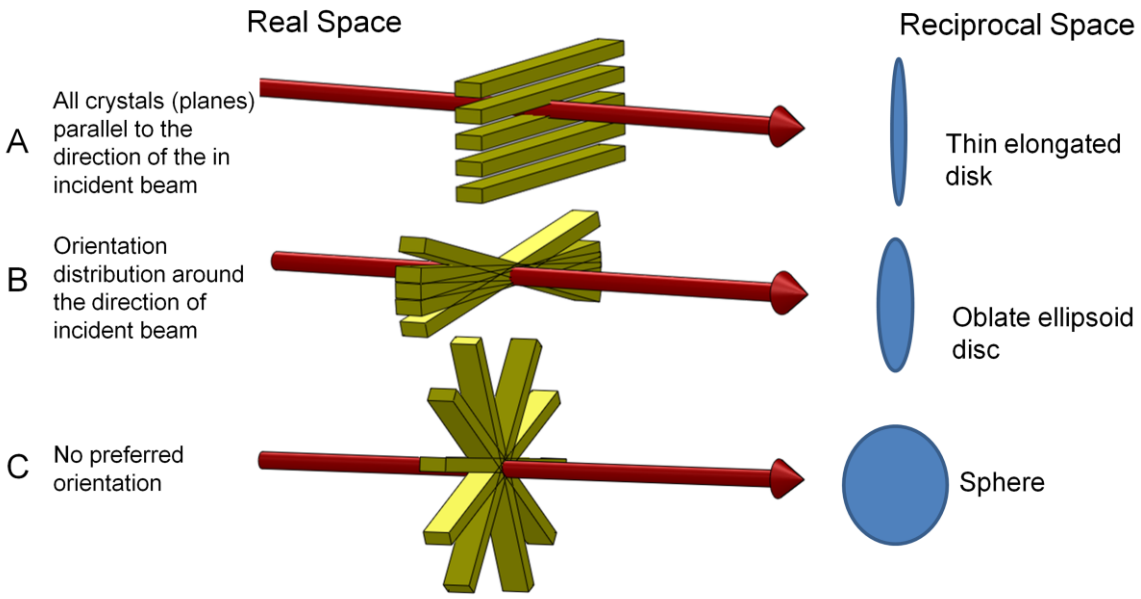

Figure 2.6: Schematic representation of SAXS patterns originating from mineral crystals in the collagen matrix. Three orientations of mineral particle arrangements are shown in A (all the crystals parallel to the X-ray beam), B (tilted by some amount) and C (randomly orientated) (219).

Each SAXS spectrum corresponds to the X-ray photons, $I(q,\psi)$ scattered around the primary beam at different wavevectors q and polar angles ψ (**Figure 2.5**). The wavevector q can be defined as $q = (4\pi/\lambda)\sin 2\theta/2$. 2θ is the scattering angle between the incident and diffracted beam (**Figure 2.2**), and λ the wave length of the incident beam. When θ is small as is the case for SAXS, q is approximately proportional to θ as $\sin(\theta) \sim \theta$. To reduce the 2D intensity distribution to 1D intensity profiles, two typical integration methods are *radial averaging and azimuthal averaging*. Such an integration may be performed by commonly used programs like Fit2D (232) where sectoral averaging is achieved using the "CAKE" command. In the CAKE command, by defining the start and end azimuth angles (degrees), the inner and outer radial limit (pixels), as well as the number of azimuthal and radial bins, a 2D sector may be reduced to a 1D intensity profile versus wave vector (q) or angle (ψ). From the averaged line profiles for I(q), for example, one can extract size distribution and spatial arrangement of mineral crystals from a SAXS spectrum (233), as described in the following subsection.

Orientation of the mineral crystals

The predominant orientation of mineral platelets (ψ_o) can be estimated by radially averaging elliptically shaped 2D SAXS spectra. Phenomenologically, for an ellipsoidal profile the integrated 1D profile $I(\psi)$ usually results in two peaks separated by 180° on top of a constant background (233). The predominant orientation of mineral crystals (rotated by 90°) can be obtained by estimating the polar angle of those peaks $I(\psi)$. In **Figure 2.7**, A_1+A_0 is the total area under the curve $I(\psi)$ for $0 < \psi < 360$ and A_1 is the area after removal of the constant background (shown in grey).

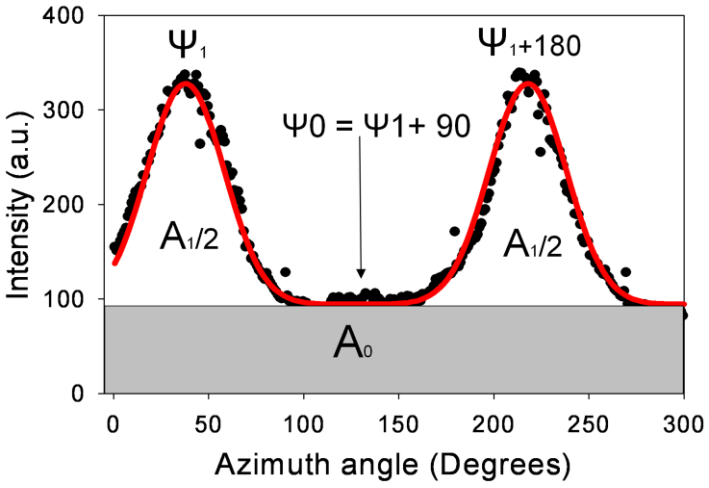

Figure 2.7: The azimuthally averaged scattering intensity *I(ψ)* is plotted as a function of the polar angle *ψ*. Due to the typical elliptical shape and the point symmetry of the 2D SAXS pattern the 2 peaks are separated by 180°. These are fitted with two Gaussian curves (red solid line) separated by 180°, having the same height and width.

The parameter ρ is used to determine the anisotropy of the SAXS pattern, and is defined as

$$\rho = \frac{A_1}{(A_1 + A_0)} \quad \text{Equation 2.8}$$

where A_0 is the total SAXS intensity caused by randomly oriented mineral particles and A_1 is the total SAXS intensity due to the particles aligned parallel to a certain direction ψ_o.

If there is no predominant orientation of the mineral crystallites, then $\rho = 0$; if all crystals are aligned in one direction, then $\rho = 1$. This is admittedly an approximation. Considering **Figure 2.4**, it can be seen that even if H is larger than B, $1/H$ is nonzero, leading to a finite width of the ellipse even in the short-direction (vertical in the **Figure 2.4**). As a result, a radial average of the intensity even for a single (perfectly aligned) parallelepiped of the type shown in **Figure 2.4** will have a small nonzero intensity at the minimum of the plot (region indicated by grey colour (A_0) in **Figure 2.7** above). However, as the H/B ratio increases, this off-axis intensity level will become less and less relative to the maximum. In the current study, it was assumed implicitly that this small contribution can be neglected for a single (perfectly aligned) platelet. The simplified definition was used in this thesis to compare results with previous work using the ρ-parameter (233, 234). The predominant orientation-direction (Ψ) of mineral particles also can be found from the azimuthal intensity plot, by adding 90º to the peak intensity angle (233). With the assumption that mineral platelets are aligned parallel to the collagen fibril axis, the ρ parameter also reflects the degree of collagen fibril orientation.

2.2.1 Scanning SAXS

One of the main features in the hierarchically-structured systems like bone is that material properties depend sensitively on microscale gradients in individual nanoscale properties. To resolve the gradients of (averaged) nanostructural parameters at the microscale, scanning SAXS – where a focused X-ray beam provides a 2D raster of SAXS images − was applied to map micro- and nanoscale heterogeneities in bone tissue by Fratzl and co-workers (70) and to characterise mineral-crystal changes with development (231), disease-induced disruptions of nanostructure (235) and structure at the bone-implant interface (236). The combination of SAXS with focused X-ray beams for scanning with in experimentally-feasible amounts of time, requires high photon fluxes for both fast measurement and sufficiently high count statistics for micron-sized beams. Such can only be provided by synchrotron radiation sources and highly efficient and fast detector systems. Gradients of nanostructural properties in bone were found, for example, by Pederson and co-workers who observed evidence of greater mineral alignment close to implanted tantalum implants and gradients in mineral platelet

thickness (237) . Such an increased alignment was interpreted as due to local mechanical forces induced by the implant material. These studies support the idea that the structure may vary over the tissue on a micron length scale. These nano- and microstructural bone mineralisation patterns will be significantly altered in metabolic bone diseases, which would, in turn change how *in-vivo* mechanical load is transduced down to the force-distribution locally. Altered force distributions would change subsequent tissue development, *via* mechanotransduction to the osteoblasts, osteoclasts and osteocytes (238, 239) and eventually cause profoundly misformed bone, as is the case in muscular dystrophy. It is therefore of direct experimental relevance to apply scanning SAXS methodologies in this work.

Previous studies (235, 236, 240) and in this thesis, scanning SAXS was carried out by moving the sample, using computer controlled stages, in the plane perpendicular to the incident beam in both vertical and horizontal directions. Combining this with a small-diameter X-ray beam (specific beam sizes are given in **Chapter 4**) allows for position resolved analysis by scanning the sample across the X-ray beam. **Figure 2.8** shows an example of a SAXS composite map, which illustrates the distribution of the measurement positions (240). Differently shaped SAXS signals arise due to variable trabecular direction in the region of interest **(Figure 2.8D)**, indicating a spatial variation of the mineral particle orientation.

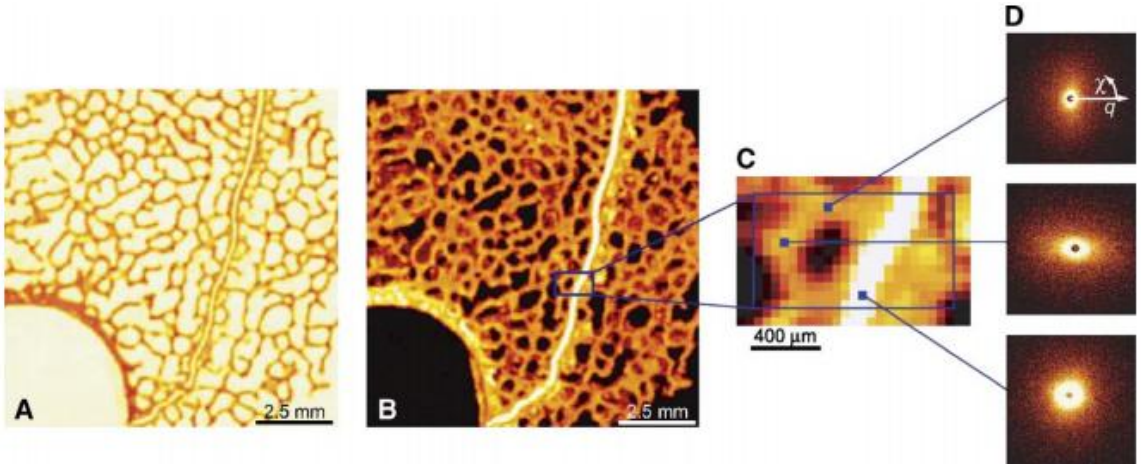

Figure 2.8: X-ray transmission and scanning SAXS images of the vertebral cross-section containing the growth plate. (A) X-ray transmission scan. (B) Scanning SAXS intensity scan shows the integral SAXS intensity in the q range from 0.01 to 0.35 nm^{-1}. (C) High resolution

scanning SAXS scan of the selected region of interest marked in B. (D) SAXS patterns obtained from different regions shown in C. The direction of the X-ray beam is perpendicular to the plane of the figure (adapted from (240))

2.2.2 *In situ* SAXD nanomechanics on bone

Concurrently, the staggered axial arrangement (**Figure 2.5**) of tropocollagen molecules (32) in the collagen fibril is also highly regular. Such an axial periodicity in electron density, denoted *D*, is equivalent to a one-dimensional lattice of the type mentioned previously (**Chapter 1, section 1.2**). It consequently gives rise to a series of Bragg reflections in reciprocal space along the fibril axis (meridional) direction, which can be picked up in the SAXS regime of an X-ray detector due to the magnitude of $D \sim 65 – 67$ nm (depending on tissue type and degree of hydration) corresponding to a wavevector of $q_D = 2\pi/D$ of about 0.094 – 0.097 nm^{-1}. Therefore SAXD on mineralised collagenous tissues provides information on the collagen fibrillar *D* - period (107) and the mineral crystal structure (241). Due to the externally applied stress, this periodicity is increased (31, 104).

2.3 Synchrotron Techniques

As explained in the previous chapter, bone has a rich hierarchical structure from the macroscopic down to the nanometre length scales. Detailed characterization of the structure and mechanics at all hierarchical levels is important to develop the link between the structure and the function of the bone. Synchrotron radiation from a third-generation source is a probe of high brilliance which can be focused to very small areas (down to the nanometre scale). Therefore synchrotron radiation allows imaging of a multitude of physical parameters due to its coverage of almost the whole spectrum of electromagnetic radiation from infrared (10 to 0.10 nm wavelength) to hard X-rays (0.10 to 0.01 nm wavelength). Furthermore position-resolved experiments using X-rays require a small beam at the sample position and – in particular for small angle scattering – a low beam divergence to minimize contributions from the direct beam at low wavevectors (242). Rotating anode generators, together with modern X-ray multilayer mirror optics can be used to reach monochromatic X-ray beam with size down to submicron level (228). These developments led to construction of microfocus beam lines such as ID13 at

European Synchrotron Radiation Facility (Grenoble, France), the μ-Spot beamline at BESSY II (Berlin, Germany), and more recently P03 (The micro- and nanofocus X-ray scattering beamline) at PETRA III (Hamburg, Germany), and I22 beamline at DLS, UK. These beamlines have introduced several cutting edge developments in instrumentation (high throughput beamlines, robotic arms etc.) to the field of materials research, which include a wide range of materials from metals through carbon nanotubes to polymers and biopolymers.

2.3.1 Working principle of synchrotron

A synchrotron consists of three components: the linear accelerator, the booster and the storage ring (**Figure 2.9**) which produce the intense synchrotron light which require for experiments.

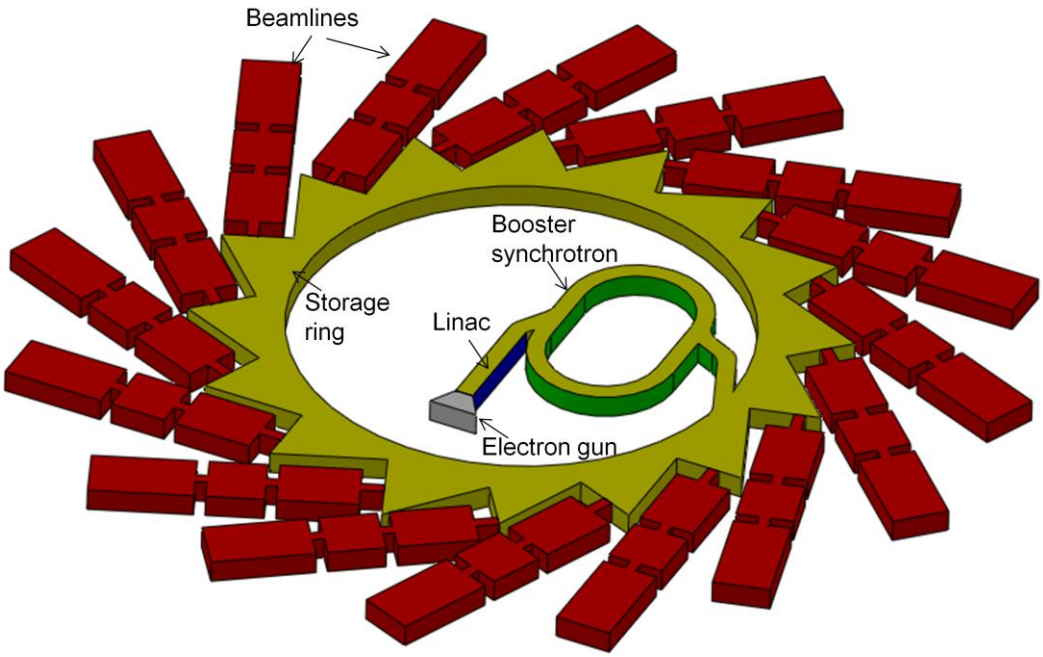

Figure 2.9: Schematic of Synchrotron facility

Electrons are generated in the electron gun by heating high voltage cathode which will increase the thermal energy of the electrons to break away from the surface. These electrons are accelerated to almost the speed of light by two particle accelerators, namely the linear accelerator and the booster. Once the energy of the electrons reaches to ~ 3 GeV (energy required to produce the whole spectrum of electromagnetic radiation -

nearly the speed of light) they are transferred into the storage ring. The storage ring is a polygon, which consists of specially designed magnets called insertion devices (they are usually inserted in the straight parts of the storage ring) and a radio frequency voltage source to deflect the electrons around the bends and to re-accelerate the electrons in the straight sections respectively. There are mainly two types of insertion devices: wigglers and undulators. The storage ring is maintained in a high vacuum condition. If the electrons were to travel through air as they orbited the storage ring they would quickly collide with air molecules and be lost from the electron beam. To minimise these losses, the electrons circulate around the storage ring in a vacuum chamber in which the pressure has been reduced to approximately one million times lower than atmospheric pressure. At this pressure the useful lifetime of the electron beam is about 20 hours. Synchrotron light is emitted when the electrons travel at a relativistic speed and undulate within the powerful magnetic field inside the storage ring (243-246).

2.3.2 Beam line

Synchrotron light is then guided through to the beamlines which are placed at tangents to the storage ring. Each beamline is made up of three basic compartments, an optic hutch, an experimental laboratory and a control room (244). In the optic hutch (**Figure 2.10C**) a sequence of components including silicon mirrors, slits and crystals are used to filter the various colours provided by the synchrotron light and in this instance, to focus the X-rays beam down to a few hundredths of a millimetre. In the experimental hutch (**Figure 2.10B**), the X-rays shine into the sample and interact the atoms and molecules within it. Special cameras and CCD detectors are used to capture the interactions taking place. In the control room (**Figure 2.10A**), scientists are able to control the experiment and to analyses the data obtained by the detectors (66).

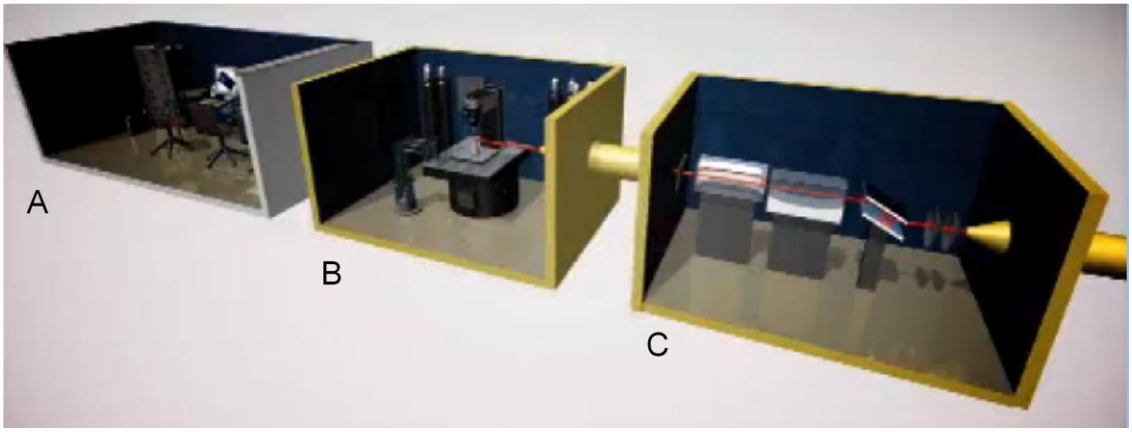

Figure 2.10: Beam line at synchrotron facility (figure adapted from (244)). (A) Control cabin. (B) Experimental laboratory. (C) Optics hutch

The principal setup for an X-ray scanning experiment is shown in the **Figure 2.11**. Measurements are almost exclusively performed in a transmission mode. A monochromatic X-ray beam penetrates the thin sample and the scattered X-ray photons are detected by an area detector. Sample thickness should be ideally similar to the size of the beam to avoid losing position resolution by averaging along the beam path (242). Depending on the distance between sample and detector (at a typical wavelength of $\lambda \sim$ 1Å), either a WAXD pattern (distance ~ 5-30 mm) or a SAXS pattern (distance ~ 500 - 5000mm) is acquired. When using the modern area detectors (large active areas and small pixel sizes) with high brilliance synchrotron radiation sources (high photon flux and small divergence) the detector can be placed much closer to the sample without compromising spatial resolution. This allows compact experimental setups to obtain SAXS and WAXD signals which can even be measured simultaneously with the same detector, covering the wide range of scattering angles (63). Scanning speed is determined by the primary X-ray intensity, by the illuminated volume and by the scattering power of the specimen. The recording of a scanning image (100 × 100 patterns) takes about 3 hours at the microfocus beam line (~ 10 × 50 µm beam size and 10^{11} photons/s, while it would take months with the laboratory equipment. The time for the typical load – deformation test of bone takes 1-10 minutes. The real-time acquisitions of intense SAXS patterns are thus enabled with third generation synchrotron sources (82).

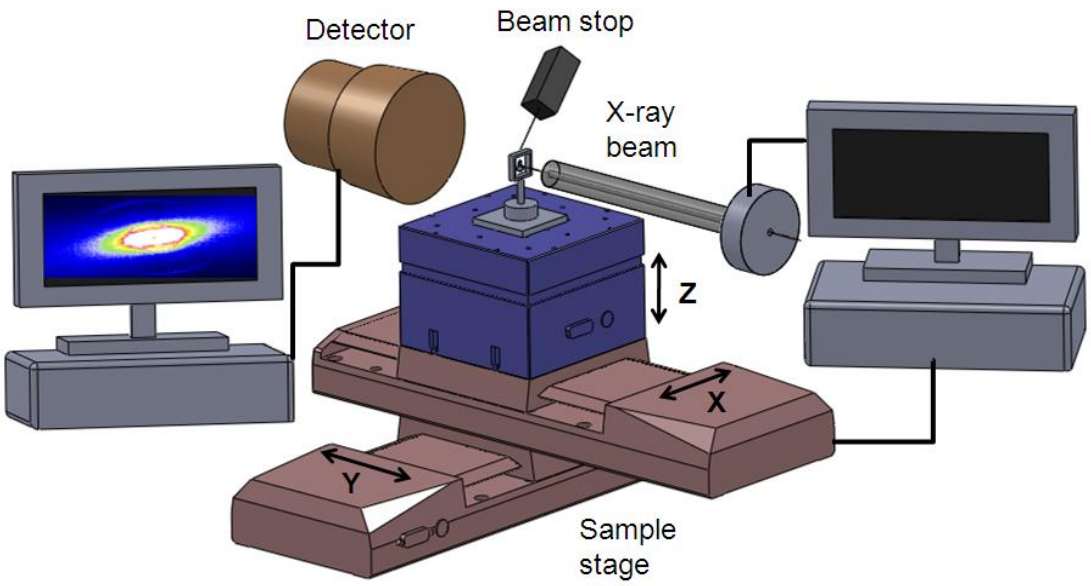

Figure 2.11: Experimental setup for scanning micro-focus SAXD beam line I22, DLS.

2.3.3 Radiation damage

Radiation damage plays a considerable role in SAXS and WAXD investigations in hierarchical biological tissues during scattering experiments using synchrotron radiation with high photon flux density. Several studies have been performed to investigate the possible effects of high energy X-ray doses on the mechanical properties of bone (247, 248). Radiation doses for several X-ray scattering experimental setups are given in **Table 2.1**. Note these irradiation dosage were calculated for specifically for cortical bone. It was found that plasticity of bone was suppressed after radiation doses over 70 kGy, and fracture resistance was reduced by a factor of a fifth after 210 kGy of radiation (78). Crystal structures of organic crystalline phases are very sensitive to radiation damage. It was also found that, with irradiation time, intensity of Bragg reflections reduces significantly (249). The irradiation dosages for mouse cortical bone were determined for the each experimental setup as follows:

Photon flux density = Photon flux / area of the X-ray beam at the sample

The flux density can be converted to energy density

Energy density (E) = Flux density × 1.6 ×10^{-19} J/eV × Radiation Energy in eV

The transmission, T, of X-rays through a material, of thickness l, is often expressed as:

$$T = e^{-\alpha\rho l} \qquad \text{Equation 2.9}$$

Where α is the mass attenuation coefficient (cm^2/g) and ρ the density. This is generally referred to as the Beer–Lambert Law.

The fraction of X-rays absorbed (A) by the sample is given as (1−T). The dose rate, *D*, can then be obtained from:

$$D = \frac{AE}{m} \qquad \text{Equation 2.10}$$

Where, *m* is the mass of the bone absorbing the radiation. Given a reasonably uniform distribution for the absorption of X-rays within the sample, the total irradiation dose received during each exposure is then found from the dose rate and the total exposure time (247).

Table 2.1: Radiation doses for mouse cortical bone during typical *in-situ* synchrotron SAXS experiments

Type of *in- situ* experiment	Synchrotron location	Radiation energy (keV)	Flux (photons/ s)	Flux density (photons/s/ mm^2)	Radiation dose rate (kGy/s)	Typical radiation dose (kGy)
Small -angle X-ray scattering (SAXS) (82)	Hamburger Synchrotron strahlungs lab (HASYLAB), Deutsches Elektronen-Synchrotron (DESY)	8.27	1×10^{9}	1.67×10^{8}	2×10^{-4}	~ 0.04–0.12
Wide-angle X-ray scattering (WAXS) (86, 111, 249)	Advanced Photon Source (APS), Argonne National Laboratory	80.7	1×10^{10}	1×10^{12}	0.2	~ 6–30
SAXS, WAXS	Advanced Light Source (ALS), Lawrence Berkeley National Laboratory	10	2.15×10^{12}	2.2×10^{12}	5	20
Main beam SAXD (without liquid path) (85)	I22 Beam line DLS.	10	6×10^{12}	1.53×10^{13}	1×10^{4}	1.05×10^{3}
Microfocus SAXD (without liquid path) (250)	I22 Beam line microfocus end station, DLS.	14	3.57×10^{9}	3×10^{12}	8.87×10^{5}	8.87×10^{2}

The major course of radiation damage in biological specimens is secondary damage due to free radical diffusion. Cryocooling of biological tissues is one of the solutions to avoid the free radical radiation damage. However at cryogenic temperatures considerable amount of background scattering occurs, especially with SAXS. Furthermore cryocooling cannot be used with *in situ* mechanical testing. The next best solution is to minimize the radiation damage by performing very fast measurements. By reducing the exposure time the radiation dose can be reduced significantly. Faster measurements are feasible with modern detector systems such as PILATUS 2M or RAPID, available at synchrotron facilities such as DLS (242).

*2.4 Quantitative back scattered scanning microscopy (*qBSE*)*

Back scattered scanning electron microscopy (BSE) is a technique to measure the bone mineral density. It was first introduced by Boyde and Jones in 1983 to study mineralised tissue (251). The SEM uses a beam (beam spot size typically 1nm -5nm) of electrons to systematically scan across the surface of a specimen (15). Several possible signals are generated from the interaction between the beam and the specimen (**Figure 2.12**). Some electrons may be scatter elastically, some may absorbed by the specimen and generate secondary electrons with low energy, and some may absorbed by the sample and emit visible light.

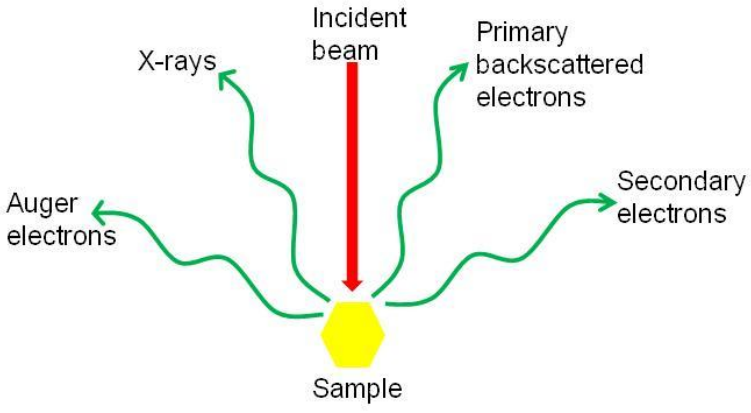

Figure 2.12: Interaction between electrons and specimen and possible outcomes

BSE imaging is based on the detection of electrons backscattered by the primary electron beam on the surface layers of the specimen (15). Backscattered electrons are defined as electrons that are emitted from the surface of the specimen with energies greater than

50eV. The scattering intensity of electrons increases with an increase in the atomic number and is proportional to concentration of mineral in bone. Atoms with high atomic numbers scatter strongly and appear brighter on BSE images allowing compositional information to be obtained. In bone, of the organic matrix (H, C, N, O, P, S) and mineral (Ca, P, O, H, C, Mg) components, the concentration of calcium, the constituent with the highest atomic number (Z = 20), dominantly influences the intensity of the backscattered electrons. Detection of the BSE signal produces a grayscale image where each pixel assigned to a gray value from 0 to 255, with 255 being pure white and 0 being black. Therefore BSE qualitative images can be used as a quantitative measure of the local mineral content of bone tissue (15, 52, 74, 76, 252).

Calibration of gray-level for backscattered electron signals is very important in quantification process, which performed using two polymers with high atomic numbers. Thermoset dimehacrylate esters derived from the reaction of halogenated phthalic acids (monobromo: $C_{22}H_{25}O_{10}Br$) and glycidyl methacrylate (monoiodo: $C_{22}H_{25}O_{10}I$) have a BSE coefficients higher than osteoid and bone (higher than practically all calcified cartilage) respectively (253). Conversion of the calibrated grey levels into Ca wt % is performed by measuring osteoid (0 Ca wt %) and hydroxyapatite (39.86 Ca wt %) as reference. The conversion procedure assumes that the backscattered electron grey levels are determined entirely by hydroxyapatite content (74). It is critical to maintain the stability (beam current) of the SEM microscope to acquire the reliable quantification within one run and the duplication of results between runs.

Bone mineralisation density distribution (BMDD) histograms are deduced from BSE images on a pixel basis and can provide quantitative analysis of local variations in bone mineral content. It forms an asymmetric bell curve, with shoulder to the left of the peak which is interpreted as the constantly remodelling and development of adult bone. In contrast to BMD areal measurements performed by DXA, which is an estimate of the total average mineral content in the scanned area, BMDD measurements can differentiate between local changes in degree of bone mineralisation of bone matrix. BMDD reflects the bone turnover, mineralisation kinetics and average tissue age (74, 76). The effects of different rates of remodelling can be seen in the **Figure 2.13**.

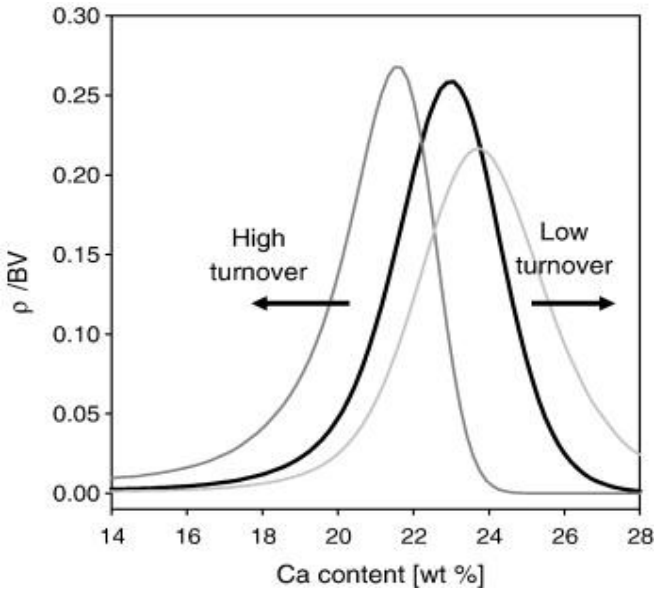

Figure 2.13: A bell shaped curve is typically produced, with a peak of the most frequently occurring degree of minerlisation, and tails both side showing hypo and hyper mineralisaed areas. Dark solid line is the reference BMDD. Other 2 lines are low and high turnover due to the disease induce abnormal mineralisation (adapted from (254))

Using BMDD histograms the five parameters can be derived and they are Ca_{mean}, Ca_{peak}, Ca_{FWHM}, Ca_{low}, Ca_{high}. Ca_{mean} is the mean calcium concentration of the bone matrix obtained from the integrated area under the BMDD curve in units of Ca wt%. Ca_{peak} is the peak position of the histogram, which indicates the most frequently measured Ca concentration in the bone area. Ca_{FWHM} (Full width at Half Maximum) describes the degree of microscale heterogeneity of mineralisation in the field of view. Ca_{low} and Ca_{high} are the percentages of bone matrix that is mineralised below the 5 % and above the 95 % of the reference range respectively (76) as shown in the **Figure 2.14**.

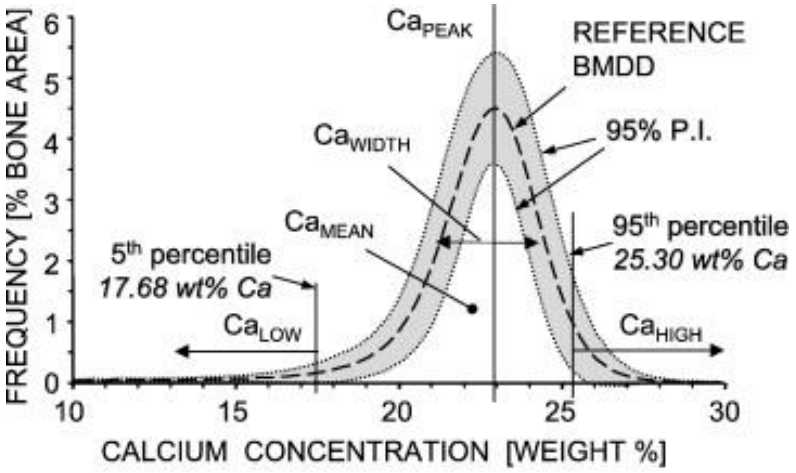

BMDD-parameter	mean ± SD
Ca_{MEAN} [wt% Ca]	22.20 ± 0.45
Ca_{PEAK} [wt% Ca]	22.94 ± 0.39
Ca_{WIDTH} [Δwt% Ca]	3.35 ± 0.34
Ca_{LOW} [% bone area]	4.93 ± 1.57
Ca_{HIGH} [% bone area]	5.55 ± 3.32

Figure 2.14: Dark dash line is the mean BMDD obtained from 52 individuals including various biological factors (gender, age and origin etc). Grey area surrounded by the dotted lines is 95% prediction interval. Mean mineralisation parameters (Ca_{mean}, Ca_{peak}, Ca_{FWHM}, Ca_{low} and Ca_{high}) calculated from BMDD histograms of 52 individuals given in the table (adapted from (76))

BMDD can be use as a parameter reflecting the age and the size distribution of the bone packets within the tissue and several studies have shown that constant values was observed at healthy adult individuals independent of age, gender, ethnic origin and skeletal site (231). Deviations in BMDD parameters were observed with metabolic bone diseases or treatments. Thus measurements from BMDD histograms are used widely to detect the metabolic bone disease and efficacy of the treatment methods in bone field as a clinical and research tool (76, 78, 231, 235, 255).

Since the bone material consist of MCFs, the mineral volume fraction in different compartments (extrafibrillar and intrafibrillar) affects the mechanical properties of bone. The degree of mineralisation in human bone can be varying between 0 – 43 vol % mineral content due to the continuous replacement of old bone (secondary phase of mineralisation) (8). The calcium weight percentage found in the qBSE results can be

converted to a volume percentage Φ, as described by Roschger and co-workers (256). The Ca wt. % is first converted to mineral – Hydroxyapatite (HA) weight percentage using the stoichiometric relation HA wt. % = 2.51 x mean Ca wt. %. Using the densities of collagen 1.47 g cm^3 (ρ_{org}) (257) and mineral phase (ρ_{HA} = 3.18 g/ cm^3) the volume fraction can be written as:

$$\Phi = \frac{HA_{wt}}{HA_{wt} + (1 - HA_{wt})(\rho_{HA} / \rho_{org})} \quad \text{Equation 2.11}$$

2.5 Quantitative micro computer tomography

MicroCT is a non-destructive technique that allows in depth exploration of samples at micon scale in 3D. X-ray microtomography scanner was initially designed by Elliott and Dover in 1981 in order to measure and map the local mineral concentration in biological hard tissues (258). MicroCT was used extensively in clinical and scientific research in the field of bone due to its non destructive nature and prior sample preparation is not needed (259-261). Even though data acquisition was quite slow with energy dispersive photon counting apparatus they gave accurate measurements of the X-ray linear attenuation coefficient (LAC). LAC (cm^{-1}) is the fraction of a beam X-rays that is absorbed or scattered per unit thickness of the material. These first generation scanners are capable of producing a single slice 128 × 128 pixels image in 12 hours. In contrast fourth generation microCT scanners are generating Giga voxel images in minute (262). MicroCT scanners use the similar principal of the medical CT scanners. MicroCT and CT scanners both consist of fixed X-ray source, detector and the rotating sample stage. In contrast, X-ray source and detector of medical CT scanners are mobile. In microCT, sample is mounted on the rotatory stage with in the X-ray beam as shown in the **Figure 2.15.** During the experiment sample is rotating 180°, and at each step images are acquired by the microCT detector with fast readout time. Fourth generation microCT are capable of producing nano size beam spots which allows high resolution and high signal to noise ratio imaging (263).

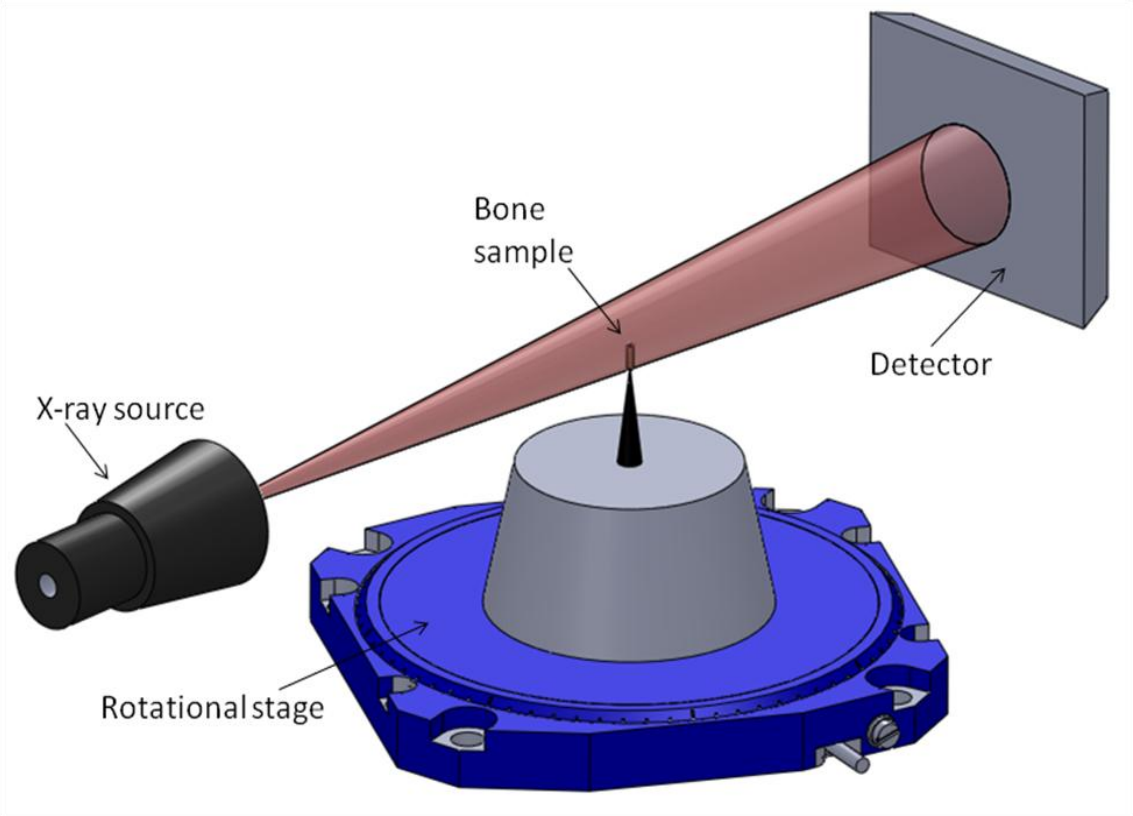

Figure 2.15: A schematic for X-ray microCT setup

Bone architecture (especially trabecular bone) has been studied quantitatively and qualitatively using microCT for many years (259, 260, 264). For example osteoarthritis-induced alterations in trabecular bone have been studied (265). These researchers observed significant difference in volumetric BMD and subcondral cyst formation in osteoarthritic conditions. Reconstructed microCT images have been used extensively to measure different trabecular parameters: trabecular thickness, spacing, number and orientation. These trabecular structural parameters used to investigate the bone quality changes at the micro level during osteoporotic conditions (266). With current advances it is also possible to perform Finite Element Analysis (FEA) on data obtained from microCT. These analyses are useful to understand the structural and mechanical alterations during pathological conditions of bone at the microscale (261, 267, 268). In this thesis microCT (Tring, Hertfordshire, UK, now part of Nikon Metrology, Leuven, Belgium) was used to investigate the changes in volumetric mineralisation during metabolic bone diseases and as an approach to correct for porosity at the microscale.

2.6 Mouse-model phenotypes of bone disease.

The random nature of N-ethyl-nitrosurea (ENU) induced mutations facilitates a phenotype driven approach to mutation detection. ENU mutagenesis make no assumptions about the nature of the genetic change underlying observed phenotypes, and thus provide a powerful tool for identifying novel genes and pathways contributing to disease pathogenesis (269). After administration of the chemical mutagen (ENU) most of the mutagen rates occurs in the premeiotic spermatogonial stem cells (270). ENU transfer its ethyl group to oxygen or nitrogen radicals in DNS, resulting in mispairing and base-pair substitution if not repaired. This technique has a capability of isolating single gene of choice in one out of every 175-655 gamete screened (271, 272).

2.6.1 ENU mutagenic mouse model for Human -linked Hypophosphatemic Rickets (XLHR)

In this thesis, a new mouse model (Hpr) was utilised for X-linked hypophosphataemic rickets (XLHR). The Hpr model is created by ENU induced mutation due to a missense Trp314Arg mutation of the Phosphate regulating gene with homologies to Endopeptidase on the X-chromosome (*Phex)*, It is designed as a model system to investigate alterations in nanoscale deformation associated with defective bone mineralisation in rickets. Hpr mice are also phenotypically similar to those in other reported mouse models of XLHR such as *Gy* (273) and *Hyp* (274) mouse models which are also caused by mutations in the *Phex* gene. In addition to the plasma and radiographic abnormalities observed in Hpr and *Hyp*, male *Gy* mice were also hyperactive, sterile and showed reduced viability (275). Previous studies have undertaken measurement of both structural and macromechanical alterations in the *Hyp* mouse (275). Carpinelli et al performed biochemical and molecular characterisation of mouse treated with ENU (276). These mice show unmineralised epiphyseal growth plate, reduced thickness in mid dyaphyseal cortex and the proximal metaphysic has increased trabecular which are characteristic features of rickets. In addition *Hyp* mice have been shown delayed growth plate calcification and impaired bone mineralisation with a decreased mineral content in long bones (277). X-Linked hypophosphatemic mice shows reduced serum phosphate levels and markedly elevated serum alkaline phosphatase levels (183) which are features consistent with XLHR in

man. Thus, Hpr mouse, which is due to a missense *Phex* mutation, is a suitable model system for studies investigating the structural and mechanical alterations associated with persistent hypophosphatemia and defective bone mineralisation commonly seen in XLHR patients.

Several research groups have studied pathological mechanical and structural alterations in defective rachitic bone tissue. Camacho et al. (1995) measured mechanical behaviour in torsion of XLHR mice femora at the tissue level. XLHR mice femora underwent more angular deformation before failure than wild-type, indicating a reduced torsional stiffness. These researchers proposed that differences in mineral content, distribution and molecular nature of the mineral in the long bones contributed to reduced macromechanical properties, but the size of the mineral particles (measured with X-ray diffraction) was not observed to change. Similar results were found in other studies (183, 184, 276, 277).The mineral phase in *Hyp* mice, however have demonstrated increased mineral crystal size (crystallinity) in the long bones on another study (277).

2.6.2 ENU mutagenic mouse model of Cushing's syndrome with glucocorticoid-induced osteoporosis (GIOP)

In mouse models, GIOP was found to reduce the trabecular bone micro architecture and the degree of bone mineralisation compared to the placebo mice and ovariectomised mice (177, 278) due to the adverse effect of steroids on cellular activity, (down-regulating of osteoblasts and long life span of osteoclasts) (279, 280), but there was no overall change in Young's modulus. However in mice treated with prednisolone (steroids), size of osteocytic lacunae were increased, localised reduction in elastic modulus surrounding osteocytes and unmineralised regions "halos" around the lacunae were observed (178) with a decrease in the mineral: matrix ratio. These focal changes observed in glucocorticoid-treated mice were not seen in estrogen-deficient mice or placebo treated mice. This suggests that glucocorticoids may have a direct effect on osteocytes in order to induce these localised changes in bone structure at the micron length scale. Hence, these alterations in the localised material properties (osteocyte microenvironment) and reduction in bone mass also may be linked to excess bone fragility in glucocorticoid-treated animals. GIOP bone in humans has been shown to exhibit trabecular plate

thinning, with perforation and connectivity alterations seen almost universally in patients (281), a phenomenon similar to what is observed in GIOP mouse models. A mouse model of GIOP, induced with prednisolone pellets, was compared to placebo mice and also to GIOP mice treated with risedronate, to investigate the effect of the residronate treatment on structural changes such as trabecular volume and thickness (177). Using synchrotron microCT, SAXS and TEM, these researchers shown that the bone architecture changes at micro- and macrostructural levels in GIOP compared to placebo treated mice, specifically reduction in trabecular bone mass, microarchitecture, the degree of mineralisation and elastic modulus within the trabeculae. These changes were reversed by the risedronate treatment (177). This study also used bone biopsies from human iliac bones to compare glucocorticoid, placebo and risedronate and observed consistent mineral heterogeneity in glucocorticoid group compared to placebo and risedronate administration. Similar to the findings from mice bone, risedronate treatment improved the bone architecture in humans. This study thus showed the ability to translate findings from mouse to human studies and the similarities in the alterations in GIOP in both species, thus helping to validate mice models as a structurally accurate model of human GIOP (177).

An inherited mouse model for Cushing's disease that results in GIOP by endogenous production of steroids was used in this thesis to detect the influence on ultrastructural deformation mechanisms in altered microscale mineralisation. This mouse model has been developed by Roger Cox and co-workers at the Mammalian Genetics Unit at the Medical research council via chemical (ENU) mutagenesis, and induced mutation of the corticotrophin releasing hormone (*Crh*) promoter (Bentley et al, 2012 Bentley). The most frequent cause (approximately 70%) of endogenous hypercortisolism is Cushing disease and this is normally arising due to the pituitary tumour arising from adrenocorticotrophic hormone secreting corticotroph cells (282). Glucocorticoids have a direct effect on bone in Cushing's disease leads to decreased bone density and the increased risk of fracture (283). There are several mouse models (284-287) developed for phenocopy aspects of Cushing's disease, although not all aspects of the bone phenotypes are fully understood yet. *In vivo* assessment of $Crh^{-120/+}$ mice revealed them to have, when compared to wild-type ($Crh^{+/+}$) mice, obesity, hypercorticosteronaemia, hyperglycaemia, and low BMD

(Bentley et al, 2012 – manuscript in preparation). Furthermore, *Crh*$^{-120/+}$ mice, when compared to wild-type mice, had reduction in: mineralising surface area; mineral apposition rate; bone formation rate; and osteoblast number which was accompanied by an increase in adipocytes in the bone marrow consistent with steroid induced osteoporosis. Thus, the *Crh*$^{-120/+}$ mice represent a model for Cushing's syndrome and GIOP (Bentley et al, 2012 manuscript in preparation). It has also been found in *Crh*$^{-120/+}$ mice increased trabecular bone volume and trabecular number, reduced trabecular thickness, cortical bone volume and cortico-endosteal bone covered in osteoblasts which were not reported in the *Crh* transgenic mice (287). Some of the similarities between *Crh*$^{-120/+}$ mice and transgenic *Crh* mice include obesity, muscle wasting, hair loss, thin skin and elevated plasma corticosterone levels (288). A reduction in bone quality and osteoporotic characteristics observed in this mouse model highlights the potential utility in studying structural and mechanical alterations in steroid-induced osteoporosis and therapeutic interventions.

2.6.3 Klotho – a mouse model for pre mature ageing with removal of the klotho gene

Most of the information on the alterations in bone development come from animal models where there is early senescence: Senscence-accelerated mice (SAMP6) (289) and klotho mice (290) models. A mouse model for premature ageing has identified by deletion of klotho gene which determines inherited premature ageing syndromes and causes rapid development of multiple age-related diseases early in life, while overexpression extends the mouse lifetime (291). Knockout of klotho gene predominantly expressed in renal tubules. These mice are exhibit various bone phenotypes resembles in patients with premature ageing syndrome: ageing, arteriosclerosis, skin atrophy, osteoporosis and emphysema (290) and they were appeared only in homozygous transgenic animals. Klotho deficient mice have similar characteristics to steroid induced osteoporosis which is cortical thinning mainly due to the increased osteoclastic activity and distinct from postmenopausal osteoporosis (292). Almeida et al have found that increased production of glucocorticoids in C57BL/6 mice which is associated with ageing process (293). Similar effects found in human with

increase in endogenous glucocorticoids in old age which leads to enhanced skeletal fragility (294, 295).

In another study performed with the klotho model, it was found that due to the early death of osteocytes, the cell interaction with bone matrix is altered (193) which may lead to inability to repair the cracks and increasing crack propagation with age (191, 192). Klotho mice appeared to have all the phenotypes within them while for SAMP6, different phenotypes are distributed among different SAMP6 studies. The phenotypes for the klotho mice also appeared faster in age than for SAMP6. Hence klotho mouse model is an excellent model for studying age-related alterations over a short time period.

Chapter 3

Design of *In situ* Micromechanical Testers for Synchrotron SAXD

The contents of this chapter explains the design process and operational principals underlying the mechanical testing machines developed during this study

3 Design of *In situ* Micromechanical Testers for Synchrotron SAXD

In the previous chapter the principle of the use of SAXD while applying external loading in order to understand nanomechanical properties of bone material was discussed. The mechanical testing of bone together with X-ray diffraction presents several distinct challenges which cannot be attained with conventional mechanical testing rigs (Instron™ etc). Therefore, it was crucial to design a custom made micro mechanical testing machine to study the mineralised tissues *in situ* at the synchrotron. One of the design requirements of the machine was to apply external loads by stretching or bending the bone sample while the sample was immersed in the phosphate buffered solution. The equipment should also have telescoping inlet and outlet X-ray windows to control the X-ray beam path through the liquid as well as an optical viewing window to enable a CCD camera to image markers on the specimen moving during loading (additional requirements and their justification listed in the later section (3.2)). Development of this testing rig followed an established design phase illustrated in **Figure 3.1.**

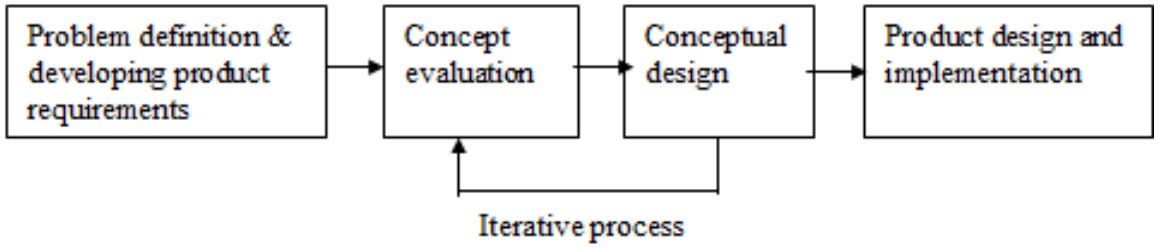

Figure 3.1: Design process: Iterative processes were carried out between the phases for each subsystem of the mechanical testing machine

The first part of the design process identifies the essential requirements of the mechanical testing rig, design requirements and the prioritisation of these requirements.

3.2 Specifications

The identified product specifications of the micro mechanical testing machine are as follows:

- The micro testing rig was designed for *in situ* mechanical tests at synchrotron sources especially for the microfocus end station at the beam line I22 at DLS. This equipment was designed to be housed at DLS, following completion of the project for the benefit of the wider small angle X-ray scattering community.

- The micromechanical testing machine should be able to measure the small loads (2N -30N) and elongations (~ 2 %) required to deform the microscale (50-200 μm) bone samples.

- The mechanical testing machine grips shall allow delicate bone samples to be easily mounted in the instruments without damaging the bone structure. Micro-size bone specimens are very sensitive to being damaged by off-axis forces incurred during mounting, so a precise and reproducible mounting system is essential.

- Bone samples shall be fully immersed in phosphate buffered solution throughout the experiment in fluid chamber in order to mimic the physiological environment around the bones *in-vivo*.

- Total path of the X-ray beam through phosphate buffered solution fluid chamber must be as short (~1-5mm) as possible to minimise X-ray absorption. As the X-ray absorption in water is a function of the X-ray energy, different lengths may need to be used for different beam energies. On the other hand, absorption of X-rays may also be beneficial, by reducing the radiation dosage to the bone specimen, which has been previously shown to affect mechanical properties (296).

- The mechanical testing machine shall have a viewing window off-axis to the X-ray path. Images captured by a CCD camera through this viewing window will be used to calculate the tissue strain.

- The mechanical testing machine shall be computer-controlled via a LabVIEW™ interface located in the user control room (10 m away from the testing machine) at the I22 beam line at DLS.

- Total cost (material and manufacturing) needs to be within a budget of £5000, as per the consumables budget of the PhD studentship.

The goal of the requirement definition phase was to understand the problems and to establish the foundation to the remainder of the design process. This formulated requirement list has been presented and discussed with the supervisors.

3.3 Conceptual designs

Decisions made at the concept development phase were crucial as they would affect the downstream phases in the design process. Several designs were generated, however some of the designs were discarded during this phase as they are not feasible to manufacture within the budget.

Brainstorming was the initial source that has been used for generating conceptual designs. Ideas from the primary and industrial supervisors were also incorporated during the design process. Manufacturer catalogues were another good source of information used during the concept generation.

Initial concepts were sketched by pencil and then translated into 3D drawings using Solidworks™ CAD software (Dassault Systèmes SolidWorks Corporation, Waltham, USA). This allows the designer (the present author) to evaluate the concepts from 3D. More importantly, 3D drawings allowed the designer to simulate the assembly of all the subsystems and thereby, the functionality of each conceptual design was evaluated before making final decisions. 3D Solidworks conceptual drawings have also been used as a good communication tool to illustrate ideas to a third party such as project supervisors, technicians etc.

During the initial brainstorming sessions it has been identified that the micromechanical testing device can be divided into 4 subsystems:

- Sub system 1- Motorised linear encoder stages

- Subsystem 2 – Load cell
- Subsystem 3 – Sample grips
- Subsystem 4 – fluid chamber

Since this micromechanical testing machine was specifically designed to use in the micro-focus facility at I22 beam line, space availability for the mounting of this machine was given the highest priority when deciding the size of the various components. Available space for the machine was restricted to 150 mm^3 (**Figure 3.2**). Several designs of machine assembly prototypes were produced which include possible combinations of subsystems. The main goal was to choose the most compact design due to the restricted space of the sample environment at the beam line.

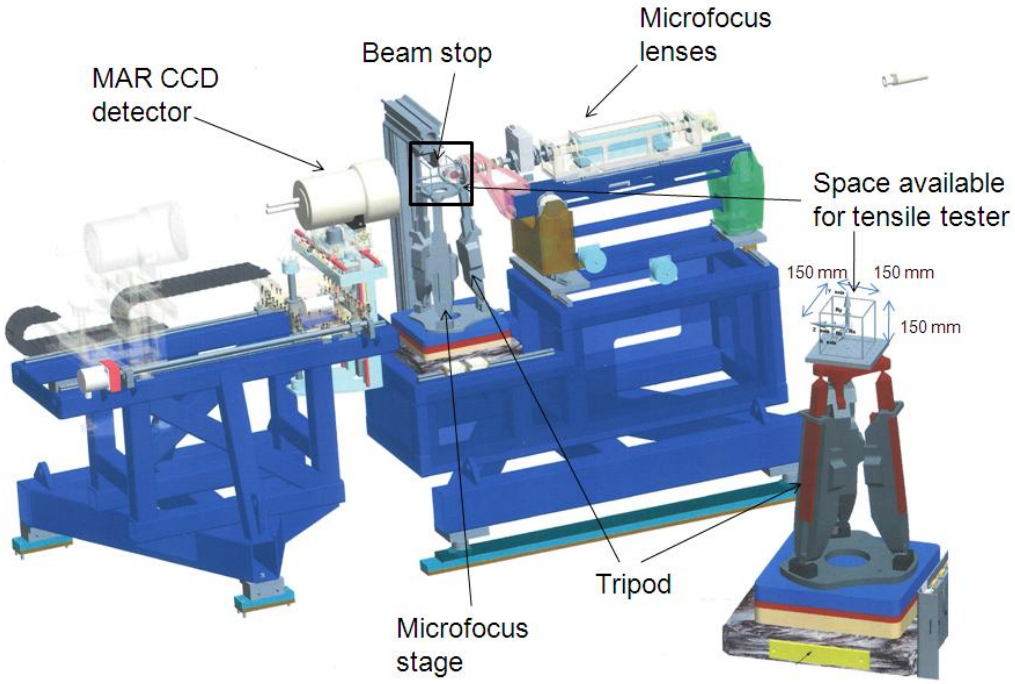

Figure 3.2: Microfocus setup at the I22 beam line, DLS. Mechanical testing machine will be mounting on the tripod stage (150 mm × 150 mm). Due to the beam stop assembly above the tripod height also restricted to 150 mm

3.4 Concept evaluation

3.4.1 Sub system 1- Motorised linear encoder stages

Testing machine should be simple and easy to manufacture and have little assembly time. Some of the prototypes considered are shown in the **Figure 3.3** opposite. Prototype *A*, *B* and *C* equipped with 2 M230.10 DC Mike high resolution linear actuators (M230.10DC linear actuators, Physik Instrumente, United Kingdom), and 22 N model 31 tension/compression load cell (SLC31/00005, RDP electronics, West Midlands, United Kingdom). 10 mm travel range actuators were chosen which have 0.05 µm minimum incremental movement. The highest length of this assembled prototype was ~350 mm. Therefore these three concepts had to be removed from the design process due to the space restrictions in the microfocus beam line.

Prototype *D* (**Figure 3.3**) was equipped with a DC servo motor connected to the external lead screw system to obtain the bi-directional movement which increased the complexity. Prototype *E* and *F* (**Figure 3.3**) featured bi-directional motion of two DC linear-encoder stages (M110.1DG, Physik Instrumente, United Kingdom), which has a minimum incremental motion of 0.1 µm. Load was measured with a 22 N model 31 tension/compression load cell.

Concept E and F were chosen for further consideration. Two M110.1DG compact micro translation stages were bought from Physik Instrumente Ltd, United Kingdom. These compact stages have submicron resolution and precision with < 0.5 µm straightness of travel.

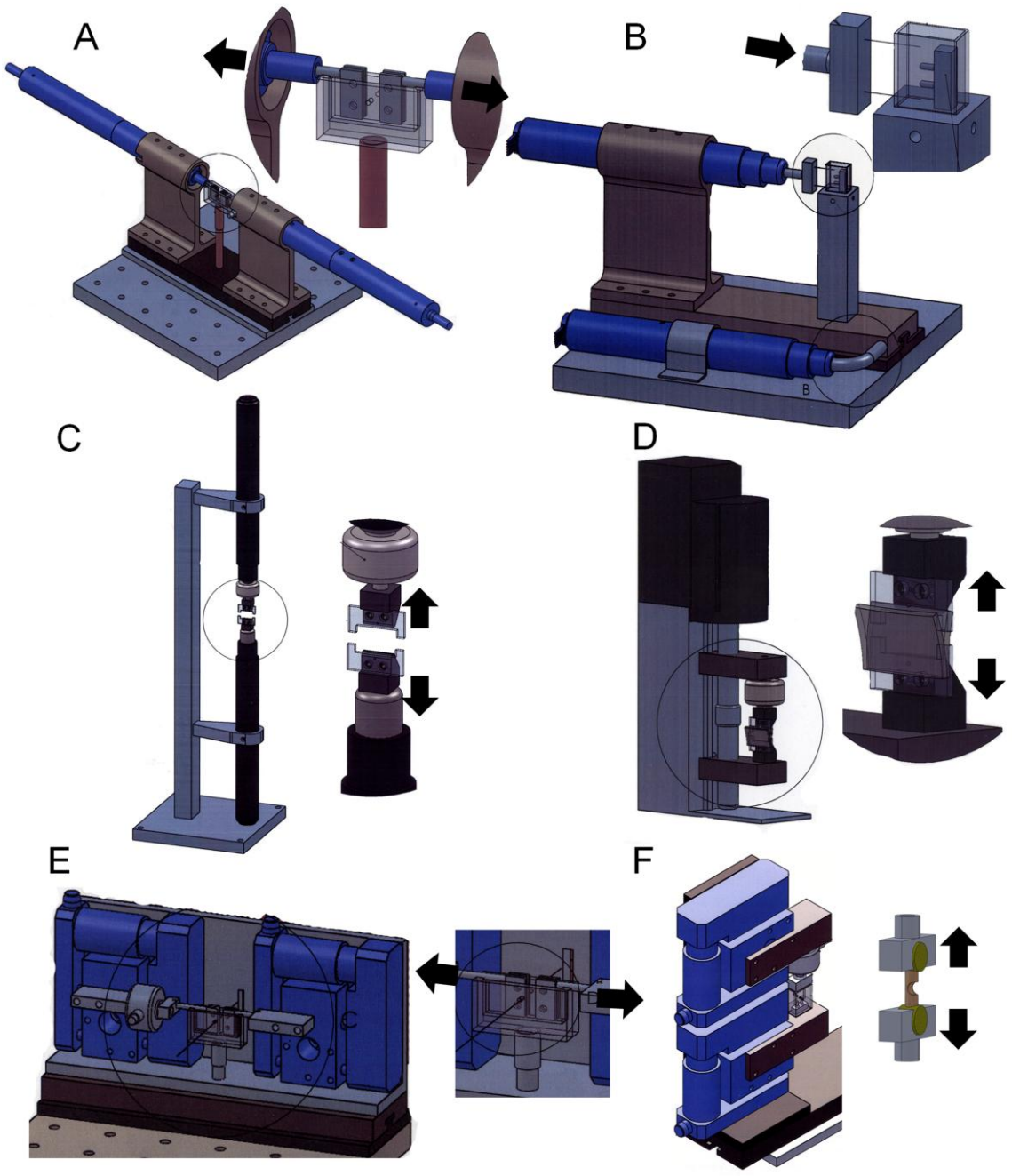

Figure 3.3: (A) M230.10 Linear actuators connected in horizontal configuration (B) 4 point bending machine equipped with 2 M227.10 linear actuators which are connected in horizontal configuration (C) Tensile testing configuration - 2 M227.10 linear actuators which are connected vertically (D) C136.10 closed loop DC servo motor drive combined with a lead screw system (E) M110.10 DC linear-encoder stages (M110.1DG, Physik Instrumente, United Kingdom) assembled in vertical configuration (F) Vertical configuration of concept in E. The loading directions are represented by black arrows

3.4.2 Subsystem 2 – Load cell

When selecting the load cell the following requirements were considered

- The load cell should be capable of measuring up to 20 N in tension and compression modes. Due to the space restriction it should be small in size. Load values could be obtained easily by the controlling computer without using intermediate interfaces.

22 N model 31 tension/compression load cell (SLC31/00005, RDP electronics, West Midlands, United Kingdom) was chosen after extensive market research. This load cell satisfied most of the requirements listed above. One of the main features of this load cell is its small sensor (< 5 mm). A disadvantage of the model 31 load cell was that it requires an additional amplifier in order to convert the analogue output to a digital output, which was added to the cost.

Subsystem 2 and 3 were manufactured in-house due to the customised structure. At this stage it was discovered that the vertical configuration of micro-mechanical tester (**Figure 3.3F**) was more feasible when designing the fluid chamber and sample grips. Additionally it has more flexibility to change into different loading modes (tensile testing to bending setup).

3.4.3 Subsystem 3 – Sample grips

Designing the sample gripping system was an iterative process involving several brainstorming sessions. These grips have to fulfil a number of requirements.

1. Since this testing machine was designed to test the mechanical behaviour of mice bones during different loading conditions, sample grips had to be designed separately and connected to the testing machine, therefore, they should have the flexibility (easy removal) to replace with different grips when changing to another test method.

2. Applied load by the machine shall be transmitted directly to the bone specimen; compliance effects in the grips must be kept to the minimum to minimize errors in tissue strain readings from motor displacement.

3. Grips shall not create significant stress concentrations on the sample (e.g. bony ends should not be over-tightened by the grips).

4. Sample grips shall be fixed into the machine smoothly to avoid any jerking and twisting movements during the deformation.

Two different sample gripping systems were developed for the micromechanical tensile and bending testers.

3.4.3.1 Tensile testing grips

The grips were designed with a circular shaped hole (6 mm in diameter and 3 mm in depth). Both ends of the femur were secured in dental cement (Filtek^{TM} Supreme XT, 3M ESPE, USA). These dental ionomer ends have a clearance dimension of 5 mm to fit into tensile tester grips. Sample preparation will be explained in **Chapter 4**. This method of sample gripping avoids any additional forces applied on the bone sample by conventional tightening gripping systems, which may introduce stress concentrations at the grip ends.

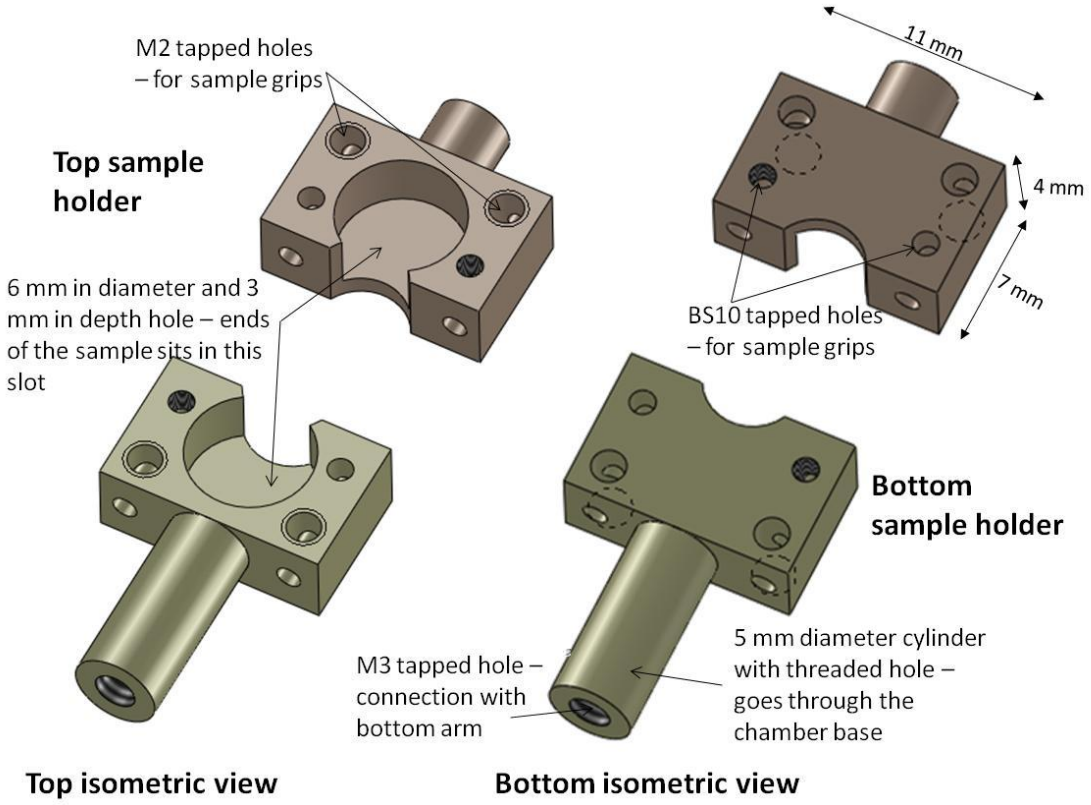

Figure 3.4: Tensile testing sample grips were made of medical rated stainless steel to avoid corrosion when they are in contact with saline solution. They both have circular shape hole with 6mm in diameter and 3 mm in depth

The bottom side (flat side) of the sample holders can be used when testing the samples (i.e. soft tissues) that need tightening to the surface.

3.4.3.2 Bending tester grips

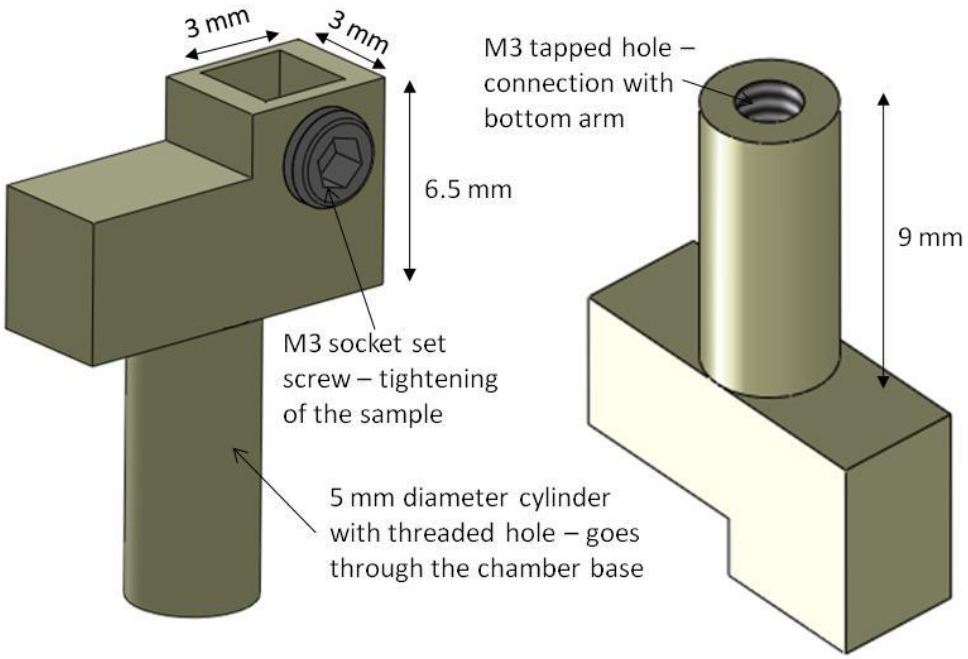

Figure 3.5: Bending tester sample holder. A 3 mm2 square hole in the sample holder has the depth of 5 mm which enables the experimenter to secure the dental ionomer block in the testing machine

Bony ends were included in the dental ionomer (see Chapter 4 for the sample preparation procedure) in order to mount the bone sample inside the square hole (3 mm × 3 mm) of the bending tester as shown in **Figure 3.5**.

3.4.4 Sub system 4 - Fluid chamber

The main requirement of the fluid chamber is to keep the bone hydrated in a condition close to the physiological environment of the bone tissue, by immersing the samples in phosphate buffered saline solution. Furthermore, the chamber should provide a mechanism to create a narrow pathway between the X-ray inlet and outlet to minimize the absorption of X-rays in the saline. To enable this feature, the fluid chamber was designed with tubes protruding into the chamber from the front and back surfaces. These tubes are covered with Ultralene film (Spex SamplePrep, Metuchen, NJ, USA), which contributes a negligible background X-ray scattering in the SAXS regime.

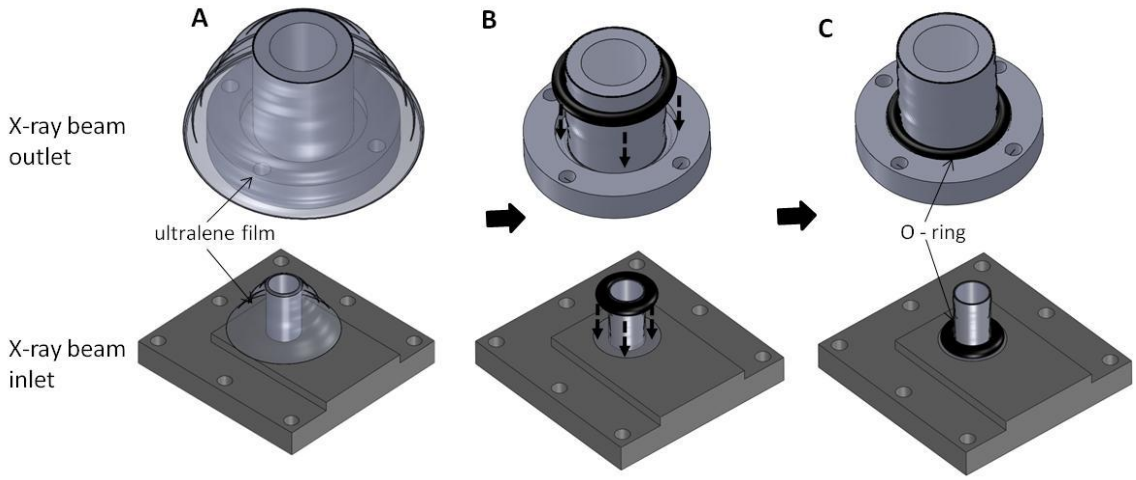

Figure 3.6: Preparation of X-ray outlet tube with fixing the Ultralene and O – ring (A) Place the piece of ultralene film on top of the outer surface of the tube (B) Gently press down the rubber O – ring until it touches the bottom surface (C) Leave for 10 to 15 mins to fix the Ultraleane fllm to the surface of the inlet tubing

The compact size of this fluid chamber was very important to reduce the X-ray path length though the liquid (mass attenuation coefficient of the water is 5.529 cm^2/g, when the 10 keV X-ray beam travels through saline water, 95 % of the energy has been absorbed by the water). This feature necessitates a shortening of the total path of the X-ray beam in the phosphate buffered solution to approximately 6 mm. The inlet and outlet windows have the diameters of 6 mm and 10 mm respectively. The outlet window was designed with a larger diameter compared to inlet in order to avoid shadowing. The fluid cell (**Figure 3.7**) designed for this micromechanical tester features a viewing window 90º to the X-ray inlet in order to obtain the video extensometry images through the saline solution. A clear (transparent) view through the solution was obtained by fixing a glass slide to the viewing window.

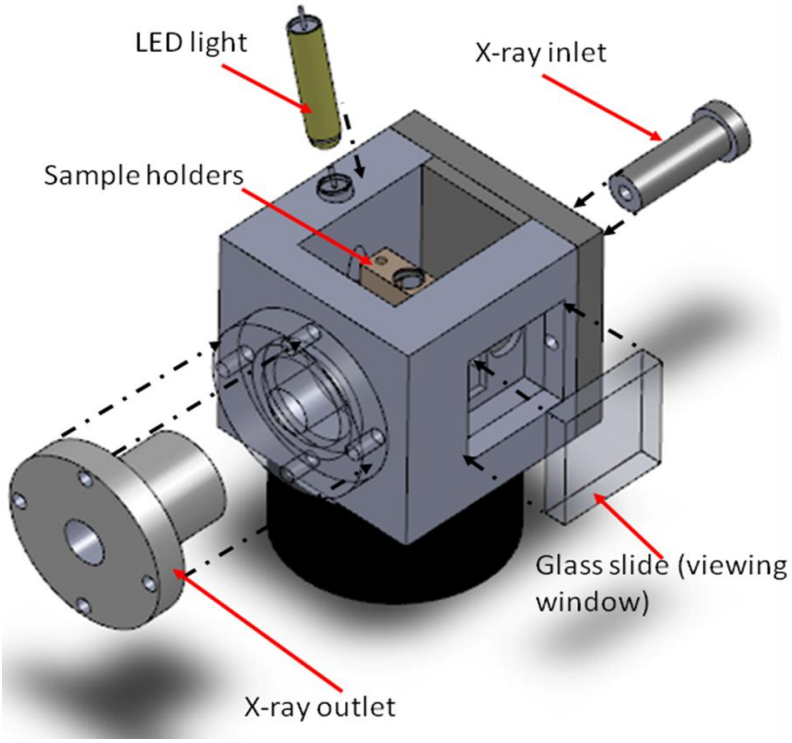

Figure 3.7: Fluid chamber assembly drawing. Chamber was made of medical rated stainless steel

Two markers were put on the sample by a water-proof ink pen and the tissue strain was estimated by measuring the displacement of these marks. The interior of the fluid chamber was illuminated by fixing an LED light inside the fluid chamber as shown in the **Figure 3.7,** which increases the quality (contrast between marks and bone) of the images captured by the CCD camera.

3.5 Assembly of Micromechanical tensile testing machine

The main subsystems of the testing machine were described in the previous sections. These subsystems need to be assembled together with several additional parts which were manufactured by the technical support team at School of Engineering and Materials Sciences, Queen Mary University of London.

3.5.1 Upper arm assembly

Load cell and the top sample holder assembled to the upper arm using a cylindrical metal component and a rectangular component.

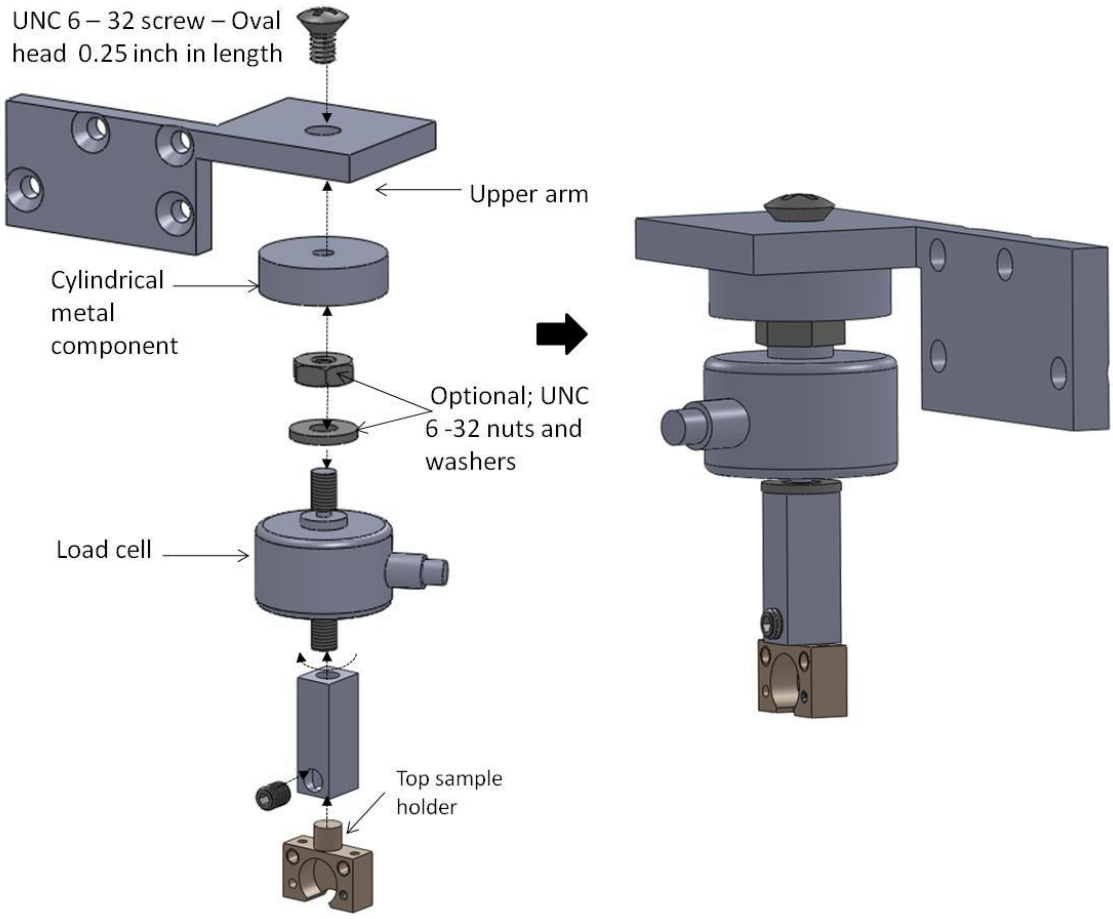

Figure 3.8: Load cell and top sample holder assembly to the upper arm - Place the sample holder inside the slot of the metal component and screw in M3 grub screw to secure the holder inside the hole

3.5.2 Lower arm assembly

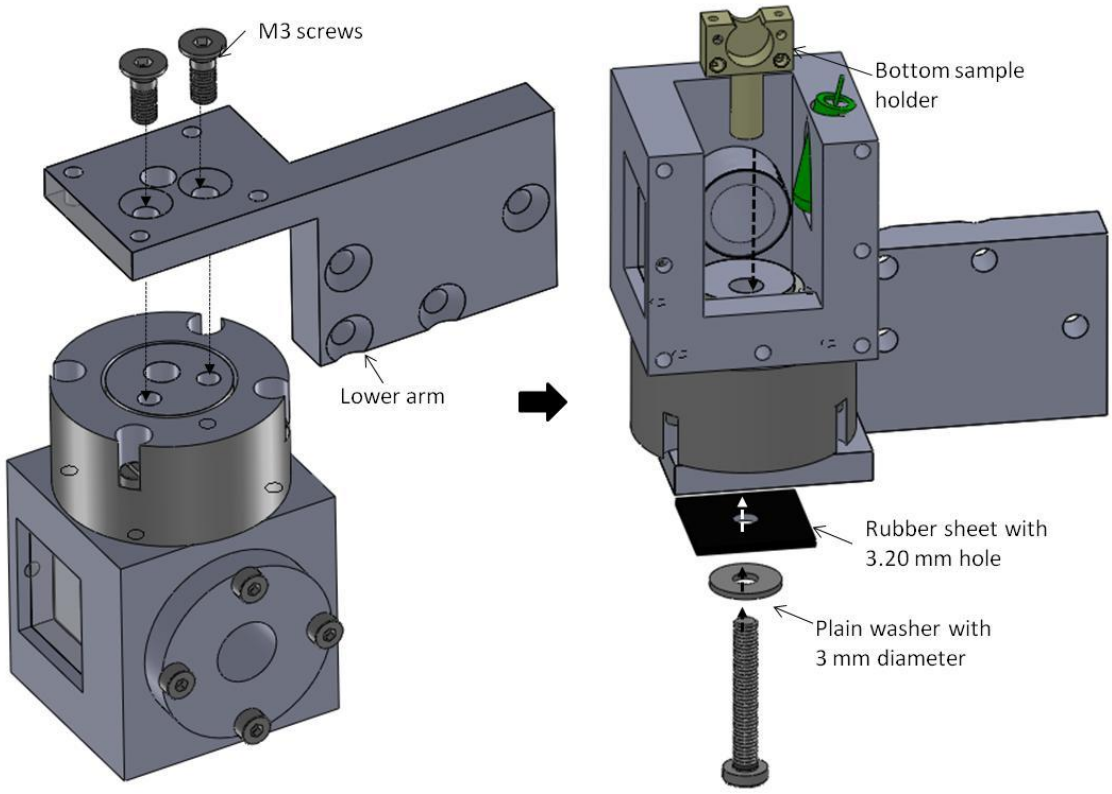

Figure 3.9: Fluid chamber and bottom sample holder assembly to the lower arm – Push the bottom sample holder through the hole and screw in M3 screw (20mm in length) in to the bottom sample holder through the lower arm and the fluid chamber base

This device uses two oppositely driven DC linear-encoder stages (M110.1DG, Physik Instrumente, United Kingdom) to stretch the sample, thus ensuring that the middle of the sample remains at the same position with sub-micron precision. Thus, when a micron-size X-ray beam irradiates the sample, the initial scattering volume will not shift out of the beam during the tensile deformation. This enables the load-induced nanostructural changes in the same microstructural region to be followed in real time, and is critical when combining micromechanics with micron-size X-ray optics in order to ensure changes in SAXD spectra which are taken from the same scattering volume.

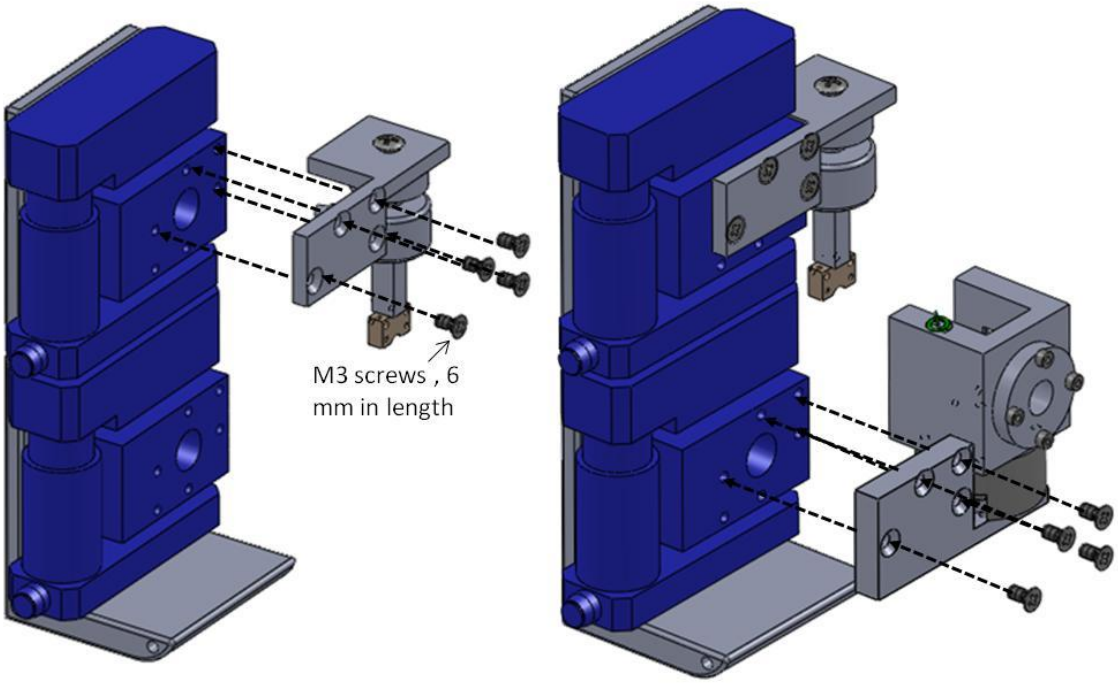

Figure 3.10: Assembly of the lower and the upper arms: Fluid chamber is connected to the bottom stage via chamber holder and load cell connected to the top stage via load cell connector

3.6 Assembly of Micromechanical cantilever bending testing machine

A custom made micro-tensile tester (**Figure 3.11**) was modified to carry out cantilever bending combined with spatially-resolved microfocus SAXD with 5 μm step-size across the width of the bone sample. This experiment is explained in greater detail in **Chapter 6**. One M110.1DG stage was used to apply the bending force via load pin on the bone sample and the alignment of the sample under the load pin was performed by the other linear stage.

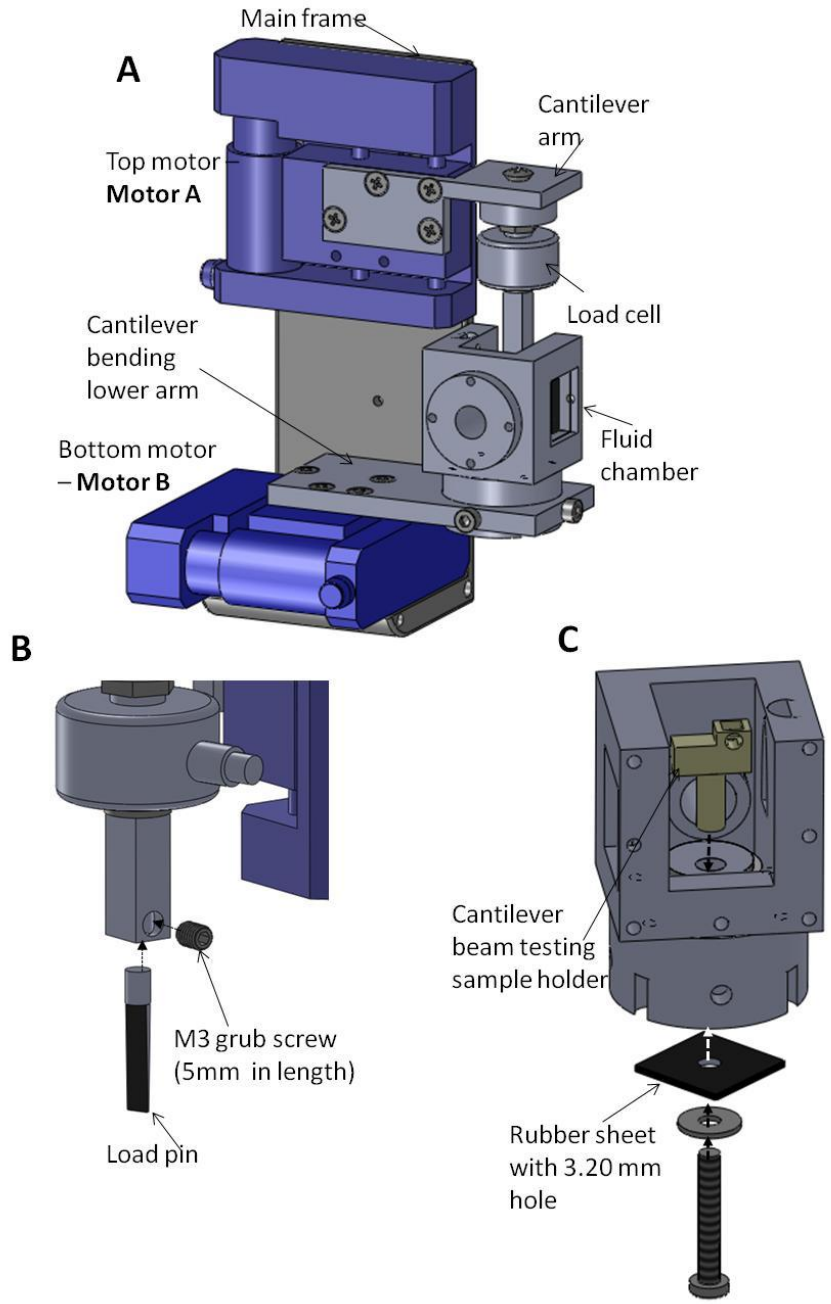

Figure 3.11: (A) Front view of the cantilever bending tester (B) Load pin assembly to the upper arm (C) cantilever bending sample holder assembly to the bending machine using M3 screw

Chapter 4

Sample Preparation and Experimental Protocols

This chapter provide the overview of sample preparation procedures and experimental protocols developed during the study. Most of the contents in this chapter have been published in

- A Karunaratne, CT Esapa, J Hiller, A Boyde, R Head, JHD Bassett, NJ Terrill, GR Williams, MA Brown, P Croucher, SDM Brown, RD Cox, AH Barber, RV Thakker, HS Gupta. *Significant deterioration in nanomechanical quality occurs through incomplete extrafibrillar mineralisation in Rachitic bone: evidence from in-situ synchrotron X-ray scattering and backscattered electron imaging*. *2012*, J Bone Miner Res. 2012 27(4):876-90.

- A Karunaratne J Hiller, CT Esapa, NJ Terrill, AH Barber, RV Thakker, HS Gupta. *Hypophosphatemic rickets is associated with disruption of muscle stress-mediated mineral orientation at the nanoscale in the flat scapular bones of rachitic mice with development. 2012*, Bone. 2012 51(3):553-62

- A Karunaratne J Hiller, CT Esapa, NJ Terrill, AH Barber, RV Thakker, HS Gupta *Symmetrically reduced stiffness and increased extensibility in compression and tension at the mineralized fibrillar level in rachitic bone* , 2012 (In press - Bone)

- A Karunaratne, GR Davis, J Hiller, Liz Bentley, CT Esapa, NJ Terrill, SDM Brown, RD Cox, RV Thakker, HS Gupta. *Functional link between material level structural alterations in steroid induced osteoporotic bone and its increased fragility*, 2012 (prepared to submit for either PNAS or JBMR)

4 Sample Preparation and Experimental Protocols

4.1 Sample preparation

Tensile testing and cantilever bending experiments used two different protocols for sample preparation. Specimen thickness is very important in SAXD experiments in order to obtain the maximum scattering intensity. Following equation (**Equation 4.1**) shows that scattering intensity increase linearly as a function of sample thickness, but X-ray absorption increases exponentially. The scattering intensity (*I*) can be formulated as:

$$I \alpha d e^{-\mu d} \quad \text{Equation 4.1}$$

where, d and μ are the thickness of the sample and the linear absorption coefficient respectively.

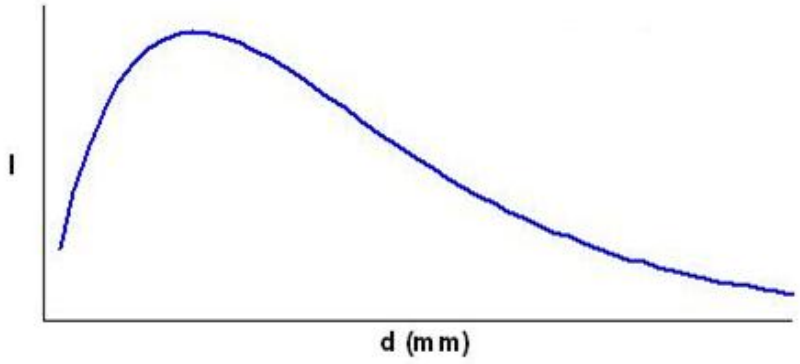

Figure 4.1: The optimal thickness of the sample is obtained at the maximum of the curve

Differential equation can be given by

$$\frac{\partial I}{\partial d} = (1 - \mu d) e^{-\mu d} \quad \rightarrow d_{optimal} = 1/\mu \quad \text{Equation 4.2}$$

Using the linear attenuation coefficient of mouse cortical bone (40 cm^{-1}), optimum thickness for the test specimen was calculated (~ 200 µm).

4.1.1 Tensile testing - Sample preparation

Dissected femora from mice were skinned, muscle tissue removed, wrapped in gauze soaked in phosphate buffered saline, and stored at -20^{o}C until mechanical testing (approximately one week). Animals used in this thesis were sacrificed at different ages (**Table 4.1**); hence two different methods were used for initial preparation for tensile testing depends on the lengths of the femur.

Table 4.1: Mouse models used in this thesis, their phenotypic diseases and age

Mouse model	Disease	Age
Hpr	Hypophosphataemic rickets	4, 7 and 10 weeks
Crh$^{-120/+}$	Glucorcoticoid induced osteoporosis	26 weeks
klotho	Ageing	5 weeks

Steps of the systematic sample preparation are shown as a block diagram in the **Figure 4.2**. *Crh*$^{-120/+}$ and klotho mice femora were bigger than the Hpr mice bone, therefore they were sliced longitudinally into two sections before including bony ends in the dental ionomer.

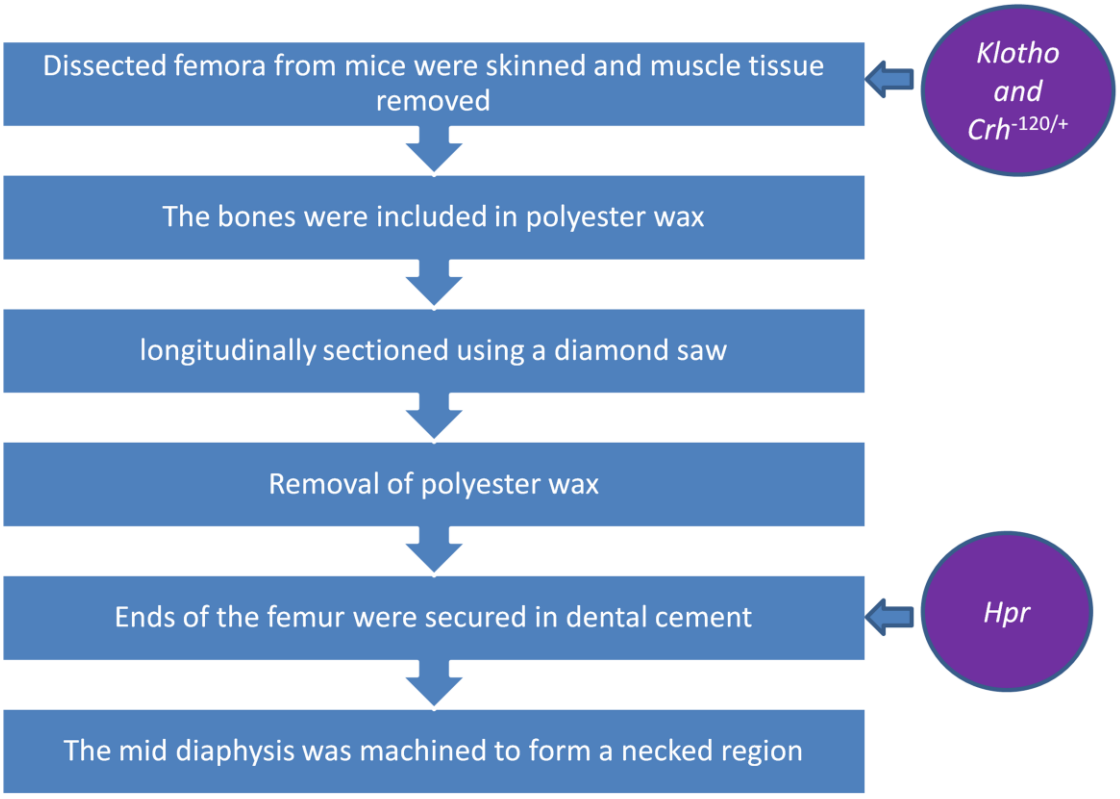

Figure 4.2: Sample preparation process for tensile testing experiments. Femora dissected from Hpr mice were not sliced into 2 halves

Dissected bones were included (**Figure 4.3E**) in polyester wax (Electron Microscopy Sciences, Fort Washington, PA) (297) and longitudinally sectioned using a diamond saw under constant irrigation. After sectioning samples were dewaxed, followed by hydration as described (297). The use of wax as an embedding block for mice bones enable production of bone strips (**Figure 4.3F**) of reproducible size with minimal damage. Only anterior sections of the femora were used in this experiment.

For mechanical testing, the distal and proximal ends of the femur were secured in dental cement (Filtek^{TM} Supreme XT, 3M ESPE, USA.) as shown in the **Figure 4.3G** to grip the samples in the tensile testing device. A custom sample holder for potting the ends of the bones reproducibly was made from acrylonitrile butadiene styrene (ABS) molds. A push out system was used for removing the specimens after the cement had set as shown in the **Figure 4.3C**. Both bony ends were coated with a bonding agent (OptiBond SOLO plus, Kerr, West Collins, U.S.A.) before placing inside the ABS molds (**Figure 4.3B**) to

increase the adhesion between the bony end surface and the dental cement. The water resistant dental cement enabled the tensile test to be carried out with the bone specimen fully immersed in phosphate buffered solution (pH 7.4) to simulate physiological conditions during *in situ* strain experiments.

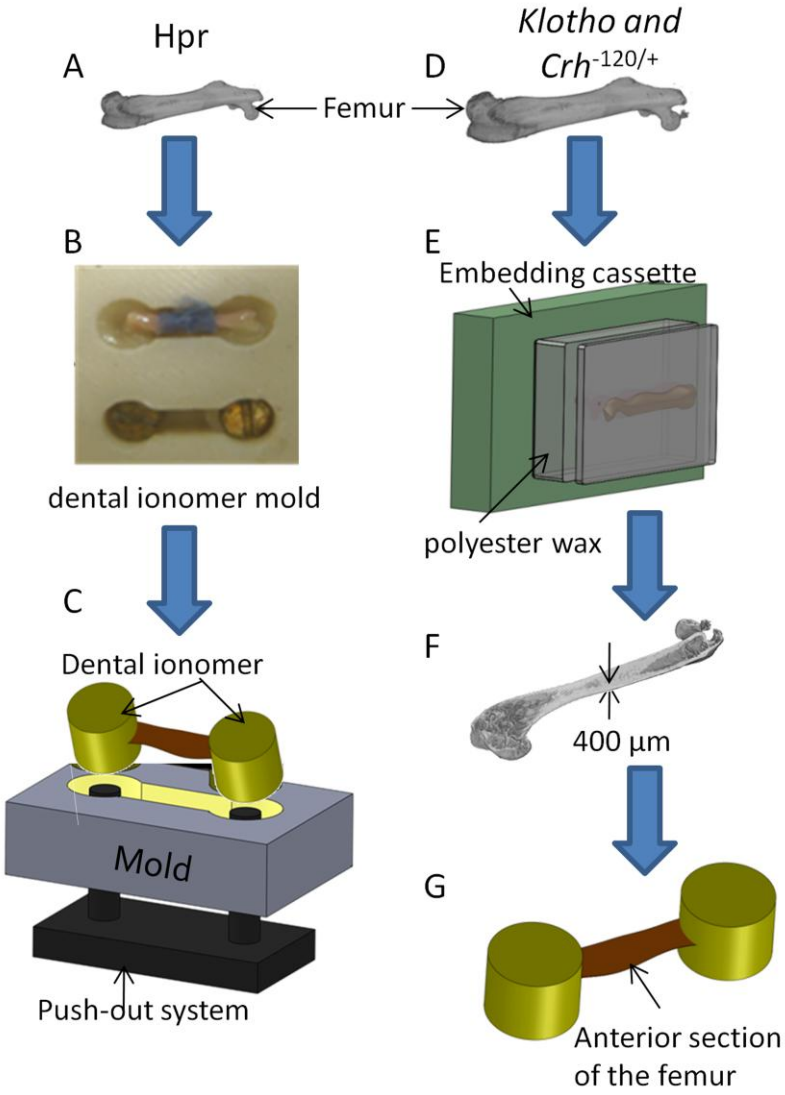

Figure 4.3: Sample preparation process for Hpr (A, B, C) and Klotho & Crh$^{-120/+}$ (D, E, F, G) mice femora for tensile testing (B) Securing bony ends in the dental ionomer material (C) Mold and push out system (E) Mouse femur (klotho & Crh$^{-120/+)}$ was embedded in polyester WAX and embedding cassette was used to hold the WAX block during the cutting. 0.2 mm thick WAX slice with the femur was cut using the low speed diamond saw. After removing the WAX (dewaxing procedure was followed as in (297)) around the bone strip, bony ends were secured in the dental ionomer.

Embedded femurs (**Figure 4.3G**) were machined to form a necked region in the mid diaphysis using a custom-made micromilling machine (**Figure 4.4**). The milling machine consisted of two DC linear-encoder stages (M110.1DG linear stages, Physik Instrumente, UK) connected to a computer via 2 motor controllers (C883 Mercury controllers, Physik Instrumente, UK). A fixed high speed rotatory milling tool (Dremel 300 series, Dremel Inc, Uxbridge, United Kingdom) with 0.8 mm diameter cutting tool (Dremel Engraving cutter product No. 111, Dremel Inc, Uxbridge, United Kingdom) was used to mill the specimen, which was clamped in a fluid chamber mounted on the moveable bi-directional linear stages. Specimens were machined from the posterior quadrants leaving a 200 µm thick anterior quadrant. The width and the thickness of each specimen were measured after milling using a Basler A101f monochrome CCD camera (Basler Vision Technologies, Ahrensreide, Germany). High resolution (1024 × 768) images of the milled specimens were captured, transferred to the computer and dimensions were measured using Image J software (Image J, NIH, USA). The typical dimensions of the gauge regions were approximately 0.2 mm (thickness), 1.0 mm (width) and 5.0 mm (length). Five samples were examined by scanning electron microscopy to check whether the machining protocol induced any damage, and no extraneous cracks, notches or defects in the tissue were found.

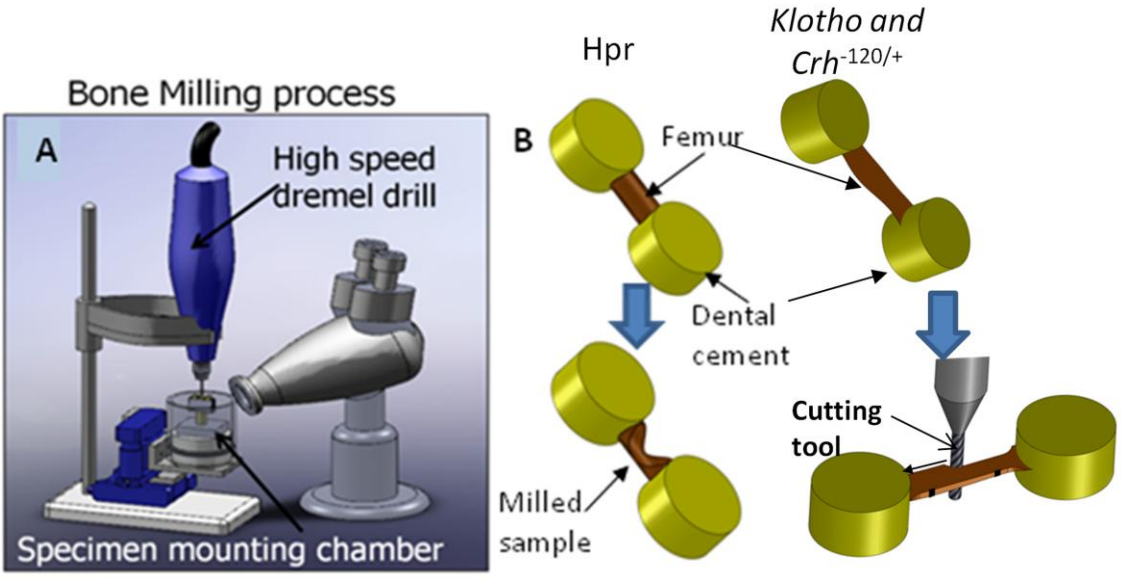

Figure 4.4: (A) Custom made micro milling machine. (B) Embedded bone sample before and after the milling process. Anterior section is only left after milling process. Lateral and medial

sides of the embedded bone sample were milled using 0.8 mm cutting tool (moving direction of the cutting tool was shown by the arrow). Black lines on the bone are reference markers for tissue strain measurements.

4.1.2 Cantilever bending - Sample preparation

Mouse humeri was dissected and transversely sectioned along the mid diaphysis into 2 halves (**Figure 4.5B)** using a diamond saw under constant irrigation. The proximal half of the humerus was used and the head of the humerus was secured in a dental cement using a specially made ABS mold system (**Figure 4.5C**) in order to mount the bone sample in the bending tester (as shown in **Figure 4.5D**). The securing process involved applying a dental adhesive to the humeral head and placing it upright into the dental cement within an ABS mold as shown in **Figure 4.5C**, where the cement was set with 20 seconds of UV light exposure. Using a custom made diamond wire saw, the bone was further sectioned along the long axis (from the mid diaphysis to the dental block surface) of the humerus. This procedure generated an elongated cantilever bending strut of ~5 mm length (L), ~ 200 μm thickness (b) and ~ 500 μm in width (d) from the anterior quadrant of the humerus (**Figure 4.5E**). Samples were wrapped in phosphate buffered solution soaked tissue paper and stored at -20^0 C until required (approximately 1 week) for mechanical testing.

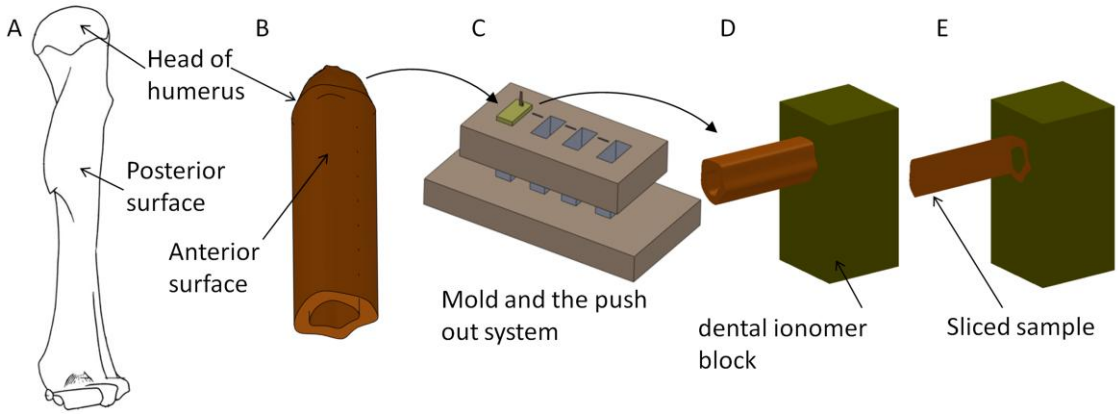

Figure 4.5: A schematic illustration of the specimen preparation technique for in situ cantilever bending. (A-B) Dissected mouse humerus was transversely sectioned along the mid diaphysis using a low speed diamond saw. (C) The head of humerus was potted in a dental ionomer block using acrylonitrile butadiene styrene (ABS) mold and a push out system used to remove the sample from the mold, (D-E) Anterior quadrant of the humerus is shown intact

with dental ionomer block. Other three quadrants were removed by sectioning along the long axis using diamond wire saw.

4.2 Experimental protocols

4.2.1 Synchrotron nanomechanical experiments

4.2.1.1 *In situ* tensile testing

Systematically prepared mice femora from a range of ages and disease/ wild-type conditions (See **Table 4.1** for breakdown) were mounted in the micro-tensile tester (**Figure 4.6**) mounted on a 3-axis motorized stage in beamline I22 (DLS) as shown in **Figure 4.8**. In the customized micromechanical device strain is applied by the bi-directional motion of two DC linear-encoder stages (**Figure 4.8** inset i), which has a minimum incremental motion of 0.1 µm. Load was measured with a 22 N model 31 tension/compression load cell (**Figure 4.8** inset ii). The stress was calculated from post-test measurements (SEM images of the fracture surfaces (**Figure 4.7**)) of sample area. Stress values were corrected for porosity using **Equation 4.6.** Due to an initial slack-range in the grips, the stress-strain curve shows an initial toe-in region, which was not considered during the data evaluation.

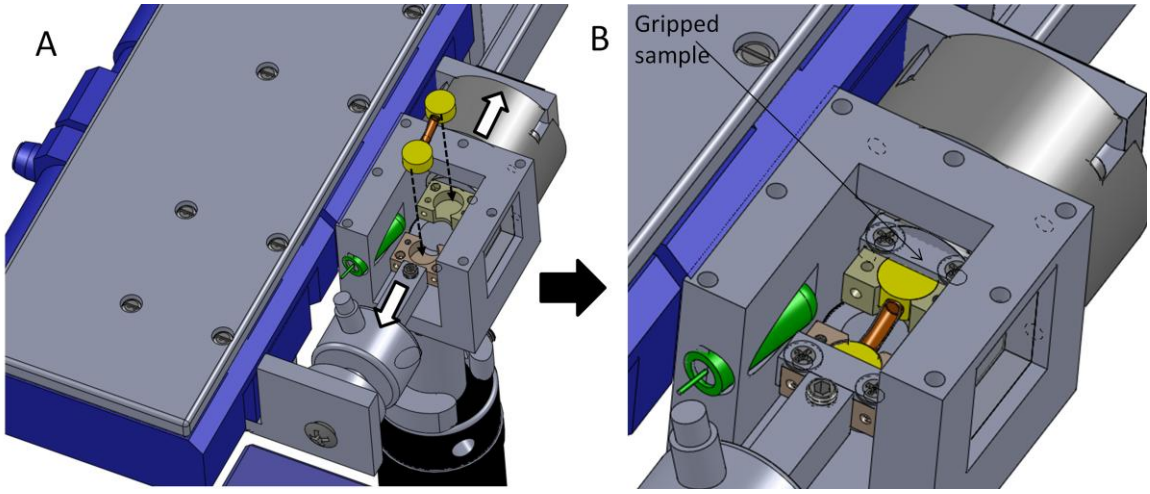

Figure 4.6: Schematic view of the sample mounting process inside the fluid chamber of the micro tensile testing. The sample is immersed in phosphate buffered saline. (A) Motors A and B need to move up and down respectively in order to adjust the space between the holders.

(B) The ends of the sample (dental ionomer blocks) were placed inside the holes of the top and bottom sample holders.

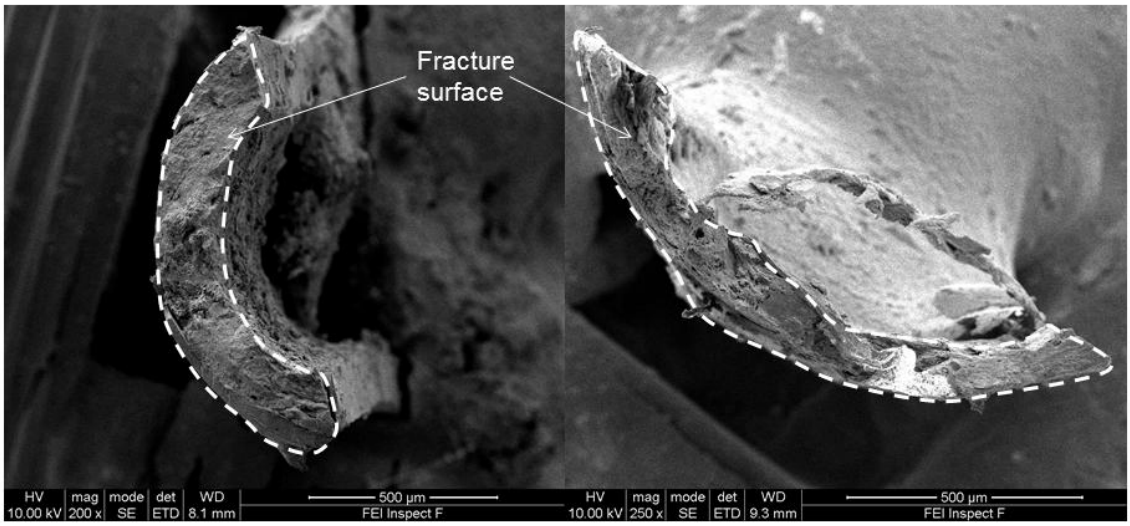

Figure 4.7: SEM images of tensile tested mice femora. Dash line polygon is drawn around the fracture surfaces. Area of the fracture surface was measured using Image J software.

In situ tensile testing was carried out with synchrotron SAXD in two different configurations; main beam (200µm × 200µm) and microfocus beam (10µm x 12µm).

SAXD parameters for main beam experiments

A synchrotron X-ray beam (beam diameter = 200 µm, wavelength λ = 1.24 Å) was used to measure the SAXD patterns, which were collected by a 2D gas filled multiwire RAPID2 detector system (298) with exposure time 10 seconds. The sample to detector distance was 7.57 m as measured with a calibration standard (type I collagen from rat tail tendon). Each SAXD data frame had a pixel resolution of 512 × 512 pixels and a pixel size of 383.4 × 383.4 μm^2.

SAXD parameters for microfocus beam experiments

The microfocus synchrotron X-ray beam (beam size = 10 × 12 µm, wavelength λ = 0.8857 Å) was used to measure the SAXD patterns. SAXD patterns were collected on a PILATUS2M detector system with a pixel resolution of 2048 × 2048 pixels and a pixel size of 172 x 172 μm^2. The sample to detector distance was 1.034 m. During the experiment, exposure time was kept to approximately 1 second, limiting the total X-ray

radiation dosage to 29.4 kGy to minimise the influence of the X radiation on the bone mechanical properties. Radiation exposure in SAXD has been shown to mainly reduce post yield deformability in bone, rather than the initial elastic properties (296). In this thesis, the elastic regime of bone deformation was only considered, and hence only data collected from the linear elastic range (as identified from the stress/strain curve) were used for further analysis.

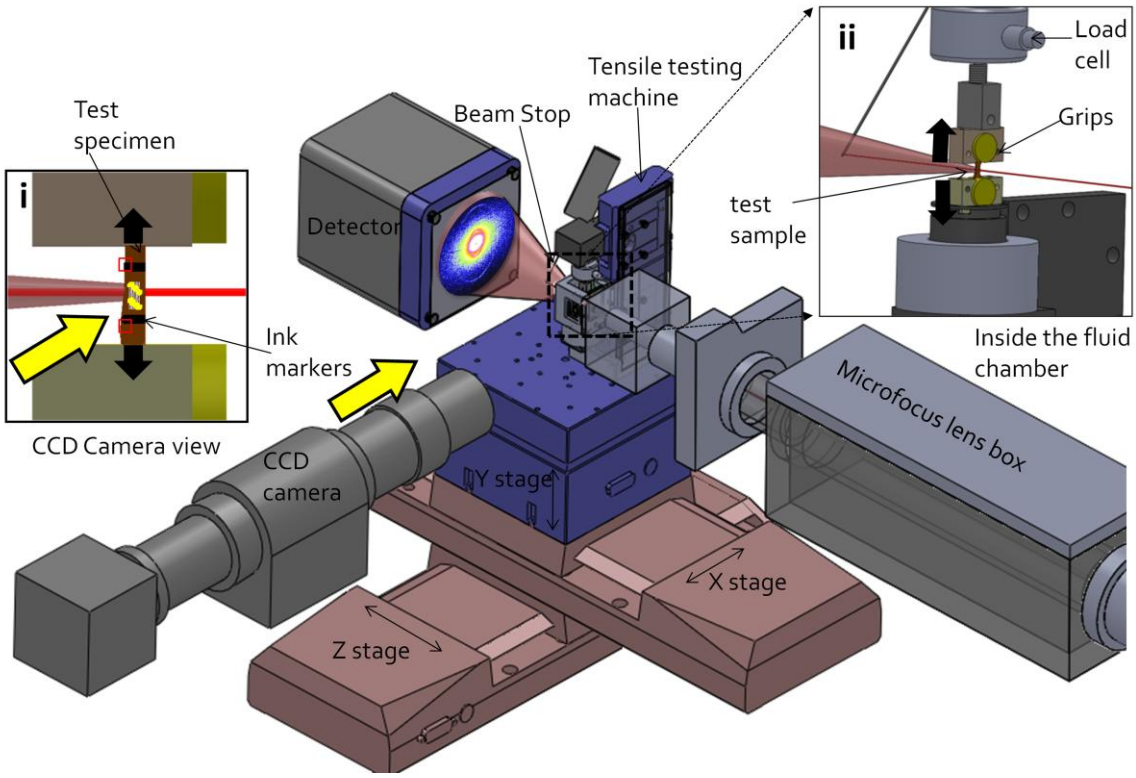

Figure 4.8: The experimental setup for the in situ microtensile testing with microfocus SAXS at the I22 beam line, DLS. The CCD camera views the sample at a 90° angle to the X-ray beam as not to block the beam path (inset i). Sample is immersed in the fluid chamber by securing in the grips as shown in the inset ii

Non-contact video extensometry

The samples were loaded at a constant velocity of 1 µm/second (strain rate = 0.02%/s) in a custom-made micromechanical testing machine up to failure. Tissue strain was measured by non-contact video extensometry by imaging the separation of two horizontal lines that were marked (**Figure 4.8** inset i) on the bone mid diaphysis surface. The tensile tester fluid chamber interior was illuminated by fixing a waterproof LED

light within the chamber, which increased the contrast quality between marks and bone. Images were captured by a CCD camera (Basler Vision Technologies, Ahrensreide, Germany) viewing the chamber from the side (normal to the X-ray beam). These high resolution (1024 × 768) images were later analysed using an in-house LabVIEW/NI Vision-based digital image correlation package for tracking optical marker displacement to measure microstrains (299). While all samples were deformed to fracture, only the data from the linear (elastic) regime of deformation was used for analysis. The linear region was identified by noting where the transition to the inelastic regime took place from changes in tangent modulus. For each tissue strain value, the tangent modulus was calculated over a region of 0.1 % starting from that tissue strain value. The transition to the inelastic regime was defined as the point where the tangent modulus reduces 10% or less compared to its initial value **(Figure 4.9)**.

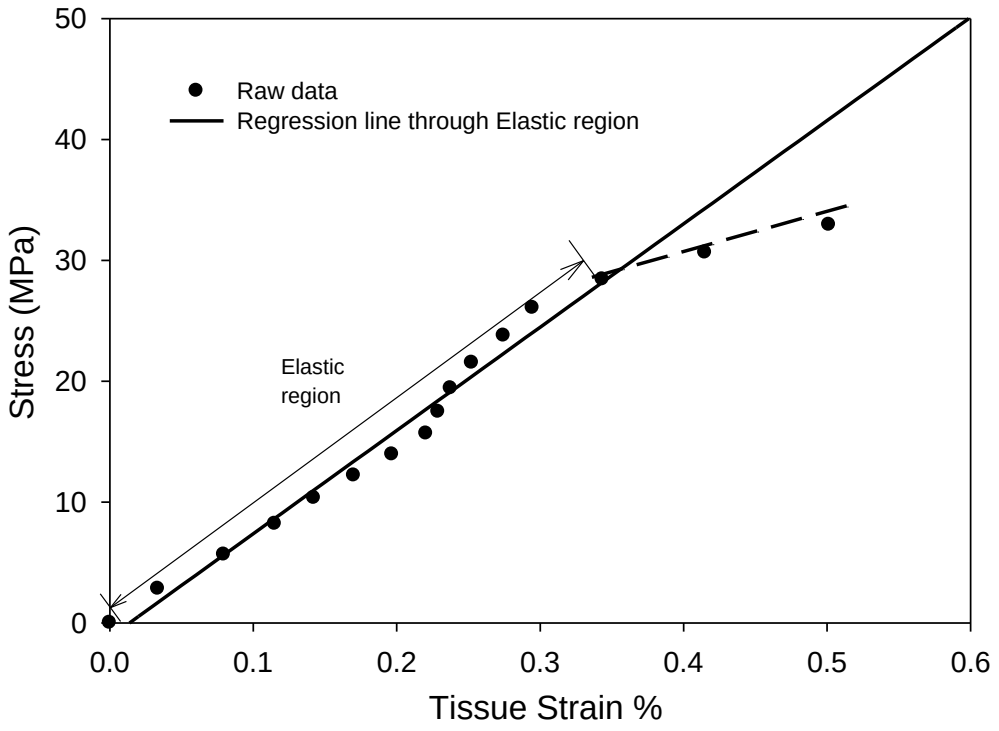

Figure 4.9: The criterion for the elastic region. Representative stress-tissue strain % curves are shown for the tensile tests of mouse bone sample. Yield point of each stress strain curve was determined by the data point where the tangent modulus (slope of the stress strain curve) changes by the 10% or less compared to its initial value (long dashed lines are guides to eye)

4.2.1.2 *In situ* cantilever bending

A custom made micro-tensile tester previously developed for *in situ* tensile testing (85) was modified to carry out cantilever bending combined with spatially-resolved microfocus scanning SAXD with 125 μm step-size. The cantilever bending test machine consists of one DC linear-encoder stage, 22 N model 31 tension/compression load cell and a fluid chamber which provided a physiological environment for bone during the experiment. As shown in the **Figure 4.10**, the dental block was inserted into a metal rig and tightened within the fluid chamber of the testing machine.

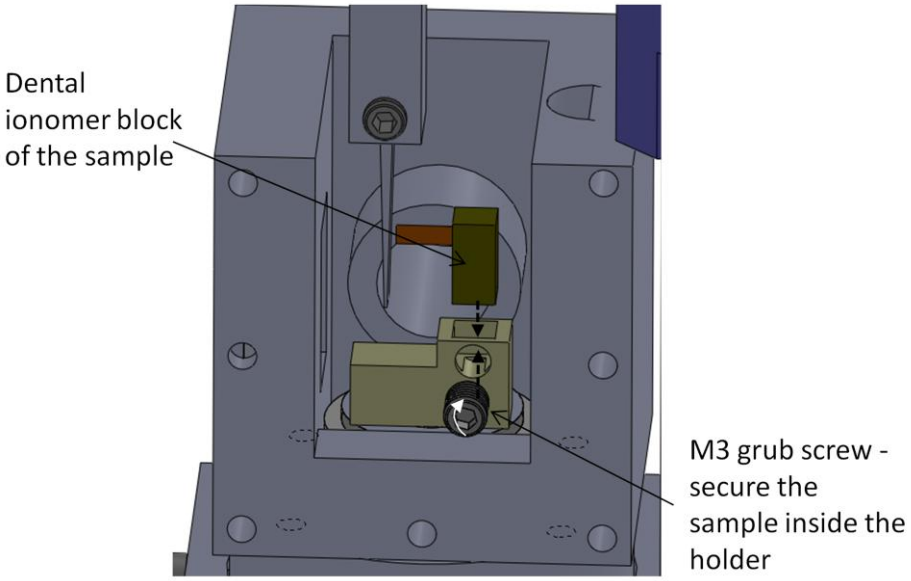

Figure 4.10: Inside view of the fluid chamber – dental cement block was inserted inside holder and tightened using a M3 grub screw

The loading pin with a sharp edge was set at the end of the exposed length of bone and moved at the constant deflection velocity (1 μm/s) for all samples. Specimens were loaded until fracture; load values were recorded by the load cell, and deflection measurements were obtained by tracking the movement of the linear motor at the point of the contact of load pin and the bone specimen. The bending (flexural) modulus (**Equation 4.3**), bending stress (**Equation 4.4**) and tissue strain (**Equation 4.5**) were calculated from the load deflection data using the following equations (300):

$$E = \frac{4L^3}{bd^3} * \left(\frac{F}{v}\right) \qquad \text{Equation 4.3}$$

$$\sigma = \frac{6FLy}{bd^3} \qquad \text{Equation 4.4}$$

$$\varepsilon = \frac{6FL}{Ebd^2} * y \qquad \text{Equation 4.5}$$

where: E is the bending modulus, σ is the bending stress (MPa), ε is the tissue strain, *L* (mm) is the length of the bone specimen, b is the thickness, d is the width, F is the load measured from the load cell, *v* is the deflection movement of the load pin, and *y* is the distance from the neutral axis to the point where the synchrotron SAXD measurement (for the fibril strain) was carried out for each specimen. The above equations (**Equations 4.3, 4.4 and 4.5**), based on Euler-Bernoulli beam theory, are only valid for long slender beams with a large *L/d* ratio > 6 (301). *L/d* ratio of cantilever beam samples were maintained within the specified limit during the sample preparation and the average was 10.4 ± 2.8. While all samples were deformed to fracture, only the data from the linear (elastic) regime of deformation was used for analysis, where the transition to the inelastic regime was defined for each sample as the point where the tangent modulus reduces 10% or less compared to its initial value as explained above.

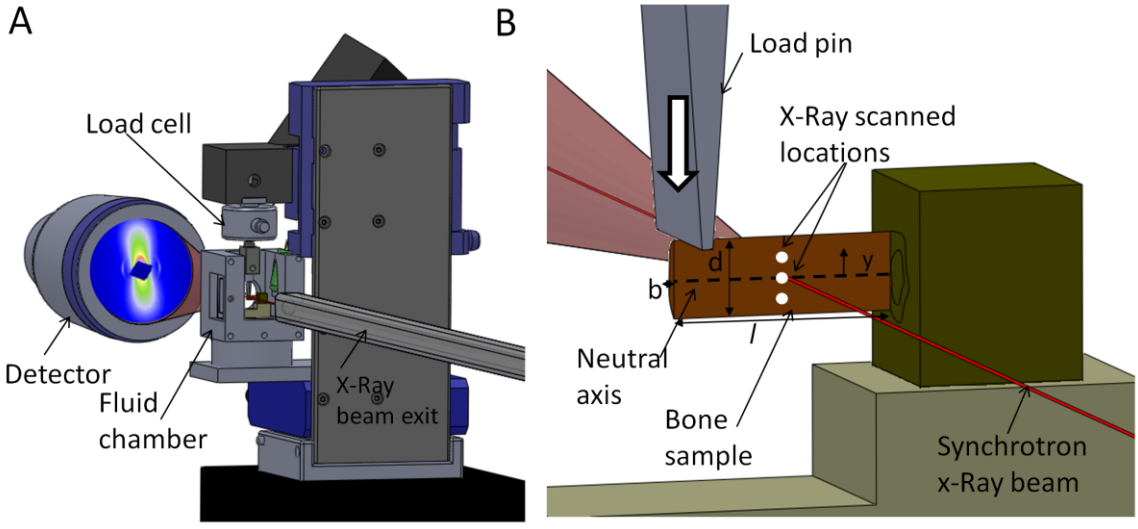

Figure 4.11: (A) The experimental setup for the in situ cantilever bending with microfocus SAXD at the I22 beam line, DLS. Test specimen was immersed in the fluid chamber by securing

inside the metal rig. (B) Zoomed in view of inside the fluid chamber. Anterior quadrant of the humerus is shown intact with dental cement block. White arrow shows the loading direction of the load pin. SAXD spectra were taken at the middle region (white dots) of the test specimen for each load step by moving the microfocus sample vertical stage.

SAXD spectra were collected after every 30 μm step displacement of the end of the bone by the motor (moving direction is shown by white arrow in **Figure 4.11**), up to failure of the bone. SAXD spectra were taken both above and below the neutral axis of the bent bone cantilever shaft, enabling a spatially resolved measurement of fibril strain in the tensile and compressive zones as a function of loading. One SAXD frame from above and one SAXD frame from below the neutral axis (y = ±125 μm offset relative to the neutral axis) was taken by moving the Z-direction (vertical) stage of the I22 microfocus sample platform. A synchrotron X-ray beam with wavelength λ = 0.8857 Å and beam cross section of 30μm × 20μm was used to measure the SAXS patterns. SAXS patterns were collected on read by a 2D area detector system. The sample to detector distance was 1 ± 0.1 m. Each SAXD data frame had a pixel resolution of 2048 × 2048 pixels and a pixel size of 80 × 80 μm^2. Exposure time did not exceed 5 seconds at each point in order to limit the total X-ray radiation dosage to 29.4 kGy; this minimised the influence of the X-rays on the mechanical properties of bone (247).

4.2.2 Data reduction for SAXD

Fibril strain was measured from the percentage shift in peaks of an axial diffraction pattern, arising from the meridional stagger D of collagen molecules in the fibril, as previously described (82, 107). The 1st or 3rd order meridional collagen reflection was used to measure fibril strain. 2D SAXD patterns were radially integrated in narrow cake-shaped sectors of 10^0 angular widths and centred along the (vertical) tensile axis (**Figure 4.12A**) and horizontal axis for cantilever bending. Subsequently, the meridional fibrillar reflections were fitted (**Figure 4.12B**) in batch mode using custom scripts (written in the Perl language) to obtain the peak position q_0, which equals $2\pi/D$, where D is the axial fibrillar periodicity. The percentage increases in D at non-zero external stresses (relative to the unstressed state) provide the critical fibril strain parameter ε_F. Fibril strain ε_F, was plotted versus tissue strain ε_T (**Figure 4.12D**) and the gradient $d\varepsilon_F/d\varepsilon_T$ calculated from a

linear regression of fibril strain versus tissue strain. The gradient can be interpreted as the fraction of total strain taken up at the fibril level, and has been previously used as an indicator of the nanoscale deformation type (14, 82).

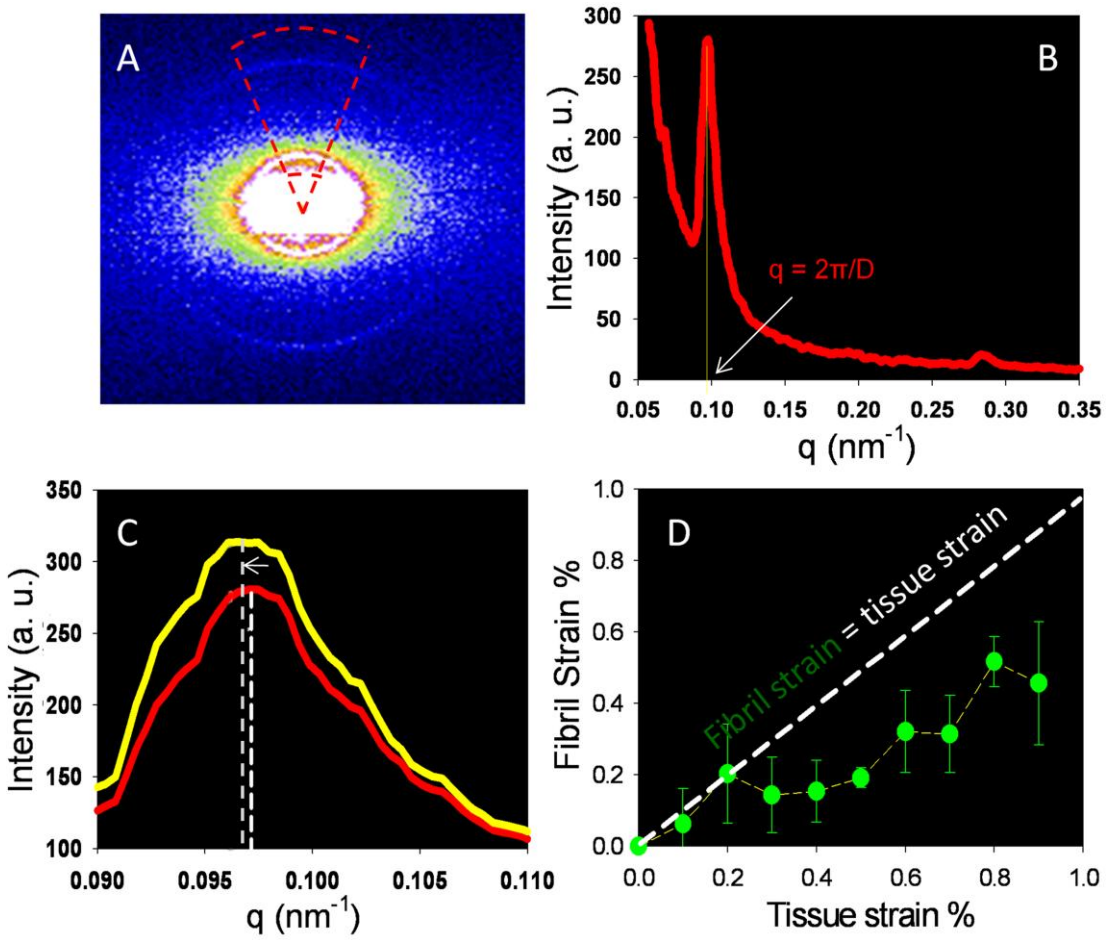

Figure 4.12: (A) 2D SAXD pattern from parallel fibred bone, showing the discrete reflections arising from the collagen D period, and the diffuse scattering intensity from the mineral nanocrystallites. (B) Integrated intensity profile in the radial directions in the angular region (red dash lines) shown in (A), showing the collagen reflections. (C) Shift of the 1st order collagen peak position with increasing tissue strain, for tissue strain = 0% (Time = 0) (gray line) and tissue strain = 0.5% (Time = 240s) (white line). (D) Fibril strain ε_F (tracking the shifts of the 3rd order collagen reflection peak position) plotted for an externally applied tissue strain ε_T (non contact video extensometry by imaging the separation of ink markers).

4.2.3 Data acquisition for mechanical testing machine

Data acquisition control system is consisted of two stages, named setting and measurements (**Figure 4.13**). In the setting stage the user is able to feed the parameters to

the control system. During the measurement, the user is running the experiment with preferred parameters and also it is capable of changing the parameters online.

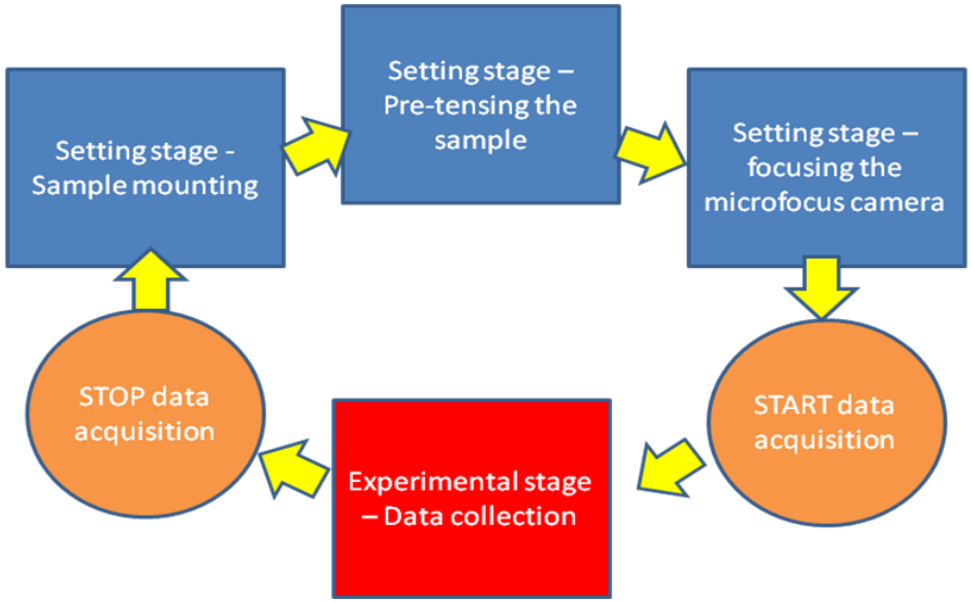

Figure 4.13: Different stages of data acquisition

Mechanical testing machines are controlled by a custom made program developed with LabVIEW software. In the setting interface (**Figure 4.14**) user can move the motor A and B in order to align the sample in the machine and pre-tensing. Also user needs to specify the experimental parameters and choose a location for data to be saved. Once the user is ready to start the experiments, loading can be initiated by pressing the start button on the setting window.

4.2.3.1 Stage 1 – SETTING

Experimental parameters

1. Loading mode – The user needs to select the suitable loading mode (tensile, compressive, cantilever or 4 point bending) required for each experiment. For the tensile or compression loading experiments, the user has the capability of bi-directional or uni-directional movement. In cantilever bending, only one motor is required during the experiment.

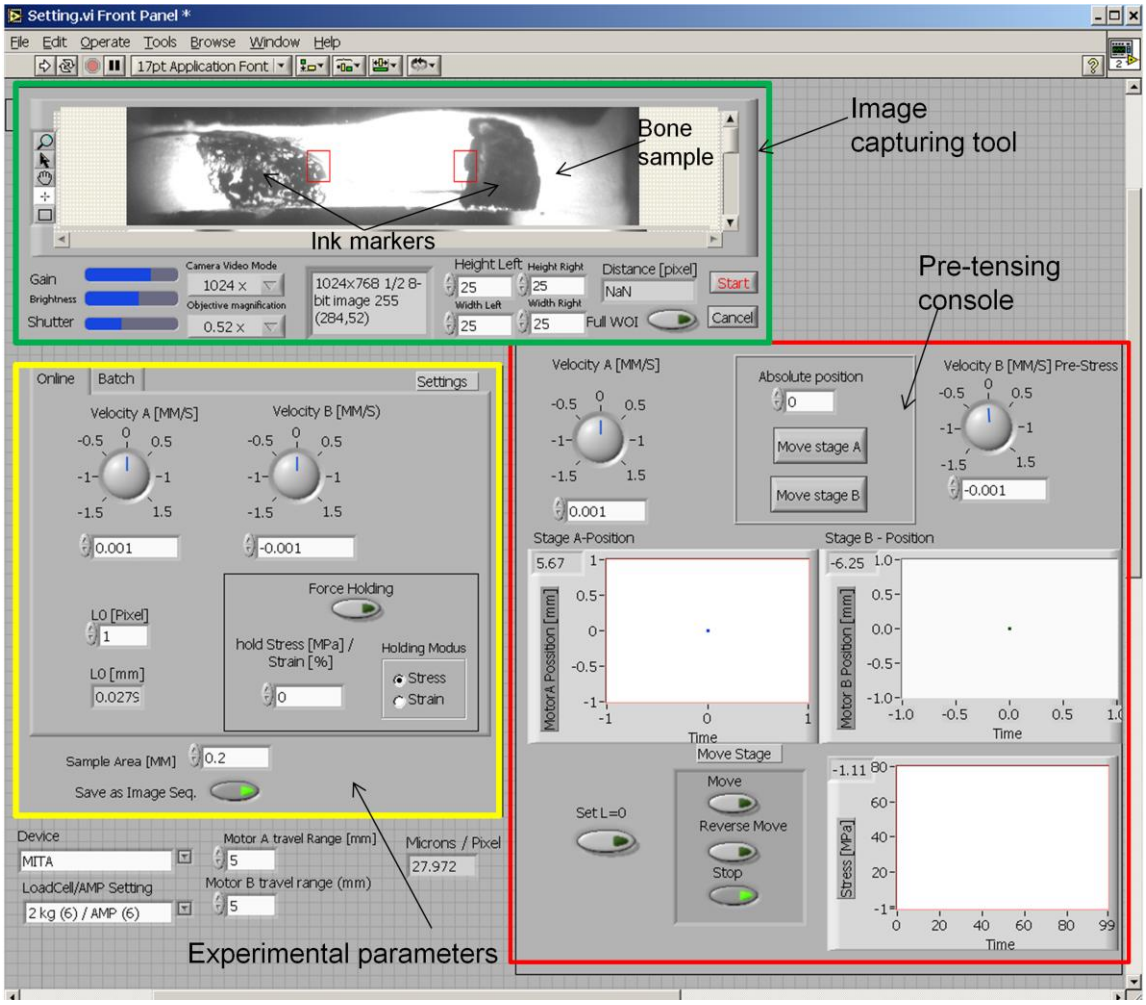

Figure 4.14: User interface on setting window. Green coloured box – Image capturing tool, Yellow colour box – Experimental parameters and red box – pre-tensing console

2. Velocity of the stages (mm^{-1}) – User is required to input an equivalent motor velocity for the preferred strain rate. Maximum velocity for the M110 1DG motors is 1mm/sec.

3. Sample initial/gauge length (mm) – The User needs to insert the initial length of the sample in mm especially for the tensile or compression experiments in order to calculate the strain of the sample during the experiment.

4. Sample cross sectional area (mm^2) – System is capable of acquiring load values from the strain gauge (load cell)**.** These load values are converted to stress values using a specific cross sectional area (mm^2) of the sample inserted by the user into the system.

Pre-tensing /compressing of the sample

The control system has online plots which show the stress vs. strain. During the setting mode the user can align and pre-tense/compress the sample for the experiment.

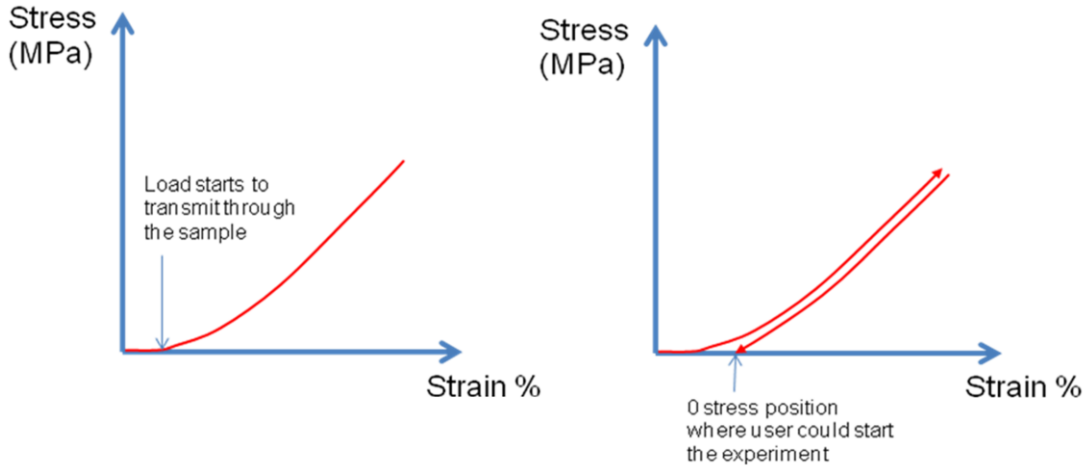

Figure 4.15: Schematic representation of stress vs. strain plot during the pre-tensing of a test specimen

Once the sample is being mounted in the testing machine, the motors need to move (motor A: up and motor B: down) until observes the stress value on the plot (**Figure 4.15**). Initially, the user might not see any stress value for a given motor movement. This could be due to the sample ends are not perfectly aligned within the grips. Therefore, pre-tensing/compressing is essential to align the sample before starting the actual data collection. Then the motors need to move back (relaxing) to the 0 stress position where data collection can be started.

Tissue strain was determined by calculating the percentage increase in the distance between two markers (**Figure 4.12**). This measurement was performed on images collected by the CCD camera whereas the edge detection of the markers was performed using in-house software as explained in the section before (Non-contact extensometry). Live image from the CCD camera can be observed on the user interface (stage 1 – setting interface), where it allows the user to select the region of interest for image capturing and adjust the contrast, brightness and the amount of light gain (**Figure 4.14** green box). After defining the above mentioned parameters, by pressing the start button the software switches to the measuring stage.

4.2.3.1 Stage 2 – MEASUREMENTS

In this stage, following steps are processed until the test is stopped by the user. The load is read out by the load cell and transmitted to the computer where the applied stress on the sample is calculated. Continuous stream of images are acquired by the CCD camera at a maximum rate of 5 frames per second, while the edge detection is applied and the strain is calculated. Measurement interface (**Figure 4.16**) displays strain values from custom built edge detection routine as well as the strain (motor strain) calculated from the motor movement. As example motor strain for tensile testing experiment is determined by following relationship.

Motor strain = (Motor A movement + Motor B movement) / Initial length of the sample

where, Motor A movement + Motor B movement is assumed to be sample elongation (Δl)

User could also send the following commands to the motor controller during the experiments.

- Velocity changes
- Direction changes of the motor movement
- Holding at a fix position

Finally control system display all the results using live updating plots (i.e. stress vs. strain) and save the data to the text file.

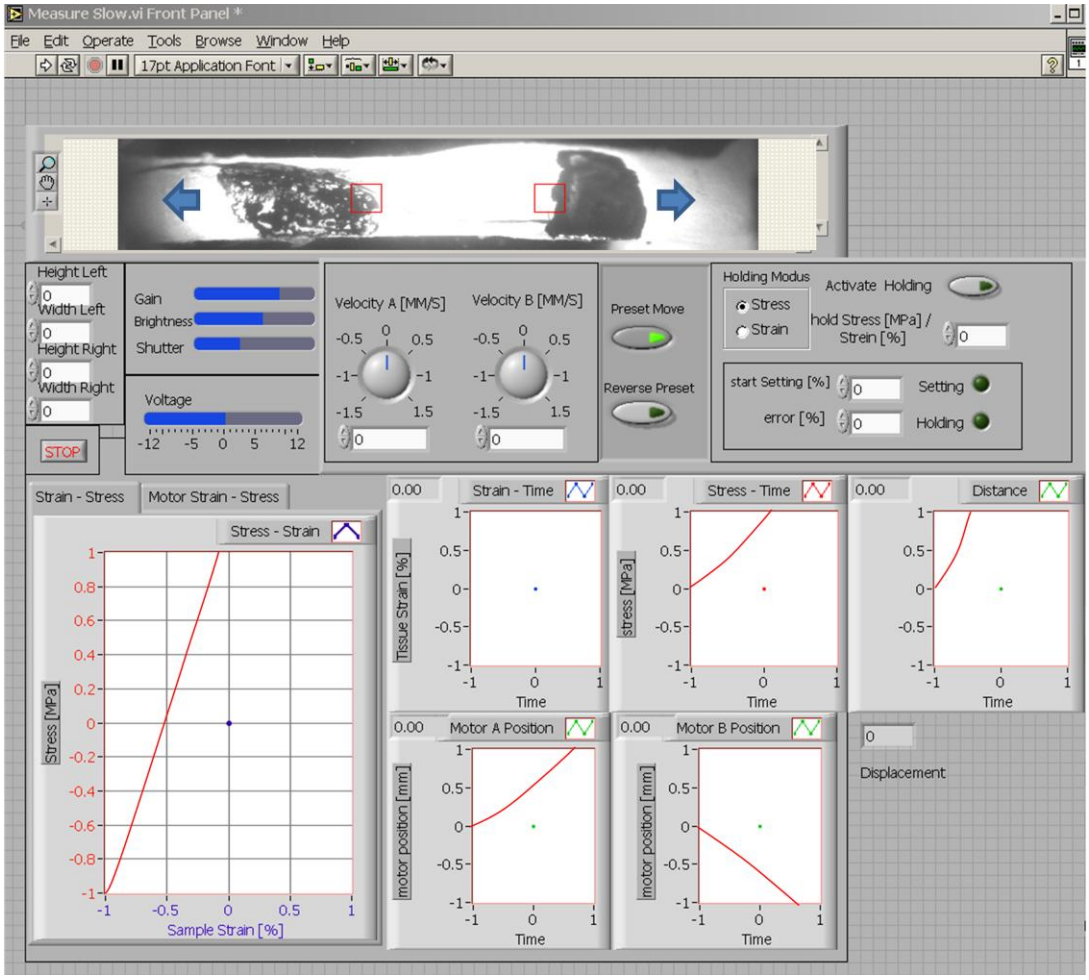

Figure 4.16: Screen shot of the measurement user interface showing the edge detection live video, online stress vs. strain plots, motor movements and load values as a function of time

4.2.4 Collagen Fibril Orientation

Further information on the degree of mineral crystal and fibril orientation can be extracted from the unstrained SAXD spectra. To determine the degree of orientation of the collagen fibrils with respect to the loading axis, the FWHM of the meridional 3rd order reflection $I_c(\chi)$ was estimated. To include the intensity solely from the collagen *D*-period reflections without any contribution from the mineral scattering background, both the total azimuthal intensity $I(\chi;q_0)$ at $q = q_0$ and the azimuthal distribution of mineral-scattering $I_{m;c}(\chi)$ alone were calculated. $I_{m;c}(\chi)$ was calculated by averaging $I(\chi)$ at wave-vectors lower (q_l : **Figure 4.17A inner ring**) and higher (q_h : **Figure 4.17A outer ring**) than the 3rd order peak position q_0 (**Figure 4.17A middle ring**). The total azimuthal intensity $I(\chi;q_0)$ was estimated by radially integrating the intensity in a narrow band

around q_0. $I_c(\chi)$ (**Figure 4.17B**) was then calculated from the difference between $I(\chi;q_0)$ and $I_{m;c}(\chi)$. The angular intensity of the 3rd order fibril reflection $I_c(\chi)$ is plotted in **Figure 4.17C**.

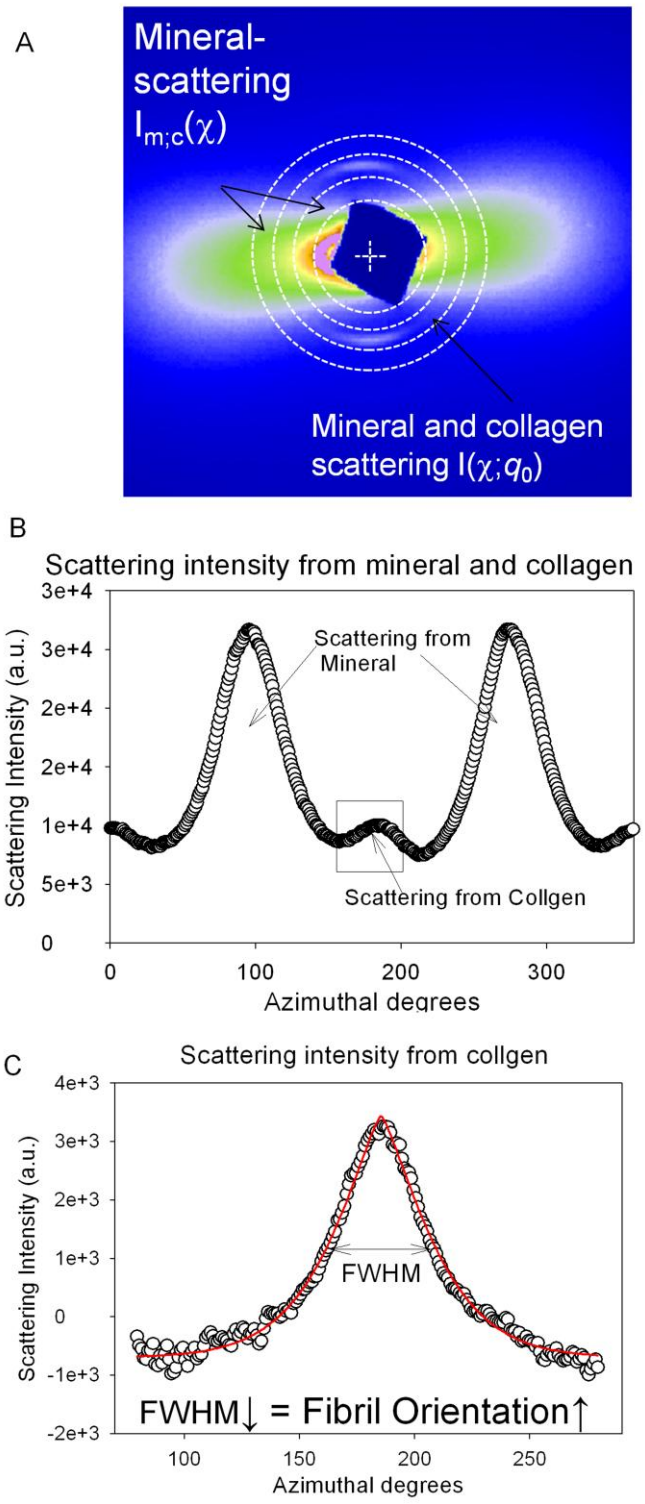

Figure 4.17: (A) 2D SAXD pattern from a test specimen, showing the 3rd order discrete reflection arising from the collagen D period, and the diffuse scattering intensity from the mineral nanocrystallites. (B) Total integrated angular intensity profile (middle ring shown in A) of the 3rd order collagen reflection (square) and mineral background. (C) The angular intensity distribution of the 3rd order fibril reflection $I_c(\chi)$.The angular intensity distribution was measured by radially integrating the intensity in three narrow bands around q_0. $I_{m,\ Inner}(\chi)$, $I_{m,\ Outer}(\chi)$ and $I_{c\ Middle}(\chi)$ (bands were surrounded by white dash lines in A).

4.2.5 Scanning Small Angle X-ray Scattering (sSAXS)

Dissected bones were skinned, cleaned of muscle tissue, wrapped in gauze, soaked in phosphate buffered saline, and stored at -20 ^{o}C until the scanning SAXS experiment. Just before the experiment, each bone specimen (section or the whole bone) mounted in a saline sample chamber with Ultralene® foil windows, as shown in **Figure 4.18A and B**.

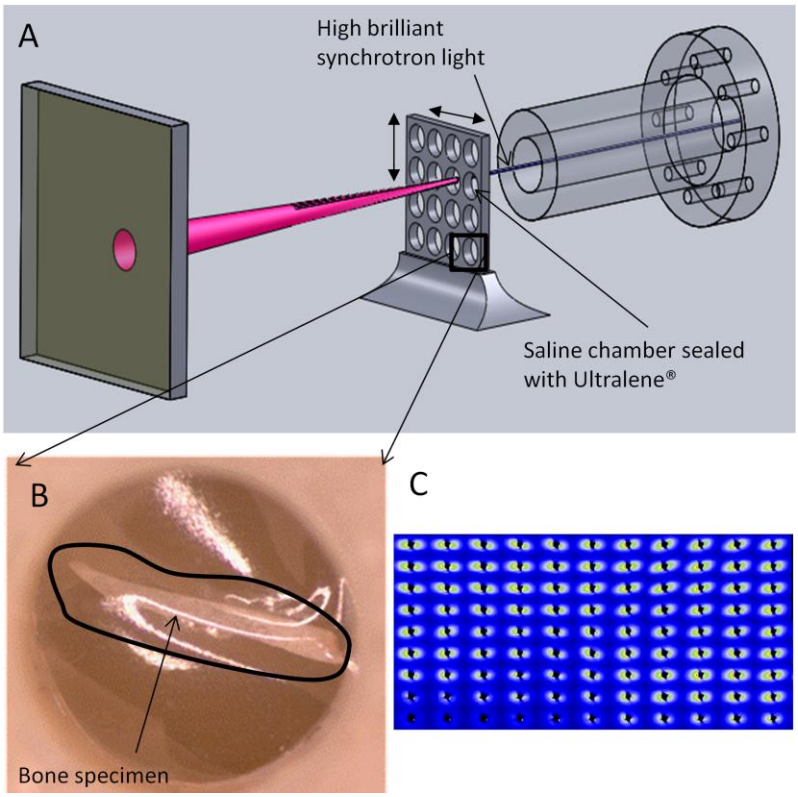

Figure 4.18: Scanning synchrotron SAXS on mouse scapula (A) Schematic of dissected scapular spine mounted in a saline sample chamber sealed by Ultralene® foils. Black solid line shows the incident X-ray beam. (B) Light microscope image of scapula spine from a 4 week-old male wild-type mouse. (C) A composite map of SAXS images obtained by scanning across the scapula spine shown in (B)

The sealed sample chambers containing the bone specimen from a range of ages and diseased or wild-type conditions were mounted on a 3-axis motorized linear stage on beamline I22. A schematic of the setup is shown in **Figure 4.18A**. Scanning experiments also carried out using both main beam (200 μm) size and the micro-focus beam (10 μm × 15 μm). For synchrotron beam parameters see section 4.2.1.1

SAXS patterns of the sample were collected by moving X and Z stages with a step size of 200 μm for main beam and 25 μm for microfocus beam in both horizontal and vertical directions. **Figure 4.18C** shows an example of a SAXS composite map, which illustrates the distribution of the measurement positions. 2-D SAXS images were analysed as described in detail in Rinnerthaler et al (233) and **Chapter 2** section 2.2. Two numerical parameters were determined from each SAXS pattern in this study: the degree of orientation (ρ) and the direction of predominant orientation (ψ) of mineral particles (see **Chapter 2 section 2.2** for the definitions).

4.2.6 Quantitative backscattered Scanning electron (qBSE) imaging

The mechanically tested samples (tensile testing and cantilever bending) were prepared for further analysis by BSE microscopy, to determine tissue mineral content. One single sample for each disease condition at each age point was used. Samples were dehydrated in a graded ethanol series and embedded in poly-methyl-methacrylate (PMMA). PMMA blocks were sectioned using a low speed diamond saw, and finished with grinding papers and polished using diamond liquid suspension with progressively finer grain size down to 1 μm. This procedure was carried out in such a way that the final polished surface (surface of interest) was plane parallel to avoid imaging artefacts. All the samples were mounted on a square aluminium raft using double-sided adhesive carbon tape. A thin conductive carbon coating was applied on the polished surface by vacuum evaporation.

Digital BSE imaging was performed with a Zeiss DSM 962 digital scanning electron microscope equipped with an annular solid state BSE detector (K.E. Electronics, Toft, Cambridge, UK). The sample to detector distance was constant, the electron beam was adjusted to 20kV accelerating voltage and 0.5 nA sample current was used to perform the analytical imaging. Calibrated digital BSE images containing 1024×1024 pixels with a

pixel separation of 2.175µm and a grey level resolution of 256 were generated using halogenated dimethacrylate standards as described previously (253, 302). The gray level distributions of BSE pictures were converted into Ca weight % of the mineralised tissue to produce BMDD histograms (74, 256). In this thesis two parameters were used from BMDD histograms - Ca_{mean} and Ca_{FWHM} (256) - as a function of development and genotype in order to understand mineralisation defects in rickets, osteoporotic and ageing condition. In addition, the fraction of microscale porosity was calculated. The porosity fraction, for selected regions of interest (100 × 100 pixels each) from qBSE images of the anterior cortex, was calculated by taking the ratio of pixels with gray level < a threshold value of 40 to the total number of pixels in the region of interest, using a standard plugin (BoneJ) (303) for the image processing program ImageJ. Five regions of interest were taken per age/disease condition. Using these porosity fractions, the nominal stresses σ_{nom} (from *in situ* tensile loading) were converted to the corrected stress σ_{corr} by the equation below.

$$\sigma_{corr} = \sigma_{nom} \frac{1}{1 - porosity} \qquad \text{Equation 4.6}$$

This corrected stress will hereafter be referred to simply as the stress. The cross-sectional area was corrected for porosity solely to correct the stress, and not the (fibril) strain, which is estimated independently via SAXS. Hence, the above relation was used to calculate the corrected stress, instead of previously published correlations in (304) between macroscopic elastic modulus (tissue level stress/tissue level strain) and porosity.

4.2.7 X-ray microtomography

MicroCT was used to assess the cortical and trabecular bone architecture qualitatively and mineral content of disease and wild-type mice bones. A high-definition MuCat scanner (262) was used, comprising an X-tek ((Tring, Hertfordshire, UK, now part of Nikon Metrology, Leuven, Belgium)) ultrafocus X-ray generator and Spectral Instruments (Tucson, Arizona, USA) 800 series CCD camera in a time-delay integration readout mode. Whole bones (femur or scapula) were scanned using an accelerating voltage of 40 kV (**Figure 4.19**). From the calibrated projections (equivalent to 25 keV

monochromatic energy), microCT images were reconstructed using a cone-beam back-projection algorithm to form a 3D image with voxel size of 15 × 15 × 15 μm^3. Volume-rendered images were produced to analyze the microstructure of the cortical and the trabecular bone.

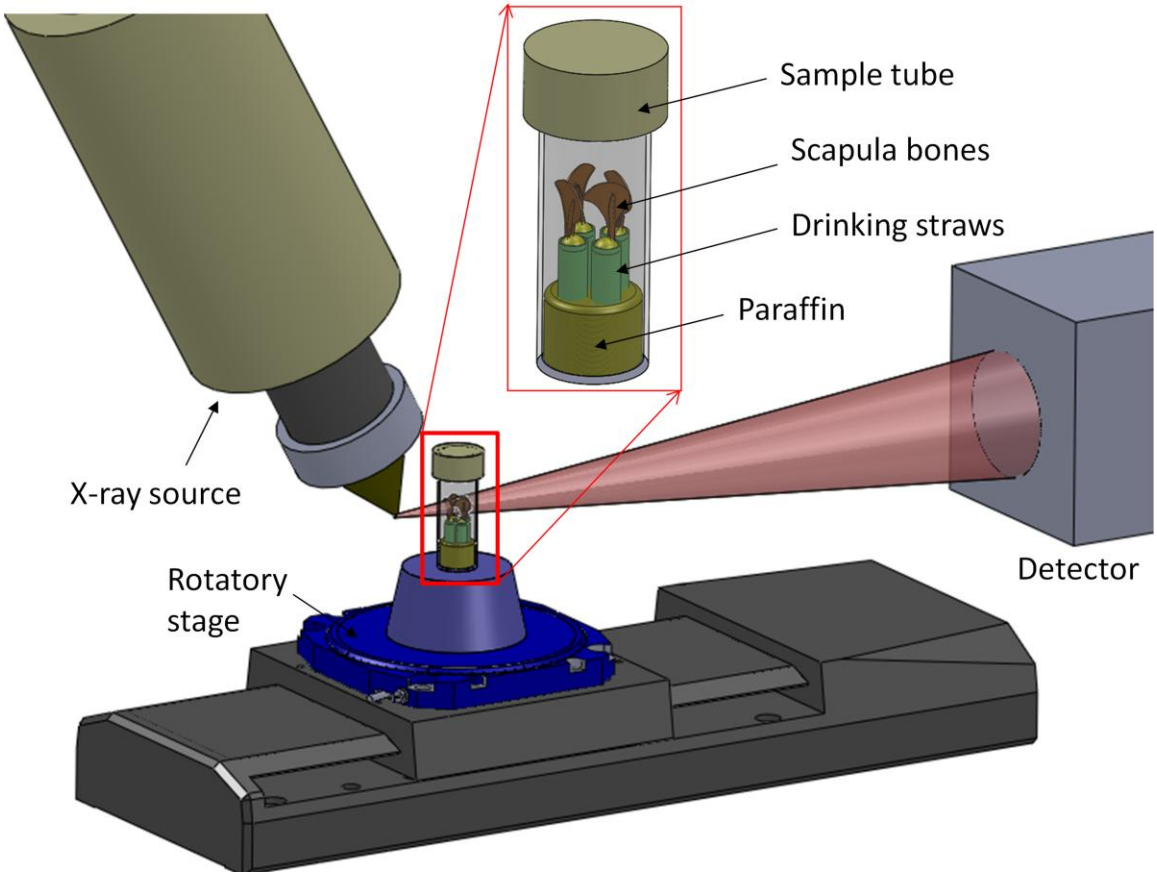

Figure 4.19: Schematic diagram MicroCT experimental setup with the 4th generation scanner developed by Davis and Elliott (2003), showing the ultrafocus beam system. Scapular bones mounted inside the sample tube (inset)

Tomograms were also used quantitatively to assess the degree of mineralisation in the bone samples with increasing developmental age. Gray levels in the tomograms represent the LAC (μ) of the sample, which was related to the degree of mineralisation in bone by the following relationship:

$$Mineral_{conc} = \frac{\mu - \mu_o}{\mu_p - \mu_o} \rho_s$$ Equation 4.7

In this equation, μ, μ_o (0.5 cm^{-1}), and μ_p (11 cm^{-1}) are the measured, pure organic and pure sample material LACs, respectively, and ρ_s (3.16 gcm^{-3}) is the sample material density.

The tomograms were converted into a series of 15 μm thick 2D bitmap stacks using Tomview software (in-house software). The histogram of the mineral concentration, denoted as the degree of mineralisation, was normalised against the bone volume of the sample and calculated for the regions of interest using Image J software.

Chapter 5

Deterioration in Nanomechanical Quality in Rachitic Bone

The contents of this chapter have been published in

A Karunaratne, CT Esapa, J Hiller, A Boyde, R Head, JHD Bassett, NJ Terrill, GR Williams, MA Brown, P Croucher, SDM Brown, RD Cox, AH Barber, RV Thakker, HS Gupta. *Significant deterioration in nanomechanical quality occurs through incomplete extrafibrillar mineralisation in Rachitic bone: evidence from in-situ synchrotron X-ray scattering and backscattered electron imaging*. *2012*, J Bone Miner Res. 2012 27(4):876-90.

5 Deterioration in Nanomechanical Quality in Rachitic Bone

5.1 Synopsis

Disruptions of the physiological and biochemical processes that regulate deposition and removal of carbonated apatite in bone tissue are characteristic signatures of certain metabolic bone diseases, including osteoporosis (305) and rickets (306) as reviewed in **Chapter 1**. Diagnosing the onset of these changes, especially early on during disease progression, is critical for timely therapeutic intervention. The methods available to assess this decreased mechanical stability include plain radiography, DXA, Faxitron X-ray microradiography, ultrasound, microCT, SAXS, histology and qBSE imaging. BMD assessment by DXA, is currently the standard technique to determine risk of fracture. However, BMD measures only total mineral content (quantity) and not the structure or mechanics of the bone matrix, i.e. the bone quality (210). It is important to understand how disease-induced changes in bone material quality (at the nano- and microscale) contribute to reduced mechanical competence. In this chapter it was assessed the use of time-resolved SAXD combined with *in situ* micromechanics, to characterise the mechanistic role of altered nanoscale mineralisation occurring in a mouse model for hypophosphatemic rickets (Hpr), and determined how this new approach can provide functionally relevant information inaccessible by other methods.

SAXD is uniquely capable of determining mineralised collagen fibrillar strain in bone tissue (31, 104) as discussed in **Chapter 2**. The high brilliance of synchrotron sources enables short-exposure times for SAXD images, and real-time imaging during mechanical loading. The experiments reported in this chapter are the first, to apply this method to image the mechanical changes at the nanoscale in a biochemically well-defined metabolic bone disease phenotype as a function of bone development and disease state. Indeed very recent study (87) where synchrotron SAXD has been applied to analyze the nanoscale contribution to bone fragility in ageing bone, due to increased collagen crosslinking. Structural changes at this level – for example, in osteoporosis (altered collagen crosslinking (180)), osteogenesis imperfecta (altered tropocollagen

helix structure (307)) or osteopontin deficiency (308) reduce macroscopic mechanical properties, but the quantitative mechanisms are very little understood at the nanoscale.

Rickets is a diseased state which has a structurally well-characterized alteration in the nanoscale bone matrix (reduced extrafibrillar mineralisation) whose mechanistic consequences, in terms of altered fibrillar deformation, are unknown. In this chapter, mouse model XLHR due to an ENU-induced mutation in the *Phex* gene was used, whose phenotype is previously validated (85) by standard methods like DXA and Faxitron X-ray microradiography.

5.2 Material and methods

5.2.1 Animals

C57BL/6J male mice were treated with ENU, bred to untreated C3H females, and the progeny investigated for dominantly inherited phenotypes using dysmorphology and radiography protocols as previously reported (309) (this activity was performed at the Medical Research Council).

5.2.2 Sample preparation for *in situ* tensile testing with SAXS

Dissected femora from 4, 7 and 10 week (postnatal) old female mice were systematically prepared for mechanical testing as explained in **Chapter 4**. The typical dimensions of the gauge regions were approximately 0.20 mm (thickness), 1.0 mm (width) and 5.0 mm (length). The biochemical analysis showed (85) no differences between male and female, hence the samples from female mice were used for the SAXD measurements and the following qBSE experiments.

5.2.3 *In situ* tensile testing with fibril strain measurement from SAXS

Samples were loaded at a constant velocity of 1 μm/second in a custom-made micromechanical testing machine (**Figure 5.1**) at beamline I22 of DLS. The numbers of mice investigated at 4, 7 and 10 weeks were: 4, 3 and 2, respectively, for wild-type mice; and 4, 2 and 4, respectively, for Hpr mice. Bone specimens were maintained in physiological saline in a fluid chamber in the tester and strained at 0.02% s^{-1}, with SAXD spectra (ten second exposure time) taken every 0.02% tissue strain up to failure (~ 0.5 -

1.0%). Due to an initial slack-range in the grips, the stress-strain curve shows an initial toe-in region, which was not considered during the data evaluation.

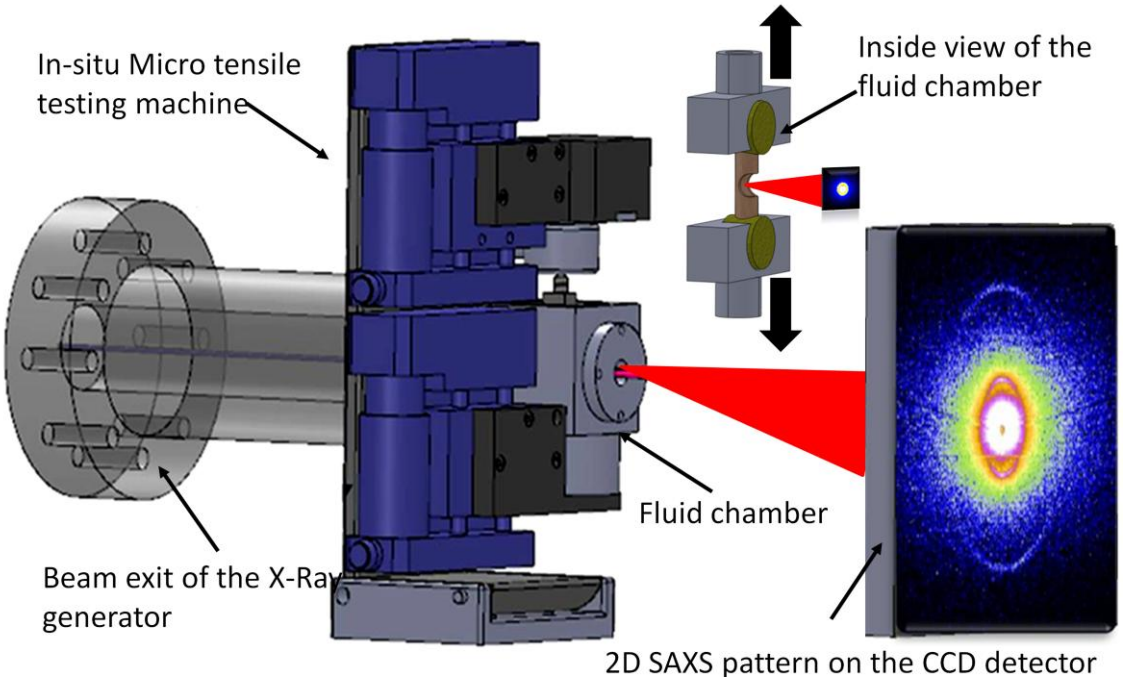

Figure 5.1: Schematic view of the micro tensile testing with synchrotron SAXD. The sample is immersed in phosphate buffered saline. In the inside view of the fluid chamber (inset, dashed lines) the sample geometry is indicated. After milling the posterior side of the mid diaphysis away, the anterior section forms the centre of the sample gauge length. Tensile load is applied along the parallel collagen fibril axis as shown in the schematic (black arrows) of MCF

5.2.4 Sample preparation for BSE measurements

The ends of mechanically tested samples (used for SAXD in the previous section) were prepared for further analysis by backscattered scanning electron (BSE) microscopy, to determine mineralisation parameters at the micro level. One single sample for each disease condition at each age point was used (from 1 to 16 weeks postnatal). Note that two additional age-points (1 and 16 weeks postnatal) is included in the BSE compared to the SAXD data.

5.2.5 Quantitative backscattered electron (qBSE) imaging

One grey scale image was collected from the shaft transverse cross section of each limb. Data points which had a corrected grey level of less than 5 were discarded in order to exclude unmineralised bone matrix. Using BMDD histograms from the anterior cortex, Ca_{mean} and Ca_{FWHM} (74, 256) were estimated to analyse the alterations in mineralisation

of Hpr and wild-type mice with development. The fraction of microscale porosity was also calculated for 4, 7 and 10 weeks wild-type and Hpr mice using BSE images to correct the nominal stress values obtained from *in situ* tensile loading (detailed procedure is shown in **Chapter 4,** section 4.2.6).

5.3 Results

5.3.1 *In situ* tensile testing

The tensile force on the bone samples was continuously measured along with fibril strain (from SAXD images) during stretch-to-failure tests. The stress was calculated from post-test measurements (SEM images of fracture surfaces – **Figure 5.2**) of sample area and plotted versus fibril strain as a function of development (age) and genotype. Stress values were corrected for porosity using **Equation 4.6**. The porosity is significantly (p<0.01) larger for the Hpr mice versus the wild-type at all ages (**Table 5.1**). The range of yield stress (15 – 35 MPa) for Hpr mice was significantly lower than the range for wild-type (30 – 85 MPa).

Table 5.1: Porosity fraction measured for 4, 7 and 10 weeks wild-type and Hpr mice

Age	Wild-type	Hpr
4 weeks	0.0876±0.0106	0.1582±0.0267
7 weeks	0.0706±0.0098	0.2616±0.0382
10 weeks	0.0506±0.0161	0.2030±0.0218

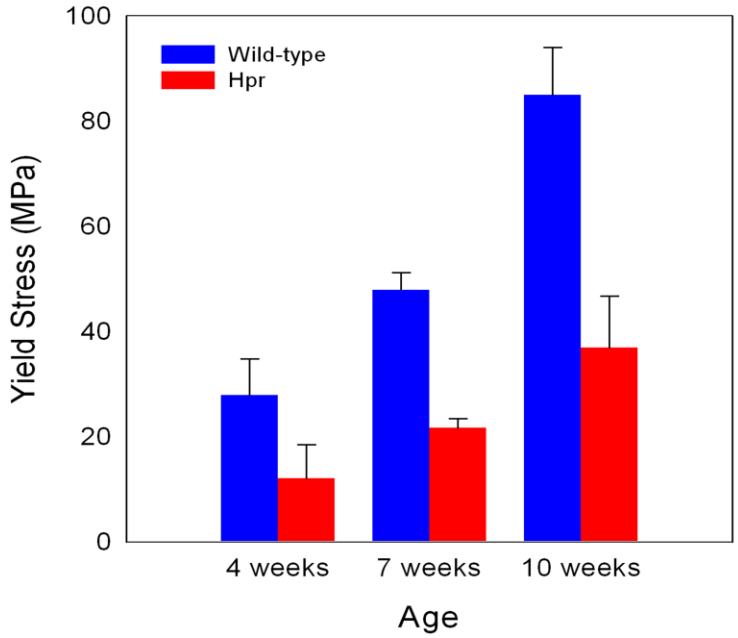

Figure 5.2: The yield stress increases with age in both wild-type (blue) and Hpr (red), but yield stress of Hpr was less than the wild-type mice at every age point.

An examination (**Figure 5.3A-D)** of the combined data sets for (macroscopic) stress and (nanoscale) fibrillar strain in the region of elastic deformation for the different ages in wild-type and Hpr mice revealed differences in the effective fibril modulus, which is defined as $E_f = d\sigma/d\varepsilon_f$, and denoted by the slope. The effective fibril modulus increased by 27 GPa (13 to 40 GPa) from 4 weeks to 10 weeks in wild-type mice. In contrast, the effective fibril modulus in Hpr rachitic mice increased only 6 GPa (4 to 10 GPa) from 4 to 10 weeks **(Figure 5.3E)**. Moreover, the Hpr mice underwent significantly more deformation (fibril strain) in the elastic region than their wild-type counterparts at every age **(Figure 5.3F)**.

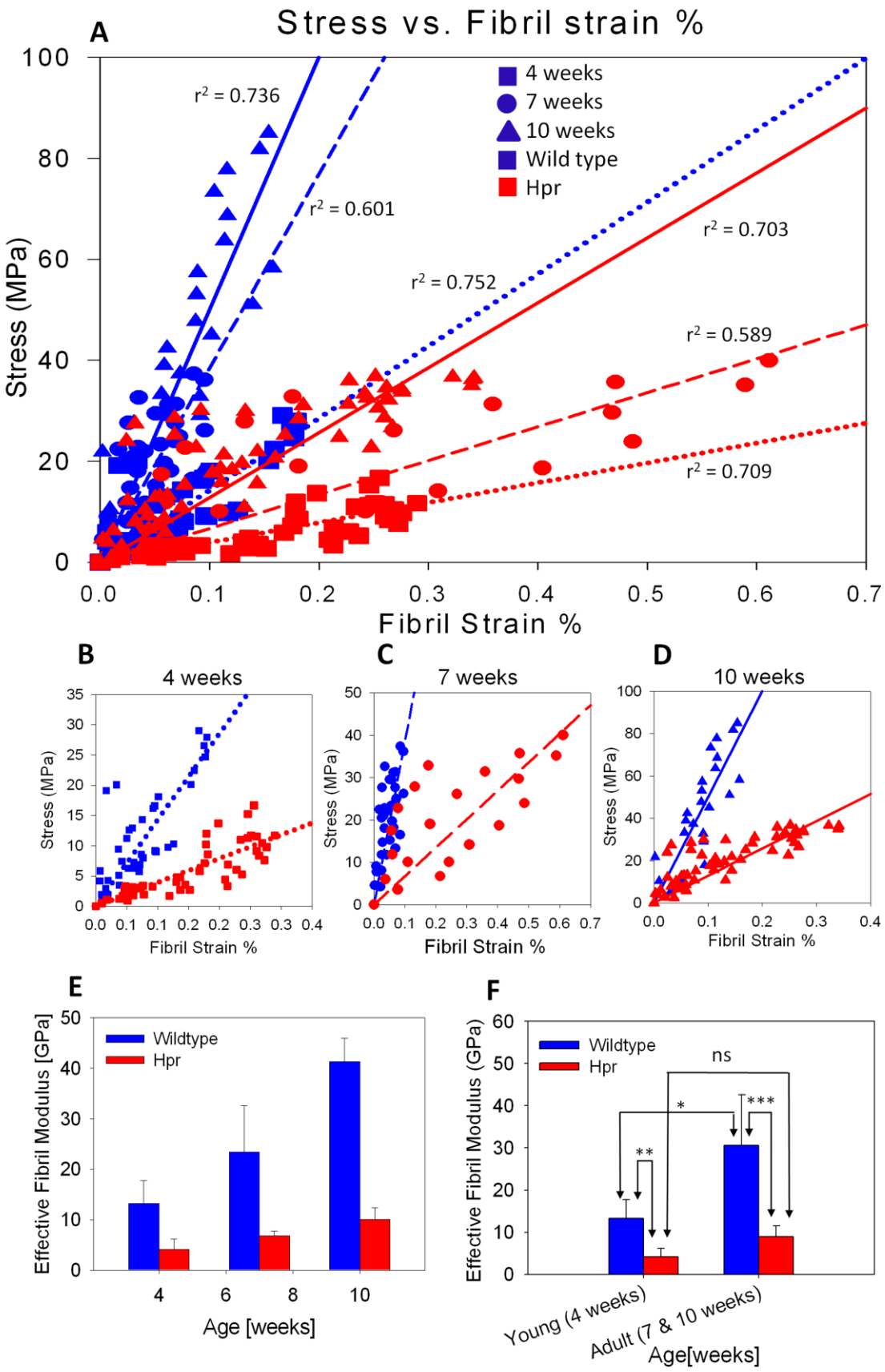
A
Stress vs. Fibril strain %
Stress (MPa)
Fibril Strain %
4 weeks
7 weeks
10 weeks
Wild type
Hpr
r² = 0.736
r² = 0.601
r² = 0.752
r² = 0.703
r² = 0.589
r² = 0.709
B
4 weeks
C
7 weeks
D
10 weeks
E
Effective Fibril Modulus [GPa]
Wildtype
Hpr
Age [weeks]
F
Effective Fibril Modulus (GPa)
ns
*
**
***
Young (4 weeks)
Adult (7 & 10 weeks)
Age[weeks]

Figure 5.3: (A) Stress versus measured fibril strain as a function of disease state (red symbols /lines: Hpr mice; blue symbols/line: wild-type mice) and age (4 week: squares/dotted line; 7 week: circles/dashed line; 10 week: triangles/solid line). (B) - (D) show plots of stress versus fibril strain at each age group (4 week: squares; 7 week: circles; 10 week: triangles) and disease condition (blue symbols/line: wild-type mice; red symbols/line: Hpr mice) individually, to reduce data overlap. (E) Average effective fibril modulus plotted pair-wise as a function of age and disease condition. (F) Adult (combined values of 7 and 10 weeks) average effective fibril modulus and young (4 weeks) average effective fibril modulus, plotted pair-wise as a function of disease condition (blue: wild-type mice (n=4); red: Hpr mice (n=6)) Error bars are standard deviations. Student t-tests were used to compare fibril moduli at different ages and genotypes. Pair-wise brackets denote statistical significance (*P<0.05, **P<0.01, ***P<0.001, ns: not significant).

5.3.2 Quantitative backscattered electron (qBSE) imaging

BSE images **(Figure 5.4)** were collected from femoral cross sections of wild-type and Hpr mice ranging in age from 1 week to 16 weeks. A striking difference in cortical microstructure between the Hpr and wild-type mice was observed. While the overall cortical thickness was similar, the cortices of Hpr mice had a very large fraction of unmineralised tissue which appeared as black on the BSE image **(Figure 5.4)**. In contrast, at each age, the wild-type mice had a denser cortical cross section. However, from 10 weeks onwards, the wild-type mice also had a significant reduction in porosity at the microstructural level.

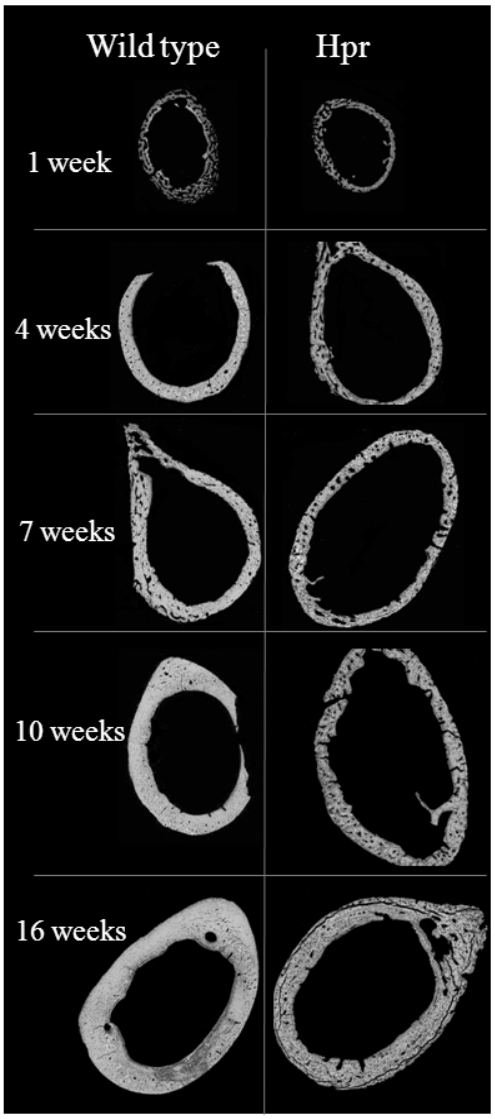

Figure 5.4: Quantitative Backscattered Scanning Electron microscopy images collected from the shaft of the cortical bone of wild-type and Hpr mice aged between 1 to 16 weeks. (n=1 of each genotype at each time point)

The bone mineralisation density distributions (BMDD) in wild-type and Hpr mice were similar at 1 week of age, and in both groups a significant increment in peak Ca wt % was observed from 1 week to 4 weeks which subsequently stabilised (**Figure 5.5A**). However, the change in width of the BMDD histogram was far less pronounced in Hpr mice between 1 and 4 weeks, indicating that the observed increase homogeneity with age in mineralisation was much less in the Hpr mice.

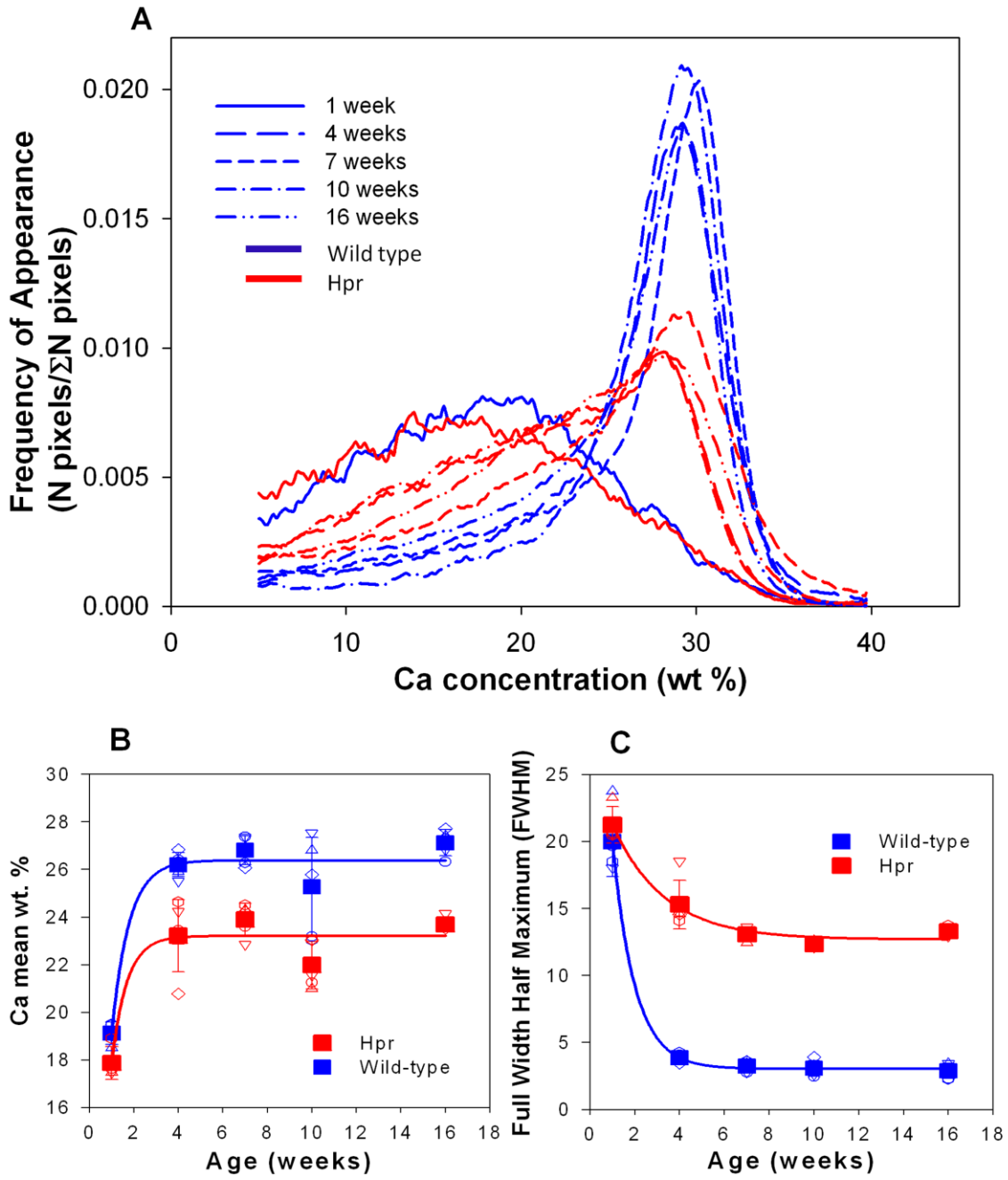

Figure 5.5: Quantification of qBSE results: (A) Bone Mineral Density Distributions (BMDD) were produced for each genotype (blue: wild-type and red lines: Hpr mice) and for each age between 1 to 16 weeks. (B) Mean Ca % and (C) FWHM plotted as a function of age from 1 week to 16 weeks and genotype (in wild-type: large blue symbols & blue line, and in Hpr mice: large red symbols & red line). Errors shown are standard deviations. Small gray symbols at each age are the individual data points. Lines are best fits to single parameter exponential functions Mean Ca% = a (1 – exp (– b × Age)) and FWHM = a exp (– b × Age) + c, where a, b, and c are constants and are intended as guides to the eye only.

The mean Ca weight % (Ca_{mean}) increased in wild-type and Hpr mice, but at different rates, which are indicated by the best-fit two-exponential rise-to-maximum curves (**Figure 5.5B)**. A sharp increment in mean Ca weight % (17% to 24%) was observed in wild-type mice between 1 week and 4 weeks. Subsequently, the mineralisation rate decreased from 4 weeks to 16 weeks, such that the Ca_{mean} increased from approximately 24% to 28%. In contrast, in Hpr mice, the mineralisation rate was significantly lower, as evidenced by the lowered height and reduced rate of increase in the best fit curve at 4 weeks **(Figure 5.5B)**. After 7 weeks, there was no noticeable increment of Ca_{mean} in the Hpr mice. The Ca_{FWHM} of the BMDD decreased substantially both in the wild-type and Hpr mice **(Figure 5.5C)** between 1 and 4 weeks. However, this reduction was nevertheless more profound in the wild-type than the Hpr mice. Thus, the Ca_{FWHM} decreased by ~ 12 % from 1 week to 4 weeks in wild-type mice and subsequently stabilised for later ages, but in the Hpr mice, the Ca_{FWHM} decreased only by ~ 4% over the same time period. In the wild-type mice, the heterogeneity of mineralisation stabilised at a little over 4% of Ca_{FWHM} at 16 weeks, but in the Hpr mice at a comparable age it had reached only 14%.

5.3.3 Model

To develop a simple mechanism linking changes in nanoscale material properties of the mineralised fibrils to observed nano-mechanical behavior, the *in situ* SAXD and qBSE results were combined. Previous structural studies have shown collagen fibrils coated with mineral adherent to the fibril surface (68, 69). Scanning electron microscope (SEM) studies (11, 310) have shown that at the initial stages of mineralisation, mineral is deposited inside the collagen fibril and subsequently forms outside the collagen fibrils. At the scale of the fibril mineralisation is patchy to begin with, but becomes continuous in healthy bone (310). However, SEM images on hypophosphatemic rachitic patients clearly show (**Figure 5.6A and B)**, taken from a previous study (11)) that this continuation of mineralisation is blocked due to the deficiency in phosphorus (11). Collagen bundles away from the mineralisation front showed continuous layer of mineral where as in rickets, the partial mineralisation prevails after the mineralisation front has passed, i.e. after the matrix should have been mineralised (11, 15). Consistent with these previous findings, in the current study BMDD curves from qBSE analysis show a

shoulder region in Hpr mice of 4, 7, 10 and 16 weeks old, indicating a higher proportion of unmineralised or partly mineralised collagen fibrils in rachitic bone even in the mature condition (**Figure 5.5**). Taking these SEM (**Figure 5.6A and B)** images and qBSE (**Figure 5.5**) observations into consideration, it was concluded that in rachitic bone, there exist zones of collagen fibril bundles which are incompletely or patchily mineralised.

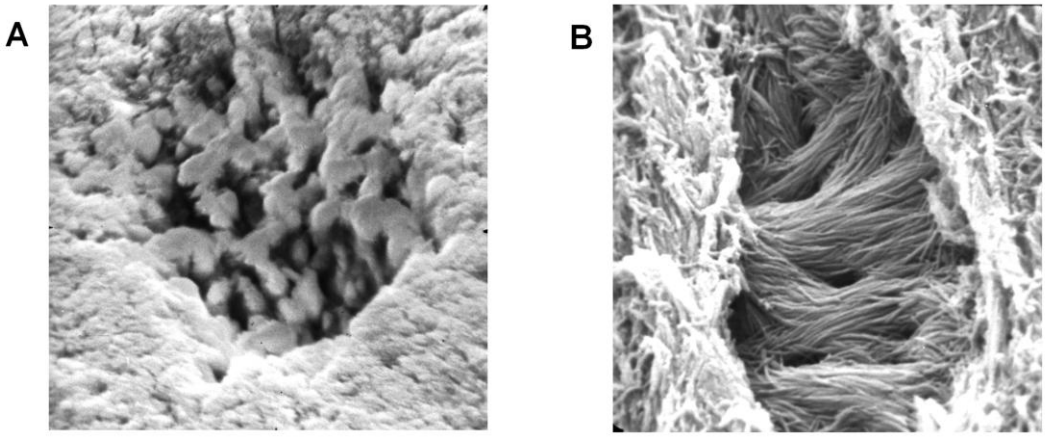

Figure 5.6: (A, B) Scanning electron microscopy images and proposed variation of MCF structure between wild-type and Hpr mice and the variation of relative fibril strain as function of mineral coverage. Samples were treated with sodium hypochlorite to dissolve unmineralised collagen (A) Abnormal patchy mineralisation of collagen fibrils in bundles in osteocyte lacuna wall in hypophosphatemic patient (field width 20 µm) (B) Normal mineralisation of collagen fibrils in bundles in osteocyte lacuna wall (field width 20 µm). Data in (A)-(B) taken from part of a previous study (11)

Based on this representation derived from structural data (**Figure 5.6A and B)**), schematic was developed for the mineralised fibrils in Hpr and wild-type mice as in **Figure 5.7A and B)**, with the fibril bundles in Hpr mice being partially mineralised and the wild-type fully mineralised. In this simple picture, a single fibril (insets in **Figure 5.7A and B)**) would have zones of high and low mineralisation. Hence in this model, an average collagen fibril from mature wild-type mice was considered as fully occupied with mineral, while in the Hpr mice was considered that the average fibril is only partly mineralised, even in fully mature tissue (11).

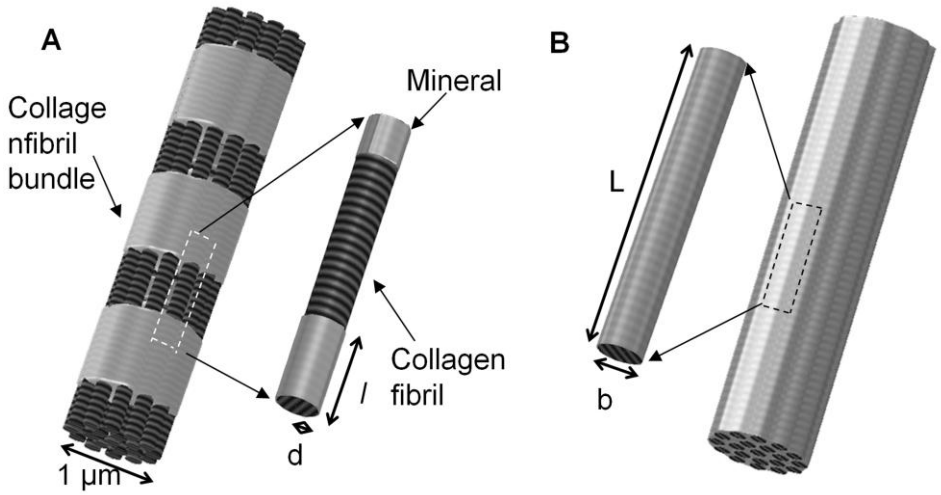

Figure 5.7: (A) In this scheme partially transparent gray zones and banded zones denotes the mineral phase and collagen fibrils respectively. In Hpr mice, the collagen fibril bundles are only partly filled and covered by mineral which is also discontinuous along the length (inset showing partially mineralised fibril). (B) In wild-type mice, the full length of collagen fibril bundle is covered with mineral (inset showing fully mineralised fibril).

Based on this, the nano-structural deformation model parameters (fibril strain and effective modulus) were determined and compared them with the experimental results as a function of age. The model predictions were calculated for two different assumptions of the extra/intrafibrillar mineral division: low (25% intrafibrillar) and high (60% intrafibrillar). For a given external force, ε_f was defined as the total percentage elongation of the mineralised fibril (fibril strain). The elastic moduli of the mineral phase and MCF are denoted by E_m and E_f, respectively. The extrafibrillar mineral coating has uniform thickness (d) and the fibril diameter is denoted b and taken to be a constant of 50 nm (311) (**Figure 5.8**). For a given external force F along the fibril axis, the total strain of the fibril is the weighted average of the strains in the uncoated portion (ε_1) and the fully covered portion (ε_2), leading to the following relation:

The simple force balance equation was applied to the naked fibril (uncoated)

$$\varepsilon_1 = \frac{\sigma}{E_f} = \frac{F}{Area} \times \frac{1}{E_f}$$

$$\varepsilon_1 = \frac{F}{\pi\left(b/2\right)^2} \times \frac{1}{E_f}$$ Equation 5.1

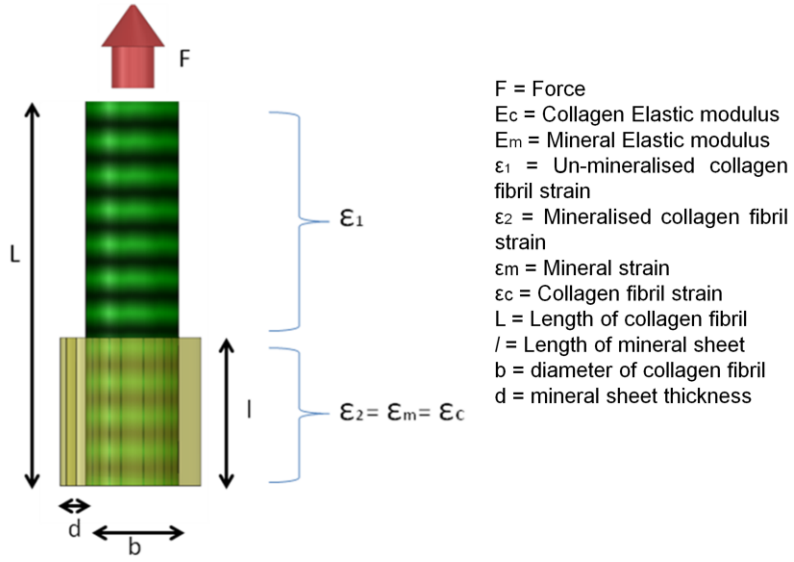

Figure 5.8: Schematic of partly MCF. (Collagen fibril; black and dark gray section denoted by L and mineral; light gray denoted by *l*

Previous structural studies have found that each collagen fibril is coated with mineral strongly adherent to the fibril surface (68, 69). Therefore strain (ε_2) of the fully coated region is equal to the collagen fibril stain (ε_f) or mineral phase strain (ε_m).

$$\varepsilon_2 = \varepsilon_m = \varepsilon_c$$
$$\sigma_m = \varepsilon_2 \times E_m$$
$$\sigma_c = \varepsilon_2 \times E_f$$
$$F = A_m \times \sigma_m + A_f \times \sigma_f$$
$$F = \left[\pi \left(\left(\frac{b}{2} + d \right)^2 - b^2 \right) \times \varepsilon_2 \times E_m \right] + \left[\pi \left(\frac{b}{2} \right)^2 \times \varepsilon_2 \times E_f \right]$$
$$F = \varepsilon_2 \left[\pi \left(d^2 + db \right) E_m + \frac{\pi b^2}{4} E_f \right]$$

$$\varepsilon_2 = \frac{F}{\left[\pi \left(d^2 + db \right) E_m + \frac{\pi b^2}{4} E_f \right]} \qquad \text{Equation 5.2}$$

For a given external force, ε_T was defined as the total percentage elongation of the fibril (fibril strain). The total length of the fibril is taken to be L, of which a portion *l* is covered by the mineral coating (for a fully mineralised fibril *l* = L). The remainder of the fibril (L – *l*) is uncoated. The ratio *l*/L can be considered as the degree of mineralisation. Total fibril strain (ε_f) for partly mineralised fibril can be estimated by applying rule of mixture composite.

By combining **Equation 5.1** and **Equation 5.2**:-

$$\varepsilon_f = \varepsilon_1 + \varepsilon_2$$
$$\varepsilon_f = \frac{L - l}{L} \varepsilon_1 + \frac{l}{L} \varepsilon_2$$
$$\varepsilon_f = \left(\frac{L - l}{L} \right) \bullet \frac{F}{\pi \left(b/2 \right)^2 E_f} + \frac{l}{L} \left(\frac{F}{\left(\pi b^2 / 4 \right) E_f + \pi \left(d^2 + db \right) E_m} \right)$$

$$\varepsilon_f = \frac{4F}{\pi b^2 E_f}\left[\left(1-\frac{l}{L}\right)+\frac{l}{L}\bullet\frac{1}{1+\frac{4\left(d^2+db\right)}{b^2}\frac{E_m}{E_f}}\right] \qquad \text{Equation 5.3}$$

For an unmineralised fibril, $l = 0$, and the above equation can be written as

$$\varepsilon_{f,u} = \frac{4F}{\pi b^2 E_f} \qquad \text{Equation 5.4}$$

Taking as a reference the fully mineralised fibril (completely covered with mineral both outside and inside **(Figure 5.8**), $\varepsilon_{f,0}$ was defined as the equivalent (reference) strain in this structure under the same force.

While for a fully mineralised fibril ($l = L$)

$$\varepsilon_{f,0} = \frac{4F}{\pi b^2 E_f}\left[\frac{1}{1+\frac{4\left(d^2+db\right)}{b^2}\frac{E_m}{E_f}}\right] \qquad \text{Equation 5.5}$$

In the following, the relative change of fibril strain ε_f was calculated with respect to the reference strain ε_{f0} as a function of diseases condition (Hpr versus wild-type) and ageing (development).The ratio of the fibril strain at intermediate mineralisation ($0 < l < L$) to that of the fibril at full mineralisation ($l = L$) is

$$\frac{\varepsilon_f}{\varepsilon_{f,0}} = \frac{\dfrac{4F}{\pi b^2 E_f}\left[\left(1-\dfrac{l}{L}\right)+\dfrac{l}{L}\times\underbrace{\dfrac{1}{1+\dfrac{4\left(d^2+db\right)}{b^2}\dfrac{E_m}{E_f}}}_{K}\right]}{\dfrac{4F}{\pi b^2 E_f}\left[\underbrace{\dfrac{1}{1+\dfrac{4\left(d^2+db\right)}{b^2}\dfrac{E_m}{E_f}}}_{K}\right]}$$

$$\frac{\varepsilon_f}{\varepsilon_{f,0}} = \frac{\left(1-\dfrac{l}{L}\right)+\dfrac{l}{L}\times\dfrac{1}{k}}{\dfrac{1}{k}}$$

$$\underbrace{\frac{\varepsilon_f}{\varepsilon_{f,0}}}_{y} = \underbrace{\frac{l}{L}}_{x}\times\underbrace{-1\left(k-1\right)}_{m}+\underbrace{k}_{c}$$

$$\frac{\varepsilon_f}{\varepsilon_{f,0}} = \frac{l}{L}\times-1\left(\frac{4\left(d^2+db\right)}{b^2}\frac{E_m}{E_f}\right)+\left(1+\frac{4\left(d^2+db\right)}{b^2}\times\frac{E_m}{E_f}\right) \qquad \text{Equation 5.6}$$

Based on previous studies, it was assigned the mineral modulus E_m = 100 GPa (105) and the modulus of a MCF as 2.4 GPa (83). For the higher level of intrafibrillar mineralisation (60%) a higher modulus (12 GPa) was assumed. It is clear that the unmineralised or partially mineralised fibrils will exhibit a much larger strain than the fully mineralised fibril for the same force.

The information on local mineral concentration from qBSE results (**Figure 5.5B**) was used to determine which extrafibrillar sheet thickness *d* corresponds to the experimental data. The Ca wt. % found in the qBSE results converted to a volume percentage φ as described by Roschger and co-workers (256) and **Chapter 2** section 2.4 (**Equation 2.9**).

Table 5.2: Mineral volume fraction % values calculated using calcium weight percentage data given in the Figure 5.5B of main data

Age	Wild-type (%)	Hpr (%)
4 weeks	40.73 ± 4.08	33.30 ± 2.40
7 weeks	44.08 ± 4.02	38.46 ± 2.72
10 weeks	46.64 ± 4.42	33.22 ± 3.14
16 weeks	51.69 ± 2.46	35.56 ± 1.76

Based on the above qBSE results, the mineral volume fraction of 16 week wild-type mice is 51.69%, which is very close to the values of 52% taken for fully mineralised bone (108, 312, 313). Therefore the fibrils (**Figure 5.7B**) in the 16 week wild-type tissue was considered to be fully mineralised (l = L) and mineral volume fraction at 16 weeks wild-type condition denoted as $\phi_{TM,0}$.

The division of mineral into extrafibrillar ϕ_{EF} - versus intrafibrillar ϕ_{IF} compartments is still not well-established, but estimates have been provided in Kinney et al, 1995 (314). Kinney et al, 1995 estimates that intrafibrillar volume fraction ($f_{IF,25\%}$) of 25 % of the total mineral phase in fully mineralised bone (i.e. a volume % $\phi_{IF,25\%}$ of 12.92%) is intra-fibrillar (315). Other researchers claim a larger intrafibrillar mineral fraction $f_{IF,60\%}$, up to 50-60% (i.e. a volume % $\phi_{IF,60\%}$ of 26% - 31.2%). From **Table 5.2**, it was shown that the mineral volume fraction at the earliest stage of development (4 weeks) is greater than this value. This indicates that the intra-fibrillar space available for mineralisation in both wild-type and Hpr mice has been already filled up by 4 weeks. As the collagen fibrils are identical in Hpr and wild-type (79), the intra-fibrillar environment is the same. Therefore, the amount of intra-fibrillar mineral is the same in both cases for all the ages and for both disease conditions, and can be taken as a constant. The variation of mineral content is achieved solely by varying the fraction of the fibril covered by mineral (l/L).

To calculate the thickness d of the mineral sheet, extra fibrillar mineral volume fraction $\phi_{EF,0}$ of the fully mineralised 16 week wild-type case was considered, where l = L.

$$\frac{Extrafibrillar\ Mineral\ volume}{Fibril\ volume + Extrafibrillar\ Mineral\ volume}$$

$$= \frac{\pi\left(\left(\frac{b}{2}+d\right)^2 - \left(\frac{b}{2}\right)^2\right)L}{\pi\left(\frac{b}{2}+d\right)^2 L} = \phi_{EF,0} = \phi_{TM,0} - \phi_{TM,0} * f_{IF}$$

$$= \frac{\pi\left(\left(\frac{b}{2}+d\right)^2 - \left(\frac{b}{2}\right)^2\right)L}{\pi\left(\frac{b}{2}+d\right)^2 L} = \phi_{EF,0} = \phi_{TM,0}\left(1 - f_{IF}\right)$$

$$= 1 - \frac{b^2}{b^2 + 4bd + 4d^2} = \phi_{TM,0}\left(1 - f_{IF}\right) \qquad \text{Equation 5.7}$$

In the above calculation the diameter of an individual collagen fibril was taken to be 50 nm (311). A mineral coating thickness of d = 7 nm and 3 nm were obtained for 25% and 60% intrafibrillar mineral volume fractions respectively. In 16 weeks Hpr condition it was assumed that coating thickness stay the same, but coverage less compared to the healthy case which is $l \neq L$. Since intrafibrillar mineral volume fraction in Hpr mice is same as wild-type intrafibrillar mineral volume fraction, reduction in total mineral volume fraction due to the reduced extrafibrillar mineralisation. Therefore for any given intermediate mineralisation ($\phi_{TM(...)}$) degree of extrafibrillar mineral coverage l/L can be estimated by (79, 277, 312, 316)

$$\frac{Extrafibrillar\ Mineral\ volume\left(\text{int}ermidiate\right)}{Collagen\ volume + Extrafibrillar\ Mineral\ volume} = \left(\phi_{TM(...)} - \phi_{IF}\right)$$

$$= \frac{\pi\left(\left(\frac{b}{2}+d\right)^2 - \left(\frac{b}{2}\right)^2\right)l}{\left[\pi\left(\frac{b}{2}\right)^2 L\right] + \left[\pi\left(\left(\frac{b}{2}+d\right)^2 - \left(\frac{b}{2}\right)^2\right)l\right]}$$

$$= \frac{\frac{l}{L}}{\frac{b^2}{4\left(bd+d^2\right)} + \frac{l}{L}} \qquad \text{Equation 5.8}$$

Degree of extrafibrillar mineral coverage *l/L* will be calculated for intrafibrillar volume fraction (ϕ_{IF}) of 25% and 60%.

Using these parameters, the variation of relative fibril strain $\varepsilon_F / \varepsilon_{F0}$ (**Equation 5.6**) was plotted against the degree of mineralisation (*l*/L). Because the effective fibril modulus $E_f = d\sigma/d\varepsilon_f$ is inversely proportional to ε_f for the same stress, a direct comparison of the model to the experimental results is possible. If E_{f0} is defined as the effective fibril modulus for 16 week (fully mineralised) wild-type mice, then $\varepsilon_F / \varepsilon_{F0} = E_{F0} / E_F$. Plotting these points together with the model curve (**Figure 5.9**) for both wild-type and Hpr mice shows a similar reduction of E_{F0} / E_F with increased mineralisation. Thus the variation of relative fibril strain $\varepsilon_F / \varepsilon_{F0}$ (**Figure 5.9**) was determined in this model system and experimental results, showing that the fibril strain in Hpr is significantly ($p < 0.05$) higher than that in wild-type mice.

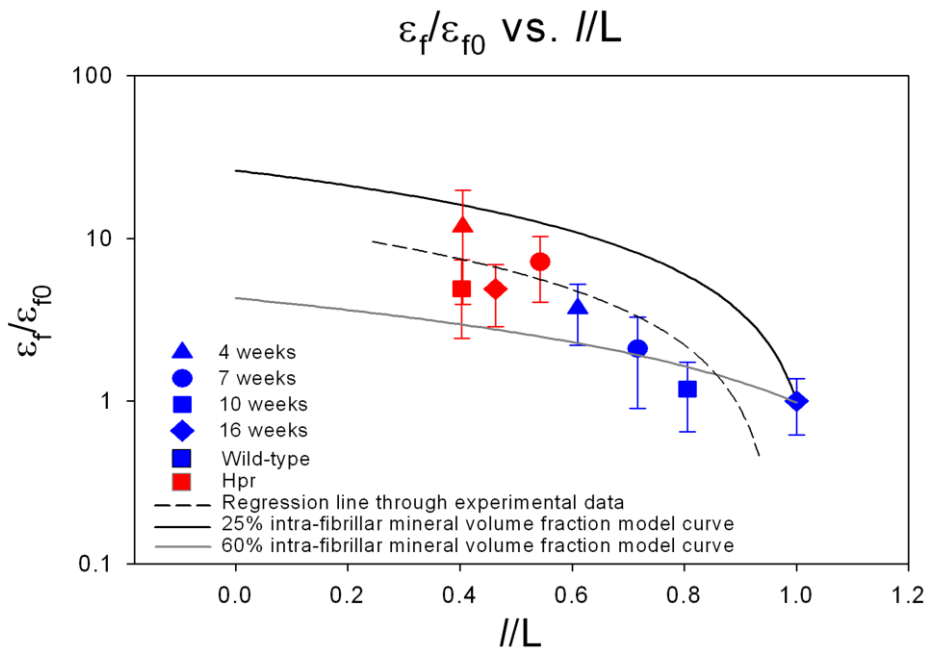

Figure 5.9: Relative fibril strain $\varepsilon_f/\varepsilon_{f0}$ (inverse of ratio of effective fibril moduli Ef/Ef0; effective fibril moduli given in Figure 5.3) plotted as a function of degree of mineralisation l/L. The solid black line denotes 25 % intrafibrillar mineral volume fraction. Filled symbols and the dashed line denote experimental data points together with a linear regression over the points. Error bars are standard deviations. Black symbols and gray symbols denote wild-type and Hpr mice, respectively, between 1 to 16 weeks of age.

5.4 Discussion

The results report on the characterization of the structure and nano-mechanics of the bone abnormalities in an ENU-induced mouse mutant, Hpr, which is representative of XLHR in man and is due to a missense Trp314Arg mutation of the *Phex* gene. Previous studies investigating the pathological, mechanical and structural alterations in Hyp mice, have reported abnormalities of the femora, which had angular deformations, thereby indicating a reduced torsional stiffness, which was attributed to differences in mineral content, distribution and the molecular nature of the mineral in the long bones (79, 183, 184, 276, 277) (discussed in **Chapter 2,** section 2.6.1)

The results reveal that the effective fibril modulus (σ/ε_F) increased consistently with development at each age. In the hierarchical staggered model (107), such a change may be due to an increased extrafibrillar matrix stiffness over this period. The effective modulus of the Hpr mice at every age was significantly ($p < 0.01$) less than their wild-

type littermates. According to the same staggered model such a decrease would indicate reduced extrafibrillar stiffness in rachitic bone, possibly due to lower secondary mineralisation in the extrafibrillar space. In addition, these results showed that the fibrils strain much more in the region of elastic deformation in Hpr than in wild-type femora of the same age (**Figure 5.3A-D**). This may also be due to the changes in extra-fibrillar mineral environment that occurs in rachitic bone. During the growth period, from 4 weeks to 10 weeks, extrafibrillar mineralisation is increased, by the fusion of mineralised regions along the collagen fibril. Mineral within adjacent fibrils fuses together laterally forming a fused fibril array (317). As a result of this tight straitjacketing of mineralised fibrils, the deformability of the MCFs is substantially reduced. It can be proposed that in Hpr mice, the extracellular inorganic phosphate (P_i) level is decreased, reducing mineralisation of the extrafibrillar space. This in turn leads a reduction in the effective stiffness **(Figure 5.3E and F)** of the extrafibrillar mineral layer, lowering the lateral straight-jacketing effect and resulting in an increased tensile stretching of collagen fibrils.

The mineral content assessment from qBSE, reveals the mean level and the extent of heterogeneity of the level of mineralisation in the bone tissue (76), showed that Hpr femora/cortical bone had a highly heterogeneous mineralised matrix at the microscale, with a large fraction of poorly mineralised cortex. In contrast, wild-type mice had a mineralisation pattern that was more uniform and denser in the older animals, consistent with previous studies (235). Moreover, the Hpr femora/cortical bone had hypomineralised periosteocytic lesions **(Figure 5.4)**, similar to those reported in patients with osteomalacia (316, 318). Differences in the progression of mineralisation at the earliest stage of maturation (1-4 weeks) were also observed between Hpr and between wild-type mice. Thus, at one week, the cortex of the wild-type and Hpr mice mid-diaphysis bone is similar, but by four weeks of age the wild-type cortex is much denser, consistent with the Hpr mice having a reduction in the process of rapid primary mineralisation which likely comprises up to 70% of the final content in trabecular bone (76). The slower secondary mineralisation phase, which was marked by a gradual increase in mineral content from 4 to 16 weeks of age in wild-type mice was absent in Hpr mice. These abnormalities in the primary and secondary mineralisation phases in the Hpr mice are likely associated with the hypophosphatemia.

For quantitative analysis of these mineralisation changes, the statistical BMDD approach is useful (74, 302). The mineralisation rate is greater from 1 week to 4 weeks and subsequently reduces from 4 weeks to 16 weeks in wild-type **(Figure 5.5B)**, indicating a change from rapid primary mineralisation to slow secondary mineralisation. The reduced local (micro) primary mineralisation rate in Hpr compared to wild-type mice is most likely linked to the overall reduction in mineralisation due to the low levels of phosphate (220, 276, 319). Moreover, the constant mean Ca wt. % (no increment) in Hpr mice after 7 weeks implies impaired secondary mineralisation. Reduced secondary mineralisation in rachitic bone in mice has been known to cause irregularity and low density of calcification at the mineralisation fronts in the mid-diaphysis (276). These differences in mineralisation mechanisms in rachitic bone have long-term consequences for the final mineral content in the adults (16 week old) Hpr mice, which is 21% lower than wild-type (**Figure 5.5B**).The Ca_{FWHM} of the BMDD, which gives a measure of the homogeneity of mineralisation at the microscale, was found to decrease with age in the wild-type and Hpr mice. However, the time dependence and magnitude of this decrease is different in the two types of mice (**Figure 5.5C**). The large (12%) reduction in heterogeneity between 1 week to 4 weeks – leading to more uniform mineralisation – observed in wild-type mice is absent in the Hpr mice (~3% reduction). Thus, in wild-type mice, mineralisation rapidly becomes more homogeneous from 1 week to 4 weeks, subsequently approaching a plateau over 4 – 16 weeks. This homogenization is likely due to the free water in the matrix being slowly replaced by mineral (310). However, this process is markedly reduced or absent in Hpr mice.

A tentative structural explanation of partial extrafibrillar mineralisation in rachitic bone also predicts a larger deformability and lower fibril modulus in Hpr mice. An unambiguous comparison with this data is not possible because the model is highly dependent on the assumed relative amounts of intra- versus extrafibrillar mineral. To observe its sensitivity to these parameters, its predictions were plotted for two different intrafibrillar volume fractions (25% and 60%) and find that while the trend is the same, the absolute magnitudes (gradient of the model curve) decreased by 34.6%. And it was found that the experimental results are lower for 25% intrafibrillar filling and higher for 60% intrafibrillar filling than the model predictions (**Figure 5.9**).

The model includes several further approximations and assumptions. For example, it was assumed that all fibrils stretch to the same extent, but fibrils which are off-axis to the main direction of loading will stretch less than the fibrils aligned parallel to the applied force. Indeed, X-ray diffraction analysis included contributions from off-axis fibrils, which reduces the calculated strain, increasing the deviation from the model curve in the observed direction (to lower E_{F0}/E_F). In addition, interactions or shearing between collagen fibrils has not been included in the model, and it has been previously shown that under tensile deformation there is significant interfibrillar shear between fibrils (82, 107). In this model, such interfibrillar deformation would reduce the fibril strain at a specific force level, as there would be a component of interfibrillar deformation as well. Such a reduction would lower the strain predictions of the model curve, thus bringing it into closer alignment with experiment. Further, the interfibrillar adhesion of the mineralised segments of one fibril to an adjacent fibril will reduce the total fibril strain compared to model prediction. This correction (lower E_{F0}/E_F) again adjusts this model toward a closer match with experimental results (**Figure 5.9**). Thus further refinements to the model, implementing these parameters are required.

The model suggested in this study differs from other previously proposed mechanisms for mineralised collagen fibrillar deformation (82, 99, 105-109). Many of these model systems focused mainly on the mechanical properties of a single collagen fibril as a function of intrafibrillar mineral platelet parameters. In contrast, model presented in this study particularly focuses on the altered extrafibrillar mineralisation that occurs during the metabolic bone disorder of rickets, and its influence on the nanoscale mechanical properties.

5.5 Conclusion

In summary, *in situ* synchrotron SAXD combined with micromechanical testing was utilised to serve as an *in-vitro* functional imaging technique to measure the degradation in bone quality that occurs in a mouse mutant for hypophosphatemic rickets, Hpr. Results shown Hpr mice to have significant elevation in fibrillar strain and reduction in effective fibril modulus and that these changes are exaggerated with age. Concurrently, the overall degree of mineralisation is lowered and more heterogeneous in Hpr and shows a slower

time-course of maturation. Experimental results were compared with a nanoscale mechanism of the MCF in rachitic bone in which incomplete extrafibrillar mineralisation leads to a larger elongation and a lower effective fibril modulus. Further refinement of this model to take into account inter-fibrillar deformation and multiple fibril orientation in lamellae will be necessary to provide a closer match with experimental results. However, this approach illustrates the potential utility of synchrotron-based *in situ* X-ray nano-mechanical imaging in identifying functional alterations in bone quality at the nanoscale in the study of metabolic bone diseases.

Chapter 6

Disruption in Fibrillar Level Deformation Mechanisms in Rachitic Bone at Tensile and Compressive Zones

The contents of this chapter have been submitted and accepted (26/10/2012) for publication in *Bone*

A Karunaratne J Hiller, CT Esapa, NJ Terrill, AH Barber, RV Thakker, HS Gupta Symmetrically reduced stiffness and increased extensibility in compression and tension at the mineralized fibrillar level in rachitic bone, 2012

6 Disruption in Fibrillar Level Deformation Mechanisms in Rachitic Bone at Tensile and Compressive Zones

6.1 Synopsis

Mechanisms at the nanometre length scale, such as altered extensibility via reduced extrafibrillar mineralisation (85) and stiffening via collagen cross linking (205), will alter bone quality; the macroscopic deformation and fracture mechanisms of bone in ageing and disease. Nanoscale deformation mechanisms in bone have been investigated in uniaxial tensile (14, 85, 205) and compressive loading (86), but not as extensively under physiological forces and stress (25), such as bending. Bending deformation of bone involves concurrent compression and tension, in spatially separated zones. In this regard, it is noteworthy that at the macroscopic scale, direct compressive and tensile deformation behaviours are different (88, 320). It is well known that the post yield zone in compression is shorter, and does not show the linear hardening observed in tension (89). However, the existence and roles of any differences between elastic properties in compression and tension remain to be elucidated. For example, in human femoral diaphyses, mechanical properties (failure stress, modulus and yield strain) were reported to be lower in tension compared to compression (321). Tissue modulus calculated from torsional testing experiments is different between compression and tension experiments (322). In contrast, a small but significant increase in modulus was observed in tension relative to compression in compressive and tensile zones of metacarpal bone during bending, using *in situ* electronic speckle interferometry (320). These conflicting results raise the possibility that the observed differences may arise from deformation mechanisms at a specific length scale (fibril, lamellar or osteonal/trabecular). However, it is noteworthy that a direct comparison between compressive and tensile deformation at the fibrillar level has not been reported. Furthermore, disease-specific alterations in bone quality at the scale of the fibril may change the mineral/collagen arrangement, as has been reported in osteomalacia, rickets (79, 85) and osteogenesis imperfecta (219). Consequently, if there are intrinsic changes in nanoscale compressibility and extensibility at the fibrillar level, these may be dramatically amplified in disease-induced changes in

bone quality, and critically affect fracture risk, which is known to involve determinants other than bone quantity (203).

These nanoscale mechanisms have been investigated by synchrotron SAXD and WAXD combined with micromechanical testing (14, 86) to measure the altered fibrillar level deformation mechanisms in normal bone. In the previous chapter this nano mechanical imaging approach has been applied for the first time to measure the nanoscale fibril strain at each level of externally applied load, enabling parameters such as effective fibril modulus and maximal fibril strain to be studied in response to macroscopic stress in metabolic bone diseases (85). These approaches have been also used to investigate the deformation mechanisms in compression (86, 323) in bone, utilising normal bone, but there are few studies examining nanoscale deformation mechanisms in bending of normal bone and even less in bending deformation in well-defined metabolic bone disease phenotypes.

To bridge the gap, this chapter perform the first simultaneous *in situ* measurement of compressive and tensile deformation at the fibrillar level in bones (humeri) obtained from the same mouse model (Hpr) representative of XLHR in man, used in the **Chapter 5**. It has been suggested that mineral composition and altered distribution in these mice may contribute to changes in macromechanical properties (79). SEM images of bone from patients with XLHR shows poorly mineralised regions surrounding osteocyte lacunae (also known as 'beards' or halos or circumlacunar lesions) which develop at the level of the mineralizing front, i.e., as a result of a primary failure of mineralisation (79). These lesions are related to a prolongation of the mineralisation lag time leading to failure of the fusion of the growing mineral particle clusters (79, 85). However, while these structural defects are undoubtedly important in altering the properties of rachitic bone locally, they do not, in themselves, indicate the nature of the underlying nanoscale deformation mechanisms which dictate the impaired mechanical properties in rickets.

Indeed, study performed in **Chapter 5** demonstrated that the nanoscale abnormalities in the bone quality (incomplete extrafibrillar mineralisation) have a significant effect on deformation in the Hpr mice. Thus, in tension, Hpr mice were shown to have a

significantly reduced fibril modulus and increased fibril strain, consistent with a nanoscale model of fibrils with incomplete or patchy extrafibrillar mineralisation (85). Whether this mechanism is also relevant (beyond tension) for physiologically relevant loading (**Figure 6.1**) like bending and compression is not known. In this study microfocus *in situ* synchrotron SAXD (µSAXD) combined with cantilever bending was used to resolve nanoscale fibril strain in tensile- and compressive tissue regions separately, with quantitative backscattered scanning electron microscopy used to measure microscale mineralisation.

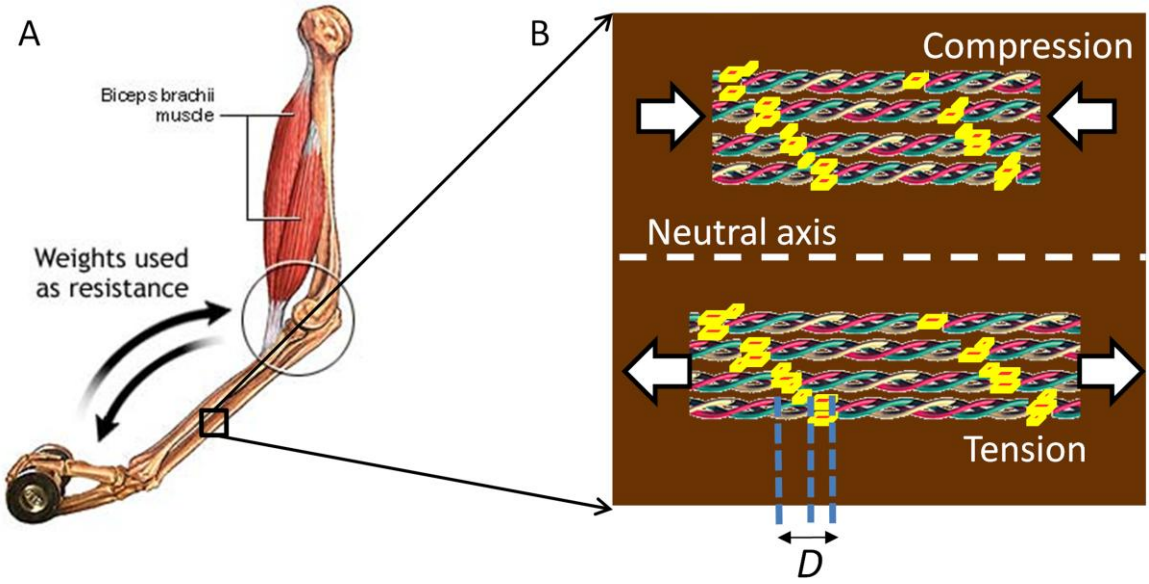

Figure 6.1: (A) schematic of weight lifting. Ulna and radie acts as cantilever beam. (B) Zoomed in section of bone matrix showing the mechanical behaviour of MCFs

6.2 Material and methods

6.2.1 Animals

An Hpr mouse-strain with an ENU-induced missense Trp314Arg *Phex* mutation was used (309). Wild-type and Hpr female mice aged 4, 7 and 10 weeks were studied. The numbers of mice investigated at 4, 7, and 10 weeks were: 4, 3, and 4, respectively, for wild-type mice; and 4, 6, and 5, respectively, for Hpr mice. These age points were chosen to cover the period of rapid skeletal growth in mice.

6.2.2 Sample preparation and cantilever bending combined with µSAXD

Dissected mouse femora from Hpr and wild-type mice were prepared for cantilever bending experiments as explained in **Chapter 4** section 4.1.2. Using the modified micro mechanical testing machine, cantilever bending combined with spatially-resolved microfocus scanning SAXD with 125 µm step-size was carried out across the width of the bone shaft. Samples were tested in stepwise loading into the yield region (tracked by macro-scale stress behaviour). At each load step, µSAXD scans were collected across the width of the cantilever beam (**Figure 6.2**).

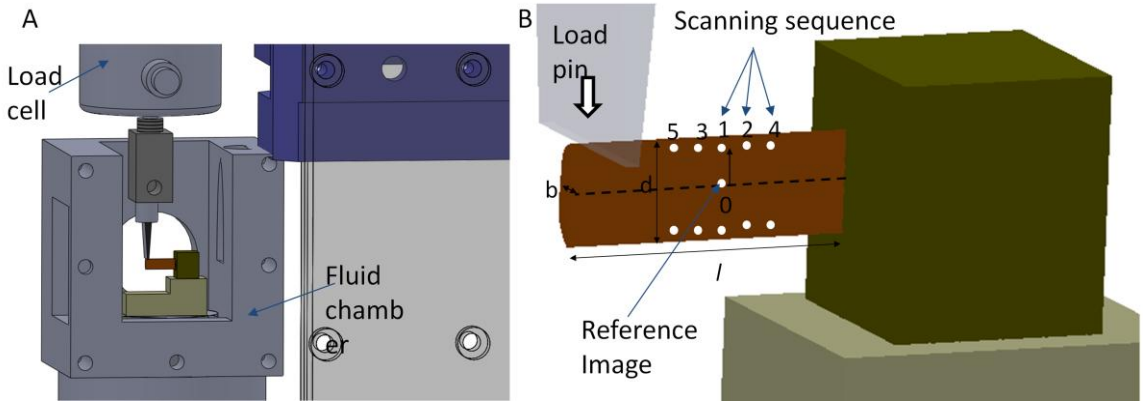

Figure 6.2: (A) Schematic of fluid chamber and the bone specimen. Full mechanical testing machine is shown in the Figure 3.11. (B) Zoomed in view of the bone sample within the testing machine. Scanning SAXD spectra was taken with the distance of 125 µm from the middle of the sample to the both tensile and compression zones

Initial reference SAXD image was taken at the middle of the sample. Then after every 30 µm step of deflection 2 SAXD images were taken from tensile and compression zones (above and below the neutral axis) as shown in the **Figure 6.2B.** Detailed experimental procedure is explained in **Chapter 4** section 4.2.1.2.

6.2.3 BSE Imaging

Humeri from one wild-type and one Hpr mouse at each age point (4, 7 and 10 weeks) were prepared for BSE microscopy analysis. Sample preparation was carried out as reported in **Chapter 4**, and the final polished surface was a longitudinal cross section

from mid diaphysis to the humeral head. Six regions of interest (100 × 100 μm) from each BSE image (per sample) were used for quantitative analysis and converted to a quantifiable greyscale value. Grey levels below 76 and above 200 were discarded in order to exclude unmineralised bone tissue. Furthermore, the microscale porosity was calculated for 4, 7 and 10 weeks wild-type and Hpr mice in order to correct the nominal stress values (from *in situ* cantilever bending experiments). The porosity fraction, for selected regions (5 regions from each sample) of interest (100 × 100 pixels each) from qBSE images of longitudinal cross section of each humerus, was calculated as explained in the **Chapter 4**. Corrected stress will hereafter be referred to simply as the stress.

Statistical analysis

Macro and nanomechanical and structural results from tensile and compressive zones were analysed by a Student's t-test. Single factor ANOVA was used to determine the significant levels for changes of these parameters with the developmental age points (4, 7 and 10 weeks).

6.3 Results

6.3.1 *In situ* cantilever bending testing with μSAXD

The flexural modulus of each specimen was calculated using **Equation 4.3** (**Chapter 4** section 4.2.1.2) and plotted as a function of development and genotype as shown in **Figure 6.3A**. The flexural modulus increased by 2.5 GPa (0.5 - 3 GPa) from 4 weeks to 10 weeks in wild-type mice. In contrast, the modulus in Hpr mice increased only 0.67 GPa (0.03 - 0.7 GPa) from 4 to 10 weeks. At each age point, the flexural modulus was significantly lower ($p<0.001$) in Hpr mice compared to wild-type mice. Using **Equation 4.4 and 4.3** (**Chapter 4** section 4.2.1.2), bending stress and tissue strain was calculated for the locations where the SAXS image was collected (125 μm above and below from the neutral axis). The average maximum bending stresses (**Figure 6.3B**) of the wild-type mice are larger compared to the Hpr mice at each age point, but the difference is not significant at $p = 0.05$. The bending stress significantly increased with development for both genotypes. The level of significance was higher in wild-type ($p<0.001$) compared to

Hpr mice ($p<0.05$). **Figure 6.3C** shows that the maximum tissue strain of Hpr mice was larger compared to the wild-type mice, but the difference was not significant ($p>0.05$). Also tissue strain did not significantly vary ($p>0.05$) from 4 weeks to 10 weeks.

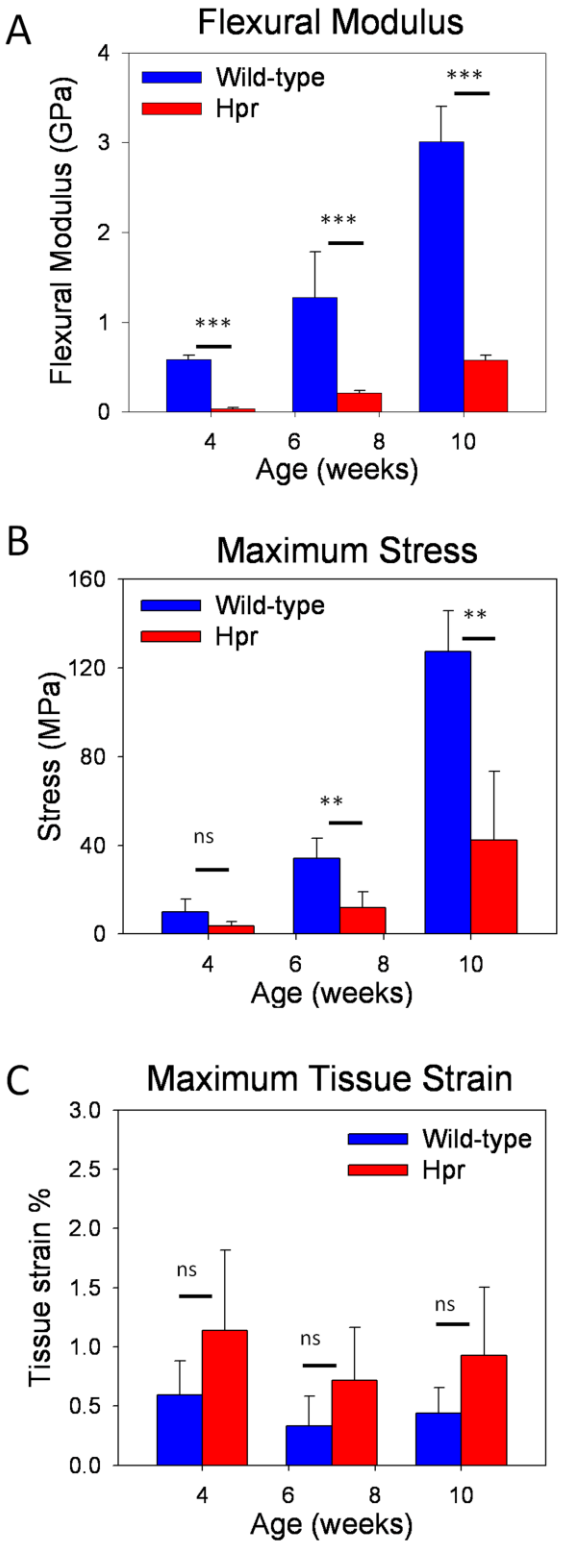

Figure 6.3: Macro mechanical testing (A, B, C) Average flexural modulus, maximum failure strain and bending stress plotted pairwise as a function of developmental age for wild-type

(blue) and Hpr (red Error bars are standard deviations. Student's t-tests were used to compare elastic moduli, maximum stress and maximum strain between wild-type and Hpr mice. Pair wise brackets denote statistical significance (*p<0.05, **p<0.01, ***p<0.001, ns = not significant).

To calculate effective fibril modulus, the stress is plotted versus fibril strain (measured from SAXS) for wild-type and Hpr for tensile and compression zones as shown in **Figure 6.4 (A-C)**. The combined plots for stress versus fibrillar strain in the region of elastic deformation in both wild-type and Hpr mice as a function of age revealed significant differences in the slope, which is denoted as the effective fibril modulus (σ/ε_F), as previously reported (85). The effective fibril modulus (averaged over all samples at a given age and genotype) was plotted as a function of age, genotype and loading zone (compressive versus tensile) of the bone specimen in **Figure 6.5**. In wild-type mice, the effective fibril modulus increased by similar amounts of 31.3 GPa (2.1 – 33.4 GPa) and 29.6 GPa (3.0 – 32.6 GPa) for tensile and compressive zones respectively over the period of 4 to 10 weeks. In contrast in Hpr mice over the same time period, the increment of effective fibril modulus was only 6.7 GPa (0.3 – 7.0 GPa) for the tensile zone and 8 GPa (0.5 - 8.5 GPa) for compressive zones. In addition, the effective fibril modulus in the compression zone was larger compared to the tension zone for both wild-type and Hpr mice at each developmental time point, although this difference was not significant ($p>0.05$).

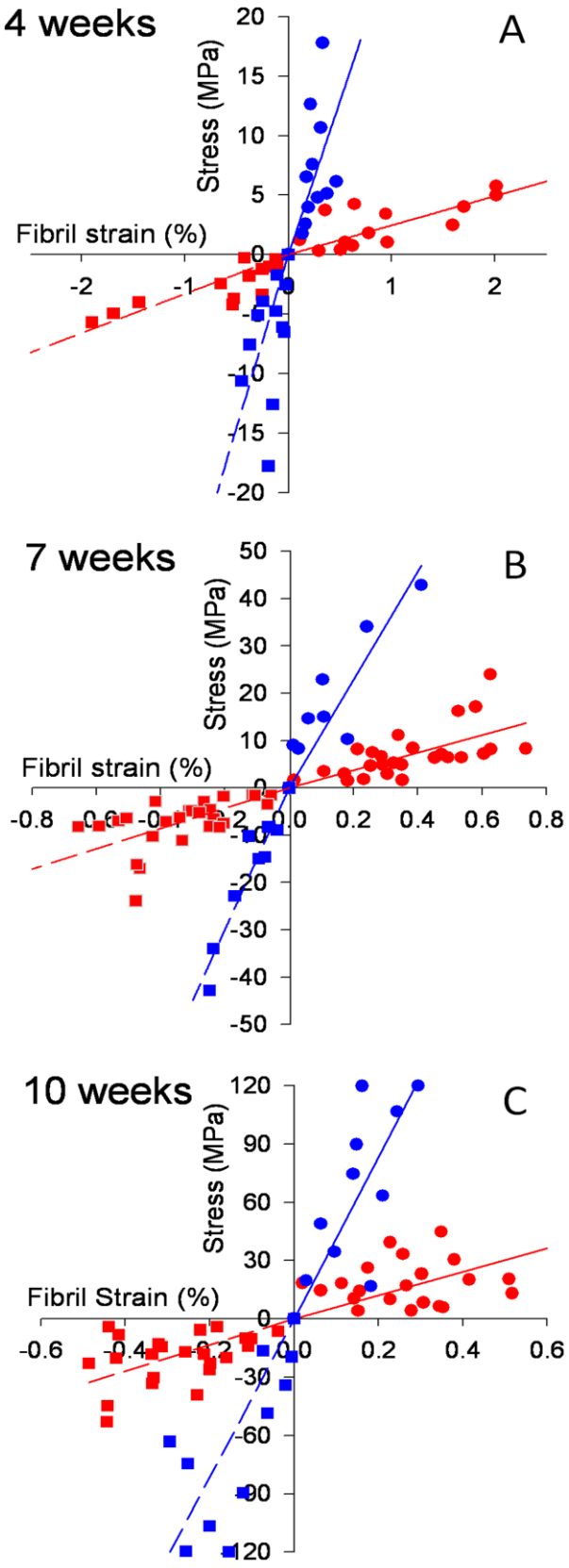
4 weeks
A
Stress (MPa)
Fibril strain (%)
7 weeks
B
Stress (MPa)
Fibril strain (%)
10 weeks
C
Stress (MPa)
Fibril Strain (%)

Figure 6.4: In situ nano-mechanical testing (A-C) Stress versus measured fibril strain at each age group for tensile (circles) and compression zones (squares) for wild-type (blue symbols) and Hpr (red symbols). The numbers of samples investigated at 4, 7, and 10 weeks were: 4, 3, and 4, respectively, for wild-type; and 4, 6, and 5, respectively, for Hpr. Lines (tension = solid and compression = dash) are average regression lines for wild-type (blue) and Hpr (red) multiple samples

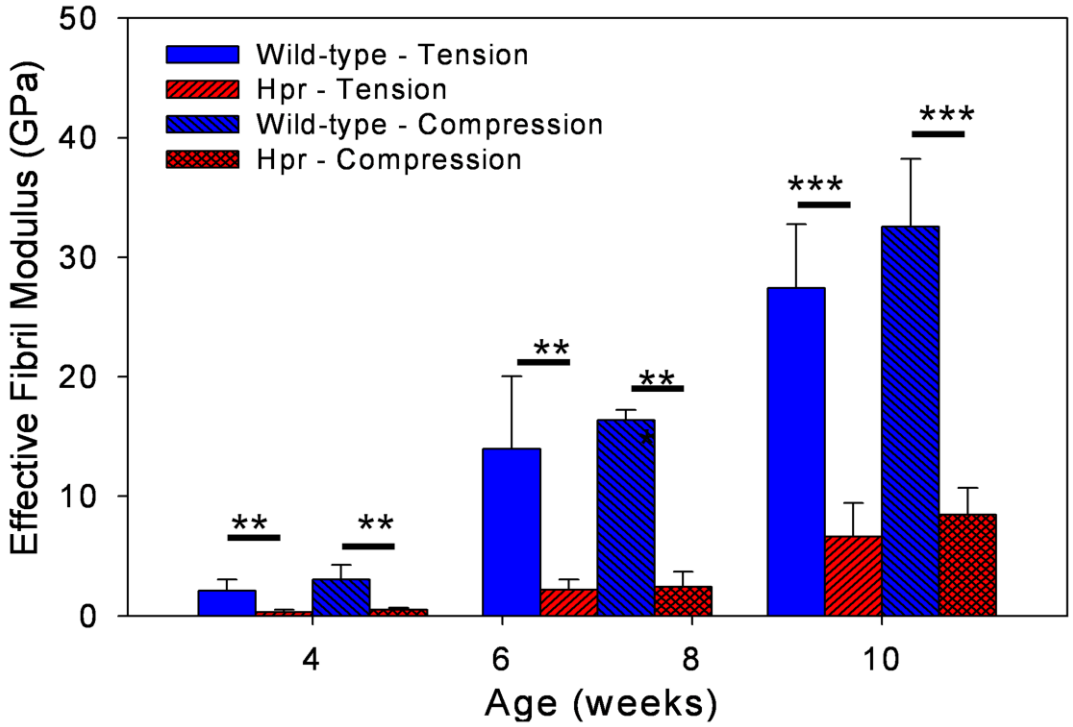

Figure 6.5: Average effective fibril modulus plotted as a function of age and loading zones for wild-type and Hpr (wild-type/tension = blue; wild-type/compression = blue filled with lines; Hpr/tension = red/ filled with lines; Hpr/compression zone = red/ filled with cross lines). Error bars are standard deviations. Student's t tests were used to compare elastic moduli, maximum stress and maximum strain between wild-type and Hpr mice. Pair wise brackets denote statistical significance (*p<0.05, **p<0.01, ***p<0.001, ns = not significant).

Furthermore, **Figure 6.6** shows that the maximum linear fibril strain for Hpr mice was larger compared to wild-type mice at every age for both the tensile and compressive zones with no significant difference**.** The percentage reduction in maximum fibril strain in the linear zone with age (over 4 to 10 weeks) was larger in Hpr mice (62 % tensile; 51 % compressive) compared to wild-type mice (47 % tensile; 36 % compressive) in both tensile and compressive loading zones. The average values of maximum linear fibril strain at the tissue yielding point in the compression zone was larger compared to the

tensile zone for the Hpr mice for 4 and 7 weeks, but the differences were not statistically significant at $p = 0.05$.

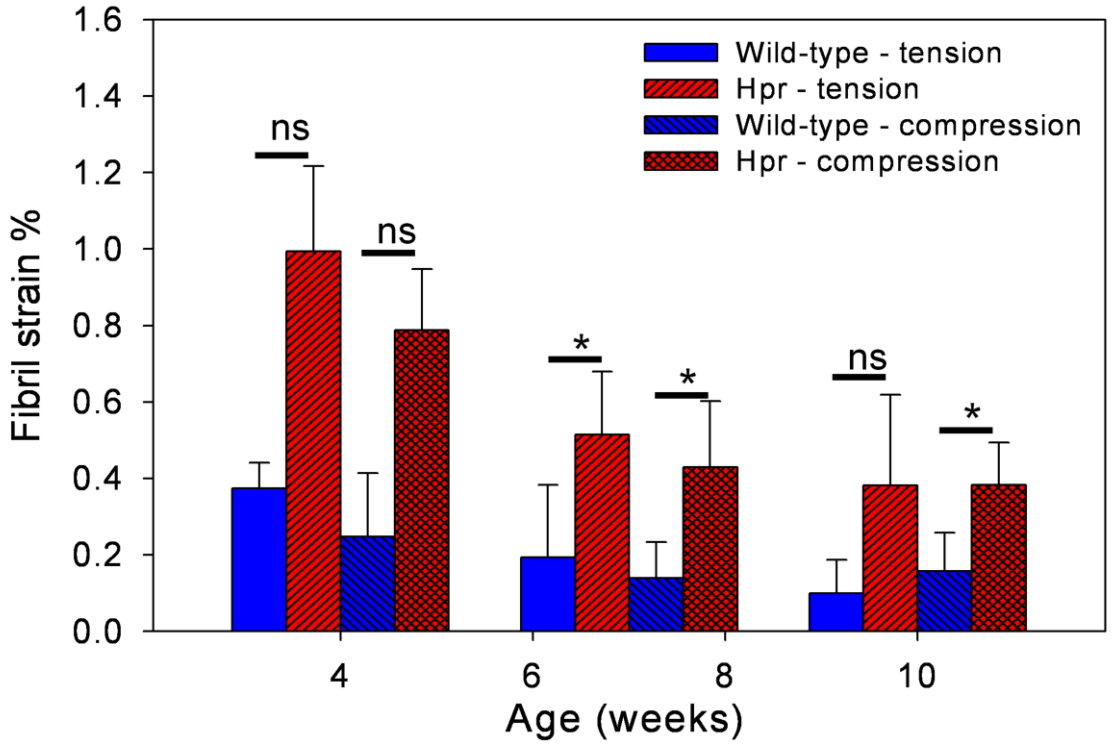

Figure 6.6: Average maximum fibrils strain at the tissue yielding point plotted as a function of age and loading zones for wild-type and Hpr (wild-type/tension = blue; wild-type/compression = blue filled with lines; Hpr/tension = red/ filled with lines; Hpr/compression zone = red/ filled with cross lines). Error bars are standard deviations. Student's t-tests were used to compare elastic moduli, maximum stress and maximum strain between wild-type and Hpr mice. Pair wise brackets denote statistical significance (*p<0.05, **p<0.01, ***p<0.001, ns = not significant).

The gradient $d\varepsilon_F/d\varepsilon_T$ was plotted against effective fibril modulus in **Figure 6.7**. The slopes of the linear regression of strain ratio gradient versus effective fibril modulus are clearly different for wild-type and Hpr. However, for both wild-type and Hpr mice, the change was not significant (*p>0.05)* with increasing effective fibril modulus. In Hpr mice, the gradient reduced by 0.45 (0.88 – 0.43) for an increment of ~7.32 (0.46 – 7.78) GPa in effective fibril modulus over the period of 4 to 10 weeks. In contrast in wild-type mice the gradient reduced by only 0.29 (0.71 – 0.42) for an increment of ~30.3 (2.7 - 33) GPa in effective fibril modulus over 4 to 10 weeks.

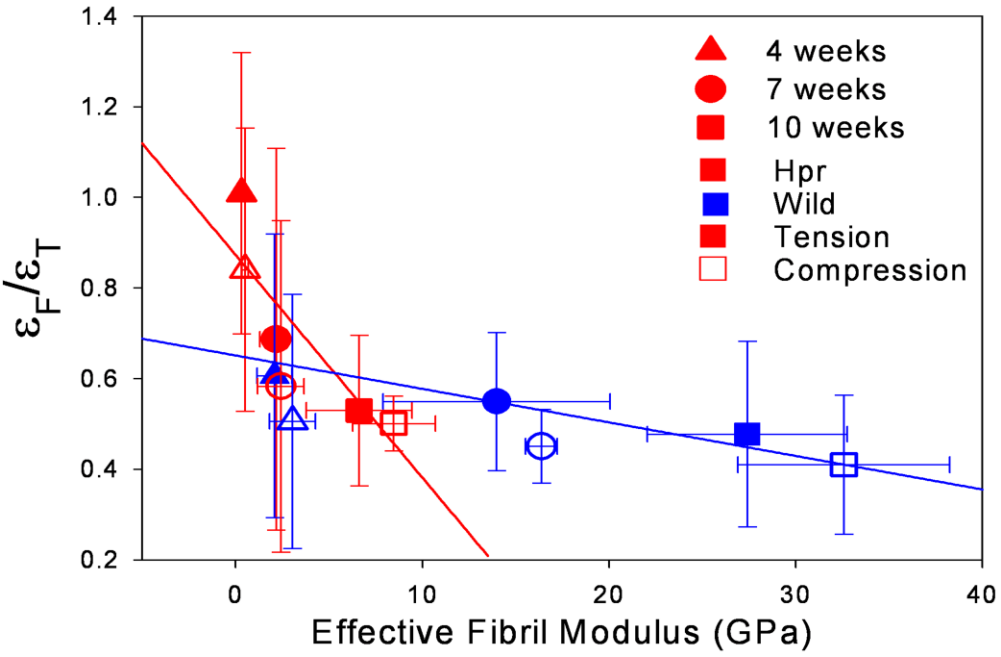

Figure 6.7: Fibril strain to tissue strain ratio ($\varepsilon_F/\varepsilon_T$) plotted as a function of effective fibril modulus (E_F) for wild-type (blue) and Hpr (red) for the tensile (filled symbols) and compressive modes (open symbols). Data plotted for all ages 4 (triangles), 7 (circles) and 10 (squares) weeks. Error bars are standard deviations. Lines (wild-type = solid and Hpr = dash) are regression lines.

To estimate possible differences in degree of fibrillar orientation in Hpr versus wild-type mice, the FWHM of the intensity distribution of the 3rd order collagen reflection was plotted as a function of genotype and all three ages (4, 7 and 10 weeks) in **Figure 6.8**. It was observed that there was no significant difference (*p>0.05)* in width between Hpr and wild-type at all ages. Furthermore, width did not change significantly (*p>0.05*) with development for both Hpr and wild-type mice. Mineral particle orientation was investigated separately for the Hpr and wild-type mice by determining the anisotropy of the SAXS pattern as described in (84, 233). The degree of mineral particle orientation (ρ) as a function of disease condition and developmental age increases significantly (*p<0.01)* with age for wild-type and Hpr mice (**Figure 6.9**). However, there was no significant *(p>0.05)* difference observed between Hpr and wild-type mice at any time point.

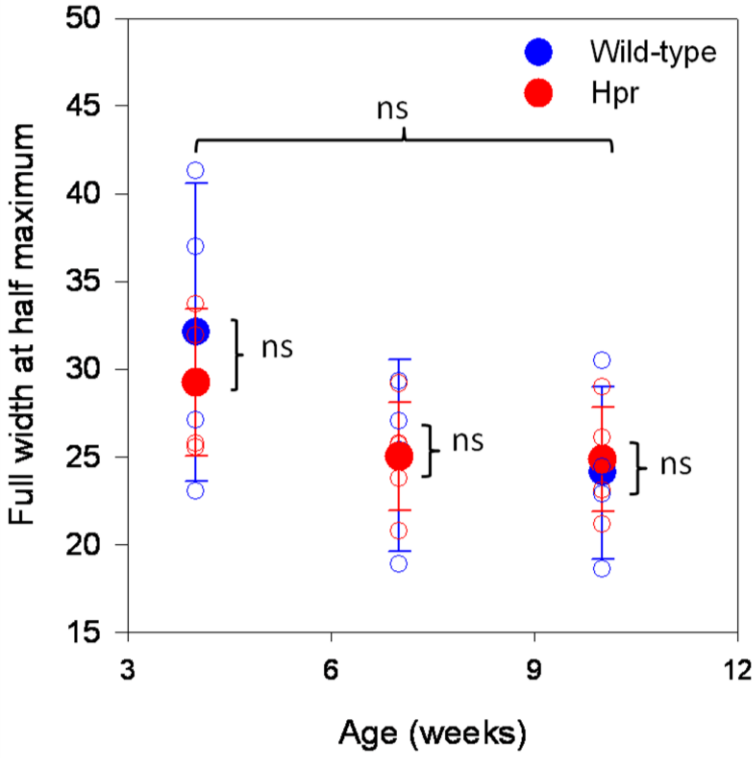

Figure 6.8: Degree of fibril orientation (refer Chapter 4 section 4.2.4) - Full width at half maximum of intensity distribution of the 3rd order fibril reflection and FWHM was plotted for wild-type (filled symbols) and Hpr (open symbols). Large symbols are average FWHM values and small symbols are individual data points. Error bars are standard deviations. Student t-tests were used to compare between wild-type and Hpr mice. One-way ANOVA tests were carried out at both wild-type and Hpr to study variation of FWHM with development. Pair-wise brackets denote statistical significance (*p<0.05, **p<0.01, ***p<0.001, ns: not significant).

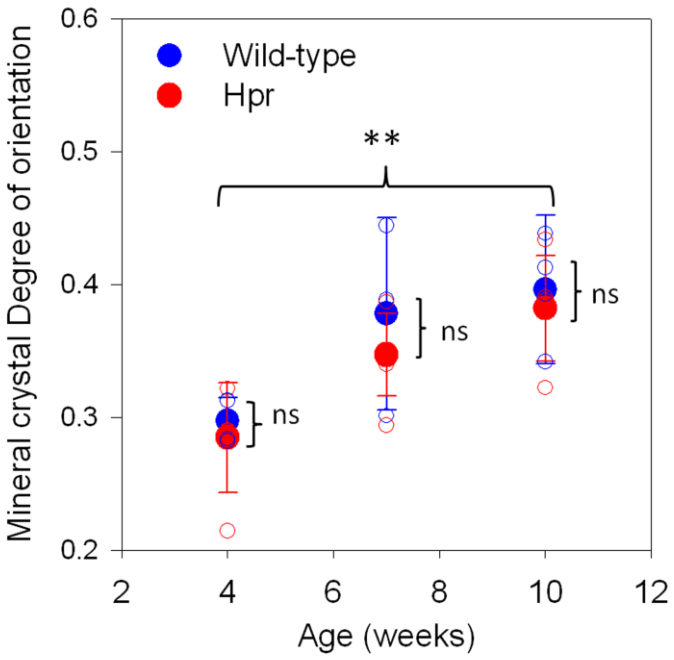

Figure 6.9: Mineral particle degree of orientation (ρ) (refer Chapter 2 section 2.2 and equation 2.8) was plotted for wild-type (filled symbols) and Hpr (open symbols). Large symbols are average ρ values and small symbols are individual data points. Error bars are standard deviations. Student t-tests were used to compare the degree of orientation between wild-type and Hpr mice. One-way ANOVA tests were carried out at both wild-type and Hpr to study variation of degree of orientation with development. Pair-wise brackets denote statistical significance (*p<0.05, **p<0.01, ***p<0.001, ns: not significant).

6.3.2 qBSE imaging

BSE images from humeral longitudinal cross-sections of the wild-type (**Figure 6.10A-C)** and Hpr (**Figure 10D-F)** mice revealed that the cortical microstructure of Hpr mice femora was markedly different to the wild-type mice cortical structure. BSE images of longitudinal cross-sections of Hpr mice showed a very large fraction of resorption cavities (15 – 30 %). In contrast, wild-type femoral bone was uniformly dense across the cortex (porosity = 5 – 10 %). In terms of the osteocyte lacunae distribution and orientation, a qualitative observation is that in Hpr mice, most notably at 10 weeks (**Figure 6.10F**), some of the roughly elliptical osteocytes are oriented perpendicular to the long axis of the bone (long white arrows in **Figure 6.10**) while in wild-type mice they are oriented mainly parallel to the long axis. It was also observed that osteocyte lacunae

in Hpr mice are less elongated than wild-type as well as being rounder in shape (most notably at 4 weeks, **Figure 6.10D**). In addition, the osteocyte network, as far as can be seen from 2D BSE images, appears to be more random in Hpr mice than in wild-type mice. Finally, the cortices in 4-week Hpr mice showed highly mineralised residual calcified cartilage (indicated at a few representative locations in **Figure 6.10D**) which was absent in wild-type cortices at the same age-point.

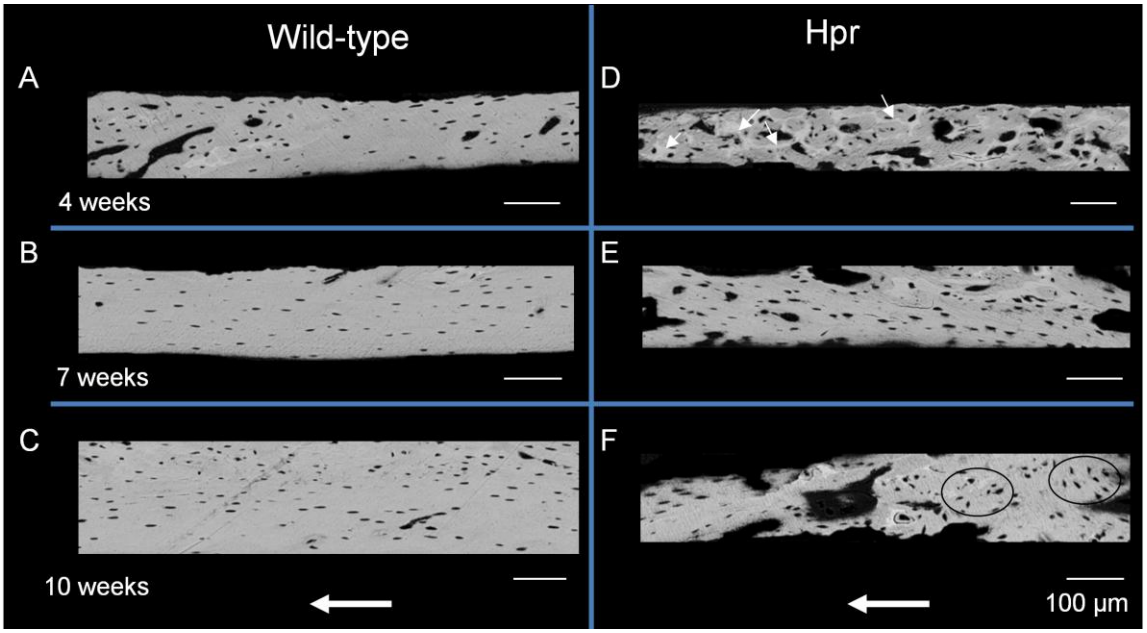

Figure 6.10: Backscattered scanning electron microscopy images collected from the longitudinal cross section of the humeral cortical bone of the wild-type (A-C) and Hpr mice (D-F) aged between 4 and 10 weeks. (n = 1 of each genotype at each time point). In (D), hypermineralised calcified cartilage is indicated by short white arrows at selected locations. The long horizontal arrows in (C) and (F) indicate the direction of the long axis of the bone.

In terms of a quantitative analysis of the BSE images, at 4 weeks, the BMDDs in wild-type and Hpr mice showed a peak at ~26 Ca wt. %, but the Hpr mice had a secondary shoulder (arrow) at ~35 Ca wt. % corresponding to the calcified cartilage noted above. By 7 weeks, the secondary shoulder has disappeared for Hpr mice, and peak position is approximately the same as in wild-type, although the distribution is wider. In both Hpr and wild-type a large increment in peak Ca concentration was observed from 4 to 7 weeks, but the change in width of the BMDD histogram was far less pronounced in Hpr

mice. Very little change in the BMDD is seen in the wild-type between 7 and 10 weeks, while the Hpr mice BMDD continues to shift to higher mineralisation (**Figure 6.11A**).

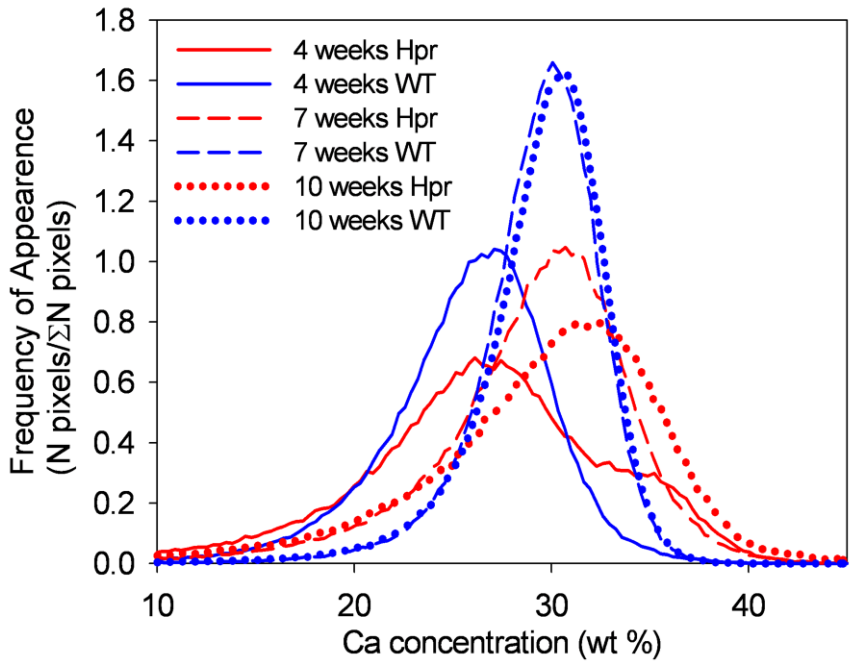

Figure 6.11: Bone mineralisation at the microscale: (A) Bone mineral density distributions (BMDD) were produced for each genotype (wild-type = blue lines; Hpr mice = red lines) and for each age points (4 weeks = solid lines; 7 weeks = dash lines; 10 weeks = dotted lines).

In terms of mean (as distinguished from peak) calcium concentrations, the average Ca_{mean} increased at a similar rate in wild-type and Hpr mice between 4 to 10 weeks (**Figure 6.12A**). However, at each age point Ca_{mean} is clearly lower in Hpr mice compared to the wild-type mice. Ca_{FWHM} in wild-type mice is clearly reduced by ~32 % from 4 weeks to 10 weeks (**Figure 6.12B**). In contrast, in Hpr mice, the reduction in Ca_{FWHM} with age is not pronounced, indicating that the heterogeneity of mineralisation remain constant at even at maturity.

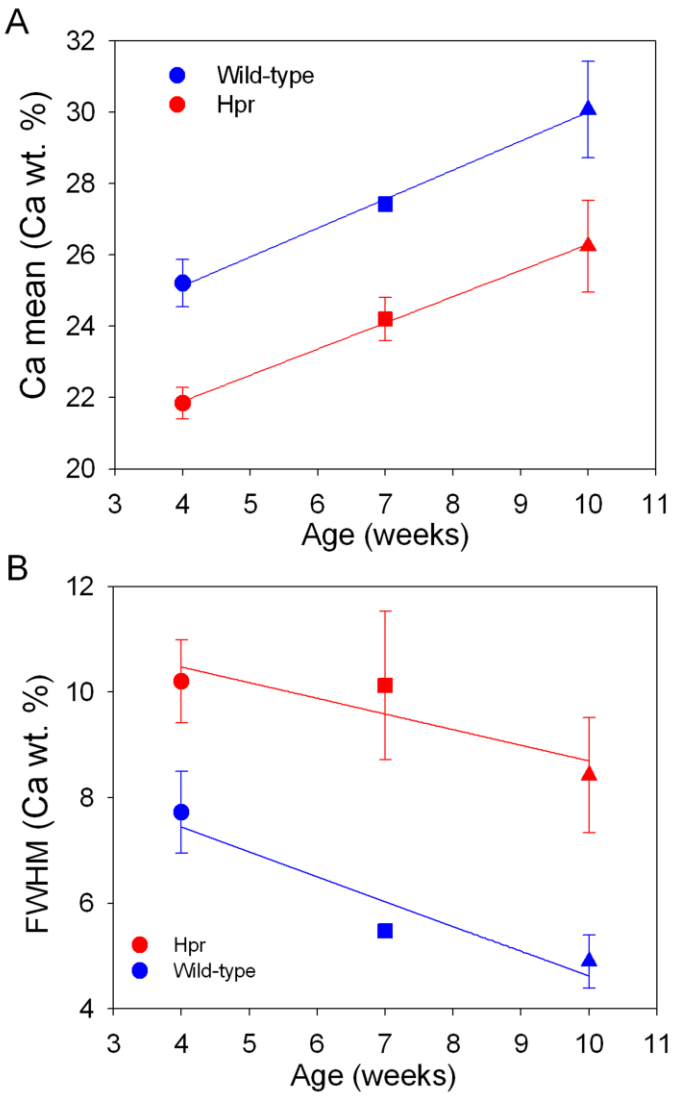

Figure 6.12: (A, B) Mean Ca% and full width at half maximum (FWHM = distribution in local variation of Calcium content) plotted as a function of age from 4 week to 10 weeks and genotype (wild-type = blue; Hpr = red). Solid lines are regression lines Errors bars are standard deviations.

6.4 Discussion

In this chapter, cantilever bending combined with a microfocus synchrotron X-ray imaging setup and a model for a form of hereditary rickets was used to obtain new results on bone material-level structural deformation mechanisms mediating increased deformability and reduced stiffness in both compression and tension. Currently, the understanding of altered macromechanical properties of rachitic bone, such as reduced

stiffness and higher deformation (79), is attributed to delayed primary and secondary mineralisation, revealed by the presence of wide bands of osteoid (324, 325) at the growing surface. In this study simultaneous *in situ* measurements of compressive and tensile deformation at the fibrillar level in Hpr mice was performed to address the following questions as starting points: (i) whether similar mechanisms operate during bending: and (ii) whether the (spatially separated) regions of tensile- and compressive stresses developed during bending of bone show distinct nanomechanical deformation mechanisms.

Regarding the first point, using microbeam SAXS (μSAXS) to resolve the ultrastructural response in the microscale zones of compression and tension (~ 200 μm each) in cantilever bending, changes in fibril strains were measured in each zone as a function of applied load. Consistent with previous studies at the tissue level (79), macroscale mechanical data showed that the flexural modulus (**Figure 6.2B**) and maximum bending stress (**Figure 6.2C**) increases with age in both wild-type and rickets, but maximum stress of Hpr was less than the normal mice. The greater failure strain in Hpr compared to wild-type mouse bone is consistent with previously reported observations from Hyp mice (79). However, there was no significant difference in failure strain observed with development, which has not been reported previously.

Figure 6.3A, B and C demonstrates that the effective fibril modulus (σ/ε_F) increased consistently with development in the tensile and compression zones. Such changes are expected, as the increase of the stiff mineral phase fraction with increasing development/mineralisation time would reduce the fibrillar deformability (14, 85, 326, 327). However, in the bones of Hpr mice, the effective fibril modulus is significantly lower compared to the wild-type mice, which may be explained by incompletely fused mineral as seen from SEM images in the rachitic mineralised fibrils (328). Results in **Chapter 5** on tensile deformation of rachitic bone showed that the differences between rachitic and wild-type bone in pure-tensile loading could be quantitatively explained by such a mechanism of incomplete extrafibrillar mineralisation (85, 328). The foregoing picture of a reduced rate of mineral reinforcement in Hpr bone and its mechanistic consequences at the nanoscale is supported by the observation that the increment of

effective fibril modulus from 4 weeks to 10 weeks was significantly lower in Hpr mice compared to wild-type mice.

The estimation of the effective fibril modulus via the relation: macroscopic stress/fibril strain requires some comment. In staggered nanomechanical models with bone-like fibrillar geometries (14, 329-332) , the stress is not uniform along the fibril. Furthermore, the stress on the fibril may not be the macroscopic stress, depending on factors such as the degree of extrafibrillar mineralisation. In this study, for simplicity, it was implicitly approximated that the tissue by a staggered model arrangement as described, for instance, in (14) where stress increases linearly from the ends of the fibril to the centre, and also considering the extrafibrillar space to be much smaller than the intrafibrillar space. In such a case, the effective modulus as defined above is the actual fibrillar elastic modulus. However, such approximations are admittedly simplistic given the complexity of the investigated bone structures at the micro- and mesostructural levels (**Figure 6.10D-F**). However, the effective modulus was defined, to analyse differences between healthy and diseased tissue and with development is informative and justified, analogous to the well-established use of nanoindentation moduli in bone research for discriminating between micro- and nanomechanical properties of healthy and diseased tissue (333). However, to highlight the above point more clearly, the experimentally measured effective fibril moduli were compared with the predictions of selected micromechanical composite models used in the literature. The models include the Voigt and Reuss models (112) and the Ji and Gao staggered model (330), and the comparison is shown in **Figure 6.13**.

Voigt composite model

$$E_f = E_m \Phi_m + E_c (1 - \Phi_m)$$ Equation 6.1

Reuss composite model

$$\frac{1}{E_f} = \frac{1}{E_m} \Phi_m + \frac{1}{E_c} (1 - \Phi_m)$$ Equation 6.2

Ji-Gao composite model

$$\frac{1}{E} = \frac{4(1-\Phi_m)}{\mu_p \Phi_m{}^2 \rho^2} + \frac{1}{\Phi_m E_m}$$

Equation 6.3

where E_f is the fibril modulus, E_m and E_c are mineral modulus (100 GPa) (14) and collagen modulus (2.5 GPa) (334) respectively, Φ_m and $\Phi_c = 1-\Phi_m$ are mineral and collagen volume fractions respectively, μ_p is the shear modulus of collagen (1 GPa, $\lambda * E_f = \mu_p$, λ is a numerical factor 0.4 (99)) and ρ is the aspect ratio of mineral particles (ρ = 40) (330). To estimate the mineral volume fraction Φ, the mean Ca wt. % measured in the BMDDs obtained via qBSE (**Figure 6.12A**) was used as described in (256) and in **Chapter 2** section 2.4 (**Equation 2.9**).

It is seen that the experimental effective fibril moduli fall between the Reuss model predictions (lower end) and the Ji and Gao,2004 staggered model predictions (upper end). Clearly, to obtain better agreement with such models as well as more recent ones (329, 331, 332) more accurate modeling needs to be combined with experimental results. These would include more refined corrections for porosity, consideration of lamellar architecture (335), intra- and extrafibrillar mineralisation and whether estimation of mineral volume fraction at the nanoscale from microscale qBSE measurements is appropriate.

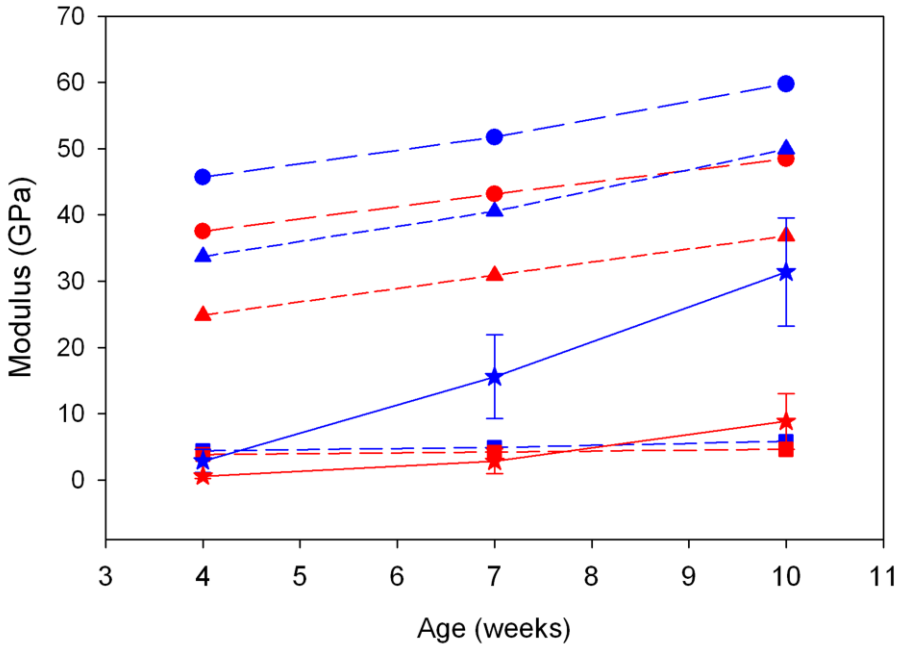

Figure 6.13: Comparison of the experimentally measured effective fibril moduli (stars with solid lines) for wild-type (filled symbols) and Hpr (open symbols) with the predictions of selected micromechanical composite models used in the literature. The models include the Voigt (circles with long dash lines) and Reuss (squares with medium dash lines) models (112) and the Ji and Gao staggered model (triangles with short dash lines) (330).

Figure 6.6 shows that Hpr fibrils are more extensible than wild-type mice at equivalent ages, which can be explained by the lowered extrafibrillar mineralisation levels leading to a reduction in the mineral "straight-jacketing" effect (1) and increased flexibility of the bone matrix. Similar to effective fibril modulus, maximum fibril strain at the compressive and tensile zone did not change significantly. As the major contribution to the intrinsic toughness for the bone is obtained from the deformation of MCFs, interpretation of these nanomechanical results is important for understanding of the effects of hypophosphataemic rickets in altering the resistance of the bone to deform and fracture. When the bending load is applied to the bone sample in the elastic regime, load is transmitted to the fibrillar level and transferred to the mineral clusters as tension and compression via shearing of the collagen matrix (14, 82, 205). In Hpr mice, due to the patchy non-fused mineralisation as shown by the previous studies (85, 328), most of the loads are transmitted through more ductile collagen phase which enhances the bone deformability of rachitic bone. In contrast, in healthy bone loads are transmitted through

the stiffer component, the completely fused mineral phase, which reduces the deformability.

The link between localised tissue-level and ultrastructural fibrillar deformation, shown via fibril to tissue strain ratio in **Figure 6.7**, leads to some interesting observations. Specifically, in wild-type mice, fibril to tissue strain ratio $\varepsilon_F/\varepsilon_T$ was ~0.4 to 0.5 - consistent with previous in-situ studies on bovine fibrolamellar bone (14, 82) - and did not change significantly with age. It is notable that this ratio of ~0.5 has now been observed in two species – bovine and mouse – which differ greatly in size, indicating some degree of commonality in the mineralised fibril motif between species. It is possible that the increasingly heterogeneous and porous microstructure in the Hpr case (**Figure 6.10**) contributes to the increased scatter in $\varepsilon_F/\varepsilon_T$. This suggestion is supported by the observation that the parameters at the mineralised fibril level – fibril orientation distribution (**Figure 6.8**) and the mineral particle (**Figure 6.9**) orientation – are not significantly different between Hpr and wild-type, leading to consider the porous microstructure as the remaining factor. A second factor may be related to presence of calcified cartilage in the tissue. It was observed in a recent study that micrometer sized hypomineralised islands were present in the mid-femoral cortical bone in rats at 4 months of age (336). Toluidine blue staining and immuno-labelling against collagen type II confirmed that these islands are calcified cartilage, which were identified to have high mineralisation using qBSE. These islands are remnants of endochondral bone formation due to the lack of remodelling in rats, which may alter the mechanical properties of bone due to the modulus mismatch (336). BSE images (**Figure 6.10**) of longitudinal cross sections of mice cortex also shows highly mineralised calcified cartilage islands. Since these structures are most abundant in Hpr mice, they may have mechanistic influences on the fibril to tissue strain ratio which would benefit from further study. The above evidence clearly shows that difference in nanomechanical behaviour observed in mouse and bovine bone (82) is most likely due to the micro structural differences.

Concerning differences between compression and tension, it was found that compressive moduli at the fibrillar level do not appear to be significantly higher than the tensile

moduli, even though in this case the experimental error in each case is relatively small. By measuring the tensile and compressive moduli on the same sample during cantilever bending testing, inter-sample variations are eliminated. The above result is to be contrasted with tissue level and material level studies (320), where Barak and co-workers found a small, but significant, increase in tissue-level modulus in tension relative to compression in equine third metacarpal bone using electron speckle pattern interferometry. However, when comparing fibril-moduli results to the tissue-level findings of these researchers, two confounding factors inherent in the current study must be noted (i) the effects of material inhomogeneity (as seen in **Figure 6.10**, especially in the diseased (rachitic) condition) and (ii) the displacement of the neutral axis due to possible intrinsic differences in tension and compression (320). As discussed in (320), if bone tissue has inherently different tensile moduli compared to compressive, then the neutral axis is no longer in the middle of the specimen but is displaced slightly into the region of stiffer tissue. The calculation of fibril moduli assumed a neutral axis in the middle of the specimen, and future fibril-level studies need to implement the 180°-flip protocol used in (320) at the tissue-level. Finally, the tissue type measured in (320) was secondary osteonal bone, which is not found in mouse bone (1, 336). However, another study (337) reported that yield stress, failure stress and Young's modulus of human mid diaphysis were lower with tensile mode compared to compressive mode. Several other studies have also claimed that Young's moduli of cortical bone are not different between tensile and compressive zones (338, 339). These discrepancies in macro-scale tests may be due to the hierarchical structure of bone, and current results show that, to a first approximation, the mechanical behaviour at the fibrillar level is not significantly different in tension and compression.

6.5 Conclusion

Results presented in this chapter are the first to directly quantify fibrillar-level compressive and bending deformation in a biochemically well-defined disease model of hypophosphatemic rickets. It can be concluded that the fibrillar nanoscale deformation mechanism identified previously in uniaxial tensile loading (**Chapter 5**) operates during physiologically relevant compressive loading as well. This result shows the clinical

relevance of this model in understanding the causes of increased bone deformation in a form of rickets. These results are also interesting in that while at the macroscale, compressive stiffness and strength is usually higher than tension; however it was shown in this study that this difference is not reflected in a differential response between tensile- and compressively-loaded zones in bone tissue at the level of the MCFs.

Chapter 7

Disruption of Mineral Orientation in Rachitic Mice with Development

The contents of this chapter have been published in

A Karunaratne, J Hiller, CT Esapa, NJ Terrill, AH Barber, RV Thakker, HS Gupta *Hypophosphatemic rickets is associated with disruption of muscle stress-mediated mineral orientation at the nanoscale in the flat scapular bones of rachitic mice with development. 2012*, Bone. 2012 51(3):553-62

7 Disruption of Mineral Orientation in Rachitic Mice with Development

7.1 Synopsis

Local, *in vivo* physiological forces generated by attached muscles and tendons are widely believed to play an important role in the formation and maturation of bone tissue. However, the majority of experimental evidence on the link between forces (generated via tendons and muscles) and mineralised nanostructure has focused on load-bearing long bones such as femur or ulna (70, 235, 237, 307), which form by endochondral ossification and are loaded under an uniaxial muscle-force system oriented along the bone long axis (although significant torsional forces are present at the extremities, for example at the femoral head). Clinical disruptions of mineralisation, such as hypophosphatasia (235), induce significant changes in bone nanostructure of long bones, with a graded decrease in mineral particle orientation along the axis to a more random distribution. In contrast, flat bones such as scapulae, ilium or calvariae develop by intramembranous ossification, in which mesenchymal cells aggregate, differentiate into osteoblasts and begin to produce bone extracellular matrix. The spatial distribution of muscle forces across these flat bones is often complex and multiaxial (340) and the impact of these forces on bone formation is poorly understood. This raises the question: what is the effect of disease-induced disruptions of the mineralisation process on the spatio-temporal development of mineralised bone nanostructure in the multi-axial force regime of flat bones? It was hypothesized that these disease-induced alterations to bone mineral formation and mineralisation patterns may have significant biomechanical consequences for the propensity of flat bones to fracture, as their material properties depend sensitively on both the individual nanoscale properties and microscale spatial gradients in the mineralised matrix (341-343).

As discussed in **Chapters 2, 5 and 6**, currently used clinical techniques provide limited or no information on the nanostructural components of bone, as their spatial resolution is limited to the scale of a few microns. SAXS, on the other hand, provides information on the size, orientation and shape of mineral platelets (~ 3-5 nm thick in bone (231) and on

the collagen fibril (50-200 nm diameter) (311) orientation. Scanning SAXS (sSAXS), where a micron-scale X-ray beam provides a composite map of SAXS images, has been used to analyse the micro- and nanoscale heterogeneities in bone tissue by several research groups (70, 231, 235-237) as reviewed in **Chapter 2**. These studies (especially (235)) showed that the surrounding mechanical forces are crucial in controlling nanostructural parameters in long bones, which are formed by endochondral ossification. However, relatively little information remains on equivalent effects in bones formed by intramembranous ossification, including flat bones such as scapulae.

As prototypical disease conditions where these effects may be systematically investigated, rickets and osteomalacia, which are bone-disorders of decreased mineralisation due to phosphorus deficiency (181), are well suited as model systems. This impaired mineralisation clearly alters the bone material quality and the functional biomechanics of the tissue at micro (79) and nano level (85) as shown in the previous **Chapters 5 and 6**. Rickets is hence a good model system to study the interaction between alteration of local bone matrix quality in pathological conditions with *in-vivo* force-distributions and tissue growth. This study, investigates the effects of rachitic disease conditions on the mineralised nanostructure of flat shoulder bones (scapulae) from this mouse model (Hpr), in order to understand the association between muscle force disruptions and alterations in mineral particle alignment across the whole bone organ, using synchrotron scanning X-ray nanoimaging methods.

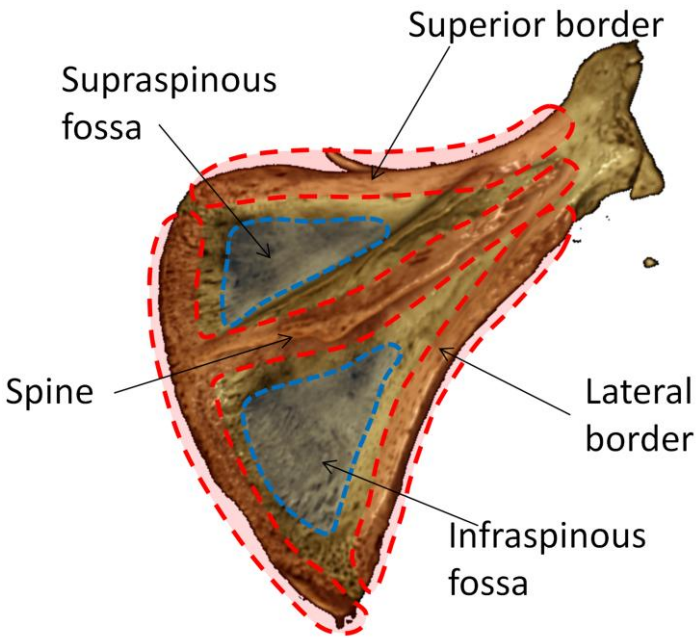

Figure 7.1: Mouse scapula (microCT rendered image), showing the anatomical regions and variability between regions of high (red transparent areas) and low (blue transparent areas) muscle force.

By way of introduction, the scapula (shoulder bone) is a large triangular flat bone which has five thick bony ridges (globoid, scapular spine, medial and lateral border and coracoids process) and two hard flat bony structures, denoted as infraspinous fossa and supraspinous fossa (340) (**Figure 7.1**). The scapula is subject to a number of muscle, ligament and joint reaction forces during movement, and the location, magnitude and direction of these forces differ extensively between tissue regions like the lateral border (bony ridge) and infraspinous fossa (flat bone) in the same scapula (340). For example Teres Minor and Major muscle groups attached to the lateral border and Infraspinatus is attached to the infraspinous fossa. Indeed, the force-variation at different muscle insertion points can be very large, with a spatially variable stress distribution ranging from 0.05 MPa at infraspinous fossa versus 60 MPa at lateral border, estimated using finite element modelling at the macroscale (340). In contrast to such macro-scale mechanical studies, possible nanostructural modulations of the bone-matrix with age (due to such muscle-mediated stress variations) have not been investigated yet; neither in the scapula specifically nor in intramembrously ossified flat bones more generally. The aim of this chapter is to bridge the gap, using synchrotron X-ray scattering with a wide

beam (200 μm), in order to rapidly and quantitatively characterise nanostructural parameters such as alignment.

7.2 Materials and Methods

7.2.1 Animals

An ENU induced mouse model for XLHR – Hpr (see full details in **Chapter 2** section 2.6.1) was used. Male wild-type and mutant mice from 4 different ages (1, 4, 7 and 10 weeks) were studied.

7.2.2 Sample preparation for sSAXS

Scapulae were dissected from 1, 4, 7 and 10 week old Hpr and wild-type mice and prepared for sSAXS as explained in **Chapter 4,** section 4.2.5. For the sSAXS measurements of specimens, 3.4 × 3.4 mm^2 areas were selected, which cover ~ 75 % of the whole scapula.

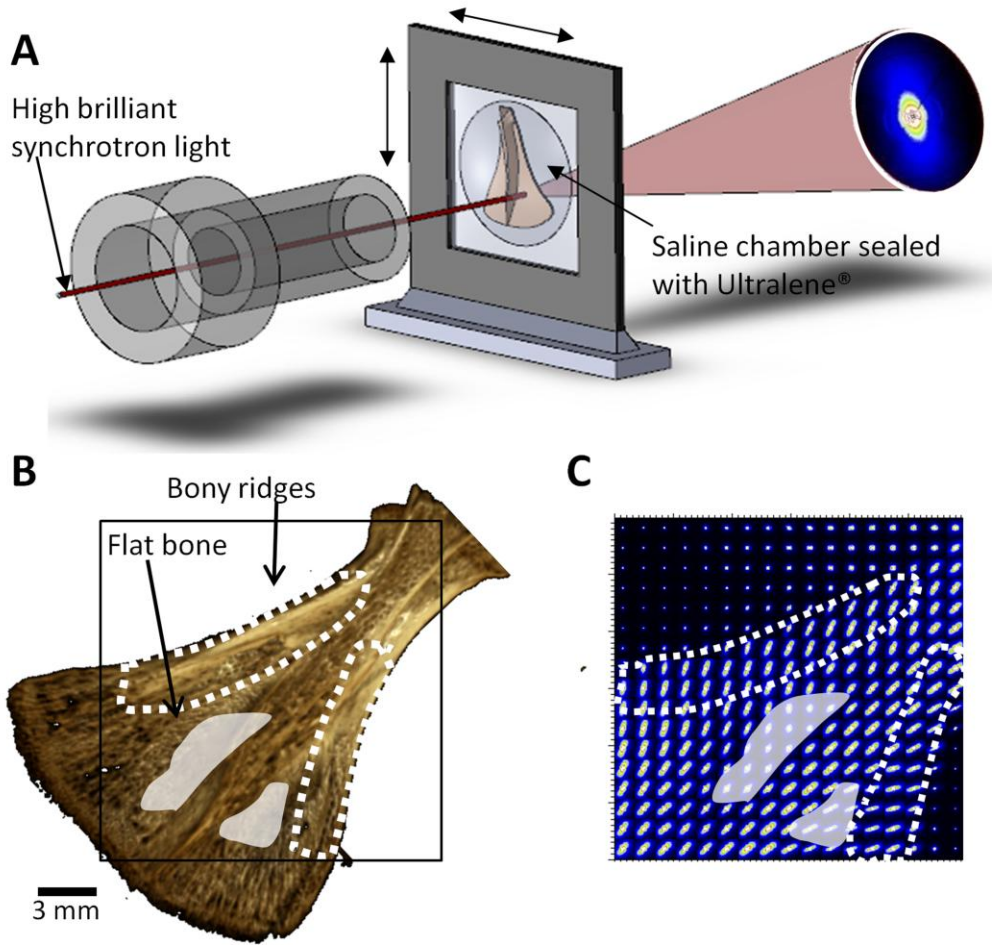

Figure 7.2: Scanning synchrotron SAXS on mouse scapula (A) Schematic of scapula mounted in a saline sample chamber sealed by Ultralene® foils. Black (colour online) solid line shows the incident X-ray beam (~200 µm radius). A representative SAXS image is shown on the right. (B) Three dimensional rendered micro-CT image of scapula from a 4 week-old male wild-typemouse. Bony ridges and flat bony areas denoted by dotted lines and shades light gray patches respectively. (C) A composite map of SAXS images obtained by scanning across the scapula bone shown in (B)

7.2.3 sSAXS of scapulae

The sealed sample chambers containing the mice scapulae (1 specimen from each age) from a range of ages (1 – 10 weeks postnatal) and diseased or wild-type conditions were mounted on a 2-axis motorized linear stage system. A schematic of the setup is shown in **Figure 7.2A**. SAXS patterns of scapulae were collected by translating the stage in X and Y directions with a step size of 200µm in both vertical and horizontal directions. The large step size was chosen in order to cover the entire scapular areal dimensions.

The lateral border and the infraspinous fossa, where high and low muscle forces act, respectively, are indicated in **Figure 7.2B**.The nanostructural parameters, including the mineral particle predominant orientation (χ) and the degree of orientation (ρ) in the scapula bone, were determined by analyzing each radially averaged SAXS profile (refer to **Chapter 2** section 2.2) from wild-type and Hpr mice at different ages (1, 4, 7 and 10 weeks).

7.2.4 X-ray microtomography

MicroCT was used to obtain tomograms and radiographs to calculate the volumetric mineral concentration of scapula bone. Three scapula samples at each time point and disease condition (24 scapulae) were scanned with MuCat scanner and the tomograms were used quantitatively to assess the degree of mineralisation (see **Chapter 4 Equation 4.7**) in the lateral border and the infraspinous fossa with the development. Volume-rendered images (**Figure 7.2B**) were also produced to obtain qualitative images of the surface structure. The degree of mineralisation histograms were produced for selected regions of interest (ROIs) in the lateral border and infraspinous fossa. Finally, weighted average mineral concentrations were determined at the lateral border and infraspinous fossa using these histograms and plotted as a function of development and genotype.

7.2.5 Statistical analysis

To compare SAXS parameters for different ages at the same anatomical region, ANOVA single factor tests were performed. For example, to compare the change of SAXS parameters at the lateral border region of the tissue with development (from 1 week to 10 weeks), a single factor ANOVA test was carried out. Student t-test was performed between two different ages (e.g. 1 and 4 weeks) at an anatomical region. Excel 2007 (Microsoft Office 2007) was used for the ANOVA and Student t-tests.

7.3 Results

A representative composite map (**Figure 7.2C**) revealed variability in 2D SAXS patterns obtained from the different regions of the scapula, specifically between the infraspinous fossa (shaded) and the lateral border (dotted) regions. SAXS pattern obtained from the lateral border (**Figure 7.3**; dotted region) show a more elongated ellipsoidal intensity

distribution (**Figure 7.3** red square inset) compared to the SAXS patterns (**Figure 7.3** red circle inset) taken from the flat bony region (white shaded area). This ellipsoidal intensity distribution is due to diffuse scattering from plate-like mineral crystallites in bone (42), as described in **Chapter 2 Figure 2.6**. Plate-like mineral crystals with a high degree of parallelism generate an anisotropic SAXS pattern whose long axis (in reciprocal space) is perpendicular to the long axis of the crystallite in real space. Conversely, randomly oriented mineral crystals result in an isotropic SAXS pattern.

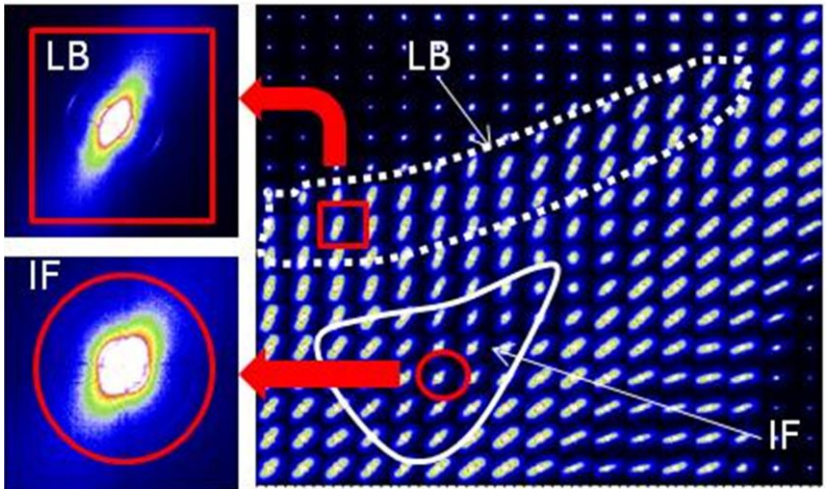

Figure 7.3: The variability of SAXS patterns (qualitatively) between regions of high (dotted lines) and low (solid lines) muscle force.

Significant differences in the degree of anisotropy of the SAXS patterns was observed between bony ridges and flat bone regions within the same scapula, indicating variation in degree of alignment of the mineral crystallites between these anatomical sites. In order to quantify these differences, the predominant orientation (crystal angle (ψ)) and degree of orientation (ρ), (**Chapter 2, Figure 2.7**) were obtained by azimuthal integration of the individual 2D SAXS images (**Figure 7.3** insets).

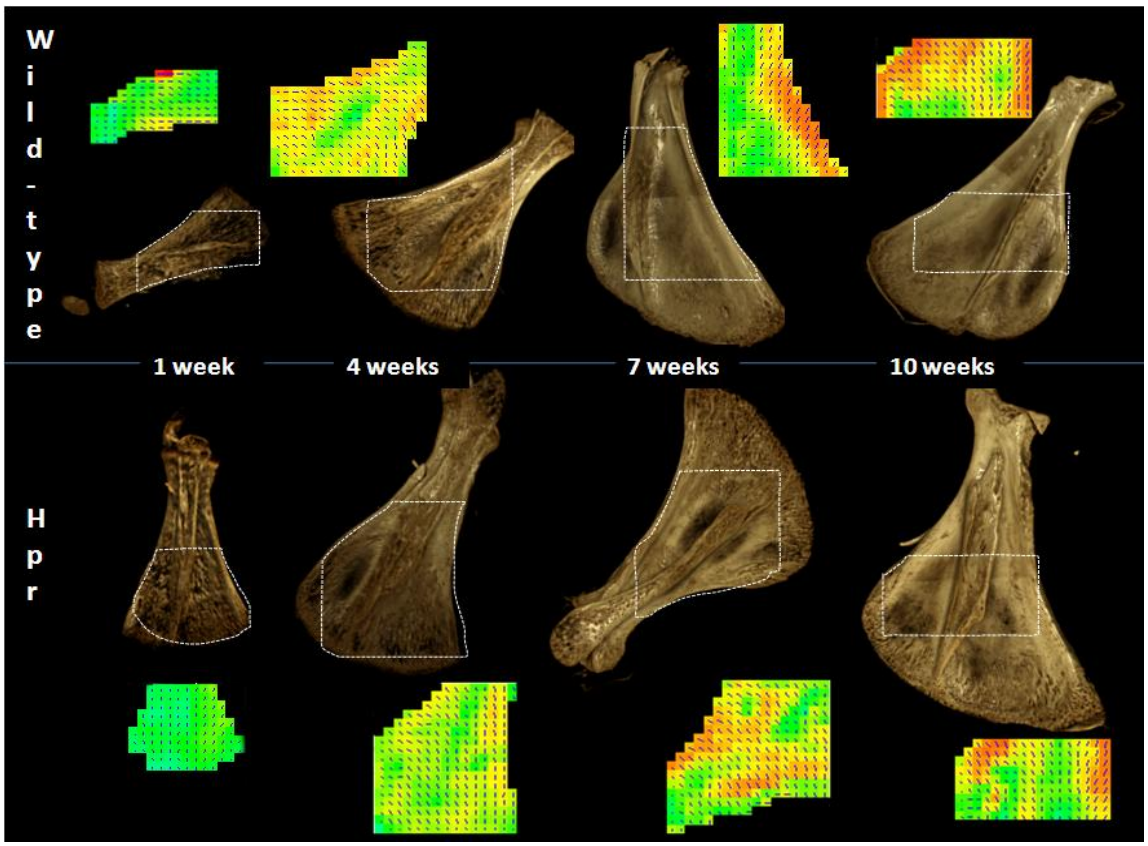

Figure 7.4: Abnormal development in Hpr mice scapula: Plots (top row - left to right) show the 3D rendered image and their 2D composite maps combining predominant orientation (direction of the lines) and degree (red = high degree of alignment, green = low degree of alignment) of mineral nanoparticle orientation in normal mice. Plots (bottom row left to right) show the same for Hpr mice.

Considering the 3-dimensional rendered images (derived from microCT measurements) of wild-type and Hpr mice (**Figure 7.4** top and bottom row, respectively) it was qualitatively observed that the surface porosity decreases with age (1 week to 10 weeks in **Figure 7.4**) in both cases. However, qualitatively, this reduction is less pronounced in Hpr condition. To compare these microstructural differences with the mineral nanostructure at the same point, the direction χ and degree of orientation ρ were plotted in a spatially resolved manner by scanning SAXS (**Figure 7.4**) on the selected areas represented by the dashed polygonal sectors. The resultant 2D maps are shown in **Figure 7.4** adjacent to the rendered images, in the form of colour plots with inset lines at each grid point. The direction of the bars indicates the mineral crystallite orientation, and the degree of orientation is indicated by the colour intensity of the underlying pixel (red

indicating higher degree of orientation). As can be seen by comparing the mean colour intensity level looking from left to right (increasing age), the mean degree of orientation increases with age. Further, in the wild-type mice, the degree of orientation increases sharply at the lateral border of the scapula. Within the Hpr mice scapulae, in contrast, the degree of orientation does not increase to the same extent in either lateral border or infraspinous fossa regions. These observations will now be quantified more precisely in the following subsection.

7.3.1 Spatial variation of average direction of mineral nanocrystallites

The direction (ψ) (**Figure 7.5**) of the predominant orientation of the mineral crystals was plotted with respect to the lateral border and infraspinous fossa of individual scapulae for 2 different anatomical regions in the same scapula. The lateral border (bony ridge; **Figure 7.5A** black box) and the infraspinous fossa (flat bone; **Figure 7.5A** white box) in the same scapula were compared, to illustrate the impact of different muscle forces on direction of mineral particle orientation. To ensure comparability, the same anatomical regions were selected in all the different ages and for both wild-type and Hpr mice. In order to compare the angle of the mineral crystals between scapulae of different ages, the direction of the lateral border (**Figure 7.5 A and B)** black dashed line) of each scapula was used as a *reference line*. **Figure 7.5 C and D** shows the mineral particle angle with respect to the lateral border as a function of age for both wild-type (**Figure 7.5C)** and Hpr mice (**Figure 7.5D**) scapula.

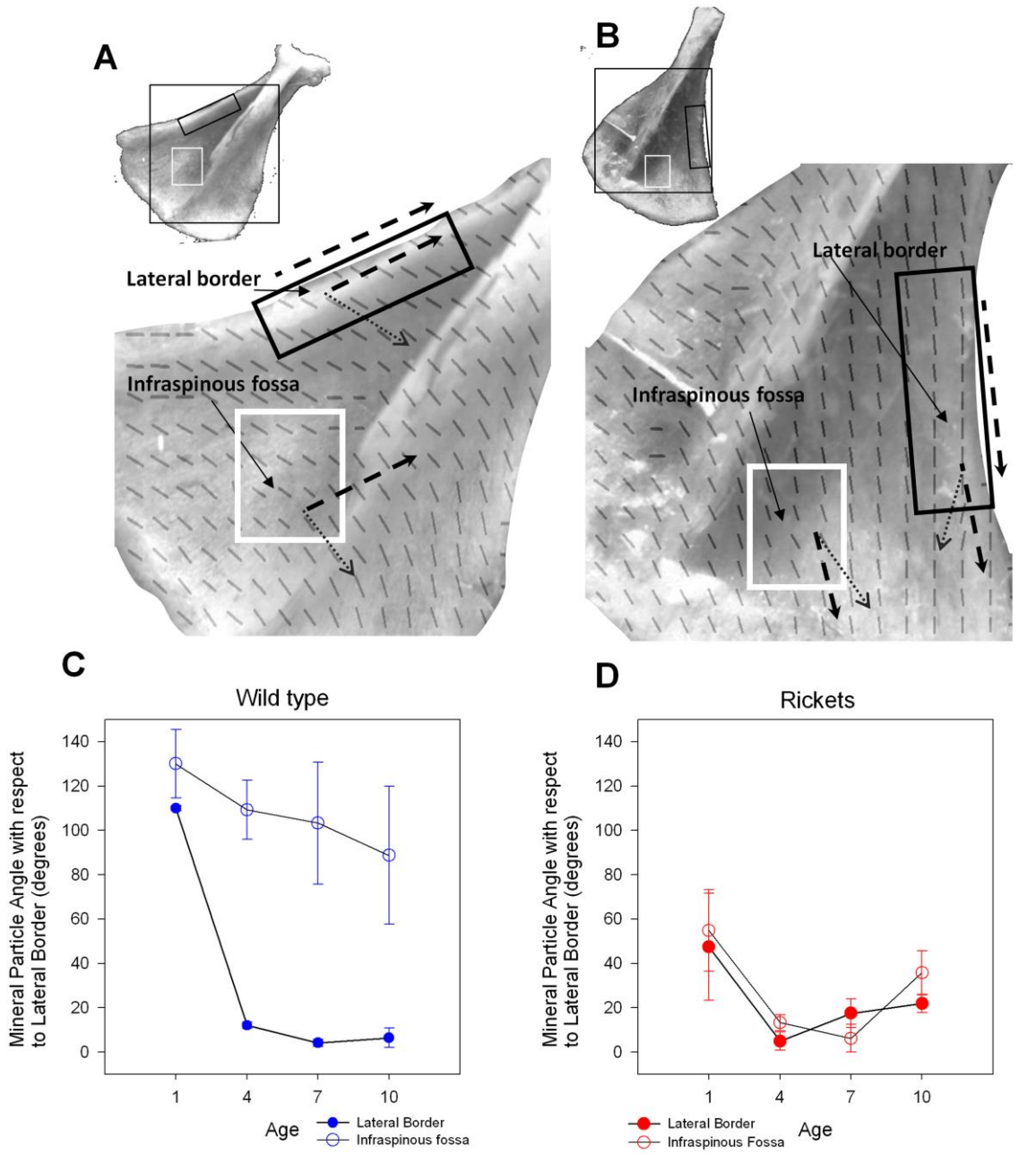

Figure 7.5: Analysis of direction of predominant orientation of mineral crystals with respect to lateral border of individual scapula. (A) Light microscope image of wild-type (4 weeks old) mice scapula and (B) Hpr mice (4 weeks old) scapula superposed with the composite map of mineral particle orientation. Two anatomical regions lateral border (black box) and infraspinous fossa (white box)(subjected to different muscle forces) were selected (insets) to measure the angle of mineral particles. The direction of the dashed arrow is along the lateral border periphery, and was used as a reference direction when calculating the angle of the mineral particle. (C) and (D) *Results*: Mineral particle angle with respect to the lateral border

plotted as a function of age for lateral border (filled symbols) and infraspinous fossa (open symbols) for both wild-type (C) and Hpr (D) mice. Error bars are standard deviations.

The angle of the mineral particles with respect to the lateral border decreases with increasing age in wild-type mice scapulae. A significant ($p < 0.001$) reduction in the angle from ~ 110° to ~10° (a 90% reduction) occurs at the lateral border between 1 week to 4 weeks in wild-type mice scapulae. Subsequently, the angle is stabilised from 4 weeks to 10 weeks. In contrast, at the infraspinous fossa, there is no such reduction in the angle from 1 week to 4 weeks, and the angle decreases by ~30% between 1 to 10 weeks. Secondly the standard deviation of the angle of orientation increases with age in the infraspinous fossa, while being far smaller in the lateral border (compare the size of error bars in **Figure 7.5C** between infraspinous fossa and lateral border). This is indicative of a randomness of the mineral particle orientation in the regions of lower muscle forces (infraspinous fossa) which increases with age.

In Hpr mice, however, the developmental changes of mineral crystallite angle observed are quite different to wild-type. As can be seen in **Figure 7.5D**, the change in mineral particle angle with development is similar for both lateral border and infraspinous fossa. Starting from a lower degree of misalignment (~ 60°) at 1 week (compared to ~110 – 130° for wild-type mice in **Figure 7.5C**), the percentage decrease of angle in both anatomical regions is similar (~85%) followed by a slight increase which is not statistically significant ($p>0.05$).

7.3.2 Degree of mineral nanocrystallite alignment

Figure 7.6 shows the values of ρ as a function of anatomical region and disease condition for all ages (1 to 10 weeks). In the wild-type animals, the degree of orientation in the lateral border increased very significantly with age ($p<0.01$). The significant increment in the degree of orientation ($p<0.01$) was observed between 1 week and 4 weeks in wild-type mice scapulae. Following 4 weeks, the degree of orientation does not increase to the same extent. In contrast, at the infraspinous fossa, no statistically significant difference ($p>0.5$) in degree of orientation with age was observed. In Hpr mice, in contrast, the degree of mineral crystallite orientation in both regions increases significantly (infraspinous fossa and lateral border: $p<0.01$). Intra-sample t-tests show

that the significant increase is from 1 to 7 weeks in both regions ($p<0.01$). Thereafter, the difference between the lateral border and infraspinous fossa is lost. These results showed in wild-type mice scapulae that degree of orientation of the mineral crystals is greater at sites where higher muscle forces are exerted compared to sites of lower force, but that in Hpr mice this spatial difference does not exist.

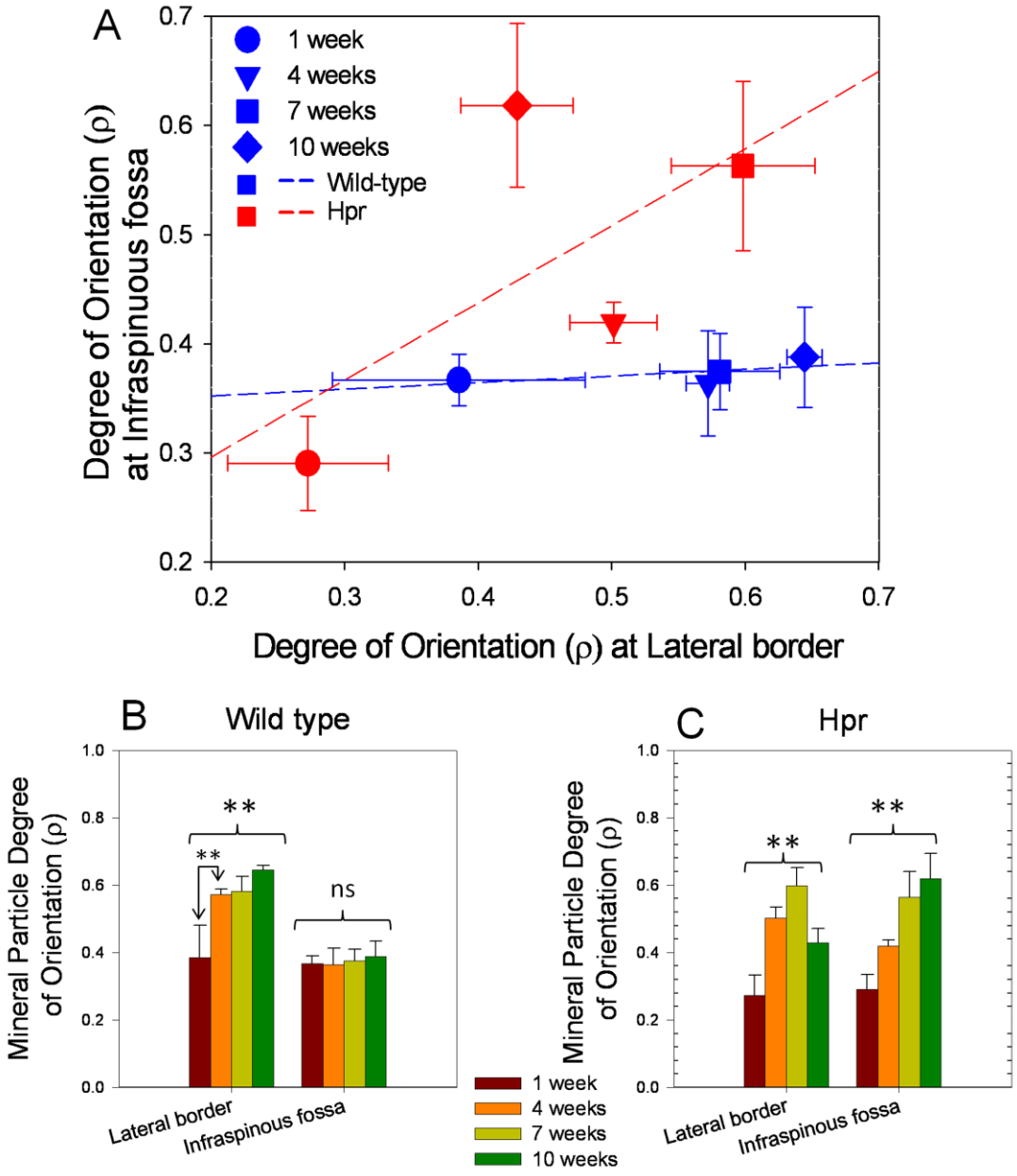

Figure 7.6: Development of degree of orientation, spatially resolved between lateral border and infraspinous fossa. (A) Mineral particle degree of orientation in lateral border plotted against degree of orientation in infraspinous fossa for wild-type (blue) and Hpr (red) mice (1

weeks: circles, 4 weeks: triangles, 7 weeks: squares and 10 weeks: diamonds). Dash lines are regression lines for wild-type (blue) and Hpr (red) mice. (B) and (C) indicates the significance levels form the statistical tests. Single factor ANOVA test was performed for lateral border and infraspinous fossa for wild-type and Hpr mice to measure the significance of the changes in mineral degree of orientation with development. Student t-tests were used to compare degree of orientation at different ages. Pair-wise brackets denote statistical significance (*P<0.05, **P<0.01, ***P<0.001, ns: not significant).

7.3.3 Degree of Mineralisation

The mean mineral concentration was plotted as a function of age for wild-type and Hpr for both lateral border (**Figure 7.7A**) and infraspinous fossa (**Figure 7.7B**). The mean mineral concentration in wild-type and Hpr mice were similar at 1 week for both lateral border and the infraspinous fossa. The rate of increase in mineralisation with age was significantly greater ($p<0.05$) in wild-type mice compared to Hpr mice in the lateral border. However, in the flat infraspinous fossa region, the rates of increase were similar for wild-type and Hpr mice. The mean mineral concentration is lower at infraspinous fossa compared to the lateral border in wild-type mice at every age, and the difference becomes more significant with age. These variations across the scapula bone in wild-type mice scapulae showed an increase in mineral content with age is greater at sites where higher muscle forces are exerted.

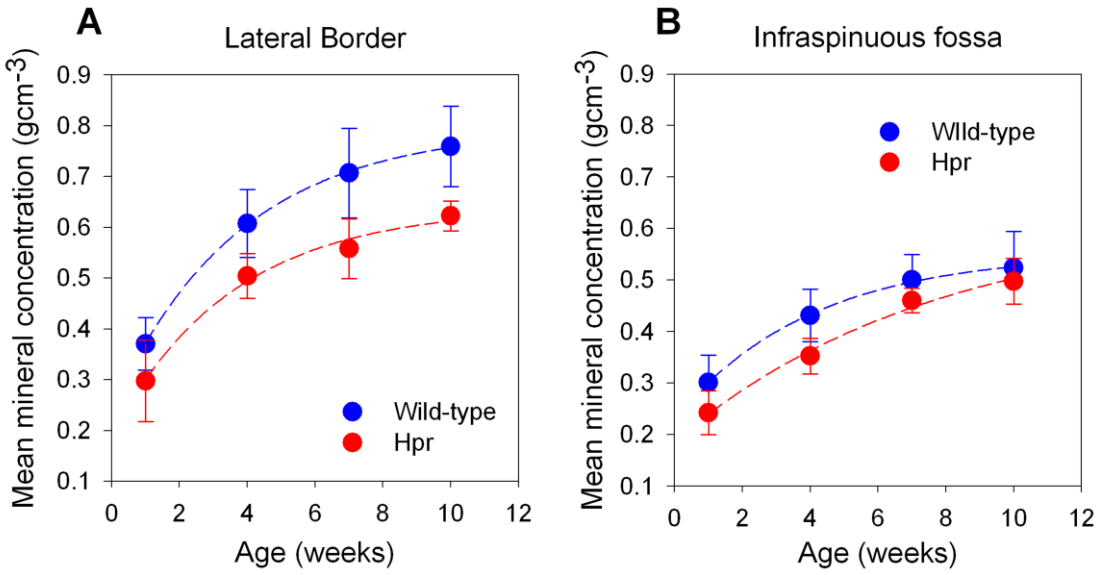

Figure 7.7: (A) Average mean mineral concentration at lateral border plotted as a function of age from 1 week to 10 weeks for wild-type (blue) and Hpr (red). Lines are best fits (Mean

mineral concentration = a (1 – exp (– b × Age) + c) where a, b and c are constants, and are intended as guides to the eye only (r^2 = 0.99)). (B) Atthe infraspimous fossa, the increment in mineralisation with age is similar in both wild-type (blue) and Hpr (red). Lines are best fit curves (Mean mineral concentration = *a* (1 – exp (– *b* × Age) + *c*) where *a, b and c* are constants, and are intended as guides to the eye only, (r^2 = 0.99)). A significant difference in mineralisation rates between lateral border and infraspinous fossa was observed only in wild-type mice (*p*<0.05 and Hpr *p*>0.05). Overall, mineral content at the infraspinous fossa is lower than the lateral border in both wild-type and Hpr mice.

7.4 Discussion

The results demonstrate an association between muscular forces acting on the bone and bone-matrix nanostructure with development in intramembranously ossified bones like the scapula, and a significant disruption of this correlation occurs under the conditions of hypomineralisation (344) and reduced muscular forces (345) observed in rickets. By using scanning synchrotron SAXS (233), it was able to rapidly map microscale variations in bone nanostructure at different stages of tissue maturity. Scanning SAXS has previously been used to show reduction in mineral particle quality in diseases such as osteogenesis imperfecta (219), hypophosphatasia (235), and excess of fluoride dosage (234). For example, in a mouse model of osteogenesis imperfecta, small crystals with a greater variability in alignment were observed in cortical long bone, which may contribute to the brittleness in this condition. Moreover the spatial pattern of mineral particle-alignment which, in wild-type mice, is found to be highest in the femoral cortical midshaft and decreases toward the metaphyses, but systematically increases with age, is lost in TNALP-deficient animals, which are a model for hypophosphatasia (235). These changes could be due to a disruption of a highly ordered metaphyseal bone matrix due to ongoing remodelling in the cortical midshaft (235). Scanning SAXS has also been used to analyze the nanostructure of human osteoporotic bone treated with NaF, and the mineral density, particle size and orientation of fluorotic bone were all found to exhibit differences compared to healthy bone (234).

However, the temporal and spatial variation of the mineralised nanostructure in bones formed by intramembranous ossification (such as scapula), where complex muscle-mediated force fields on the bone exist (340) – and the disruption of these mineralisation mechanisms in metabolic bone diseases – have not been previously investigated.

Understanding the link between the nanostructural defects and multi-axial force regime is clinically and biomechanically relevant because altered muscular forces have been shown to increase fragility (346) and skeletal deformability in skeletal disorders mediated by weaker muscle forces, as in muscular dystrophy (347) and hypophosphatemic rickets (348). Scanning SAXS can provide a unique perspective on understanding this mineralisation dynamics, as the direction of mineral particle predominant orientation (**Figure 7.5C and D**) and the degree (**Figure 7.6**) gives a measure of the organisation within the mineralised bone matrix at the nanoscale. It was found that mineral crystallites closest to the regions of greater and unidirectionally oriented muscle forces (lateral border) are more aligned to the lateral border in both wild-type and Hpr mice, compared to crystallites in the flat infraspinous fossa region subjected to lower and multiaxial force. A very large reduction in angle between mineral particle predominant orientation and lateral border was observed for wild-type mice between 1 to 4 weeks, and subsequent stabilization from 4 weeks to 10 weeks indicates that rapid alignment in the mineral phase occurs at early ages of growth in mice, is associated with the rapid growth of skeletal muscles and their elevated movements during the early postnatal weeks (1 to 4) (349). However, the change of mineral particle alignment is much lower for the lateral border in Hpr mice compared to wild-type mice, and this reduced rate and abnormal mineralisation may therefore be associated with alterations to the impaired mechanical properties of muscles (350) in rachitic mice. This suggestion is supported by the increasing randomness of mineral particle-orientation in the infraspinous fossa regions of lower muscle forces (**Figure 7.5A**). This clear difference in mineralised nanostructure between infraspinous fossa and lateral border may indicate the importance of the dynamic biomechanical stress environment for mineral particle rearrangement.

Furthermore, results show striking differences in degree (as well as direction) of orientation of mineral particles between the lateral border and infraspinous fossa regions (**Figure 4**), suggesting that spatial variances in mechanical environments within the same scapula surface may affect the degree of randomness of the mineralizing collagen fibre scaffold. Two systematic relationships were found, in this regard, in wild-type animals. Firstly, the increase of degree of orientation with age (development) can be only seen in the lateral border. It has been shown previously that transfer of major muscle and joint

reaction take place predominantly through the thick bony ridges at the lateral border (22 MPa), but a lower force (7.5 MPa) act on flat bony regions (340). This finding strongly suggests that muscle mediated stress distributions is associated with the orientation of mineral phase at the nanometre length scale in flat bones. Furthermore, in 1 week old mice, a systematic increase in the degree of orientation from flat bony regions to bony ridges in scapula is absent, which may be due to the low level of muscular force exerted in very young mice. Secondly, the rate of increase of alignment indicated by the slope of the solid lines in **Figure 7.5C** is greater from 1 week to 4 weeks and subsequently reduces from 4 weeks to 10 weeks at lateral border. This may associated with the high rate of development in muscle weight, movement and strength observed in the initial 1 – 4 week period of musculoskeletal development in mice (349). However, this close relationship between muscle-force and alignment in wild-type is far less prominent in Hpr mice. While the Hpr mice scapular mineral particle degree of orientation does increase with age, the clear differences in mineral crystal arrangement between bony ridges and flat bone regions are completely absent.

These differences in nanostructural mineral alignment can be correlated with altered biomechanical forces in rachitic bone. XLHR patients have been reported to complain of muscle weakness, and XLHR has long term effects on daily activities (348, 351). Further, a study on another mouse model (Hyp) of XLHR showed that grip strength and spontaneous movements of muscles was less in affected mice than in wild-type mice (350). As at the genetic level, the Hyp mice and Hpr mice both have *Phex* abnormalities (344), it seems highly likely that Hpr mice will have similar abnormalities in musculoskeletal parameters to those reported for Hyp mice. Due to such skeletal muscle impairment in rachitic mice, *in-vivo* forces on rachitic bones would be lower compared to wild-type tissue. Thus, altered muscular forces arising due to the deficiency in phosphate levels in the serum may be associated with nanostructural abnormalities in intramembranously ossifying bone.

These qualitative differences in mineral nanostructure are accompanied by quantitative differences in mineral concentration (measured by microCT) across the scapular bone, and its disruption in case of metabolic diseases. In wild-type, the greater rate of increase

of mineral concentration at the lateral border compared to infraspinous fossa **(Figure 7.6A)** indicates that a rapid increment in the mineral phase occurs at early ages of growth. The increment could be associated with faster muscle growth and their elevated activity levels (349) during 1 to 10 weeks in mice. At the infraspinous fossa (experiencing low force levels (340)), the above observation is less pronounced (**Figure 7.6B**). Therefore, it is highly likely that muscle mediated stress distributions influences spatial gradients in the nanostructure of the mineral phase, on a micrometer length scale. However this clear difference in mineralisation between infraspinous fossa and lateral border (observed in wild-type mice) is quite absent in Hpr mice (**Figure 7.6A and B**). The defective mineralisation in rachitic bone leads to a long-term reduced mineral content in adult (10 week old) Hpr mice.

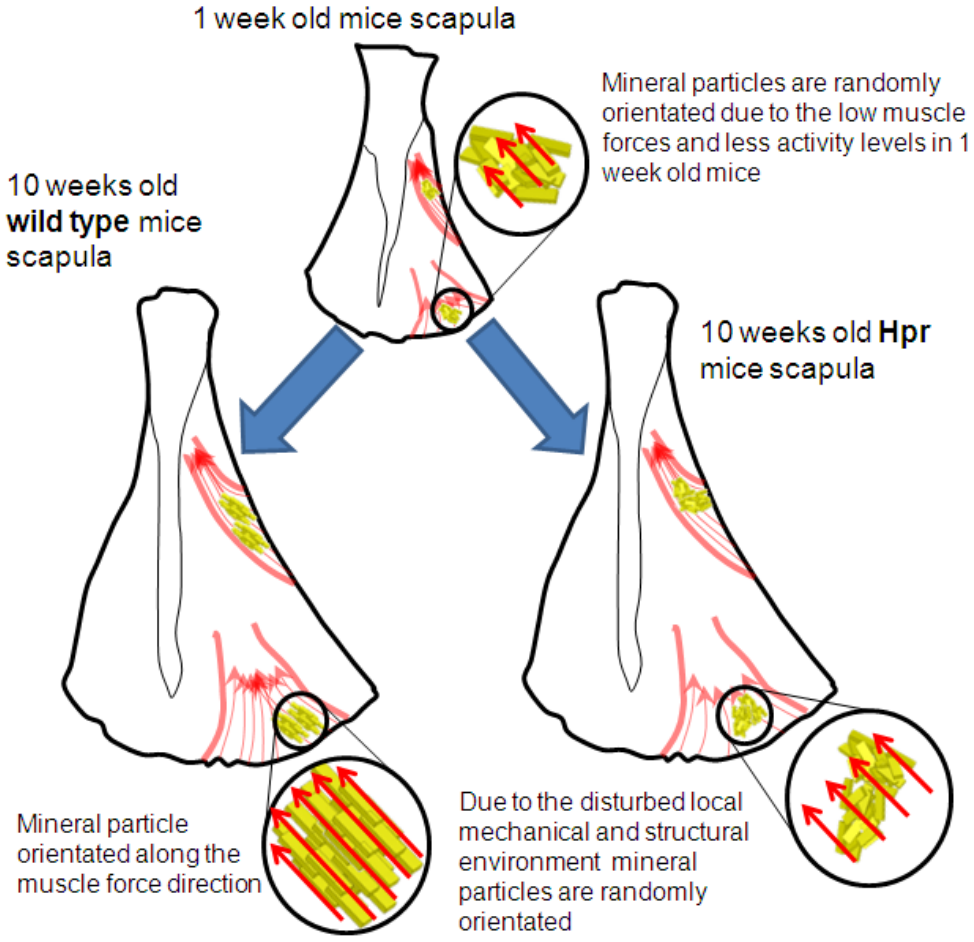

Figure 7.8: Model figure showing development of macro structure, skeletal muscles and nanostructure of wild-type and Hpr scapulae from 1 week to 10 weeks. As experimental

results (Figure 7.5 and 7.6) showed one week scapula of wild-type and Hpr mice has similar nanostructural parameters

A simple nano/microstructural model (**Figure 7.8**) was proposed to correlate both the nanostructural mineral alignment and microstructural degree of mineralisation to altered muscular force-distributions in rachitic bone. It can be hypothesized that the action of muscular stresses results in force-induced alignment of collagen fibrils and mineral crystals across the scapula bone (as shown previously for long bones (70)), which subsequently mineralizes. As bone mineral crystals have been reported to be deposited and to grow within the gap regions of the collagen type I fibrils under the influence of noncollageneous molecules (71), their orientation will follow the altered collagen fibrillar distribution. Previous calculations (340), via three-dimensional finite element modelling, showed a 3 fold higher stress level at the lateral border (22 MPa) compared to the infraspinous fossa (7.5 MPa) for healthy scapular bone. While the stress distribution on rachitic scapulae has not been studied computationally or experimentally, the skeletal muscle histology and physical performance in rachitic mice have been well investigated (348, 350-352). These reports suggest progressive weakness and wasting of skeletal muscle in clinical and mouse model studies of XLHR. *Hyp* mice have quadriceps muscle weight/body weight and strength/body weight approximately 20 - 25 % smaller than those of the wild-type mice (350). Therefore it can be hypothesized, in this model, that muscle weight and fibre diameter at lateral border and infraspinous fossa in the scapula have been similarly reduced by 22.5% in Hpr mice (**Figure 7.10** red dotted line).

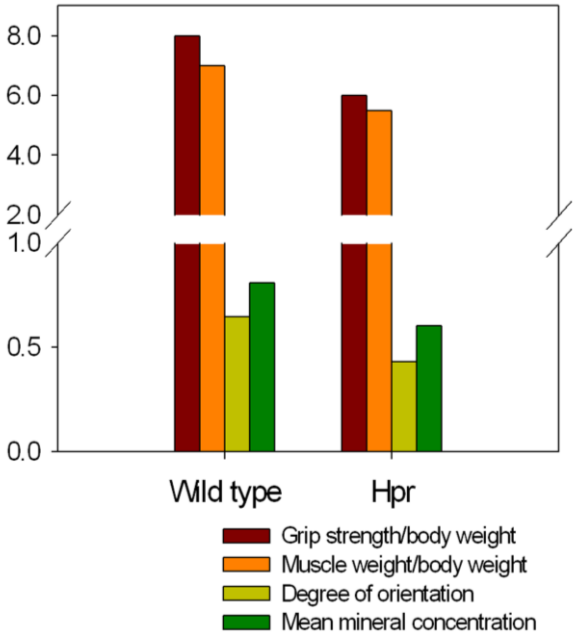

Figure 7.9: Comparison of bone mineral particle degree of orientation (light green) and mean mineral concentration (dark green) with Biceps muscle grip strength (orange) and biceps muscle weight/body weight (dark red) (data obtained from (350)) for wild-type and X-linked hypophosphatemic (*Hyp*) mice.

The previously reported grip strength (per unit body weight) of hyp mice at the same age (10 weeks) (350) was used as a proxy for muscular force. Experimental data (degree of orientation) was compared with the normalised grip strength and muscle weight for wild-type and hyp mice (**Figure 7.9B**). A clear positive correlation between the two muscular parameters (grip strength and muscle weight) and the two mineralisation parameters (degree of orientation and mean mineral concentration) was observed. The grip strength, muscle weight, mineral particle degree of orientation and mineral concentration of hyp mice were all lower than those of wild-type mice. This finding suggests that changes in the muscle forces in disease are associated with the degree of mineral particle alignment and reductions in the degree of orientation.

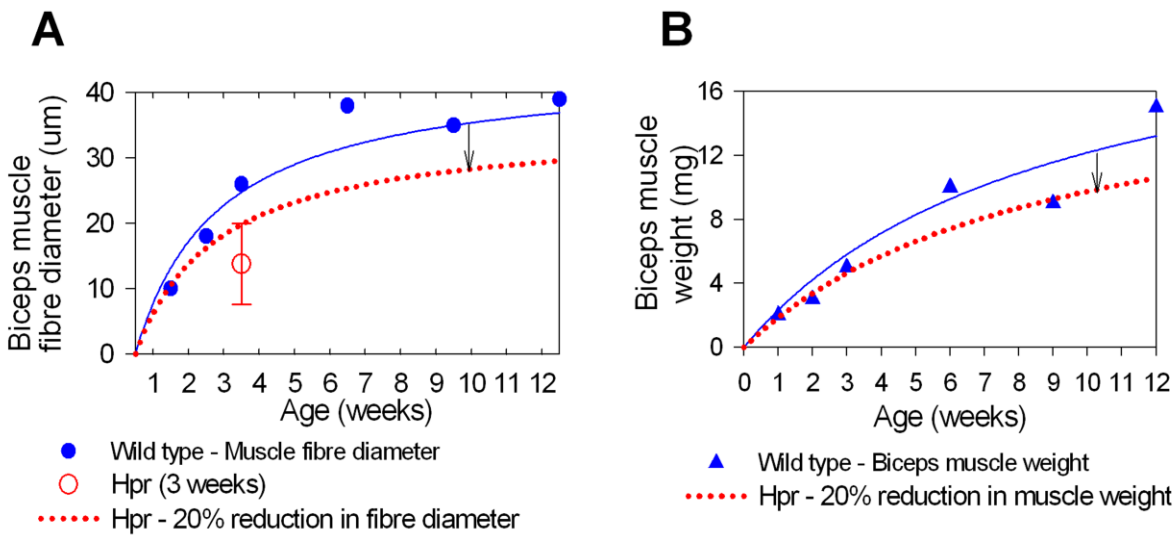

Figure 7.10: (A) and (B) Biceps muscle fibre diameter (circles) and weight (triangles) were plotted as a function of age (1 to 12 weeks) for wild-type mice (data obtained from (349)). Lines are best fits to two parameter exponential functions, Biceps muscle fibre diameter and weight = *a* (1 – exp (– *b* × Age) + *c*) where *a, b and c* are constants, and are intended as guides to the eye only, (r^2 = 0.99). Muscle strength approximately 22.5% smaller than those of the wild-type mice in X-linked hypophosphatemic (Hyp) mice (351). Therefore it was assumed, in this work, that muscle fibre diameter and muscle weight have been reduced by 22.5% in Hpr (Hpr and Hyp mice have similar abnormalities) mice (1 to 12 weeks: red dotted lines).

The link between increasing muscular force and the degree of mineral particle orientation can now be tracked during musculoskeletal development. As the forces are exerted primarily at the lateral border, a direct comparison of the mineral particle orientation at this anatomical site versus muscle force is most meaningful. Because the changes in stress distribution in the developing scapula have not been measured biomechanically, the muscular size and weight data from (349) was used on normal mice as a proxy. These researchers studied muscle fibre growth in five different muscles (*m.tibalis anterior*, *m. biceps brachii*, *m. extensor digitorum*, *m. soleus* and *m. sternomastoideus*) of normal mice (ages – newborn, 1, 2 and 3 weeks and then at intervals of 3 weeks up to 24 weeks) (349). They found that muscle weight and fibre diameter increased with age, at first rapidly (weeks 1-3) then at a slower rate after 4 weeks (**Figure 7.10**), due to altered work load and/or functional activity of the muscles. Biceps muscle diameter and muscle weight increases from birth to 10 weeks of age and subsequently stabilizes in normal mice. Their *m.biceps* muscle fibre diameter and weight data were used as force-proxies

on the scapular surface, as the biceps directly exerts forces on the scapular surface. The equivalent data in Hpr mice is generated by assuming that fibre diameter and muscle weight are reduced by 22.5% in rickets (350) (**Figure 7.10** dotted lines). By comparing **Figures 7.10** with **Figure 7.11**, a striking correlation was observed between the time course of the development of muscular force, and the structural parameters of mineral particle degree of orientation and degree of mineralisation, in wild-type mice and Hpr mice.

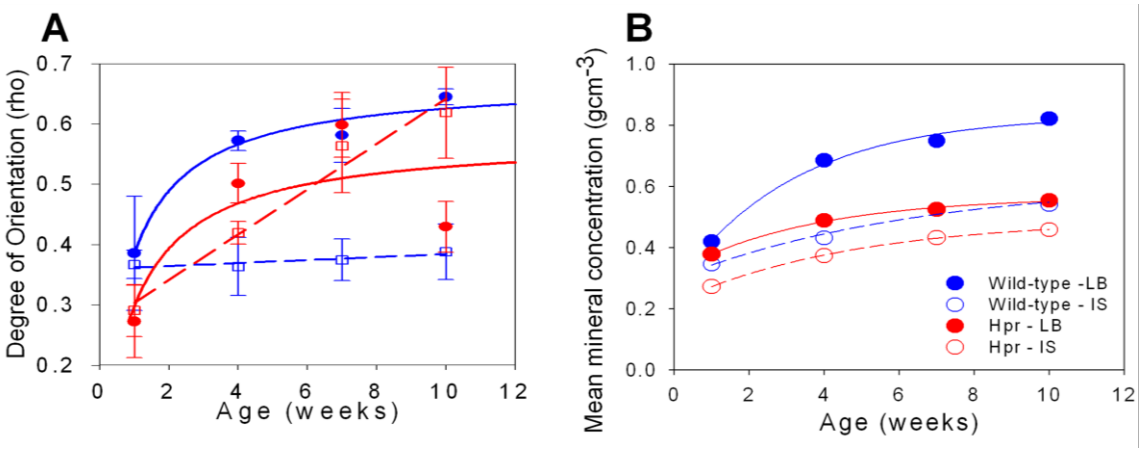

Figure 7.11: (A) Mineral particle degree of orientation (rho) for lateral border (filled symbols) and infraspinous fossa (open symbols) plotted as a function of age (1, 4, 7 and 10 weeks) for wild-type (blue) and Hpr mice (red).(B) Degree of mineralisation for lateral border (filled symbols) and infraspinous fossa (open symbols) plotted as a function of age (1, 4, 7 and 10 weeks) for wild-type (blue) and Hpr mice (red). Lines are best fits wild-type lateral border: solid black, wild-type infraspinous fossa: solid gray, Hpr lateral border: dash black and Hpr infraspinous fossa: dash gray.

In this chapter it was demonstrated that degree of orientation, predominant orientation and mean mineral content increases with age in intramembranously ossifying bone. Several previous studies have shown a positive correlation between muscle strength and bone strength index (353) and BMD (354-356) independent of measures of body size. However, the correlation between development of muscle strength and nano-structural parameters were not investigated. Even though stress distribution in the developing scapular has not been studied, forces exerted by the mice with development (1 week to 4 weeks) in forelimbs have been studied using a dynamometer (357). This study showed that muscular forces increase with age. This development of muscular forces may be

linked to the observed time course of the development nano-structural parameters of mineral particle orientation (**Figure 7.5 and 7.6**) and degree of mineralisation (**Figure 7.7**).

7.5 Conclusion

The association between muscle strength and bone mass has been established in numerous studies (358-360), and mechanical stimulation by skeletal muscles has been reported to have a dominant effect on bone gain and loss when compared to non-mechanical factors such as hormones and metabolic environments (176, 361). This is further illustrated by the increased fracture risk (implying an altered bone material structure) observed in patients with muscle wasting and neuromuscular diseases such as muscular dystrophy (362). Furthermore it has been shown that increasing muscle strength through exercise can reduce the risk of fracture and the development of kyphosis in older women with osteoporosis (363). It has very recently been clearly shown that increased fracture risk (in the case of ageing bone) is associated with changes in bone material (87) as well as reduced bone mass. To better understand the mechanisms in the bone material that mediate the alterations in gross fracture risk in metabolic bone disease, mice with XLHR, a disease that is associated with progressive weakness and wasting of skeletal muscle (364) as well as lowered bone mineral content were investigated. In this rachitic condition, deterioration in the skeletal muscle increases the deformability and fracture of bone. Results presented in this chapter provide evidence that alterations in the nanostructure of the bone matrix – such as the direction and degree of mineral particle orientation – are associated with both predicted reduction in muscle forces and mineralisation in the disease condition. Hence, it can be proposed that the nanostructural parameters of mineral particle orientation and direction may play a vital role in controlling the fracture risk in the bone tissue. Further, the nanostructural parameters like the degree of orientation and mineral particle angle could potentially be used as a marker to estimate the fracture risk in bone in metabolic and neuromuscular bone diseases.

Chapter 8

Functional Link between Material Level Structural Alterations in Steroid Induced Osteoporotic Bone and increased fragility

The contents of this chapter are prepared for publication in either PNAS or JBMR

A Karunaratne, GR Davis, J Hiller, Liz Bentley, CT Esapa, NJ Terrill, SDM Brown, RD Cox, RV Thakker, HS Gupta - *Functional link between material level structural alterations in steroid induced osteoporotic bone and its increased fragility. 2012*

8 Functional Link between Material Level Structural Alterations in Steroid Induced Osteoporotic Bone and increased fragility

8.1 Synopsis

Fracture risk in osteoporosis, affecting 3 million people in the UK and the leading cause of hospital admission for women over 50. Glucocorticoid induced osteoporosis (GIOP) is the most common form of secondary osteoporosis, affecting 1-3% of the general population and resulting in severe morbidity and develops in patients taking steroid medications (refer Chapter 1 section 1.8.1.2) (365, 366). Clinical tools like FRAX underestimate fracture risk, and fracture in glucocorticoid (steroid)-receiving patients occurs at higher BMDs than in controls (367). It is also known that the increase in fracture propensity for GIOP cannot be explained by reduction in bone quantity (BMD) alone, but must involve changes in the bone material as well (bone quality) (178). Therefore the investigation of bone quality is increasingly crucial for understanding of material level deterioration in GIOP, which is associated with increased risk of fracture (281, 368). Changes in bone metabolism (a cellular effect) due to glucocorticoid treatment have been investigated by several researchers (178, 179, 369). However, these findings do not fully explain why patients treated with glucocorticoids have higher fracture risk relative to postmenopausal women with similar levels of BMD (370, 371). At the material level, one study investigated bone microstructure and localised mechanical properties in GIOP-trabecular bone, as GIOP predominantly affects regions abundant with cancellous bone (372). This study revealed that glucocorticoid treatment reduced the trabecular bone mass, degree of bone mineralisation and localised elastic modulus within the trabeculae. Furthermore, an increased size of osteocyte lacunae, reduced elastic modulus around the lacunae, hypomineralised halo regions surrounding the lacunae and disorganized crystal orientation in glucocorticoid treated animals compared to the control were observed (177, 178). These findings led the researchers to

suggest that these microstructural and compositional deteriorations may, over time, weaken these localised areas of bone, resulting in increased bone fragility (278, 368).

At the nanoscale, bone material consists of MCFs, whose fracture mechanics is critical to macroscopic fragility as reviewed in the **Chapter 1**. In contrast to healthy bone, osteoclasts carry out rapid resorption and osteoblastic activity has been suppressed. These alterations in bone matrix structure and mineralisation will have profound effects on the fracture susceptibility. However, the changes in the fibrillar fracture and deformation mechanisms in GIOP which lead to increased fragility remain unknown (373). As these changes are critical to early detection and treatment of this debilitating condition, the aim of this chapter is to quantify them using *in situ* synchrotron SAXD.

To analyze the altered fracture mechanisms in GIOP, an inherited mouse model developed via chemical (N-ethyl-N-nitrosourea (ENU)) mutagenesis, Cushing's disease that results in GIOP by endogenous production of steroids (see **Chapter 2** section 2.6.2 for detailed information) was used. Using this model, strain to failure tensile testing was carried out concurrent with rapid acquisition of SAXD spectra. Specific experimental foci will be altered fibrillar deformability and modulus in GIOP mice bone, and whether a more random fibrillar structure exists due to altered remodelling rates.

8.2 Material and methods

8.2.1 Animals

Crh$^{-120/+}$ mice were identified in a dominant ENU mutagenesis screen at the Medical Research Council Harwell (Bentley et al 2012 - manuscript in preparation). Animals were 26 weeks of age at the time of sacrifice. Animals were anaesthetised with sodium pentobarbitone (Pentoject, Animalcare, York, UK) and; internal organs were removed from the body cavity and the whole body skeleton stored at -20°C until used (this activity was performed at the Medical Research Council).

8.2.2 Sample preparation for insitu cyclic loading

Mouse femora (*Crh*$^{-120/+}$ = 6 and wild-type = 4) from female *Crh*$^{-120/+}$ and wild-type littermates were dissected, skinned and muscle tissue removed. Dissected femur (included in polyester wax) sectioned out using a diamond saw under constant irrigation and sectioned into bone strips (5 mm × 2 mm × 0.2 mm) (see **Chapter 4** section 4.1.1. for the detailed sample preparation procedure). A dual-axis micromilling stage using a mounted Dremel drill and two DC motor stages will create necked tensile test specimens. After milling the average length, width and thickness of the gauge regions were 5.0 mm, 1.0 mm and 0.2 mm, respectively.

8.2.3 *In situ* tensile testing with fibril strain measurement from SAXS

The samples were loaded in a cyclic fashion at a constant velocity of 1 μm/second in the custom made micromechanical testing machine with a spatially resolved microfocus X-ray beam. Samples were strained at 0.02 % s^{-1}, with SAXD spectra taken every 0.05% tissue strain up to yield point (~ 0.5 - 1.0%) in physiological saline in a fluid chamber. In order to reduce the influence from the radiation damage to the mechanical properties of the bone, SAXD spectra was obtained at different locations by translating microfocus stages in X and Y directions with a step size of 50μm in vertical direction. Then the samples were compressed up to 0% strain and loaded back to the yield strain level. The collagen fibril strain ε_f was measured as the change of the centre position of the third order reflection peak divided by its location at zero load. Full experimental protocol and data reduction procedure are explained in the **Chapter 4** sections 4.2.1.1 and 4.2.2 respectively.

8.2.4 Scanning μSAXS

Humeri were dissected from the same animals used for *in situ* tensile testing and prepared for the scanning μSAXS as explained in **Chapter 4** section 4.2.5. Anterior regions of the humeri were sectioned using low-speed diamond saw under constant irrigation. Immediately prior to the experiment, each specimen was mounted in a saline sample chamber with Ultralene® foil windows. For the μSAXS measurements, three regions of interest (1.08 × 0.2 mm^2) were selected from each sample as shown in the

Figure 8.1. SAXS patterns (see **Chapter 4** for parameters) of humeri (anterior regions) were collected by raster-scanning the precision XY stage with a step-size of 15 µm and 10 µm in horizontal and vertical directions respectively. The 2D SAXS images were analysed for orientation as described in detail by Rinnerthaler et al (233) and **Chapter 2** section 2.2. The degree of orientation (ρ) of mineral particles was determined from each SAXS pattern.

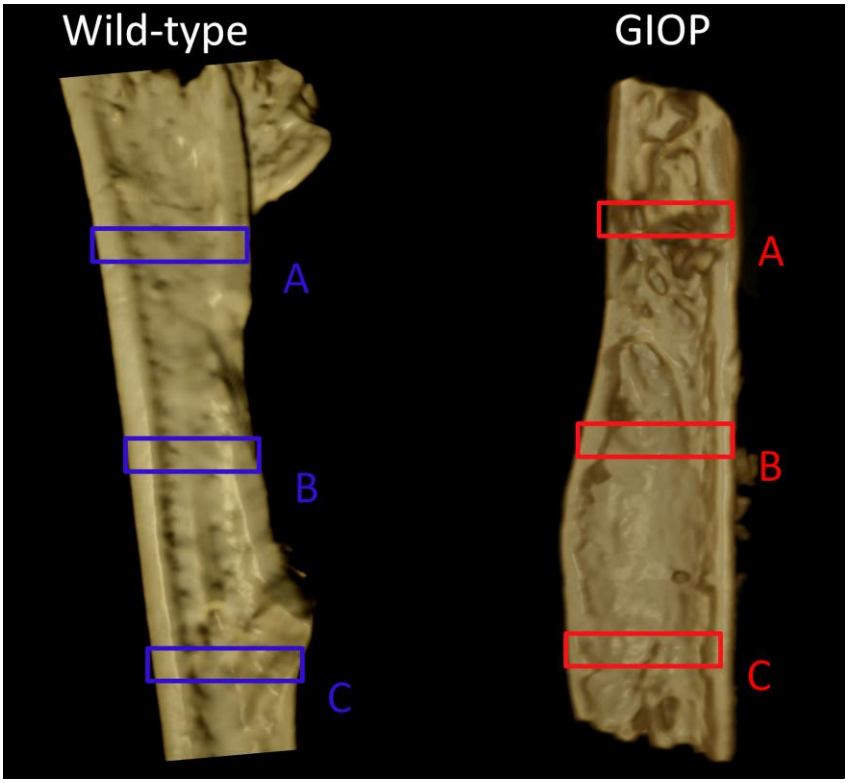

Figure 8.1: 3D rendered images from microCT images collected from anterior region of the wild-type (A) and Crh-120/+ (B) mice humeri. Blue and red square regions in wild-type and Crh-120/+ respectively showing regions of interest used to obtain the 3D rendering of mid-diaphysis region of wild-type and *Crh*$^{-120/+}$ respectively showing the regions used for scanning µSAXS.

8.2.5 X-ray microtomography

MicroCT was used to qualitatively assess the trabecular and cortical architecture in *Crh*$^{-120/+}$ and wild-type (one sample from each condition) mice femur. Reconstructed tomograms were sliced though the longitudinal cross section using in house software; tomview in order to investigate internal structure. These sliced tomograms further

converted into volume-rendered images to view the 3D structure of trabecular bone. Humeri samples used for scanning μSAXS subsequently used for microCT imaging in order confirm the homogeneity of regions of interest at macroscale level. Volume rendered images of humeri are shown in the **Figure 8.1**.

8.2.6 BSE Imaging

One femur each from wild-type and *Crh*$^{-120/+}$ mice was prepared for BSE imaging to determine the degree of mineralisation at the micro level. Femurs were sectioned into halves using a low speed diamond saw before dehydrating them in ethanol and embedding in PMMA (252, 302). One half was used for the imaging of transverse cross section at the mid-diaphysis. Other half was used for the imaging of a longitudinal section plane. Three higher magnification (300 × 300 μm fields) BSE images were also obtained from the anterior cortex of each sample for further quantitative analysis. In *Crh*$^{-120/+}$ mice bone, two distinct regions (resorption cavity region in the endosteal cortex and periosteal cortex) were observed. Two (wild-type) to four (*Crh*$^{-120/+}$: 2 from endosteal cortex and 2 from periosteal cortex) regions of interest (50 × 50 μm) from each BSE image of the anterior transverse cortex were used to produce the grey level histograms. In order to exclude the unmineralised bone tissue from the quantitative analysis grey levels within 127 and 240 were only used and grey levels outside the limits were discarded. BSE images from longitudinal cross sections were used to determine the number of osteocytes per unit area and the direction of the long axis of the elongated osteocyte lacunae.

Porosity correction

In order to correct the nominal stress values for the reduction in effective cross-sectional area due to microstructural porosity, tissure fraction was measured using microCT and BSE images. MicroCT has a spatial resolution of 15μm and hence underestimates the porosity by not including pores of smaller dimension. In contrast to BSE, however, microCT can measure porosity across the entire length of the specimen while BSE measures only in one transverse cross-section. To justify a preference for using BSE data over microCT, it was shown that there was no significant variation of porosity along the

specimen length. The porosity fraction for selected regions of interest (100 × 100 pixels each) from BSE and microCT images of the anterior cortex was determined.

Statistical analysis

To compare nano mechanical and quantitative backscattered scanning (qBSE) results between wild-type and *Crh*$^{-120/+}$ mice, the Student t-test was performed. Single factor ANOVA was used to compare the porosity fractions obtained from BSE and microCT.

8.3 Results

8.3.1 *In situ* tensile loading

The fibrillar and tissue level mechanical properties of cortical bone from femoral mid diaphyses of 26 week old wild-type (n = 4) and *Crh*$^{-120/+}$ (n = 6) mice were examined using *in situ* micro mechanical tensile testing combined with μSAXD. The tensile load applied to bone specimens was measured during cyclic loading tests and then converted into nominal stress values using measurements of macroscopic cross-sectional area (as described in porosity correction). A typical curves for nominal stress/tissue strain for one wild-type and *Crh*$^{-120/+}$ mice are shown in **Figure 8.2**. Single factor ANOVA tests of the microCT porosity showed no significant ($p>0.05$) difference across the length. Average values of microCT porosity were 1.6% ± 0.02 S.D. (wild-type) and 19.6% ± 0.04 S.D. (*Crh*$^{-120/+}$). Therefore the higher resolution (spatial resolution 2–3 μm) BSE measurements of porosity (wild-type – 3.5% ± 0.05 S.D. and *Crh*$^{-120/+}$ - 29% ± 0.04 S.D.) from the anterior transverse cross section of the femoral mid-diaphysis were used to correct the nominal stress. It was observed that, even after correction of nominal stresses for porosity, the tissue-level elastic modulus was lower in *Crh*$^{-120/+}$ mice compared to wild-type mice bone (**Figure 8.2**). Porosity-corrected stress values are hereinafter referred to as simply stress.

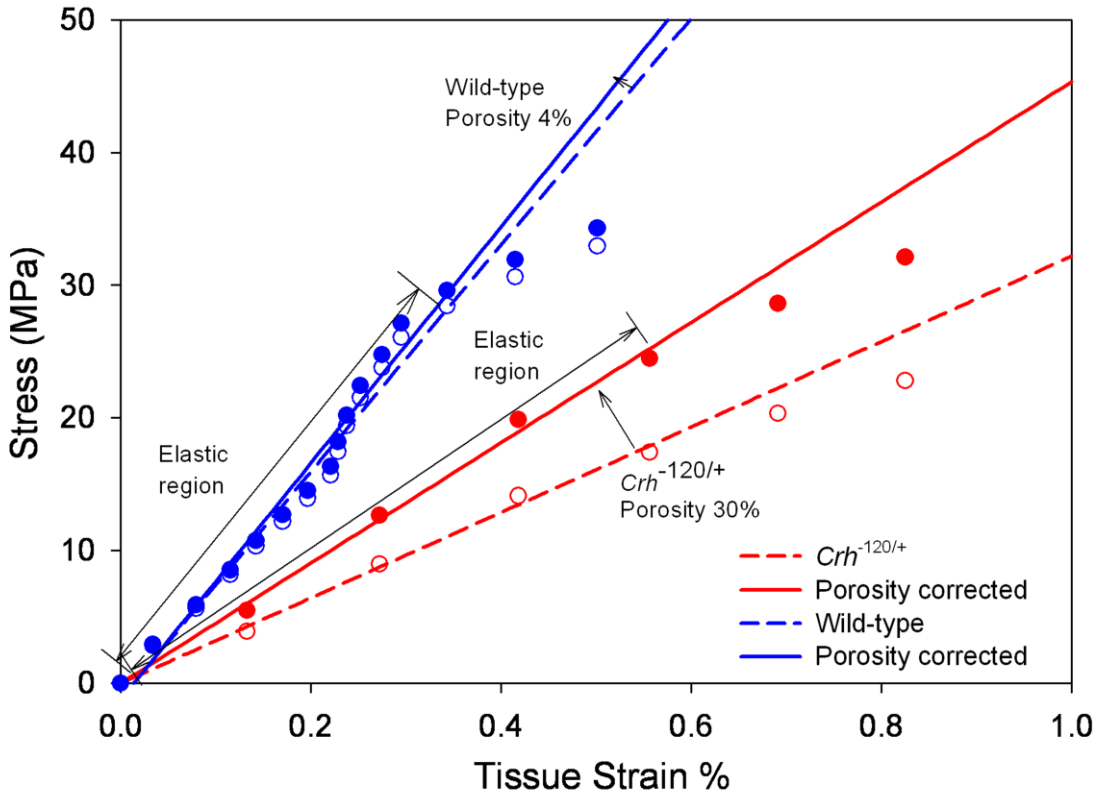

Figure 8.2: Porosity correction. Representative stress-tissue strain % curves are shown for the tensile tests of wild-type (blue) and *Crh*$^{-120/+}$ mice (red). Dash (data no corrected for porosity) blue and red lines are linear regressions for wild-type and *Crh*$^{-120/+}$ respectively. Porosity was estimated from BSE images of wild-type (4 %) and *Crh*$^{-120/+}$ (30 %) transverse cross sections of mechanically tested bone samples. Stress vales were corrected for porosity and re-plotted on the same graph, corrected data indicated with solid lines.

Stress versus tissue strain curves were plotted (**Figure 8.3A**) as a function of genotype. **Figure 8.3B** shows the tissue level elastic moduli to be significantly ($p<0.05$) lower in *Crh*$^{-120/+}$ mice relative to wild-type mice. The average maximum stress (**Figure 8.3C**) of the wild-type mice (28.2 MPa ±7.1 S.D.) is larger compared to the *Crh*$^{-120/+}$ mice (16.2 MPa ± 7.3 S.D.). However, maximum tissue strain of *Crh*$^{-120/+}$ mice was not significantly different ($p>0.05$) from wild-type mice (**Figure 8.3D**).

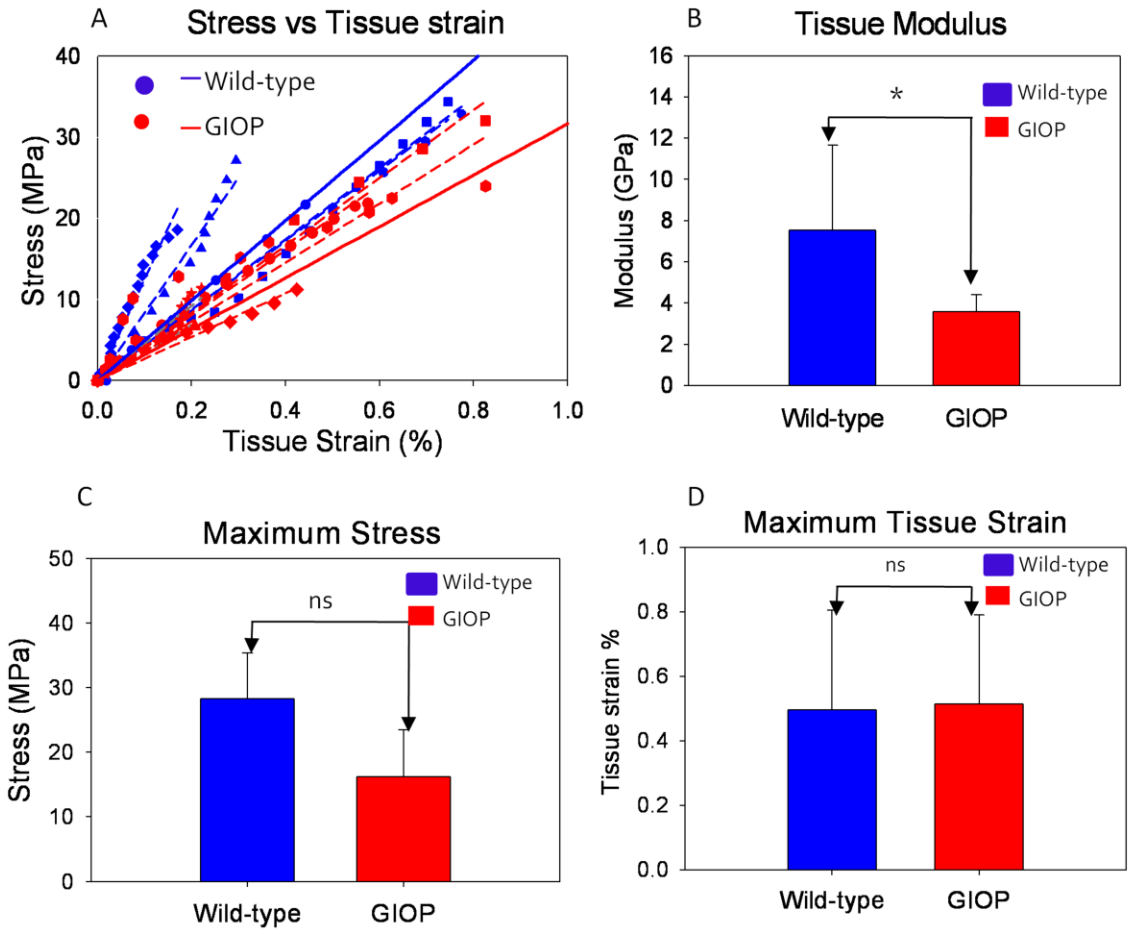

Figure 8.3: ***Macro mechanical testing results*** **(A). Stress vs. measured tissue strain % for wild-type (n = 4/blue) and *Crh*$^{-120/+}$ (n = 6/red) mice for each sample. Dash lines (wild-type = blue and *Crh*$^{-120/+}$ = red) are regression lines for each stress strain curve (r^2 wild-type = 0.98 and r^2 *Crh*$^{-120/+}$ = 0.96) for individual samples. Solid lines are average regression lines for wild-type (blue) and *Crh*$^{-120/+}$ (red) for multiple samples (B, C, D) Average tissue modulus σ/ε_F, maximum stress and maximum tissue strain plotted for wild-type (blue) and *Crh*$^{-120/+}$ (red) mice. Error bars are standard deviations. Pairwise brackets denote statistical significance (*p<0.05, **p<0.01, ***p<0.001, ns = not significant).**

The fibrillar-level, the gradient of stress versus fibril strain (**Figure 8.4A**) in the elastic regime is denoted as the effective fibril modulus ($E_f = d\sigma/d\varepsilon_f$), as per previous definition in **Chapter 5 and 6**. (85). The average fibril modulus is plotted as a function of genotype in **Figure 8.4B**. A significant ($p<0.05$) reduction of ~79% of fibril modulus occurs in *Crh*$^{-120/+}$ bone relative to wild-type. To compare fibril and tissue strains, the fibril strain was plotted as a function of the macroscopic strain in **Figure 8.4C**. The linear

regressions of all samples at each genotype (dark gray (*Crh*$^{-120/+}$) and black (wild-type) lines) are clearly different, with the fibril strain of *Crh*$^{-120/+}$ mice much higher compared to wild-type for a given tissue strain. The gradient for individual samples at each genotype was calculated, and gives the average fibril-to-tissue strain ratio. **Figure 8.4D** shows that the fibril-to-tissue strain ratio was much higher in *Crh*$^{-120/+}$ mice (1.18±0.43 S.D.) compared to 0.57±0.2 S.D. for wild-type mice.

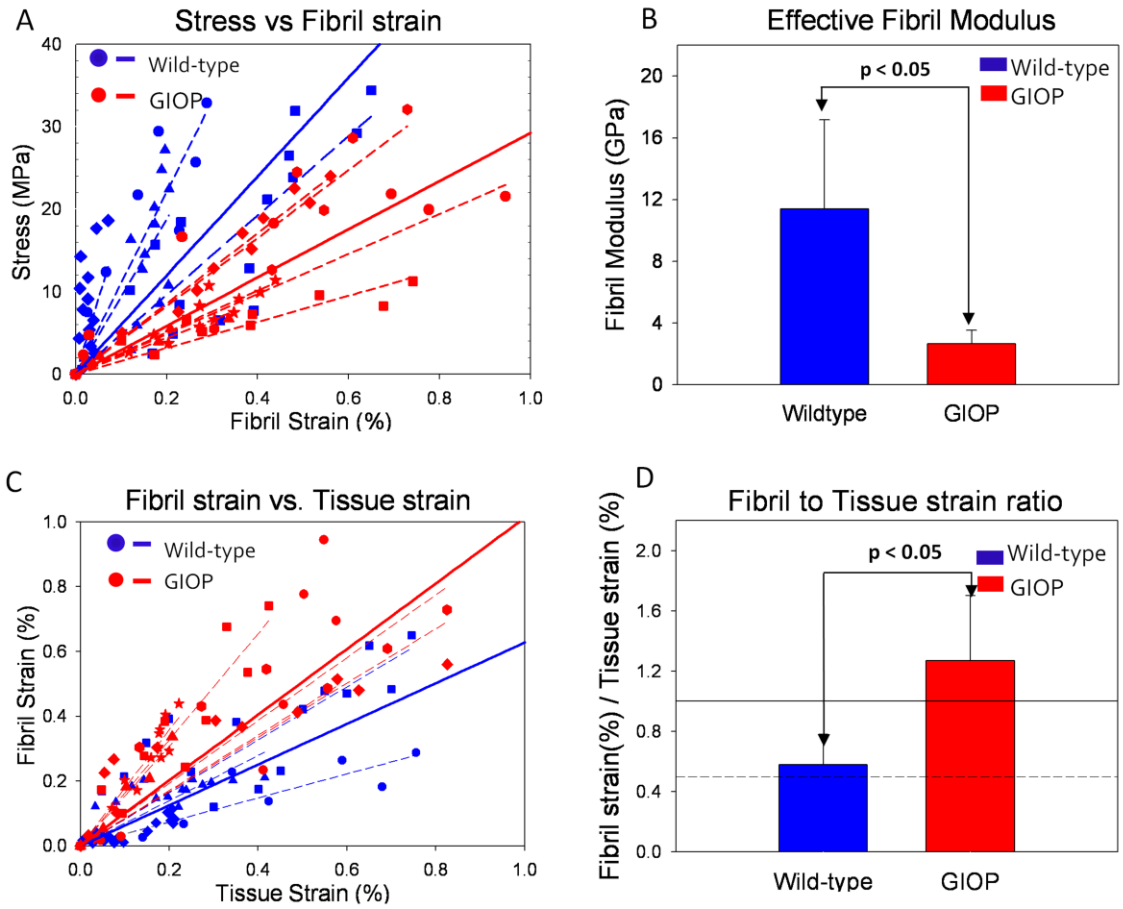

Figure 8.4: ***In situ*** **nano-mechanical and fibrillar orientation data (A) Stress vs. measured fibril strain % for wild-type (n = 4/blue) and** ***Crh***$^{-120/+}$ **(n = 6/red). Dash lines (wild-type = blue and** ***Crh***$^{-120/+}$ **= red) are regression lines for each stress fibrils strain curve (r^2 wild-type = 0.98 and r^2** ***Crh***$^{-120/+}$ **= 0.95). Solid lines are average regression lines for wild-type (blue) and** ***Crh***$^{-120/+}$ **(red) test samples. (B) Effective fibril modulus σ/ε_F plotted for elastic region of wild-type (blue) and** ***Crh***$^{-120/+}$ **mice (red) (C) Fibril strain (ε_F) % vs. tissue strain (ε_T) % as a function of disease state wild-type (blue) and** ***Crh***$^{-120/+}$ **(red) mice. Dash lines wild-type = blue and** ***Crh***$^{-120/+}$ **= red) are regression lines for each sample (r^2 wild-type = 0.88 and r^2** ***Crh***$^{-120/+}$ **= 0.87). Solid lines are average regression lines for wild-type (blue) and** ***Crh***$^{-120/+}$ **(red) test samples. (D) Average fibril**

strain to tissue strain ratio ($\varepsilon_F/\varepsilon_T$) plotted for elastic region of wild-type (blue) and *Crh*$^{-120/+}$ mice (red). Pair-wise brackets denote statistical significance (*p<0.05, **p<0.01, ***p<0.001, ns: not significant).

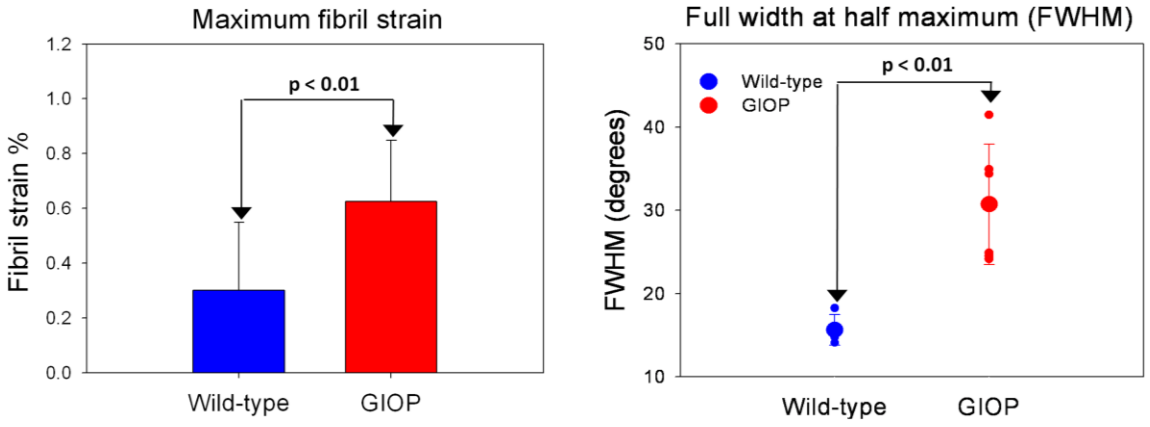

Figure 8.5: (A) Average maximum fibril strain plotted for elastic region of wild-type (blue) and *Crh*$^{-120/+}$ mice (red) (B) Full width at half maximum of intensity distribution of the 3rd order fibril reflection was plotted for wild-type (blue) and *Crh*$^{-120/+}$ (red). Large symbols are average FWHM values and small symbols are individual data points. Error bars are standard deviations. Pair-wise brackets denote statistical significance (*p<0.05, **p<0.01, ***p<0.001, ns: not significant).

Furthermore, the maximal fibril strain for *Crh*$^{-120/+}$ bone specimens (0.63 %±0.22 S.D.) was significantly higher (p<0.05) compared to the wild-type mice (0.3 %±0.25 S.D.), as shown in **Figure 8.5A.** In order to investigate possible differences in the degree of fibrillar orientation between wild-type and *Crh*$^{-120/+}$ mice, the azimuthal intensity distribution of the 3rd collagen reflection was plotted. A Gaussian curve was fitted to the azimuthal intensity distribution $I(\chi)$, and the full width at half maximum plotted as a function of genotype in **Figure 8.5B**. The FWHM for *Crh*$^{-120/+}$ mice was significantly ($p<0.01$) higher compared to wild-type, indicating a lesser degree of fibrillar alignment relative to the tensile axis in *Crh*$^{-120/+}$ mice.

8.3.2 Degree of mineral nanocrystallite alignment

The mineral particle degree of orientation and predominant orientation maps were calculated in the cortical bone of the wild-type and *Crh*$^{-120/+}$ mice anterior regions of humeri. This analysis revealed (**Figure 8.6**) that the degree of orientation (the lengths of

the lines of the maps) was greater in wild-type mice compared *Crh*$^{-120/+}$ mice. In both mice groups, the degree of orientation was showed no major differences along the length of the bone sample. It was observed that predominant orientations of the mineral particles are parallel to the long axis of the humerus in wild-type mice. In contrast, in *Crh*$^{-120/+}$ mice, the predominant orientation was random. Average degree of orientation was plotted for wild-type and *Crh*$^{-120/+}$ mice in **Figure 8.7**. Average mineral particle degree of orientation was significantly larger in wild-type compared to *Crh*$^{-120/+}$ mice.

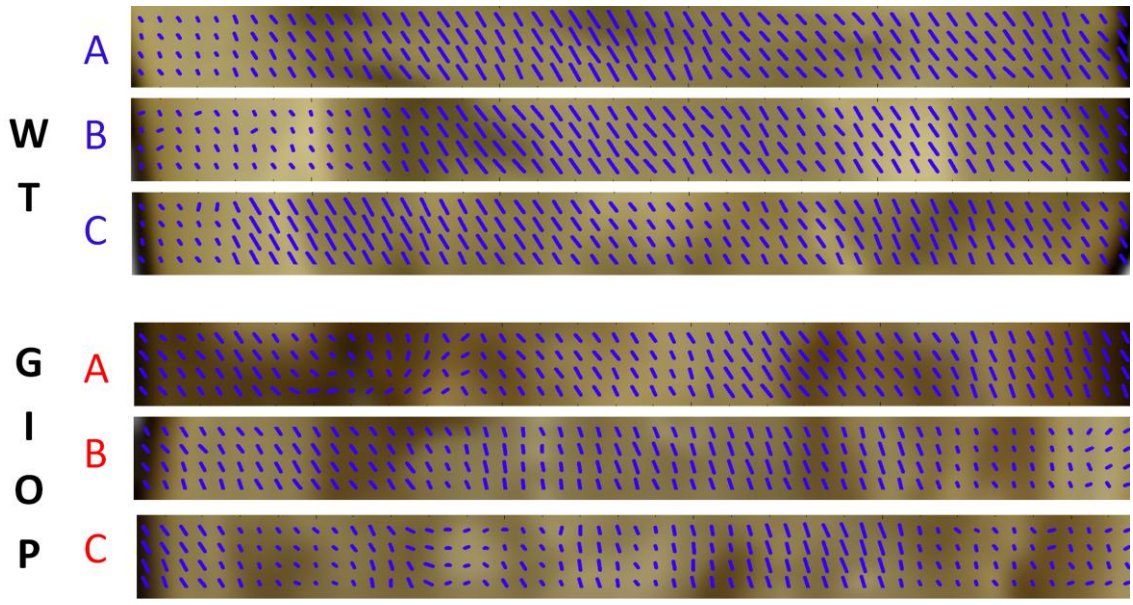

Figure 8.6: Plots show the 3D rendered images from microCT and their 2D composite maps superimposed on it. Each composite map (A, B and C) represent the regions of interest of the humerus as shown in Figure 8.1. Direction of lines denotes the predominant orientation and length of lines denotes degree of orientation mineral nanocrystallite orientation in normal mice.

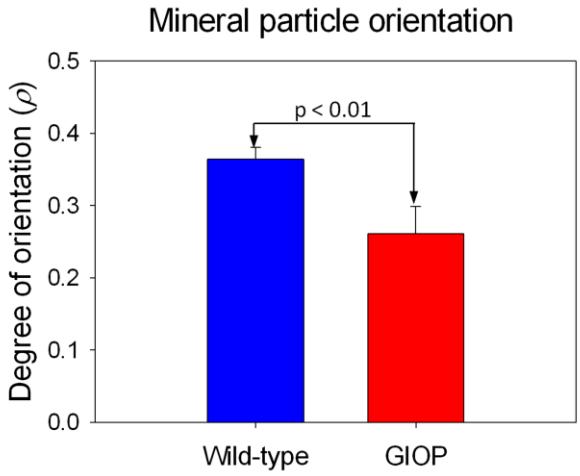

Figure 8.7: Average degree of orientation of mineral particles were plotted for wild-type (blue) and *Crh*$^{-120/+}$ (red) mice. Pair-wise brackets denote statistical significance (p*<0.05, ***p*<0.01, ****p*<0.001, ns: not significant).**

8.3.3 X-ray microtomography

Figure 8.8 depicts both the 3D rendered images and tomograms, showing qualitative differences in the trabecular and cortical microarchitecture between *Crh*$^{-120/+}$ and wild-type femora. Specifically, the rendered 3D images in the right sides of **Figures 8.8A and B** reveal trabeculae in bone in the proximal and distal ends of the *Crh*$^{-120/+}$ femur to be much thinner compared to wild-type. Further, a striking difference in the cortical microstructure between *Crh*$^{-120/+}$ and wild-type mice can be observed from the tomograms (left sides of **Figure 8.8A and B**). The *Crh*$^{-120/+}$ mice cortices were much thinner and more porous compared to the wild-type cortices. The porous cortical structure is, however, not distributed symmetrically around the bone axis, but observed primarily in the anterior section. In the anterior region, the porous tissue was observed exclusively in the endosteal region of the *Crh*$^{-120/+}$ cortex.

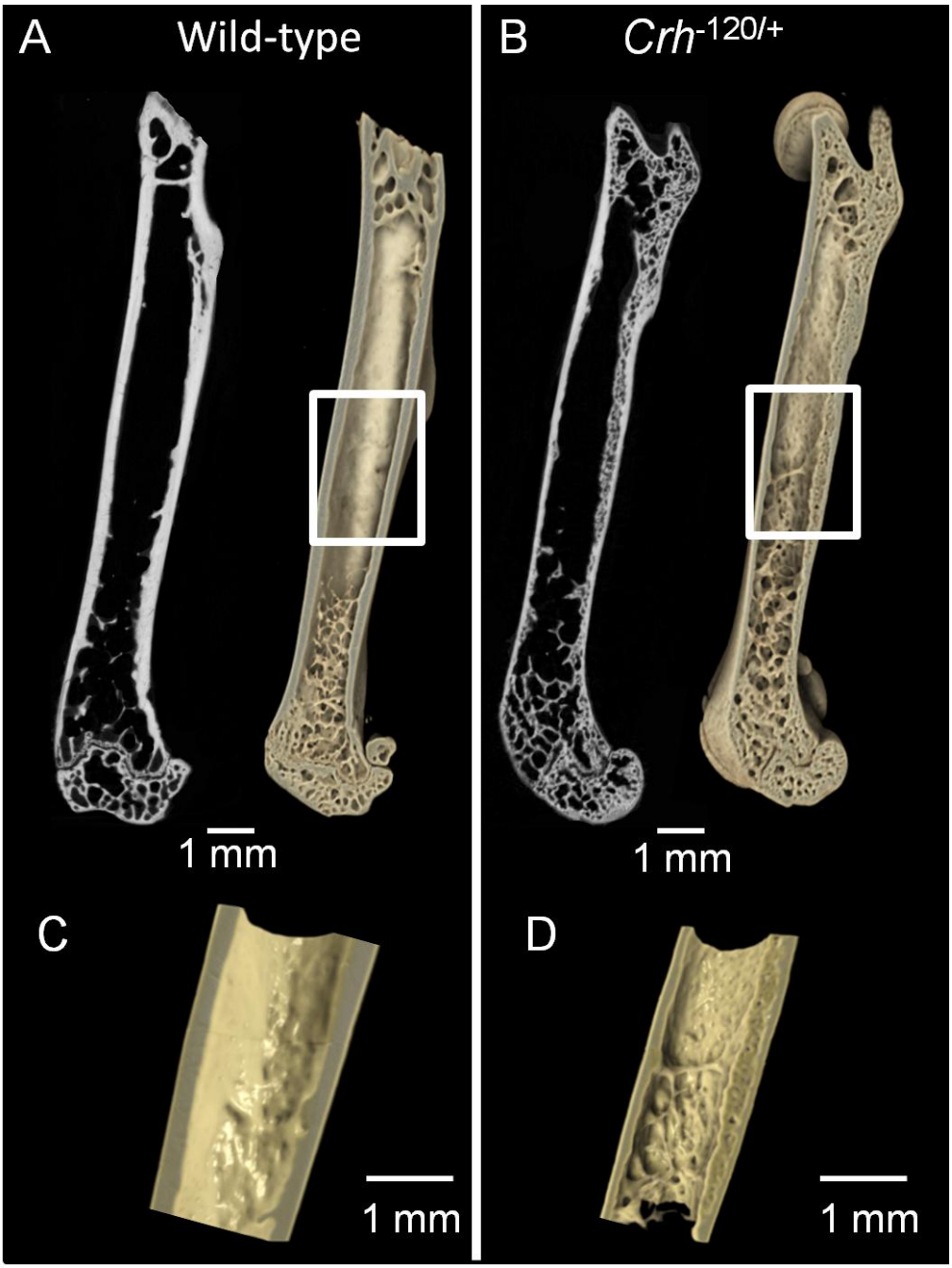

Figure 8.8: ***MicroCT images collected from longitudinal cross section of mice femur*****. (A) Tomogram (right) and 3D rendering (left) of a longitudinal cross section of the wild-type mouse femora. (B) Tomogram (right) and 3D rendering (left) of a longitudinal cross section of the *Crh*$^{-120/+}$ mouse femora. (C) and (D) 3D rendering of mid-diaphysis region of wild-type and *Crh*$^{-120/+}$ respectively showing the regions used to obtain the mechanically tested samples**

8.3.4 BSE imaging and quantitative analysis

BSE images were collected from femoral transverse cross-sections of the wild-type (**Figure 8.9A)** and *Crh*$^{-120/+}$ (**Figure 8.9B)** mice. It was observed that cortical microstructure of the *Crh*$^{-120/+}$ mice femora was markedly different to the wild-type mice cortical structure. BSE images of transverse cross-sections wild-type mice showed a uniform cortical thickness, whereas in the *Crh*$^{-120/+}$ mice, the posterior cortex was substantially thinner compared to the anterior cortex. Furthermore, the anterior, lateral and medial cross sections of *Crh*$^{-120/+}$ femora had a very large fraction of resorption cavities. In contrast, wild-type femoral bone was uniformly dense around the full cortex. High magnification BSE image (**Figure 8.9A** *bottom*) of the wild-type cortex shows uniformly distributed lacunae. However, in *Crh*$^{-120/+}$mice osteocytic area is low compared to the wild-type. The most striking observation was that *Crh*$^{-120/+}$ mice cortices had numerous localised cement lines surrounding low mineralised tissue (**Figure 8.9B (i)**) near the resorption cavities, which were absent in the wild-type cortices. These structures were around 50 × 50 µm in area, surrounded a significant number of osteocytes and localised to the endosteal cortex. Alignment of the osteocyte lacunae was determined for wild-type and *Crh*$^{-120/+}$ mice femoral longitudinal mid diaphysis cortex. Two representative images from wild-type and *Crh*$^{-120/+}$ mice femora are shown in **Figure 8.10A** and **B** respectively. The direction of the long axis of the lacunae was marked by arrows. It was observed that all the lacunae were aligned along the long axis of the bone samples in wild-type mice. In contrast, in *Crh*$^{-120/+}$ lacunae were randomly orientated indicating a disrupted osteocyte network.

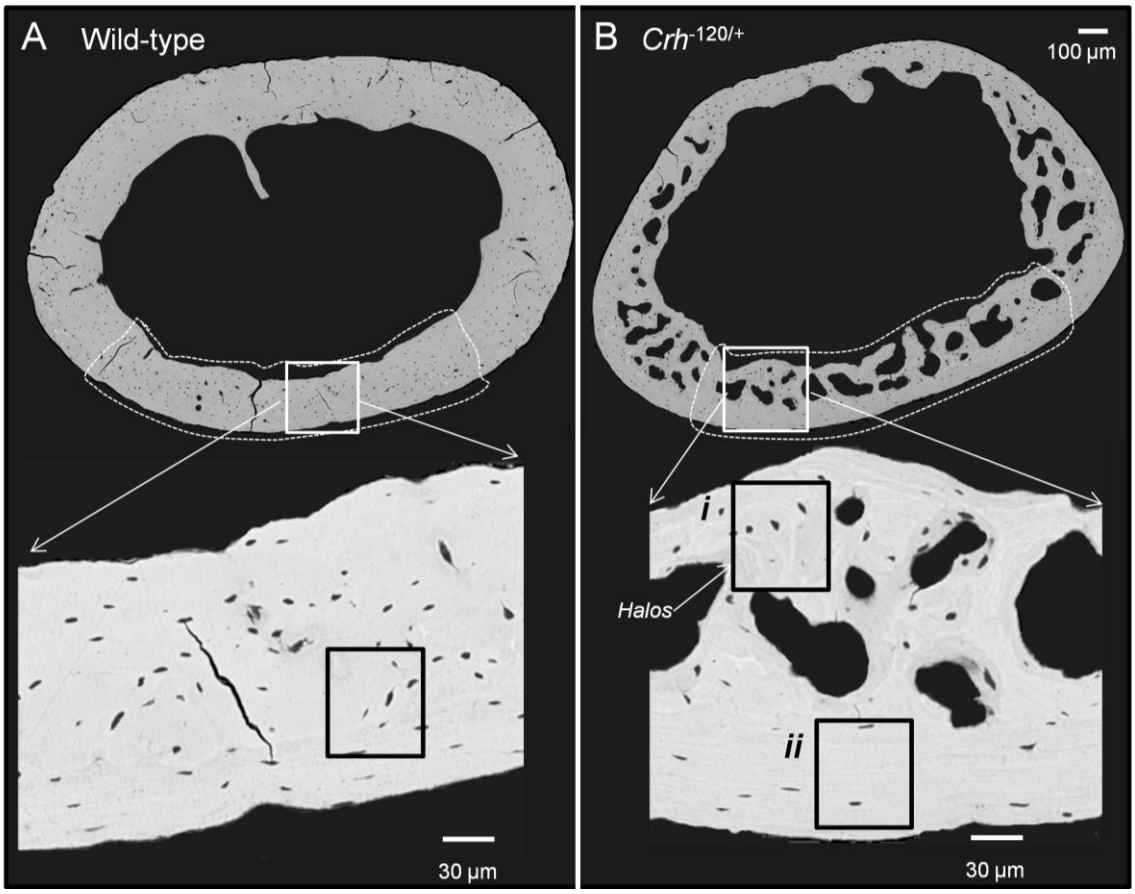

Figure 8.9: Backscattered scanning electron microscopy images collected from the mid shaft (transverse cross section) of the cortical bone of the wild-type (A) and *Crh*$^{-120/+}$ mice (B). Top image are full transverse cross section and areas surrounded by white dash lines represent cross section of mechanically tested sample. Higher magnification BSE images shown in the bottom panel are obtained from the anterior regions (white squares in top images) of the cortex. In *Crh*$^{-120/+}$ bone two distinct regions were observed. Dark grey sections (i) surrounded by white bands (cement lines) were observed near resorption cavities in *Crh*$^{-120/+}$ bone. Areas (50 × 50 µm) surrounded by black squares (*i* and *ii*) in bottom panel of A and B were used for quantification of mineralisation parameters.

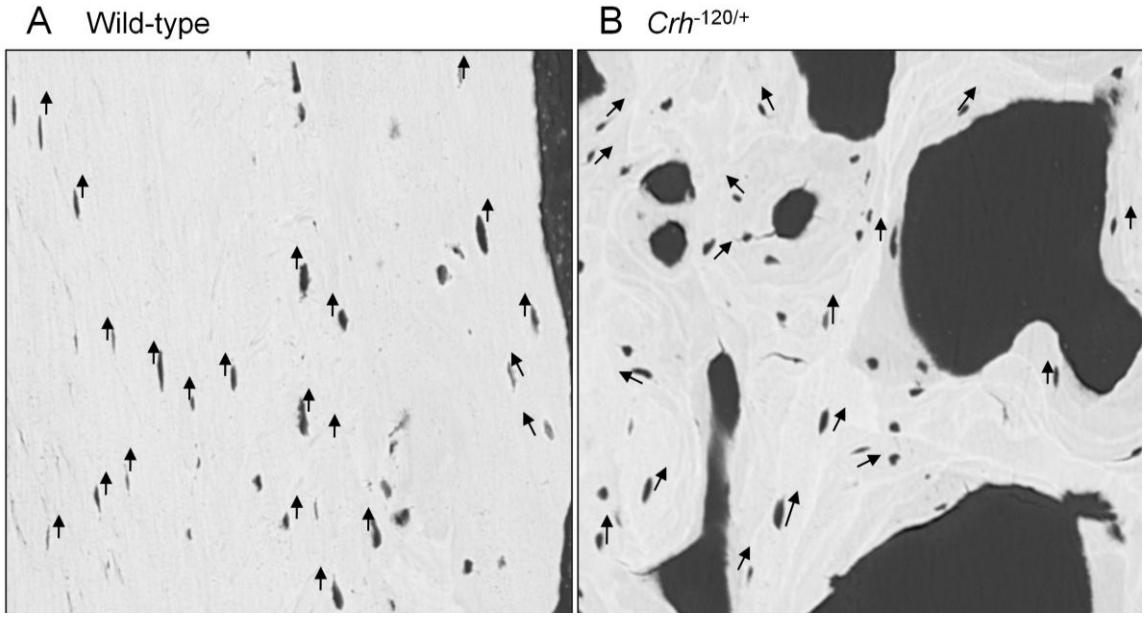

Figure 8.10: Backscattered scanning electron microscopy images collected from longitudinal sections of the cortical bone. Osteocyte lacunae orientation of mechanically tested bone sample was determined for wild-type (A) and *Crh*$^{-120/+}$ (B). Arrows show direction of the elongated lacunae long axis.

BMDD histograms (**Figure 8.11A**) were plotted for *Crh*$^{-120/+}$ and wild-type femoral transverse cross sections. Since very distinct regions of mineralisation was observed on the *Crh*$^{-120/+}$ mice femora as reported above, both regions (**Figure 8.9B i and ii)** were used separately for quantitative analysis. As shown in **Figure 8.11A** the BMDDs from *Crh*$^{-120/+}$ mice showed a lowered mineral content compared to the wild-type. Furthermore, BMDDs obtained from two distinct regions of *Crh*$^{-120/+}$ femora showed clear differences between each other. The Ca_{mean} was lowest at regions (area surrounded by the cement lines) near the resorption cavities in *Crh*$^{-120/+}$ mice (29.17±0.47 S.D.) as shown in **Figure 8.11B.** However, Ca_{mean} was significantly greater (p<0.01) at the regions (**Figure 8.9B *ii***) away from resorption cavities (30.23±0.48 S.D.) in the periosteum of the *Crh*$^{-120/+}$ cortex. In contrast to both regions in *Crh*$^{-120/+}$ mice, wild-type mice (31.65%±0.6 S.D.) had significantly higher mineral concentration. Ca_{FWHM}, which is the measure of the homogeneity of the mineralisation across the cross section, was highest at regions around the resorption cavities (5.57±0.82 S.D.) in *Crh*$^{-120/+}$ mice as shown in the Figure 7C. However, Ca_{FWHM} (**Figure 8.11C)** was significantly lower

(*p<0.01)* in regions near periosteal surfaces (4.24±0.29 S.D.) away from the resorption cavities compared to the areas surrounded by cement lines. In contrast to *Crh*$^{-120/+}$ mice bones, wild-type mice had significantly lower (*p<0.01)* Ca_{FWHM} (3.67±0.2 S.D.).

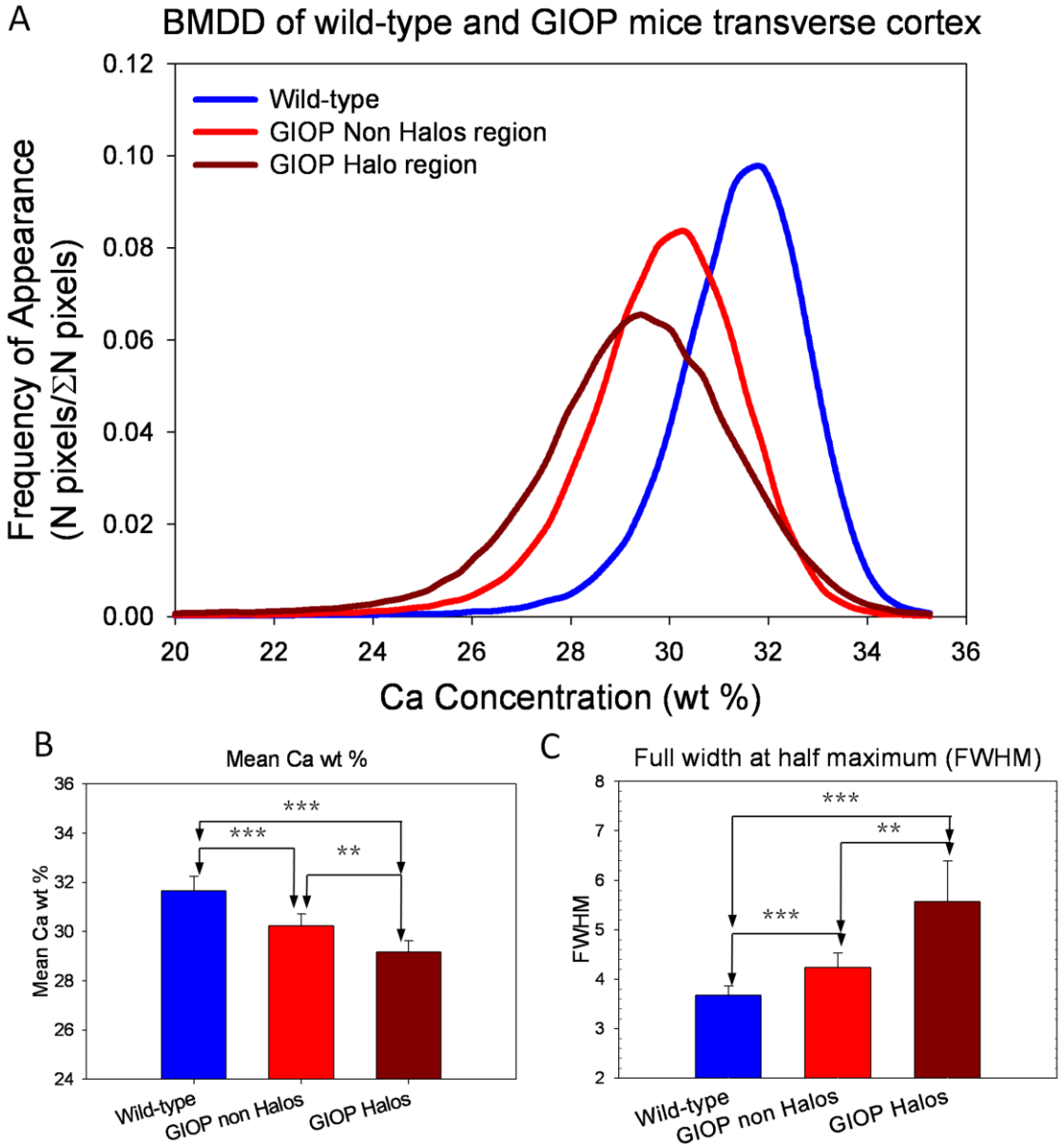

Figure 8.11: ***Quantitative backscattered scanning electron microscopy.*** **(A) Bone mineral density distribution (BMDD) was produced for wild-type (blue)** ***Crh***$^{-120/+}$ **non halos (red) and** ***Crh***$^{-120/+}$ **halo (dark red). (B, C) Mean Ca% Full width at half maximum (FWHM = distribution in local variation of Calcium content) calculated from BMDD and plotted for wild-type (blue/n = 6) and** ***Crh***$^{-120/+}$ **non halos (red/n = 6) and halos (dark red/n = 6). Errors shown are standard**

deviations. Pair-wise brackets denote statistical significance (*p<0.05, **p<0.01, ***p<0.001, ns: not significant).

8.4 Discussion

The current techniques (nanoindentation, microCT and DXA) used to assess bone quality and quantity are able to investigate the structural and mechanical properties in bone at the micro- and macro-length scales. However, bone quality changes due to osteoporosis may also occur at the ultrastructural levels (MCF ~ 100-200 nm) of the bone hierarchy, below the resolution limit of the techniques mentioned above, and far below that of clinical tools like DXA. In contrast, current study aimed to detect directly ultrastructural (fibril-level) deteriorations in cortical bone of a mouse model of GIOP by using synchrotron SAXD concurrent with *in situ* micromechanical deformation. These synchrotron measurements were complemented by microscale imaging, using microCT to measure microscale trabecular architecture, and qBSE to measure mineralisation of the bone matrix. The combination of nano- and microscale techniques enabled to obtain new insights into the functional link between bone quality alterations and increased fracture risk in GIOP.

At the macroscopic length scale, significantly reduced elastic modulus (**Figure 8.3B**) and strength (**Figure 8.3C**) were observed in *Crh*$^{-120/+}$ femora, implying changes in both bone quality and quantity. As these differences remain significant after correcting for elevated microstructural porosity in *Crh*$^{-120/+}$ (wild-type 2% and *Crh*$^{-120/+}$ 30%; **Figure 8.2**), it can be concluded that the material properties of the bone matrix are also significant factors in reducing elastic modulus in *Crh*$^{-120/+}$ by (50 %). However, the origin of these changes may lie at either or both the micro (lamellar) and the ultrastructural length scales in the bone structural hierarchy.

The MCF is a composite unit which is made out of joining the stiffer elements by a softer matrix that sustain the larger deformations (87). At this level, the deformation behaviour of MCFs in *Crh*$^{-120/+}$ is significantly different compared to wild-type, with a reduced effective fibril modulus (σ/ε_F) in *Crh*$^{-120/+}$ (**Figure 8.4B**) as revealed by *in situ* SAXD. While it is not possible yet to quantitatively explain this reduction in terms of a

mechanism at this level, it can be speculate that the alterations could be due to the reduced stiffness in extrafibrillar environment in *Crh*$^{-120/+}$ bone tissue. In **Figure 8.4C** the fibril vs. tissue strain data was plotted for the elastic region (up to the yield point). Within this linearly elastic region, it may considered that the externally applied tensile strain to be divided into a tensile stretching of the MCF and shear deformation of the extrafibrillar matrix (14, 82). Deformation of extrafibrillar matrix will only occur if the applied load is being effectively transferred from the collagen fibril (374). Effective load sharing between these two phases may prevent collagen fibrils from being exposed to larger strains (14). *In situ* SAXD results indicate that for a given strain applied to the bone tissue (in the elastic regime), mineralised fibrils in *Crh*$^{-120/+}$ deform to significantly higher strain values (up to ~0.63%) relative to the wild-type (up to ~0.3%). If the interfibrillar sliding mechanism proposed previously (14, 82) holds, the experimental result indicates that the critical interfibrillar stress is lowered, and the critical interfibrillar strain increased in *Crh*$^{-120/+}$ bone. It was observed that the fibril-strain/tissue-strain ratio in the wild-type MCFs is ~1/2 (**Figure 8.4D**), consistent with previous *in situ* SAXD on bovine fibrolamellar bone (14, 82). In contrast, the fibril-to-tissue strain ratio for *Crh*$^{-120/+}$ bone is slightly over 1, although the large experimental error bars include a ratio of 1.

However, these experimental facts pose a problem for the previous interpretation in terms of a nanoscale shearing mechanism. In an interfibrillar shearing mechanism for bone, the increase in fibril-to-tissue strain ratio occurred when the degree of mineralisation of the extrafibrillar matrix increased (82). In contrast, qBSE results (**Figure 8.11B**) show that the degree of mineralisation is reduced in *Crh*$^{-120/+}$ bone. While it is uncertain that the reduced microscale mineral concentration from qBSE imaging implies a concurrent reduction in mineralisation at the extrafibrillar matrix level, it is hard to conceive a condition where the extrafibrillar mineralisation would be increased in *Crh*$^{-120/+}$. Thus, it can be concluded that the simple, uniaxial interfibrillar shearing model, proposed previously (82), cannot fully explain observed *in situ* deformation from *Crh*$^{-120/+}$ bone. As the fibril orientation distribution (**Figure 8.5A**) and mineral degree of orientation (**Figure 8.6 and 8.7**) are more random in *Crh*$^{-120/+}$ than in wild-type, it is highly likely that alterations in lamellar architecture at the microscale and mineral

particle structural orientation in *Crh*$^{-120/+}$ may also play a critical mechanical role. To fully clarify this question, studies on *Crh*$^{-120/+}$ fibril-deformation mechanisms at a range of developmental time-points, complemented by mineral phase strain measurements using WAXD (14, 87), will be necessary.

The qBSE measurements of a reduced mineralisation in *Crh*$^{-120/+}$ (**Figure 8.11**) demonstrate that endogenous steroid production reduced overall mean mineral content and increased microscale heterogeneity of the mineralisation compared to wild-type. The overall reduction in mineral content and the increased heterogeneity (schematically shown in **Figure 8.12**) in *Crh*$^{-120/+}$ could be occurring due to adverse effect of glucocorticoid treatment on cellular activities as described previously (178, 369). Glucocorticoid treatment shortens the secondary mineralisation in *Crh*$^{-120/+}$ due to the reduced formation of osteoid by osteoblasts and prolonged survival of osteoclasts. Resorption cavities and surrounding poorly mineralised regions observed in BSE images from *Crh*$^{-120/+}$ cortex (**Figure 8.9B**) provides experimental evidence for alteration in cellular activity. The localised qBSE measurements of the *Crh*$^{-120/+}$ bones (**Figure 8.11**) demonstrated lower Ca_{mean} (**Figure 8.11B**) and higher FWHM (**Figure 8.11C**) at the regions surrounded by the cement lines in the endocortical surface relative to the periosteal cortex. These poorly mineralised regions were only observed in *Crh*$^{-120/+}$ mice bones surrounding the osteocyte lacunae which may similar to the halo regions observed in a previous study (178)**.** A few previous studies have argued that glucocorticoid treatment has a localised effect by removal of mineral by leaching and proteolytic process of osteocytes (178, 375), but the view osteocytes can directly carry out osteolysis to remove mineral has been contested for a range of disease (not including GIOP) (318). These demineralised regions were localised (**Figure 8.9B**) to the cortico-endosteal region, consistent with a previous study (Bentley et al 2012 manuscript in preparation). Bentley et al 2012 also found overall reduced osteoblast number and reduced osteoblasts coverage in the cortico-endosteal bone compared to the other regions in the *Crh*$^{-120/+}$ bone, indicating that the osteoblast-inhibitory effect of glucocorticoid treatment is more pronounced in the endosteal cortex compared to the other regions.

The microstructural alterations observed in microCT (**Figure 8.8**) and BSE imaging (**Figure 8.9**) may also affect mechanical toughening mechanisms at the lamellar and resorption cavity level (1–100 μm), which are 1-2 levels above the fibrillar deformation investigated by the *in situ* SAXD data reported above; although in the current study microstructural deformation was not measured. Crack bridging and crack deflections are two extrinsic toughening mechanisms that contribute to the fracture resistance at the micrometer (10 to 100 μm) length scale of the bone hierarchy (376, 377). The direction of the crack path (crack deflection) and its interaction with osteocyte lacunae and intra-cortical pores are the principal driving mechanisms of crack propagation (98, 378) in human cortical bone. BSE imaging (**Figure 8.9**) shows that the frequency of osteocytes is much lower in $Crh^{-120/+}$ relative to the wild-type, indicating that diminished crack deflection leads to crack propagation and increased fracture risk. The demineralised structures observed in the $Crh^{-120/+}$ mice cortices (**Figure 8.9B** *bottom*) are surrounded by cement lines, which may act as locations for initiation of cracks leading to catastrophic failure (87). Osteocytes are believed to be responsible for mechanosensation of external loading and the appearance of cracks, via their canalicular network, and to stimulate bone remodelling (52). However, in osteoporotic conditions such as the GIOP condition considered here, the osteocyte network is disrupted due to the apoptosis of osteocytes (179, 379), which may result in a failure to replace damaged bone (368), resulting in accumulation of microcracks. Several studies have also suggested that the apparent enlargement of lacunae size in GIOP has also been linked to reduced local mineralisation (**Figure 8.11B**) (177, 278). However, the direct relationship between increased lacunae size and possible initiation of demineralisation around the osteocytes has not been studied yet (278). Enlargement of lacunae is also associated with reduction in load dissipation ability of bone and may influence the pattern of crack propagation around lacunae, thus potentially increasing fracture risk in $Crh^{-120/+}$ bone (380). Using confocal microscopy it was found previously that architecture of the osteocyte network mirrors the collagen fibril organisation in the matrix (381). It was shown in the current study osteocytic network in $Crh^{-120/+}$ bone is randomly oriented compared to the wild-type (**Figure 8.10**) indicating a disorganised collagen matrix deposited by glucocorticoid affected osteoblasts.

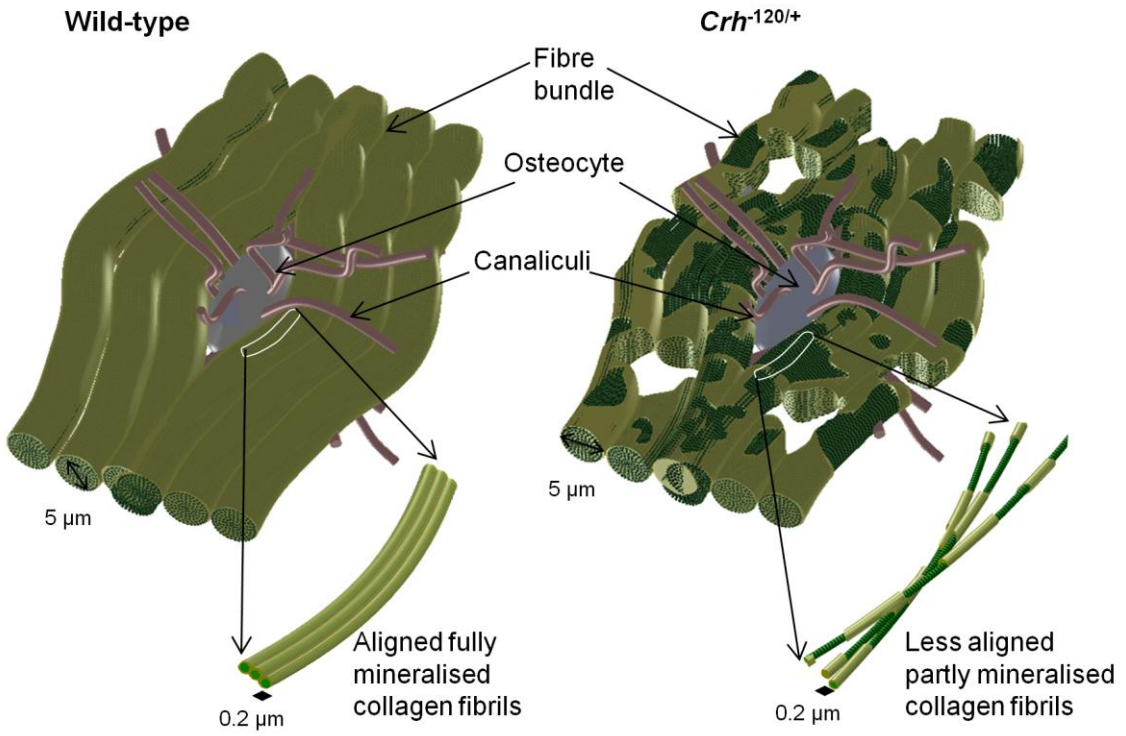

Figure 8.12: Schematic representation of the bone matrix in wild-type and *Crh*$^{-120/+}$ conditions at the microscale and nanoscale. As qBSE results only provide experimental information at micrometer length scale, hence schematic was drawn with an osteocyte (10 to 15 µm) and several fibre bundles (5 to 10 µm). In wild-type mice, fibre bundles are fully mineralised, whereas *Crh*$^{-120/+}$ bone has micro pores and less mineralised. These less well mineralised structures are more localised around the osteocytes. At the fibrillar level it was speculated that collagen fibrils are partly mineralised along the length of the fibril in the *Crh*$^{-120/+}$ condition. At this level, the wild-type MCFs are fully covered with mineral. However, the mineralised fibrils from the *Crh*$^{-120/+}$ halo regions are partly mineralised (extra and/or intra) and less orientated. These structural alterations in *Crh*$^{-120/+}$ could be explained by the nano mechanical data obtained in this study

8.5 Conclusion

In this study it was demonstrated that in a mouse model for glucocorticoid-induced osteoporosis, both the mineralisation distribution at the microscale as well as the fibrillar deformation mechanisms at the nanoscale are significantly altered when compared to wild-type litter mates. At the microscale, a lower mineral content and increased heterogeneity in mineralisation near osteocytes is observed, as illustrated in the schematic (**Figure 8.12**). In contrast, wild-type bone is more uniformly mineralised as

shown by the qBSE results. Concurrently, at the nanometre length scale, it was found altered fibrillar deformation (increased extensibility and lower fibril modulus) in *Crh*$^{-120/+}$ mice bone, as well as less oriented fibrils. In this study, the altered deformation mechanisms at the nanoscale – increased flexibility and lower fibril modulus – in conjunction with altered microstructural toughening mechanisms due to heterogeneous mineralisation was proposed. They are critical factors leading to the increased macroscopic fragility in GIOP bone.

Chapter 9

Material Level Deformation Mechanisms in Aged Bone

9 Material Level Deformation Mechanisms in Aged Bone

9.1 Synopsis

The studies described in the previous chapters have investigated how alterations in bone quality in two metabolic bone disease types – hypophosphataemic rickets and glucocorticoid-induced osteoporosis – may increase fracture risk and reduce mechanical competence via changes in fibrillar level deformation. In this chapter, human ageing was considered as a phenomenon in itself (separate from any induced disease phenotype), and the synchrotron techniques developed previously were applied to a mouse model of premature ageing. Specifically, it was considered whether changes in bone material quality with ageing (which may include increased cross-linking in the collagen matrix (36, 87), and changes in mineral particle composition and size (199)) may reduce mechanistic competence at the fibrillar level, independent of the BMD reductions concurrently observed (186) at organ level. In this regard, recent studies have shown that the structure and mechanical properties degrade with age, independent of BMD (186, 382), validating the project as worth investigation.

Bone changes in both quality and quantity with ageing, and the direction of the changes are generally in the direction to increase fracture risk. In a previous study, it was found that both the intrinsic resistance to fracture and the increasing resistance to the propagation of the crack reduce with age (137). Increased mineralisation (mean mineral concentration) with aging has also been shown to contribute in the reduction in bone deformability and fracture toughness (187, 383). Several studies reported that cortical bone becomes more brittle and thinner and the individual trabecular struts weaken with age (187-189). It has also shown that changes in collagen structure is associated with increasing brittleness due to the alterations in its cross linking profile (87) as discussed in **Chapter 1** (sections 1.3 and 1.9.5). X-ray diffraction studies on homogenized iliac crest biopsies showed bone mineral crystal size and the maturation changed as a function of age. Specifically, mineral crystal size increased during the first 25 to 30 years and then decreased thereafter, although a slight increment was observed in oldest patients of age 85 to 95 years (199). Mechanical studies have also shown that structural and material

alterations in bone quality during ageing are relevant. Significant differences in fatigue life of male human younger and older donors were observed under physiological relevant loadings involving simultaneous axial and torsional loading, suggesting that age-related variations in bone quality reduce the resistance of older bone to multi-axial failure (384). Recently, in situ SAXS/WAXD was applied to human bone biopsies and showed that age related nano-structural changes has an adverse influence on toughening mechanisms of cortical bone at different hierarchical levels. Specifically, they claimed that increased nonenzymatic collagen cross linking in aged bone leads to reduction in plasticity at the fibrillar level (87).

With these findings in mind, the goal of the research presented in the current chapter is to apply *in situ* SAXS/WAXD with mechanical testing on a mouse model of premature ageing (removal of the klotho gene) (290, 292). The klotho gene is mainly expressed in specific cells and tissues (predominantly in the kidney) and not all the organs affected in klotho mice were the result of the klotho gene (290). Most relevant for the present study, however, is the fact that the klotho knockout mice exhibited multiple phenotypes very similar to those observed during human ageing. These include decreased bone formation and increased turnover at early stages of development (290). Klotho deficient mice have shown growth retardation after 3-4 weeks of age and begin to become inactive, weak and die prematurely at about 8-9 weeks. They exhibit decrease in body movement and gait disturbance, spontaneous activities reduced with age, abnormal walking pattern, decreased mean stride lengths and deposition of calcium in tissues and organs. Genital organs of klotho mice are lost at some point after normal development and both sexes are incapable of mating. These multiple phenotypes include several very similar to those observed during human ageing such as Parkinsonian gait of aged human's emphysema (385) and Monckeberg's arteriosclerosis (386).

The experiments performed in this chapter will be focussed on both deformation (elastic) and toughening (plastic) mechanisms at the tissue and material level. Specifically collagen matrix stiffening in klotho mice with respect to the controls, and the effect of this stiffening on fibril strain will be investigated. In addition to *in situ* mechanical

testing with SAXD, cortical and trabecular micro-architectural changes as functions of ageing will be studied using SEM and microCT respectively.

9.2 Methods

9.2.1 Animals

Animals were anaesthetised with sodium pentobarbitone (this activity was performed at the Medical Research Council); internal organs were removed from the body cavity and femora was dissected from the skeleton and stored in -20 °C until used. Mouse femora (klotho (Hom) = 5, klotho (Hetero) = 5 and wild-type = 4) from 5 weeks old female klotho and wild-type littermates were used for in-situ mechanical testing.

9.2.2 Sample preparation for in-situ tensile testing

Mouse femora was initially sectioned into bone strips dimensions of 5 mm × 2 mm × 0.2 mm using the method explained in **Chapters 3 and 8**. Subsequently, these samples were included at their ends in dental cement, and the mid-diaphysis was micro milled to obtain a sample with gauge length dimensions of 5 mm × 1 mm × 0.2 mm.

9.2.3 In-situ tensile testing with microfocus SAXD

The fibrillar and tissue level mechanical properties of hydrated cortical bone from femur mid diaphyses of 5 weeks old wild-type (n = 4), klotho (Hetero) (n = 5) and klotho (Hom) (n = 5) mice were measured using in situ micro mechanical tensile testing combined with microfocus SAXD at BL I22 (DLS).The samples were loaded at a constant velocity of 1 µm/second (equivalent to a motor strain rate of 0.02 %/s) while in the path of a microfocus X-ray beam. A schematic of the experimental setup was shown in **Chapter 3**. Samples were maintained in physiological saline (phosphate buffered solution) in a fluid chamber in the tester during tensile testing. In order to reduce the influence from the radiation damage to the mechanical properties of the bone, SAXD (exposure time was 1 second) spectra was collected every 0.05% tissue strain up to failure (~ 0.5 -1.0%) at different locations, by translating microfocus sample platform in the vertical direction with a step size of 50 µm between consecutive spectra. The schematic of this setup is shown in **Figure 9.1.** Tissue strain was measured by non

contact video extensometry as explained in **Chapter 4** section 4.2.1.1. The SAXD data reduction procedure described previously (**Chapter 4** section 4.2.2) was used to calculate the fibril strain for an applied external load levels. The tensile load on the bone specimen was continuously measured, along with tissue and fibril strain, during the strain to failure test (**Figure 9.1**). Following the measurement, the porosity corrected stress was calculated for each tensile test as previously explained in **Chapter 4** section 4.2.6. The data obtained from all samples were plotted together, and binned in both fibril and tissue strain. Both fibril and tissue strain bin widths were taken to be 0.05%. The procedure was applied for each sample, and then the sample data were combined as a function of genotype and age. That is, for each individual tensile test, % fibril strain values were binned into every 0.05 % fibril strain, and if more than one data point from same sample lay in a bin, average value was calculated and taken as the sample value for that bin. Following this, for each genotype, the average and standard deviation of the binned values were calculated.

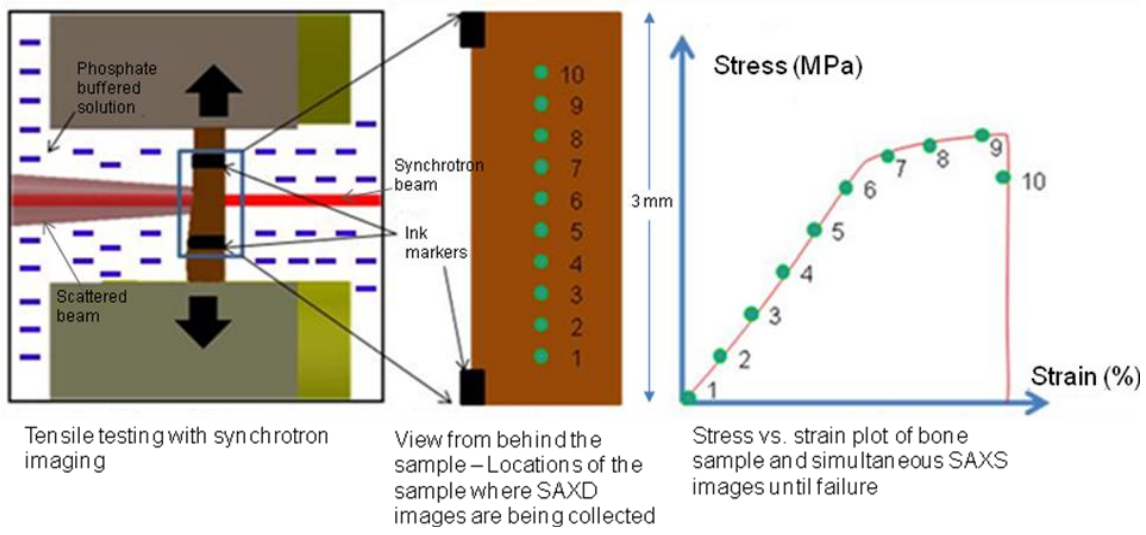

Figure 9.1: Schematic of the testing setup: Sample is immersed in the fluid chamber by securing in the grips. The CCD camera views the sample at a 90° angle to the X-ray beam as not to block the beam path. Black lines on the bone are reference markers for tissue strain measurements. (B) Zoomed in view of the tensile testing sample. Ten scan data points are numbered schematically on the sample. Each scan point was measured with SAXD, with successively higher strain values corresponding to higher numbers, as shown in (C), where a schematic representation of tensile testing stress vs. strain curve is shown.

9.2.4 X-ray microtomography

One sample each from wild-type, klotho (Hom) and klotho (Hetero) was used in microCT to qualitatively assess the cortical architecture of mice femur. The internal longitudinal cross section was investigated by slicing the reconstructed tomograms using Tomview. Volume-rendered images were also produced, to view the 3D structure of trabecular bone, and to qualitatively analyze trabecular connectivity, thickness and porosity.

9.2.5 BSE Imaging

High magnification BSE images (300 µm × 300 µm) were acquired on polished transverse cross-sections of femoral mid-diaphysis (anterior region) which had previously been used for microCT. Samples were dehydrated and embedded in PMMA. One femur from each category was transversely (PMMA block) sectioned into two halves using diamond saw under constant irrigation. Following this, the proximal end was prepared for BSE imaging as described previously (Refer **Chapter 4**, section 4.2.6 for details).

Statistical analysis

Single factor ANOVA test was performed to identify statistically significant (p<0.05) differences in tissue failure strain, failure stress, tissue modulus, effective fibril modulus, fibril to tissue strain ratio and collagen fibril orientation (FWHM) between wild-type, klotho (Hom) and klotho (Hetero) mice. Following the ANOVA test, Student's t-test was performed between every two groups if a significant difference was found from the ANOVA test across all groups.

9.3 Results

The stress versus tissue strain (**Figure 9.2**) for klotho mice exhibit clear qualitative differences across the three strains. Klotho mice have lower ultimate strain to failure compared to wild-type mice. The reduction in strain to failure is more pronounced for Klotho (Hom) mice relative other two groups. The reduction in ultimate strain is seen to be mainly due to a reduction in the yield strain. It was observed that wild-type mice has

larger plastic region compared to both klotho mice groups. In contrast to strains, yield and failure stresses were qualitatively similar between groups.

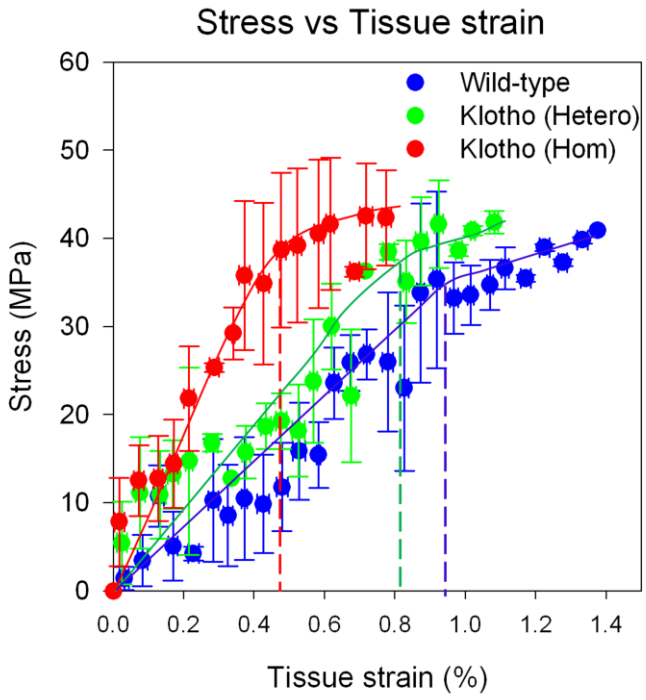

Figure 9.2: Macro mechanical tensile binned data. Stress vs. measured tissue strain % for wild-type (n = 4/blue), klotho (Hetero) (n = 5/green) and klotho (n = 5/red) mice. Solid lines are guides to eye. Data plotted for each category obtained from a range of samples (wild-type = 4, klotho (Hetero) = 5 and klotho (Hom) = 5)), binned as per the proceduire in material and methods. Dash lines (wild-type – blue, klotho (Hetero) – green, klotho (Hom) - red) show the yield point for each curve. Error bars are standard deviations. The yield point was defined as explained in Chapter 4 (Figure 4.8).

Average failure tissue strain and stress were plotted for all three groups in **Figure 9.3A and B** respectively. Single factor ANOVA showed significantly differences in failure strain across groups. The highest failure tissue strain was observed in wild-type mice (1.2 % ± S.D. 0.5) and it is significantly ($p<0.05$) different from both klotho mice groups (0.8 % ± S.D. 0.4). The failure strain is not significantly different ($p>0.05$) between klotho (hetero) and klotho (hom) mice. Single factor ANOVA showed that average failure stress was not significantly different ($p>0.05$) across wild-type and klotho mice groups.

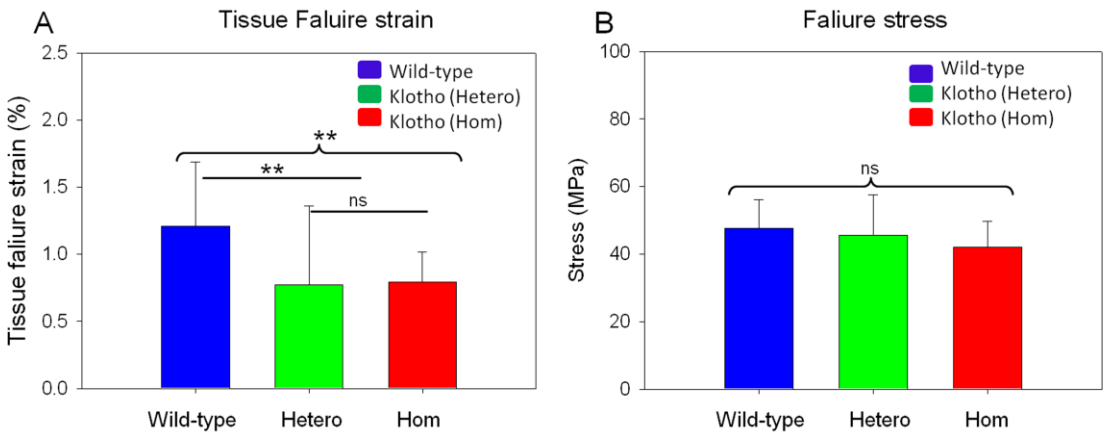

Figure 9.3: Average (A) tissue failure strain and (B) failure stress plotted for wild-type (blue), klotho (Hetero) (red) and klotho (Hom) (green) mice. Error bars are standard deviations. Curly brackets and pair wise solid lines show ANOVA and student-t test results respectively. (*p<0.05, **p<0.01, ***p<0.001, ns = not significant). When no significant difference was found with ANOVA, t-tests were not performed.

The elastic response of the tissue was investigated by considering the linear region of the stress-strain curve. The linear region for each sample was identified by tracking the slope of the stress-strain curve, and identifying the point at which the tangent modulus reduces 10% or less compared to its initial value (refer **Chapter 4**, **Figure 4.8**). **Figure 9.4** shows the average tissue elastic moduli to be significantly ($p<0.05$) larger in klotho mice relative to wild-type mice. However, elastic modulus was not significantly ($p>0.05$) different between klotho (Hom) and klotho (Hetero) animals.

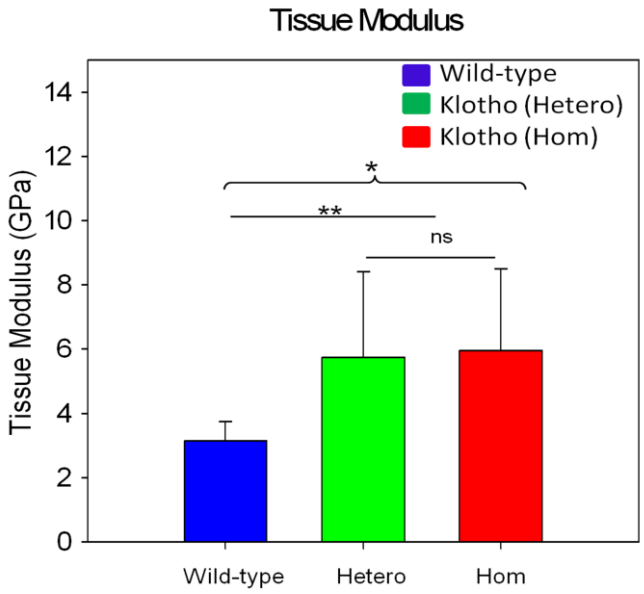

Figure 9.4: Average tissue modulus plotted for wild-type (blue), klotho (Hetero) (red) and klotho (Hom) (green) mice. Error bars are standard deviations. Curly brackets and pair wise solid lines show ANOVA and student-t test results respectively (*p<0.05, **p<0.01, ***p<0.001, ns = not significant).

To investigate the fibrillar level mechanical behaviour, the binned stresses were plotted against binned fibrillar strain values for wild-type, klotho (Hom) and klotho (Hetero) (**Figure 9.5**). It is immediately clear that the difference between the two klotho mutants (Hom and Hetero) is considerably reduced in this representation. Klotho mice (Hom and Hetero) had larger slope and smaller ultimate fibril strains compared to wild-type mice. The increase in ultimate fibril strain is mainly due to a larger fibril yield strain in wild-type mice compared to klotho (Hom) and klotho (Hetero) as seen in **Figure 9.5**, which can also be viewed as an increased strain range for elastic deformation (~ 0.35 % for Hom/Hetero vs. 0.85% for wild-type). The slope of linear portion (**Figure 9.6A**) of the stress/fibril strain curve (effective fibril moduli ($E_f = d\sigma/d\varepsilon_f$) as defined earlier) and average effective fibril moduli and standard deviations were calculated for wild-type and klotho mice groups (**Figure 9.6B**). The average fibril modulus for klotho mice groups (13.99 ± S.D. 3.45 GPa) is significantly ($p<0.01$) larger than the wild-type (4.27 ± S.D. 0.81 GPa). However, fibril modulus was not significantly ($p>0.05$) different between klotho Hom (13.39 ± 5.49) and Hetero (14.61 ± 3.46) mice groups.

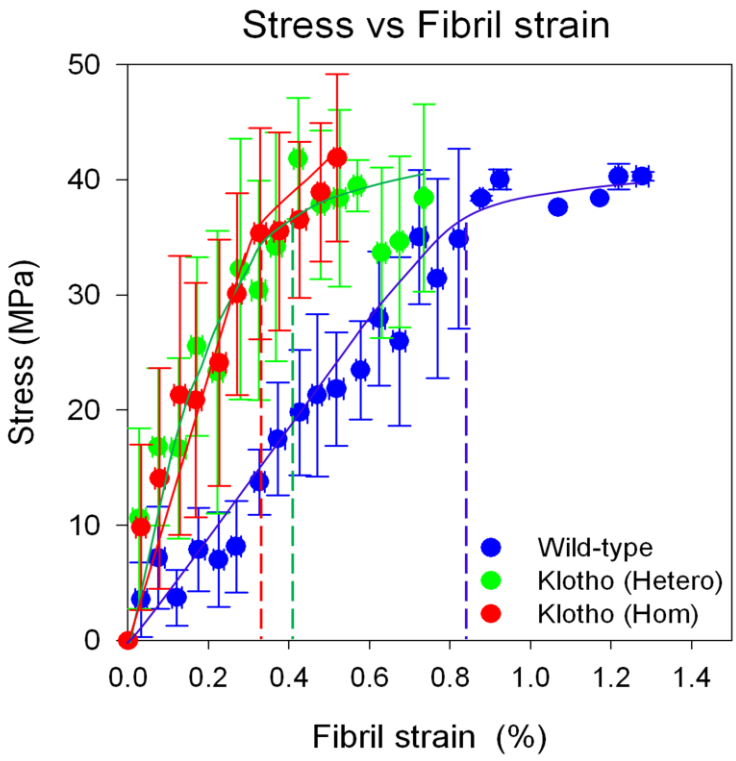

Figure 9.5: Nanomechanical tensile test data in a binned representation. Stress vs. measured fibril strain % for wild-type (n = 4/blue), klotho (Hetero) (n = 5/green) and klotho (Hom) (n = 5/red) mice. Solid lines are guides to eye. Dash lines (wild-type – blue, klotho (Hetero) – green, klotho (Hom) - red) show the yield point for each curve. Error bars are standard deviations. The yield point was defined as explained in Chapter 4 (Figure 4.8).

The fibril strain can also be plotted as a function of tissue strain. **Figure 9.7A** shows binned fibrillar strain versus binned tissue strain for wild-type and klotho groups. It can be observed that the slopes of these data were almost linear for all three groups. However, for a given external tissue strain the strain in collagen fibrils much lower (~ 30 %) in klotho mice compared to the wild-type mice. The average slope (fibril to tissue strain ratio $\varepsilon_F/\varepsilon_T$) (refer **Chapter 8**) and the standard deviations of these curves were plotted in **Figure 9.7B.** The average fibril to tissue strain ratios for klotho mice groups were significantly ($p<0.05$) lower compared to the wild-type mice.

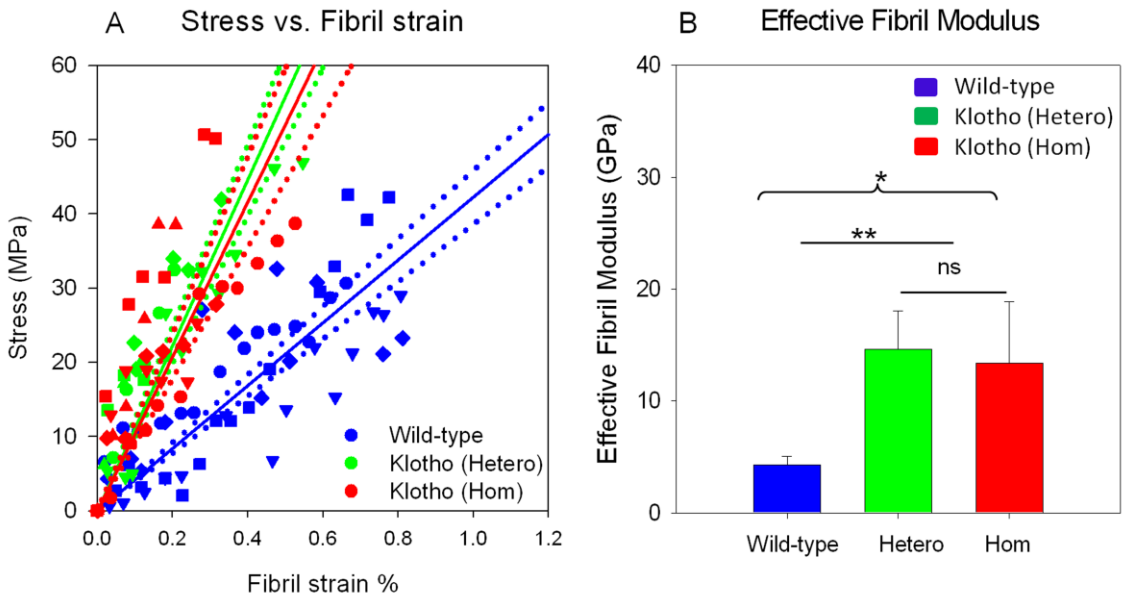

Figure 9.6: (A) Stress vs. measured fibril strain % plotted for the linear region. Wild-type (n = 4/blue), klotho (Hetero) (n = 5/green) and klotho (Hom) (n = 5/red). Solid lines are linear regressions for all sample points in each genotype. Dotted lines are 95% confidence levels for each regression line. (B) Average effective fibril modulus (Wild-type = 4, klotho (Hetero) = 5 and klotho (Hom) = 5) plotted for wild-type (blue), klotho (Hetero) (red) and klotho (Hom) (green) mice. Error bars are standard deviations. Curly brackets and pair wise solid lines show ANOVA and student-t test results respectively (*p<0.05, **p<0.01, ***p<0.001, ns = not significant).

The degree of fibrillar orientation between wild-type and klotho mice was determined from the azimuthal intensity distribution of the 3rd collagen reflection (as described previously in **Chapter 4**). It was found that the FWHM (**Figure 9.8**) for all three groups were similar; there was no significant ($p>0.05$) difference between them, indicating similar degree of fibrillar alignment between klotho and wild-type.

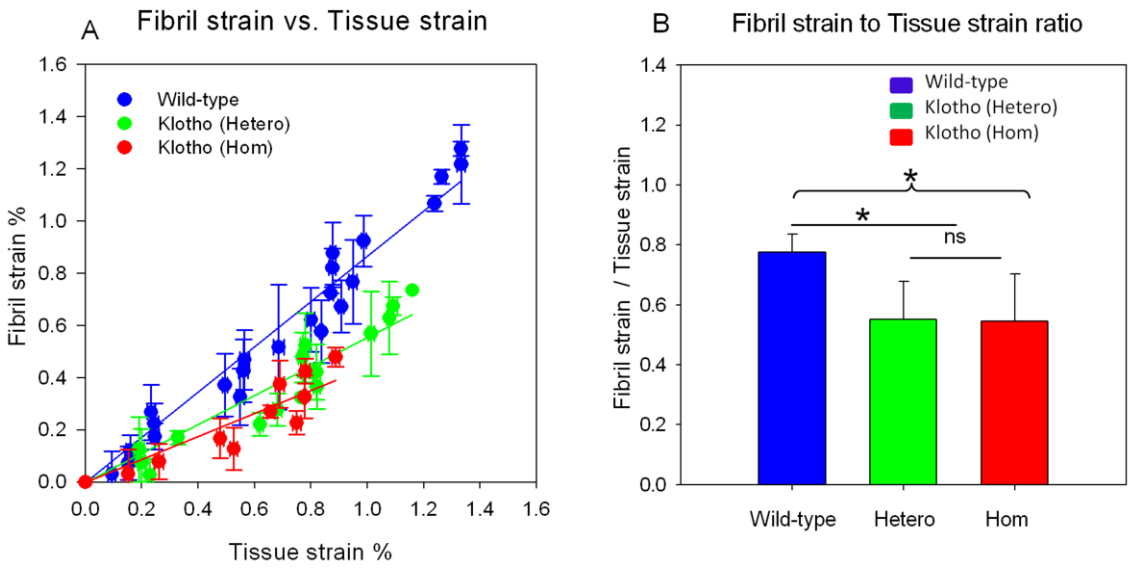

Figure 9.7: (A) Fibril strain (ε_F) % vs. tissue strain (ε_T) % as a function of disease state wild-type (blue), klotho (Hetero) (green) mice and klotho (Hetero) (green). Solid lines are regression lines for binned data (wild-type = blue, klotho (Hetero) = green klotho (Hom) = red. (B) Average fibril strain to tissue strain ratio ($\varepsilon_F/\varepsilon_T$) plotted for elastic region of wild-type (blue), klotho (Hetero) (green) and klotho (Hom) (red) mice. Error bars are standard deviations. Curly brackets and pair wise solid lines show ANOVA and student-t test results respectively (*p<0.05, **p<0.01, ***p<0.001, ns: not significant).

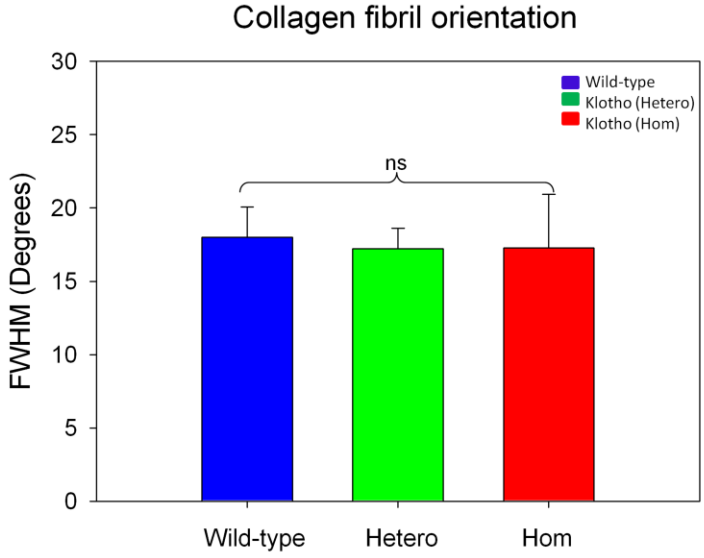

Figure 9.8: Full width at half maximum of intensity distribution of the 3rd order fibril reflection was plotted for wild-type (blue), klotho (Hetero) (green) and klotho (Hom) (red). Error bars are standard deviations. Curly brackets denote statistical significance results obtained from

single factor ANOVA test (*p<0.05, **p<0.01, ***p<0.001, ns: not significant). When no significant difference was found with ANOVA, t-tests were not performed.

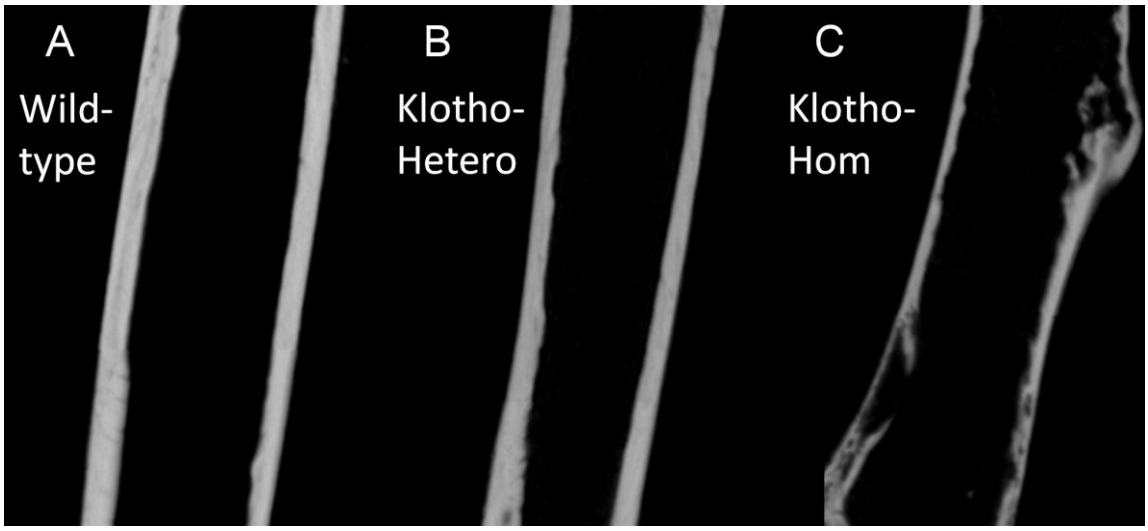

Figure 9.9: MicroCT tomograms collected from longitudinal cross section of (A) wild-type, (B) klotho (Hetero) and (C) klotho (Hom) mice

9.3.1 3D microarchitecture

The tomograms of longitudinal cross section of femora mid shaft show qualitative difference of the cortical thickness between wild-type mice and klotho mice phenotypes (**Figure 9.9**). It can be observed from these tomograms that cortical thickness of klotho (Hetero) mice and wild-type mice are similar. However klotho (Hom) mice had thinnest cortex out of three genotypes. **Figure 9.10** shows the 3D-rendered images, illustrating the trabecular microarchitectural differences between wild-type and klotho mice groups. Specifically, the rendered 3D images reveal that trabeculae in the proximal and distal ends of the klotho (Hom) femur are much thinner compared to wild-type femora. Klotho (Hetero) mice had a larger extent of trabecular network at both ends of the femur compred to klotho (Hom) mice. The lost trabeculae network is more pronounced in klotho (Hom) mice compared to wild-type and klotho (Hetero) mice. Furthermore, a striking difference in the cortical porosity between wild-type and klotho mice can be observed from the tomograms. The klotho mice cortices were much porous compared to wild-type mice. However cortical porosity in klotho (Hom) and (Hetero) mice are not different qualitatively.

Figure 9.10: 3D rendering of longitudinal cross sections of femora (A) wild-type (B) klotho (Hetero) and klotho (Hom). White ovals show the porous areas in the cortex in klotho femora. A white square shows the loss in trabecuale bone in klotho (Hom) mice.

9.3.2 2D qualitative analysis of cortical bone

BSE images were collected from 35 days old mice femoral cross sections for wild-type and klotho (Hom) and (Hetero) conditions. A qualitatively striking difference in cortical microstructure between klotho and wild-type was observed. In wild-type mice osteocyte lacunae were concentrated into the middle of the cortex (red dash polygon). In contrast,

in klotho (Hetero) mice lacunae were concentrated toward the periosteum (red dash polygon) of the cortex, whereas in klotho (Hom) it was homogeneously distributed across cortex. The most striking observation was that osteocyte lacunae of the klotho specimen were mineralised (**Figure 9.11B and C**). The boundary of the osteocyte lacunae in klotho mice cortex were demineralised, which is not seen in wild-type mice. This effect was more pronounced in klotho (Hom) mice (red arrows) compared to klotho (Hetero) mice. BSE image of klotho (Hom) mice showed very large sized resorption cavities (blue arrows) at the micro structural level.

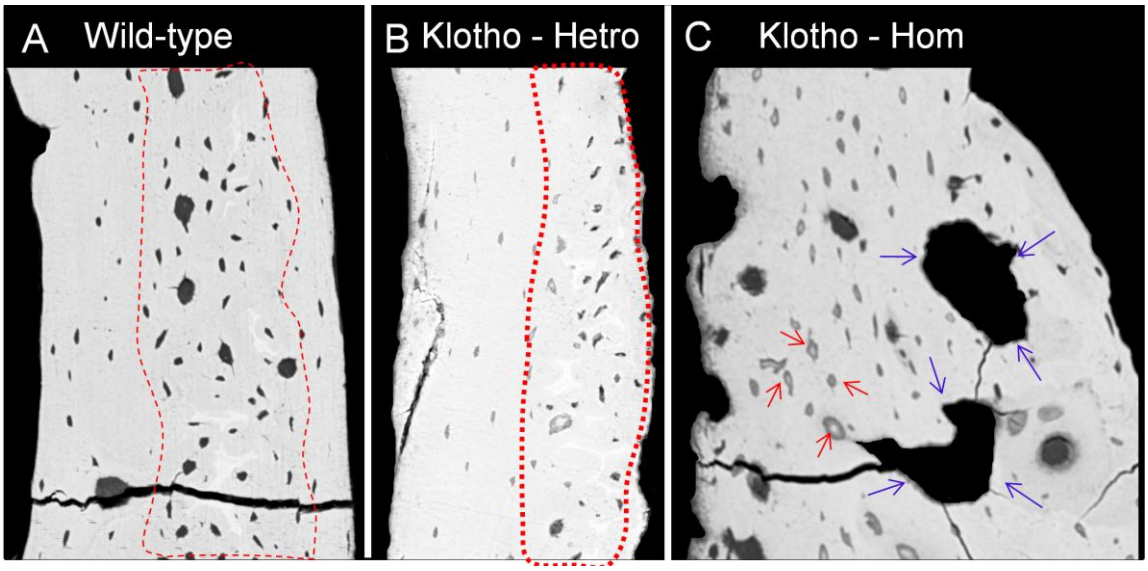

Figure 9.11: Backscattered scanning electron microscopy images collected from the anterior regions of the cortex of the mid shaft (transverse cross section) (A) Wild-type – dash line polygon was drawn around the most of the osteocyte lacunae which are concentrated into middle of the cortex (B) klotho (Hetero) mice – red dotted line polygon was drawn around the osteocyte lacunae which are concentrated to the periosteum (C) and klotho (Hom) – red arrows show the dead osteocytes and lacunae spaces are mineralised and blue arrows show resorption cavities.

9.4 Discussion

Ageing affects the fracture resistance mechanisms at different hierarchical levels of cortical bone (387, 388), and it is crucial to develop multiscale imaging techniques that can quantify these alterations. In this study, it was shown that an animal model of ageing exhibits effects consistent with an alteration in bone material quality, specifically a stiffening of the collagen fibrils, when compared to wild-type. Previously, it has been

shown that while biological ageing results in rapid bone loss, the fracture risk for older individuals may be up to 10-fold greater, when compared to younger individuals with same BMD (186). This observation provides a strong indication that increased fracture risk in ageing involves changes in bone quality as well as quantity, and the challenge has been to quantify what these changes are. However, to date there are very few studies on the mechanistically critical changes in the deformation mechanisms of the mineralised bone matrix in ageing bone, with the exception of a very recent work on human bone (87). In line with the approach taken in this thesis throughout, it was the purpose of the current study to identify whether a well-defined mouse model of ageing (the klotho gene knockout model (290, 292)) would demonstrate measurable variations in the nanoscale deformation mechanisms, which could be explained in terms of age-related bone matrix changes in the organic and/or inorganic components.

The results from macromechanical tensile tests - showing a significantly reduced tissue failure strain (loss in plasticity) in both klotho Hetero and Homo mice groups compared to wild-type animals - demonstrate a reduction in bone mechanical competence and reduced work to fracture, as expected. The increase in tissue modulus in klotho mice shows that the cortical bone tissue is (~ 100 %) stiffer compared to wild-type, which is consistent with previous macro-level mechanical testing studies (187, 188). Macromechanical results also indicate that klotho mice bones failed at a lower tissue strains (0.75 %) (**Figure 9.2 and Figure 9.3A**) compared to the wild-type bones (1.3 %), consistent with (188). Macroscopic measures of plasticity are consequences of the changed crack initiation and propagation in aged tissue (micro), as well as the lower fibrillar level deformability (nano). The direction of the crack path and how it interacts with osteocyte lacunae and intra cortical pores are principal driving mechanisms of the microcracks propagation (98, 378). In this regard, BSE images obtained in this study showed that osteocyte lacunae were mineralised in klotho mice. Therefore stiffened lacunae in klotho mice failed to deflect the crack path, thereby deteriorating the toughening mechanisms at the scale of 1 µm to 100 µm. Also a shift to a higher tissue mineral content due to the mineralised osteocyte lacunae will yield stiffer (**Figure 9.4**) but more brittle bones (**Figure 9.2**). Osteocytes are also responsible for mechanosensation of external loading through their canalicular network, and hence

stimulate bone remodelling (52). The foregoing observation has relevance to reduced mechanistic competence, as it was shown (389) that in klotho mice, growing cement lines obstruct canal network (3, 390) and disturb the bone vasculature and fluid flow to the bone cells (387, 391) due to the high rate of remodelling (thin cortex in microCT images - **Figure 9.9C** and **Figure 9.10C**) with ageing,. These disturbed canalicular networks (179, 379) leads to insufficient fluid flow to the bones cells, resulting in apoptosis of osteocytes (391). The subsequent failure to replace damaged bone due to osteocytic apoptosis leads to microcracks (368). Eventually, the fusion and propagation of such microcracks into larger cracks result in macroscopic failure. These results have clinical relevance, as similar effects have been seen (using microCT imaging) in the 3D dynamic microstructural changes associated with cortical bone remodelling across the human life span (18 - 92 years) (390). The canalicular number exhibited a complex, non-linear relation with age and changes in the dimensions of the canals, which contributed to the age-dependent increase in porosity. The foregoing increase in porosity with age dominated the pattern of microstructural change in older individuals (390).

The BSE images also showed enlargement of lacunae size in klotho (Hom) mice (**Figure 11C**), and this feature may also be associated with reduced local mechanical properties in bone tissue. While a direct relationship between increased lacunae size and initiation of demineralised boundary around the osteocytes has not been investigated yet, enlargement of lacunae size is associated with reduction in load bearing ability of bone (380). Such enlargement may alter the crack propagation mechanisms around lacunae, and increase the fracture risk in klotho bone. The current study provides experimental evidence supporting a role for such microstructural features such as hypermineralised osteocytes playing a role in early fracture in klotho mice bone.

The mechanical deterioration at the macro level will also be significantly affected by alterations in fibrillar-level deformation mechanisms. As explained in **Chapter 1**, the MCF is a composite unit, consisting of 50 – 200 nm diameter collagen fibrils in a softer matrix which undergoes large shear deformations (14, 82). These fibrils in turn consist of stiff mineral platelets of carbonated apatite separated by layers of more ductile collagen which are loaded mainly in shear (14, 99). Mineral may also be found extrafibrillarly (as

discussed in **Chapter 5**) coating the mineralised fibril. Here, the deformation of the MCFs was measured by *in situ* SAXD and it was revealed that the fibrillar plasticity of the cortical bone was clearly reduced in klotho mice as seen from a lower fibril strain in post yield region in klotho mice compared to wild-type mice. Results in this study also showed a significantly increased effective fibril modulus of klotho mice compared to wild-type (**Figure 9.6**), which indicates a difference in nanoscale structural response to externally applied stress. **Figure 9.5** shows that mineralised fibrils in klotho mice deform to lower strain values (~ 0.3 %) before reaching the plastic regime, whereas wild-type fibrils have a larger strain zone over which the stress/fibril-strain plot remains linear (~ 0.85 %). To link the macro and nanoscale mechanical properties, fibril strain was plotted as a function of measured tissue strain from noncontact extensometry. The increased value of fibril to tissue strain ratio in klotho (**Figure 9.7A and B**) indicate that for an externally applied tissue strain, deformability of the collagen fibrils are significantly reduced in klotho compared to the wild-type bone. Such increased fibril stiffness may arise due to higher crosslinking in aged bone compared to wild-type (37, 87, 164, 194)

The above speculation on increased collagen crosslinking being responsible for increased bone matrix brittleness is supported by experimental studies from other groups. Several studies have shown that ageing results in increases in both enzymatic and nonenzymatic cross links (87, 392, 393). These cross links reduce the deformability of the collagen fibrils by stiffening the inter- and intrafibrillar covalent bonds, which restricts fibrillar sliding at the submicron length scales. Such an increase in crosslinking can be both enzymatic as well as nonenzymatic (**Chapter 1, section 9.5**), and in the latter case, is associated with production of Advanced Glycation End-products (AGEs), which are increasingly important in ageing. There is also evidence to suggest that the accumulation of AGEs can be only removed by bone resorption, and the presence of AGEs associates with increased osteoclast activity while decreasing the bone formation by osteoblasts (196). If this biological mechanism is true, the microstructural picture thus envisaged would be consistent with the BSE 2D images (**Figure 9.11**) and microCT rendered 3D images (**Figure 9.10**) shown here, which show thinner and porous cortex in klotho mice. Such thinner cortices may contribute to the reduced mechanical properties and lower fracture resistance.

However, it cannot be excluded that alterations in the mineral phase of the mineralised matrix may also play a significant role in the changed micro- and nanoscale deformation mechanisms in klotho mice. The mineral morphology is known to change with ageing, as a study combining X-ray diffraction, FTIR and chemical analysis has found, with the maturity and the size of the crystals increasing (388). As stated in the previous paragraphs, there is evidence that in ageing bone, the osteocytic regulation of the mineralisation surrounding the lacunae is disrupted, leading to premature cell death and increase of the mineral content (394, 395). Such a phenomenon may also contribute to the enhanced effective fibril modulus observed in the klotho mice compared to wild-type mice, via possible alterations in extra- and interfibrillar mineral content along the lines of the model of deformation proposed for Hpr mice in **Chapter 5**. While a more detailed analysis awaits quantitative backscattered electron imaging for klotho mice, it can be concluded that alterations in fibrillar stiffness observed in klotho mice may also be associated with (as yet unspecified) structural changes in mineral reinforcement.

9.5 Conclusion

In conclusion, *in-situ* tensile testing combined with SAXD and microlevel imaging (BSE and microCT) data showed that age-related defects in toughening mechanisms are linked to changed mechanisms at the fibrillar level which then adversely affect the higher length scale mechanical and structural properties. It should also be pertinent to note that the klotho mouse model is an ideal model-system for high-resolution structural and mechanical investigation of premature ageing as it exhibits multiple phenotypes very similar to those observed during human ageing, and hence may be appropriate for studies of mechanistic alterations in dermal or cardiac tissues, for example.

Chapter 10

Thesis Conclusion and the Outlook

10 Thesis Conclusion and the Outlook

10.1 Conclusion

Bone disorders like osteoporosis (208) and rickets (79) are known to cause significant reduction in both bone quality and mechanical properties, as well as skeletal development (387). However the precise mechanisms (from the macroscopic level down to the nanometer range) by which altered structural properties and mineralisation parameters cause deterioration in mechanical competence has not been fully understood. To date the significant stumbling blocks in this endeavor are the relative inaccessibility of obtaining well-defined cohorts of human clinical subjects controlled for age- and disease state and the lack of tools to study the structure – function relationships at the nanoscale level in bone. As discussed in the previous chapters, current clinical diagnostic techniques like DXA, pQCT, histomorphometry, MRI, microCT and microFEA have the capability of measuring structural or mechanical changes, but not both together. Therefore the main focus of this thesis is to combine *in situ* SAXD with micromechanical testing, and to apply this combination to mouse models of skeletal diseases created by genetic modification, in order to characterize the altered submicron-level deformation mechanisms and relate them to nanostructural changes. In this regard, the results presented in this thesis clearly shows the potential of this technology as a high resolution diagnostic technique to detect functionally critical changes in bone quality occurring in bone diseases and ageing at very small scales, before such changes lead to fracture.

One of the primary initial objectives of this project was to design a specialised *in situ* micromechanical testing machine, capable of use in a synchrotron microfocus X-ray diffraction beamline, and with the ability to mechanically test small-scale mouse bone sample testing (size = ~200 μm width). This device enabled a concurrent measurement of the tissue level (non contact video extensometry) and fibrillar level (changes in the fibril D-period measured by synchrotron SAXD) strains for a given external load. Special challenges involved design of miniature sample holders and *in situ* fluid chamber systems, to test irregular bone tissues in close to *in-vivo* states. The micromechanical

tensile testing device was integrated into the I22 NCD beamline (85) at Diamond to understand (a) nanoscale origins of the mechanical and structural differences in prototypical models for bone disease (rickets and GIOP) induced via ENU mutagenesis and (b) alteration of bone nanomechanics and structure in a genetically modified model of premature ageing. Mouse models for disorders of bone fragility due to rickets, endogenous production of glucocorticoids, as well as ageing (**Table 10.1**) have been established as part of the ENU Mammalian Genetics Unit program at Medical Research Council Harwell where a range of animal models for skeletal disorders have been phenotyped (396). As summarised in **Table 10.1** mouse models investigated in this thesis for different bone disease conditions obtained from different age points.

Table 10.1: Mouse models studied in this thesis

Mouse model	Disease condition	Ages (weeks) of the animals studied	Loading modes studied	Macro mechanical alterations
Hpr	XLHR – reduced phosphorus level	1,4,7,10 and 16	Tensile and Cantilever bending	Increased deformability
Crh$^{-120/+}$	GIOP – excess steroids	26	Tensile	Increased fracture risk
Klotho	Ageing – removal of klotho gene	5	Tensile	Increased brittleness and fracture risk

In more detail, the rickets model is for hypophosphatemic rickets (Hpr) which is a relatively well understood bone disease, where higher deformability is believed to be due to the defective (lower) mineralisation (79).Using time-resolved *in situ* synchrotron SAXD combined with micro-mechanical testing, the effective fibril elastic modulus, ultimate tensile strength and maximum fibril strain were measured for mice femora at different stages of development in both rickets and wild-type strains. A significant reduction of fibril modulus (73.5 %) as well as an enhancement of maximum fibril strain (~3-fold) for the rachitic condition was found. Concurrently, the mineral content in the femora were estimated independently using qBSE and it was, on average, 21 % less for

the rickets than for the wild-type condition, and is far more heterogeneous at the micro level related to the overall reduction in mineralisation. Using these nanomechanical results and qBSE results,a model was developed in **Chapter 5**, which revealed that for a relatively small reduction in mineral content, a very large (3-fold) reduction in effective fibril modulus occurred. While the foregoing results were obtained in tensile deformation, clinically, bending (as opposed to tension) is the dominant mode for failure (397). At the bone-matrix level, a macroscopic torsional and bending deformation will lead to zones of tension and compression around the neutral axis. However, very little *in-situ* synchrotron X-ray data is available on the nanoscale deformation mechanisms in bending deformation in bone diseases. It is therefore of great interest to understand what the corresponding fibrillar deformation mechanisms in bending are. In **Chapter 6**, the fibrillar–level deformation in cantilever bending in the Hpr mouse model was considered. By combining the spatial resolving power of a microfocus synchrotron X-ray beam with time-resolved *in situ* SAXD during cantilever bending, positionally-resolved maps (at the microscale) of the fibril strain in tensile- and compressive zones in bone were obtained separately. Nanomechanical and microscale mineralisation parameters were measured as per the protocols described above. The fibril moduli within the tensile and compressive zones were clearly lower by ~3- to 5-fold in Hpr mice when compared to wild-type mice, which is a similar result to that obtained in uniaxial tension previously. In wild-type mice average maximum tensile stress (~51 MPa) is significantly lower than maximum flexural stress (~59 MPa). In contrast in Hpr mice maximum tensile stress (~33 MPa) is significantly higher than the maximum flexural stress (~ 22 MPa). This discrepancy in macro mechanical properties between different loading modes (tensile vs, bending) is consistent with other studies (24, 25). Average effective fibril modulus from *in-situ* cantilever bending experiments is lower when compared to effective fibril modulus obtained from pure tensile testing. However this difference is not significant ($p > 0.5$) at the nano scale level (**Table 10.2**). The qBSE images showed highly mineralised calcified cartilage islands in Hpr cortical bone. These heterogeneities may have an influence on the micro- and nanomechanical properties, and this area would benefit from further research. The new findings of **Chapter 6** was that the mechanism of greater extensibility via incompletely mineralised fibrils holds in compression as well as in tension in Hpr

mice, and that compressive and tensile zones have similar effective fibril moduli at the fibrillar level.

Table 10.2: Macro and nano level *in-situ* experimental results obtained from tensile loading and cantilever bending for Hpr and their wild type littermates.

	Wild-type			Hpr		
Age (weeks)	**4**	**7**	**10**	**4**	**7**	**10**
Tensile loading						
Yield tensile stress (MPa)	18.02 ± 5.94	44.96 ± 4.28	91.11 ± 22.08	11.33 ± 6.06	37.49 ± 3.20	50.87 ± 11.09
Effective fibril modulus (GPa)	12.76 ± 3.07	21.8 ± 8.48	37.49 ± 9.11	3.49 ± 1.70	4.57 ± 0.97	6.93 ± 1.80
Ca_{mean}	26.20 ± 0.51	26.81 ± 0.60	24.88 ± 2.06	23.22 ± 1.51	23.91 ± 0.67	21.99 ± 1.00
Ca_{FWHM}	3.87 ± 0.32	3.25 ± 0.42	3.08 ± 0.58	15.31 ± 1.81	13.08 ± 0.42	12.36 ± 0.19
Cantilever bending						
Yield flexural stress (MPa)	11.32 ± 6.30	35.05 ± 9.37	133.42 ± 19.27	5.32 ± 2.91	14.56 ± 8.68	49.61 ± 36.57
Yield flexural strain (%)	0.59 ± 0.28	0.33 ± 0.25	0.44 ± 0.22	1.14 ± 0.68	0.72 ± 0.44	0.93 ± 0.57
Flexural modulus (GPa)	0.65 ± 0.05	1.31 ± 0.52	3.15 ± 0.41	0.05 ± 0.02	0.26 ± 0.03	0.68 ± 0.06
Ca_{mean}	25.20 ± 0.67	27.42 ± 0.16	30.07 ± 1.34	21.84 ± 0.44	24.20 ± 0.61	26.24 ± 1.29
Ca_{FWHM}	7.72 ± 0.78	5.47 ± 0.13	4.90 ± 0.50	10.20 ± 0.78	10.12 ± 1.40	8.42 ± 1.08
Tensile zone						
Effective fibril modulus (GPa)	2.35 ± 1.05	14.36 ± 6.25	28.71 ± 5.61	0.46 ± 0.26	2.67 ± 1.08	7.78 ± 3.32
Maximum fibril strain (%)	0.37 ± 0.07	0.19 ± 0.19	0.10 ± 0.08	0.10 ± 0.22	0.52 ± 0.16	0.38 ± 0.24
Fibril to tissue strain ratio	0.71 ± 0.39	0.47 ± 0.15	0.39 ± 0.07	0.88 ± 0.27	0.78 ± 0.42	0.43 ± 0.17
Compressive zone						
Effective fibril modulus (GPa)	3.41 ± 1.38	16.83 ± 0.87	34.12 ± 5.93	0.72 ± 0.25	2.99 ± 1.53	9.96 ± 2.61
Maximum fibril strain (%)	0.25 ± 0.16	0.14 ± 0.09	0.16 ± 0.10	0.79 ± 0.16	0.43 ± 0.17	0.38 ± 0.11
Fibril to tissue strain ratio	0.51 ± 0.38	0.43 ± 0.08	0.28 ± 0.12	0.68 ± 0.31	0.66 ± 0.37	0.43 ± 0.06

While the etiology of reduced mechanical competence in rachitic bone is relatively well known, osteoporosis and ageing are more clinically important conditions, where the relation between changed bone quality and quantity with increased fracture risk is a topic of intense debate (208, 387). In this regard, **Chapter 8 and 9** focused on the application of the nanomechanical imaging technique (validated on Hpr rickets) to mouse models of glucocorticoid induced osteoporosis (GIOP (*Crh*$^{-120/+}$)) and ageing (klotho). In GIOP, the rapid change in bone fracture risk is indicative of steroid induced bone loss (quantity) and degradation of bone quality. There is, however, increasing evidence that neither BMD nor current biomarkers as discussed in **Chapter 1 and 8** are insufficient to explain fracture rates in patients with GIOP (172). For example, patients exposed to glucocorticoids have a higher fracture risk at a similar bone mineral density (BMD) level compared with non-users (173). A mouse model with an ENU induced corticotrophin releasing hormone promoter mutation (*Crh*$^{-120/+}$) that developed hypercorticosteronaemia and osteoporosis, was utilised to measure fibrillar deformation parameters. A significant reduction (~79 %) of fibril modulus was found in *Crh*$^{-120/+}$ mice, indicative of a lowered mechanical competence at the nanoscale. More interestingly, fibril strain/tissue strain ratio in *Crh*$^{-120/+}$ mice was mich (~107 %) larger compared to the wild-type mice for a slightly reduced (~8 %) degree of mineralisation, an observation at odds with previously proposed models of interfibrillar shearing. In a complementary manner to the nanomechanical studies in GIOP, the spatial variation in mineral alignment and orientation in humerus and the associated changes in GIOP bone were also considered. These alterations in the nanostructural parameters of the mineralised fibrillar collagen matrix, which leads to increased fracture risk in glucocorticoid induced osteoporosis (GIOP).

The study described in **Chapter 9** further confirmed the ability of nanomechanical imaging technique to detect functionally critical changes in bone matrix with ageing. A mouse model of premature ageing (achieved by removal of the klotho gene) was used to investigate mechanistic changes at the fibrillar level during the ageing process. Using the nanomechanical imaging method described above, it was found that the effective fibril

modulus was significantly higher by ~ 200% in klotho mice when compared to wild-type mice, and a reduced fibrillar plasticity was seen in klotho mice, indicating a difference in the nanoscale structural response to externally applied stress. It was observed in Hpr mice due to the reduced extrafibrillar mineralisation, MCFs are less stiff compared to wild-type mice (**Figure 10.1**). Therefore when compared to the Hpr model (where the bone quality changes are mainly due to defective mineralisation), the klotho mouse model (290, 292) is complementary, in that here it is the defective collagen structure (stiffen collagen fibrils) that is likely to be the main factor in changing the mechanical properties of the bone matrix. This increased effective fibril modulus may be due to the increased cross linking which was observed in a previous study (87) with aged bones. The GIOP mouse model had a lowered effective fibril modulus compared to their wild-type littermates which is similar to Hpr mouse model. However this similarity was not solely due to the reduced mineralisation as seen in Hpr mice. In GIOP it was also observed less orientated collagen fibrils and localised microscale defects (halos) which may have an association with reduced mechanical properties at the macroscale. However direct comparison of nano mechanical and mineralisation parameters between different mouse models was not plausible in the current study mainly due to their age variability (**Table 10.1**) and variations in sample preparation techniques used (**Chapter 4** section 4.1.1).

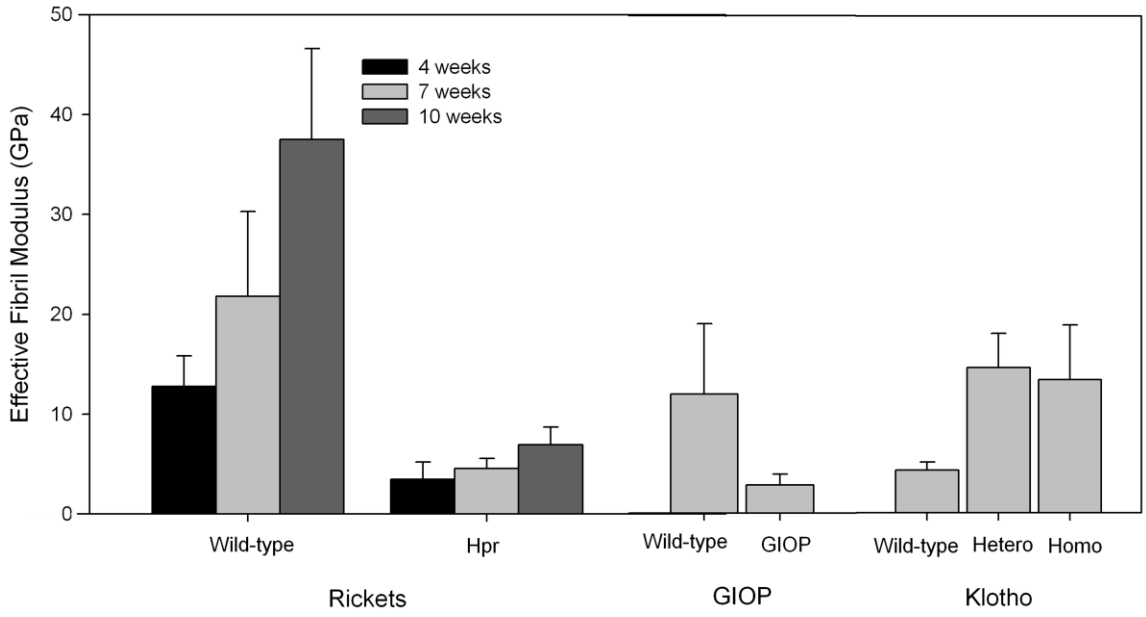

Figure 10.1: Effective fibril modulus estimated from macroscopic stress and fibril strain during *in-situ* tensile testing plotted as a function of disease conditions.

While the foregoing results focused on the nanoscale, it is important to correct for heterogeneity at the microscale level which can be significantly increased in bone diseases. Therefore all measurements of stress in this thesis were corrected for microscale porosity. After including this correction the fibrillar level strain as a function of external stress was still significantly different for all three disease conditions. Therefore, it may be concluded that the above results do indeed show that the mineralised matrix (bone quality) is significantly altered in rickets, glucocorticoid osteoporosis, and ageing, and that this may well be the case for other metabolic bone diseases.

Continuing the above theme of correcting for microscale heterogeneities, a secondary study in this thesis hypothesized that the increased deformability may also be due to microscale level variations in fibrillar orientation (as distinct from fibrillar deformation changes). In this regard, it is noted that metabolic and neuromuscular bone disorders like rickets and muscular dystrophy are also associated with altered *in-vivo* muscular force distributions on the skeletal system (364). During development, the spatial and temporal dynamics of mineralised tissue formation can be disrupted by these altered forces, but the exact mechanisms are not known. In **Chapter 7**, the Hpr mouse model studied in

Chapter 5 was used to investigate the development of the mineralised nanostructure in the intramembranously ossifying scapulae in shoulder bone. The degree and direction of mineral nanoplatelet alignment over the entire width of the scapulae, from the load bearing lateral border regions across the intermediate in tissue was quantified using position – resolved sSAXS. The average mineral nanoplatelet alignment in the lateral border with development was much larger (50 % increment) compared to the infraspinous fossa region in normal mice, but this relationship is disrupted in rachitic mice. Secondly, the platelet alignment with the macroscopic bone boundary in the lateral border increased by 90 %, but less in the infraspinous fossa region (only ~ 30 %). However, in rachitic bone, this close correlation at the lateral border is absent. Comparison with literature values reveals that the nanoplatelet degree of alignment correlates very well with *in vivo* muscular forces, muscle fibre diameter and muscle weight. The outcome of this part of the thesis was that scanning SAXS can provide evidence for the existence of spatial variations of bone fibril orientation across the bone organ and its change in rickets. It also leads to speculations that the mechanism for the (known) increased macroscopic fracture risk in metabolic bone diseases may be related to the irregular nanoscale mineral orientations associated with altered spatial distribution of forces on bones due to defective muscular actions or structure.

As an overview of the efficacy and sensitivity of the current synchrotron X-ray technique compared to currently used gold standard for assessing bone fracture risk - DXA - (208) the whole body BMD changes in the mouse models studied above were plotted against changes in effective fibril modulus in **Figure 10.1**. BMD were assessed by DXA analysis (C. Esapa et al and L. Bentley et al, unpublished data) for Hpr, *Crh*$^{-120/+}$ and klotho mice and their respective wild-type littermates. As can be seen in **Figure 10.1**, the percentage changes in BMD from wild-type to Hpr *Crh*$^{-120/+}$ and klotho mice are significantly lower compared to changes in effective fibril modulus.This demonstration clearly shows the heightened sensitivity of nano mechanical imaging (bone quality assessment) compared to existing clinical techniques like DXA which only measure BMD (bone quantity) .

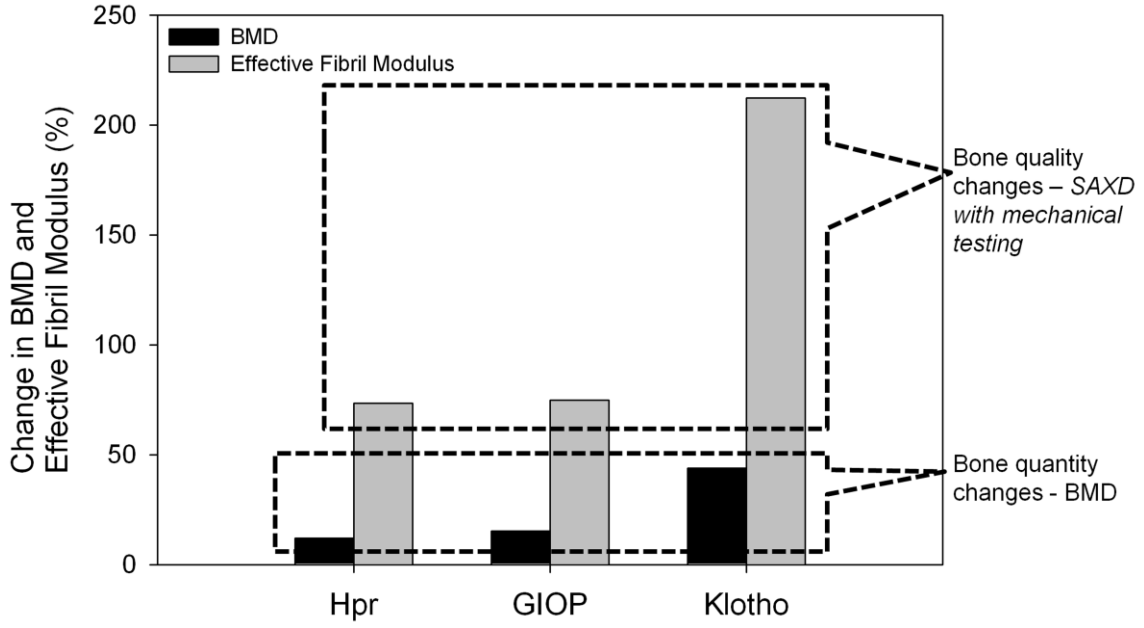

Figure 10.2: Percentage change in BMD (black) and effective fibril modulus (grey) between Hpr, GIOP and Klotho mice and their respective wild-type littermates

In summary, the studies performed here demonstrate that the technique is highly sensitive, compared to BMD determination methods like DXA, and show that small changes in mineral content or collagen deformability in metabolic diseases, when combined with abnormal nano- and microscale mineralisation, altered remodelling and possibly changes in the organic matrix structure, can lead to significant reductions in bone mechanical competence and fracture risk.

10.2 Future work

The areas of future work, further improvements and applications of the technique are discussed in the following under the main headings of (a) analyzing the efficacy of current drug treatments for bone diseases (b) methodological improvements and (c) complementary studies.

10.2.1 Efficacy of current drug treatments

In spite of several advantages of *in situ* nano mechanical imaging technique, they are often confined to basic non-clinical research laboratories and cannot be applied directly in a clinical context. The results shown in this thesis provided previously inaccessible information on disease induced alterations in the nano mechanical behavior of bone. In

order to progress further it is important to quantify the functionally relevant bone matrix changes induced by currently available drug treatments against osteoporosis and related disorders, in order to assess the efficacy of the treatments in improving the fracture resistance. BMD measurement is not capable of assessing the changes in bone quality induced by the drugs used in osteoporosis (208), and this has significant downstream effects in predicting the reduction of fracture risk. For example BMD can explain only 40 % of changes of the fracture risk which is associated with bisphosphonates (anabolic) treatments (398). Even though bisphosphonates suppress the remodeling and lead to higher degree of mineralisation, they do not repair the nano and micro level damages (399). Furthermore new drugs like teriparatide alter the bone quality by increasing the heterogeneity of the mineralisation (78), and increasing divalent cross linking in collagen (400, 401) and reducing microdamage (402). Raloxifene-like estrogen receptors enhance the fracture risk efficacy, but BMD can explain only 4 - 5 % of the resultant increase (403). Therefore in order to validate the technique introduced in this thesis at a preclinical level, and to have an impact on clinical practice, the nanoscale deformatiom mechanisms in a range of metabolic bone disease animal models, treated with current therapies, have to be analyzed. These studies need to quantify the mechanistic consequences - at the fibrillar level – of the structural alterations in tissue quantity and quality induced by the treatments mentioned above.

10.2.2 Experimental method improvements

The main aim of *in situ* mechanical testing combined with SAXD is to obtain information at the material level. Due to the hierarchical structure of bone, strain heterogeneities at the micro- as well as nano-level may be present during deformation. Indeed, when compared to the micron-sized X-ray beam, tissue level strain and stress heterogeneity (at the scale of several tens to hundreds of microns (299)) may not be neglected. Structural features enabling these heterogeneities can include (**Chapter 5**), calcified cartilage islands within the cortical bone of HPr mice. BSE images of GIOP mice (**Chapter 8**) showed less mineralised halo structures surrounding apoptosed osteocytes. These less mineralised structures may imply lower stiffness as well as cause stress concentrations due to the interface between a weak-core and highly mineralised surrounding tissues such as cement lines. Therefore sample preparation techniques need

to be refined from the current meso- and macroscale (of several hundreds of microns) to enable isolation of micro-sized samples which can selectively include or exclude structures such as those mentioned above (halos, calcified cartilage).

Ideally, the confounding effects of microscale material heterogeneities may be removed by testing homogenous samples. Focused ion beam (FIB) milling is a technique recently applied to biomineralised tissue (404) in order to prepare micron-sized mechanical test specimens of bone (405) with homogenous fibrillar orientation without complication of higher level hierarchies. Such homogeneous samples will be most essential in investigations of fibrillar level mechanics in osteoporosis and rickets. UV laser micro-dissection is another promising candidate for bone sample preparation, and has been previously utilised (14) to cut out samples from specific regions of bone tissue, with sizes of a few mm and thickness of the order of microns. The spatial resolution of the technique is defined by the size of the laser beam (1 – 3 μm). One advantage of the technique compared to FIB-milling is the ability to dissect bone in native conditions without exposing it to the vacuum of an SEM chamber, but a disadvantage is the near 2D-planar geometry required for tissue sections that are analyzed.

The presence of inhomogeneous tissue deformation along the length of the tensile test specimen was shown in a previous study (299). Therefore it is crucial to carry out pre-tensing of test samples with video extensometry to find out localised bands of high deformation, prior to the *in situ* SAXD measurements. Once the band with maximum deformation has been identified, the microfocus beam can be focused on this band to take localised SAXD measurements. This procedure will ensure that fibrillar measurements are taken at the locations where externally applied stress has been concentrated, which are the mechanically critical tissue regions undergoing inelastic/plastic deformation.

10.2.3 Complementary Techniques for in situ Mechanics

In situ micromechanical testing can be combined with other imaging techniques to investigate the alterations at different (micron and molecular) structural hierarchies in the bone. These include molecular spectroscopic methods like Raman spectroscopy and microscale methods like confocal microscopy. Molecular level alterations in bone structure may have significant influence in modifying deformation mechanisms at small

length scales, and these can be detected with spectroscopy. Possible alterations in molecular structure include accumulation of non-enzymatic cross links during ageing process, leading to stiffening of the collagen matrix and changes in the mineral morphology. By utilizing Raman spectroscopy and confocal microscopy during micromechanical testing, molecular and microlevel alterations in deformation mechanisms in metabolic bone diseases can be investigated.

10.2.3.1 In situ mechanical testing with Raman spectroscopy

Raman spectroscopy is a nondestructive chemical analysis technique, which has been extensively used for investigating the molecular structure of bone (405-407). The Raman spectrum of each molecular species of bone has characteristic bands corresponding to vibrational frequencies of the compounds comprising the bone matrix. For example, the most intense band arises from the phosphate ν_1 vibration (~ 959 cm^{-1}) (408). The amide I and III peaks represent the vibrations of collagen backbone and are indicators for protein arrangement because of the amide moiety's role in cross linking and bonding (406). Alterations in the hydrogen bonding between peptide groups affect the amide I band intensity and position (409). Several methods have been established to analyze Raman spectra to obtain parameters such as mineralisation, crystallinity and extent/maturity of collagen cross links (407, 410, 411) which can be potentially integrated with *in situ* SAXD studies. *In situ* mechanical testing was carried out with Raman spectroscopy (409, 412), and it was found that applied external stress on the bone results in changes in Raman spectra. For example confocal Raman spectroscopy was applied to cortical bone to track the band shifts (ν_1 phosphate band) as a function of externally applied uniaxial stress (stress was assumed to be uniaxial and linearly changing from compression to tension) in 4-point bending (412). Another study has shown a pressure-induced distortion on the apatite lattice. This study used notched samples that were loaded parallel to the long bone axis. The results showed that in the areas of visible microcracks, there were phosphate shifts of 4 – 6 /cm. The authors proposed that these shifts were caused possibly due to the mineral undergoing a phase transformation and/or transformation to amorphous phase (409).

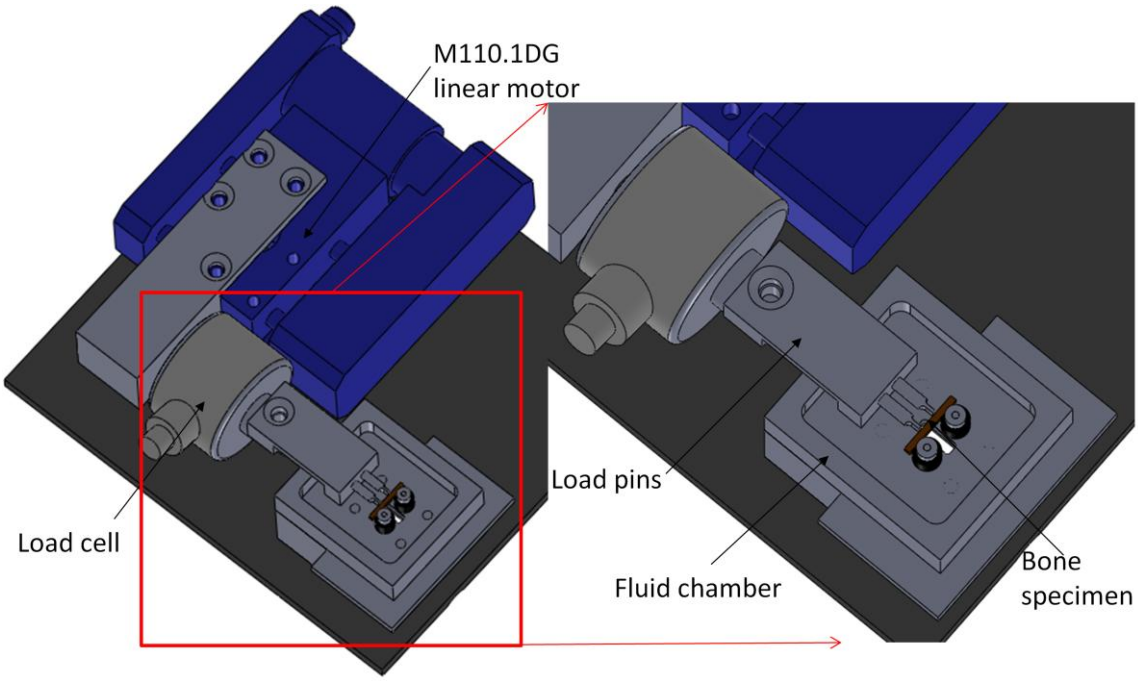

Figure 10.3: 4-point bending machine developed to use in a Raman microscope, confocal microscope and synchrotron SAXD

To enable *in situ* spectroscopic measurement during mechanical deformation, a 4-point bending testing machine was specially designed to use in a Raman microscope (Thermo Scientific Raman AlmegaXR, the School of Engineering and Materials Science, Queen Mary University of London), which is currently in the commissioning stage. This machine may also be installed in a synchrotron SAXD beamline in order to perform *in situ* bending testing with SAXD. A schematic of this machine is shown in **Figure 10.2 and 10.3.**

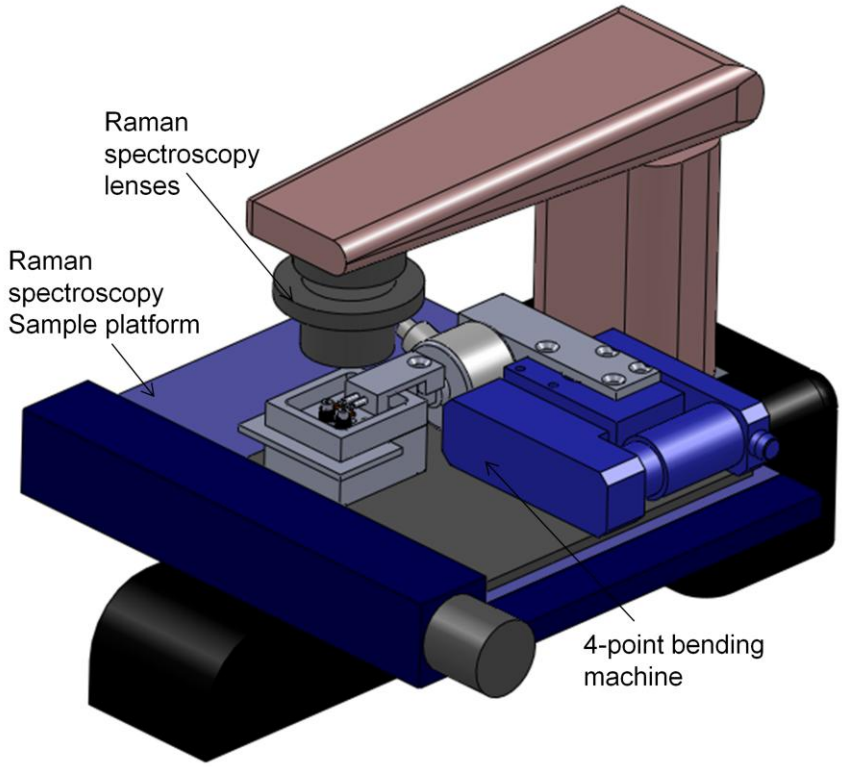

Figure 10.4: 4 – point bending machined assembled to the Raman microscope, where the Raman laser beam intersect with the sample is reflects back to the detector.

10.2.3.2 In situ mechanical testing with confocal microscopy

Confocal scanning microscopy is a microscopic technique enabling quasi-3D visualization of bone microstructure, which can be applied to assess load-induced microdamage of bone matrix. The microstructural changes that occur during metabolic bone diseases (specifically in GIOP) can be assessed via analysis of the effect of mechanical loading (microcrack initiation and propagation) using confocal microscopy combined with mechanical testing (126, 154, 376). Such studies will contribute to the understanding of mechanical effects of microstructural features such as halo structures and cement lines around the osteocyte lacunae at the microscale level of bone in GIOP (87). Microcrack growth can be assessed by utilizing a selection of calcium binding dyes (e.g alizarin and xylenol) together with *in situ* mechanical testing of bone under confocal microscopy (154). These experiments would provide insight into microlevel deformation and toughening mechanisms including microcrack formation and propagation (102, 148).

The 4- point bending machine shown in **Figure 10.2** can be also used with confocal microscopy.

10.2.4 Fast strain rate mechanical testing

Mechanical testing experiments performed in this thesis used very slow (quasi-static) strain rates of 0.02 – 0.04 %/s. However, the changes in the fibrillar fracture mechanisms in bone disorders at the high strain rates (~50-100%/s) associated with *in – vivo* fracture (373) are less well-known. It would be useful to do high strain rate (10–100%/s), bending or/and tensile testing concurrent with rapid acquisition of SAXS/WAXD spectra in the future. The challenge will be to optimize sample size, sample acquisition times, and possibly minimize air scattering by sample chamber design, and the use of appropriate detectors like the Pilatus 2M at high cycle rates up to 30 Hz. Possibly, the RAPID detector used in the first (Hpr) study could be utilised as well, as it can perform time-resolved measurements down to a few microseconds, but whether flux levels are sufficient for statistically reliable SAXD patterns remains to be seen.

10.2.5 *In situ* mechanical testing with Wide Angle X-ray diffraction (WAXD)

In the wide angle regime the mineral particles (carbonated apatite) in bone matrix give rise to diffraction peaks. Apatite has a hexagonal cubic lattice structure with the (002) or c-axis oriented along the collagen fibril axis (14). Hence the shifts in the 002 c-axis reflections (WAXD diffraction pattern) due to the externally applied mechanical force can be used to measure the mineral strain parallel to the collagen fibril orientation (14, 87). With a few design modifications to the tensile and bending test machines (broader opening for the X-ray bean outlet and increased inclination of tester) the devices may be further used to acquire WAXD signals during loading. The mineral strain data can be combined with fibril strain data to understand the disease-induced alterations in the deformation of the MCF, (for example, the specific interfacial bond energy between mineral and collagen (14).

Bibliography

1. Weiner S, Wagner HD. The material bone: Structure mechanical function relations. Annu Rev Mater Sci. 1998;28:271-98.
2. Hall B. Bones and Cartilage: Developmental Skeletal Biology: Academic Press; 2005.
3. Currey JD, editor. Bones: Structure and Mechanics Princeton, New Jersey: Princeton University Press; 2002.
4. Currey JD. Role of collagen and other organics in the mechanical properties of bone. Osteoporosis International. 2003;14(0):29-36.
5. Currey JD, Zioupos P, Davies P, Casino A. Mechanical properties of nacre and highly mineralized bone. Proc Biol Sci. 2001;268(1462):107-11.
6. Yan J. Elastic-plastic fracture mechanics of compact bone [Ph.D.]. United States -- Florida: University of Florida; 2005.
7. Lowenstam HA, Weiner S. On Biomineralization: Oxford University, New York; 1989.
8. Fratzl P, Gupta HS, Paschalis EP, Roschger P. Structure and mechanical quality of the collagen-mineral nano-composite in bone. Journal of Materials Chemistry. 2004;14(14):2115-23.
9. Fratzl P. Cellulose and collagen: from fibres to tissues. Curr Opin Colloid In. 2003;8(1):32-9.
10. Gould JL, Keeton WT, Gould CG. Biological Science 6 ed: W W Norton & Co Inc, Scranton, Pennsylvania, U.S.A.; 1996.
11. Steendijk R, Boyde A. Scanning electron microscopic observations on bone from patients with hypophosphataemic (vitamin D resistant) rickets. Calcif Tissue Res. 1973;11(3):242-50.
12. Traub W, Arad T, Weiner S. Three-dimensional ordered distribution of crystals in turkey tendon collagen fibers. Proceedings of the National Academy of Sciences. 1989;86(24):9822-6.
13. Reilly DT, Burstein AH. The elastic and ultimate properties of compact bone tissue. Journal of Biomechanics. 1975;8(6):393-405.
14. Gupta HS, Seto J, Wagermaier W, Zaslansky P, Boesecke P, Fratzl P. Cooperative deformation of mineral and collagen in bone at the nanoscale. Proceedings of the National Academy of Sciences of the United States of America. 2006;103(47):17741-6.
15. Boyde A. Scanning electron microscopic studies of bone 2ed. GH B, editor: Academic Press, New York; 1972.
16. Giraud-Guille M-M. Liquid crystalline order of biopolymers in cuticles and bones. Microscopy Research and Technique. 1994;27(5):420-8.
17. Giraud-Guille M-M. Plywood structures in nature. Current Opinion in Solid State and Materials Science. 1998;3(3):221-7.
18. Bouligand Y. Twisted fibrous arrangements in biological materials and cholesteric mesophases. Tissue and Cell. 1972;4(2):189-217.
19. Weiner S, Arad T, Sabanay I, Traub W. Rotated plywood structure of primary lamellar bone in the rat: Orientations of the collagen fibril arrays. Bone. 1997;20(6):509-14.
20. Weiner S, Arad T, Traub W. Crystal organization in rat bone lamellae. FEBS Lett. 1991;285(1):49-54.
21. Weiner S, Traub W. Bone structure: from angstroms to microns. FASEB J. 1992;6(3):879-85.
22. Riches PE, Everitt NM, Heggie AR, McNally DS. Microhardness anisotropy of lamellar bone. Journal of Biomechanics. 1997;30(10):1059-61.

23. Ziv V, Wagner HD, Weiner S. Microstructure-microhardness relations in parallel-fibered and lamellar bone. Bone. 1996;18(5):417-28.
24. Liu D, Wagner HD, Weiner S. Bending and fracture of compact circumferential and osteonal lamellar bone of the baboon tibia. Journal of Materials Science: Materials in Medicine. 2000;11(1):49-60.
25. Liu D, Weiner S, Daniel Wagner H. Anisotropic mechanical properties of lamellar bone using miniature cantilever bending specimens. Journal of Biomechanics. 1999;32(7):647-54.
26. Mishima H, Sakae T. Demonstration of Structural Variation in Rat Incisor Dentin as Determined by the X-ray Laue Method. Journal of Dental Research. 1986;65(6):932-4.
27. Boskey AL, Posner AS. Bone structure, composition, and mineralization. The Orthopedic clinics of North America. 1984;15(4):597-612.
28. Kuhn JL, Goldstein SA, Choi K, London M, Feldkamp LA, Matthews LS. Comparison of the trabecular and cortical tissue moduli from human iliac crests. J Orthop Res. 1989;7(6):876-84.
29. Kuhn L, Grynpas M, Rey C, Wu Y, Ackerman J, Glimcher M. A Comparison of the Physical and Chemical Differences Between Cancellous and Cortical Bovine Bone Mineral at Two Ages. Calcified Tissue International. 2008;83(2):146-54.
30. Rubin MA, Jasiuk I, Taylor J, Rubin J, Ganey T, Apkarian RP. TEM analysis of the nanostructure of normal and osteoporotic human trabecular bone. Bone. 2003;33(3):270-82.
31. Puxkandl R, Zizak I, Paris O, Keckes J, Tesch W, Bernstorff S, Purslow P, Fratzl P. Viscoelastic properties of collagen: synchrotron radiation investigations and structural model. Philos Trans R Soc Lond B Biol Sci. 2002;357(1418):191-7.
32. Petruska JA, Hodge AJ. A subunit model for the tropocollagen macromolecule. Proc Natl Acad Sci U S A. 1964;51:6.
33. Hulmes DJ. Building collagen molecules, fibrils, and suprafibrillar structures. Journal of Structural Biology. 2002;137(1-2):2-10.
34. Peter F. Cellulose and collagen: from fibres to tissues. Current Opinion in Colloid & Interface Science. 2003;8(1):32-9.
35. Saito M, Marumo K. Collagen cross-links as a determinant of bone quality: a possible explanation for bone fragility in aging, osteoporosis, and diabetes mellitus. Osteoporosis International. 2010;21(2):195-214.
36. Vashishth D, Gibson GJ, Khoury JI, Schaffler MB, Kimura J, Fyhrie DP. Influence of nonenzymatic glycation on biomechanical properties of cortical bone. Bone. 2001;28(2):195-201.
37. Bailey AJ. Molecular mechanisms of ageing in connective tissues. Mech Ageing Dev. 2001;122(7):735-55.
38. Knott L, Bailey AJ. Collagen cross-links in mineralizing tissues: A review of their chemistry, function, and clinical relevance. Bone. 1998;22(3):181-7.
39. Posner AS. Crystal Chemistry of Bone Mineral Phys Rev. 1969;49(4):28.
40. Posner AS. The Mineral of Bone. Clinical Orthopaedics and Related Research. 1985;200:87-99.
41. Posner AS, Perloff A, Diorio AF. Refinement of the hydroxyapatite structure. Acta Crystallographica. 1958;11(4):308-9.
42. Fratzl P, Groschner M, Vogl G, Plenk H, Jr., Eschberger J, Fratzl-Zelman N, Koller K, Klaushofer K. Mineral crystals in calcified tissues: a comparative study by SAXS. J Bone Miner Res. 1992;7(3):329-34.
43. George A, Veis A. Phosphorylated Proteins and Control over Apatite Nucleation, Crystal Growth, and Inhibition. Chemical Reviews. 2008;108(11):4670-93.

44. Thurner PJ, Lam S, Weaver JC, Morse DE, Hansma PK. Localization of Phosphorylated Serine, Osteopontin, and Bone Sialoprotein on Bone Fracture Surfaces. The Journal of Adhesion. 2009;85(8):526-45.
45. Hansma PK, Fantner GE, Kindt JH, Thurner PJ, Schitter G, Turner PJ, Udwin SF, Finch MM. Sacrificial bonds in the interfibrillar matrix of bone. J Musculoskelet Neuronal Interact. 2005;5(4):313-5.
46. Mills SE. Histology for Pathologists 3ed. Rosenberg AE, Roth SI, editors: Lippincott Williams & Wilkins 2007.
47. Seeman E, Delmas PD. Bone Quality — The Material and Structural Basis of Bone Strength and Fragility. New England Journal of Medicine. 2006;354(21):2250-61.
48. Roodman GD. Mechanisms of Bone Metastasis. New England Journal of Medicine. 2004;350(16):1655-64.
49. McLean FC, Urist MR, editors. Bone: fundamentals of physiology of skeletal tissue: University of Chicago Press; 1968.
50. Noble BS. The osteocyte lineage. Archives of Biochemistry and Biophysics. 2008;473(2):106-11.
51. Teti A, Zallone A. Do osteocytes contribute to bone mineral homeostasis? Osteocytic osteolysis revisited. Bone. 2009;44(1):11-6.
52. Bonewald LF, Johnson ML. Osteocytes, mechanosensing and Wnt signaling. Bone. 2008;42(4):606-15.
53. Buckwalter JA, Glimcher MJ, Cooper RR, Recker R. Bone biology. I: Structure, blood supply, cells, matrix, and mineralization. Instructional course lectures. 1996;45:371-86.
54. Vaughan JM. The Physiology of Bone: Oxford; 1970.
55. Goldman HM, McFarlin SC, Cooper DML, Thomas CDL, Clement JG. Ontogenetic Patterning of Cortical Bone Microstructure and Geometry at the Human Mid-Shaft Femur. The Anatomical Record: Advances in Integrative Anatomy and Evolutionary Biology. 2009;292(1):48-64.
56. Enlow DH. A Study of the Post-Natal Growth and Remodeling of Bone. American Journal of Anatomy. 1962;110(2):79-101.
57. Price C, Herman BC, Lufkin T, Goldman HM, Jepsen KJ. Genetic Variation in Bone Growth Patterns Defines Adult Mouse Bone Fragility. Journal of Bone and Mineral Research. 2005;20(11):1983-91.
58. Busse B, Hahn M, Schinke T, Püschel K, Duda GN, Amling M. Reorganization of the femoral cortex due to age-, sex-, and endoprosthetic-related effects emphasized by osteonal dimensions and remodeling. Journal of Biomedical Materials Research Part A. 2010;92A(4):1440-51.
59. Weiner S, Addadi L. Crystallization Pathways in Biomineralization. Annu Rev Mater Res. 2011;41:21-40.
60. Addadi L, Raz S, Weiner S. Taking advantage of disorder: Amorphous calcium carbonate and its roles in biomineralization. Adv Mater. 2003;15(12):959-70.
61. Beniash E, Metzler RA, Lam RSK, Gilbert PUPA. Transient amorphous calcium phosphate in forming enamel (vol 166, pg 133, 2009). Journal of Structural Biology. 2009;167(1):95-.
62. Gago-Duport L, Briones MJ, Rodriguez JB, Covelo B. Amorphous calcium carbonate biomineralization in the earthworm's calciferous gland: pathways to the formation of crystalline phases. J Struct Biol. 2008;162(3):422-35.
63. Mahamid J, Aichmayer B, Shimoni E, Ziblat R, Li C, Siegel S, Paris O, Fratzl P, Weiner S, Addadi L. Mapping amorphous calcium phosphate transformation into crystalline mineral from

the cell to the bone in zebrafish fin rays. Proceedings of the National Academy of Sciences. 2010;107(14):6316-21.
64. Mahamid J, Sharir A, Addadi L, Weiner S. Amorphous calcium phosphate is a major component of the forming fin bones of zebrafish: Indications for an amorphous precursor phase. Proceedings of the National Academy of Sciences of the United States of America. 2008;105(35):12748-53.
65. Crane NJ, Popescu V, Morris MD, Steenhuis P, Ignelzi MA, Jr. Raman spectroscopic evidence for octacalcium phosphate and other transient mineral species deposited during intramembranous mineralization. Bone. 2006;39(3):434-42.
66. Deshpande AS, Beniash E. Bio-inspired Synthesis of Mineralized Collagen Fibrils. Cryst Growth Des. 2008;8(8):3084-90.
67. Landis WJ, Hodgens KJ, Arena J, Song MJ, McEwen BF. Structural relations between collagen and mineral in bone as determined by high voltage electron microscopic tomography. Microscopy Research and Technique. 1996;33(2):192-202.
68. Sasaki N, Tagami A, Goto T, Taniguchi M, Nakata M, Hikichi K. Atomic force microscopic studies on the structure of bovine femoral cortical bone at the collagen fibril-mineral level. J Mater Sci Mater Med. 2002;13(3):333-7.
69. Hassenkam T, Fantner GE, Cutroni JA, Weaver JC, Morse DE, Hansma PK. High-resolution AFM imaging of intact and fractured trabecular bone. Bone. 2004;35(1):4-10.
70. Fratzl P, Fratzlzelman N, Klaushofer K, Vogl G, Koller K. Nucleation and Growth of Mineral Crystals in Bone Studied by Small-Angle X-Ray-Scattering. Calcified Tissue International. 1991;48(6):407-13.
71. Landis WJ. An overview of vertebrate mineralization with emphasis on collagen-mineral interaction. Gravit Space Biol Bull. 1999;12(2):15-26.
72. Fratzl P, Fratzl-Zelman N, Klaushofer K. Collagen packing and mineralization. An x-ray scattering investigation of turkey leg tendon. Biophysical Journal. 1993;64(1):260-6.
73. Ascenzi A, Bonucci E, Generali P, Ripamonti A, Roveri N. Orientation of apatite in single osteon samples as studied by pole figures. Calcified Tissue International. 1979;29(1):101-5.
74. Roschger P, Fratzl P, Eschberger J, Klaushofer K. Validation of quantitative backscattered electron imaging for the measurement of mineral density distribution in human bone biopsies. Bone. 1998;23(4):319-26.
75. Roschger P, Gupta HS, Berzlanovich A, Ittner G, Dempster DW, Fratzl P, Cosman F, Parisien M, Lindsay R, Nieves JW, Klaushofer K. Constant mineralization density distribution in cancellous human bone. Bone. 2003;32(3):316-23.
76. Roschger P, Paschalis EP, Fratzl P, Klaushofer K. Bone mineralization density distribution in health and disease. Bone. 2008;42(3):456-66.
77. Akkus O, Polyakova-Akkus A, Adar F, Schaffler MB. Aging of Microstructural Compartments in Human Compact Bone. Journal of Bone and Mineral Research. 2003;18(6):1012-9.
78. Misof BM, Roschger P, Cosman F, Kurland ES, Tesch W, Messmer P, Dempster DW, Nieves J, Shane E, Fratzl P, Klaushofer K, Bilezikian J, Lindsay R. Effects of Intermittent Parathyroid Hormone Administration on Bone Mineralization Density in Iliac Crest Biopsies from Patients with Osteoporosis: A Paired Study before and after Treatment. Journal of Clinical Endocrinology & Metabolism. 2003;88(3):1150-6.
79. Camacho NP, Rimnac CM, Meyer RA, Jr., Doty S, Boskey AL. Effect of abnormal mineralization on the mechanical behavior of X-linked hypophosphatemic mice femora. Bone. 1995;17(3):271-8.

80. Currey JD. What determines the bending strength of compact bone? Journal of Experimental Biology. 1999;202(18):2495-503.
81. Currey JD. Tensile yield in compact bone is determined by strain, post-yield behaviour by mineral content. Journal of Biomechanics. 2004;37(4):549-56.
82. Gupta HS, Wagermaier W, Zickler GA, Raz-Ben Aroush D, Funari SS, Roschger P, Wagner HD, Fratzl P. Nanoscale deformation mechanisms in bone. Nano Lett. 2005;5(10):2108-11.
83. Hang F, Barber AH. Nano-mechanical properties of individual mineralized collagen fibrils from bone tissue. J R Soc Interface. 2010.
84. Karunaratne A, Davis GR, Hiller J, Esapa CT, Terrill NJ, Brown SDM, Cox RD, Thakker RV, Gupta HS. Hypophosphatemic rickets is associated with disruption of mineral orientation at the nanoscale in the flat scapula bones of rachitic mice with development. Bone. 2012;51(3):553-62.
85. Karunaratne A, Esapa CR, Hiller J, Boyde A, Head R, Bassett JHD, Terrill NJ, Williams GR, Brown MA, Croucher PI, Brown SDM, Cox RD, Barber AH, Thakker RV, Gupta HS. Significant deterioration in nanomechanical quality occurs through incomplete extrafibrillar mineralization in rachitic bone: Evidence from in-situ synchrotron X-ray scattering and backscattered electron imaging. Journal of Bone and Mineral Research. 2012;27(4):876-90.
86. Neil Dong X, Almer JD, Wang X. Post-yield nanomechanics of human cortical bone in compression using synchrotron X-ray scattering techniques. Journal of Biomechanics. 2011;44(4):676-82.
87. Zimmermann EA, Schaible E, Bale H, Barth HD, Tang SY, Reichert P, Busse B, Alliston T, Ager JW, 3rd, Ritchie RO. Age-related changes in the plasticity and toughness of human cortical bone at multiple length scales. Proc Natl Acad Sci U S A. 2011.
88. Wang R, Gupta HS. Deformation and Fracture Mechanisms of Bone and Nacre. Annual Review of Materials Research. 2011;41(1):41-73.
89. Mercer C, He MY, Wang R, Evans AG. Mechanisms governing the inelastic deformation of cortical bone and application to trabecular bone. Acta Biomaterialia. 2006;2(1):59-68.
90. Einhorn TA. Enhancement of fracture-healing. J Bone Joint Surg Am. 1995;77(6):940-56.
91. Bates P, Ramachandran M. Bone injury, healing and grafting. In: Ramachandran M, editor. Basic Orthopaedic Sciences: The Stanmore Guide. Great Britain: Hodder Arnold; 2007.
92. Turner CH, Rho J, Takano Y, Tsui TY, Pharr GM. The elastic properties of trabecular and cortical bone tissues are similar: results from two microscopic measurement techniques. Journal of Biomechanics. 1999;32(4):437-41.
93. Chatterjee S, Blunn G. Biomaterial behaviour. In: Ramachandran M, editor. Basic Orthopaedic Sciences: The Stanmore Guide. Great Britain: Hodder Arnold; 2007.
94. Gupta HS, Schratter S, Tesch W, Roschger P, Berzlanovich A, Schoeberl T, Klaushofer K, Fratzl P. Two different correlations between nanoindentation modulus and mineral content in the bone–cartilage interface. Journal of Structural Biology. 2005;149(2):138-48.
95. Gupta HS, Stachewicz U, Wagermaier W, Roschger P, Wagner HD, Fratzl P. Mechanical modulation at the lamellar level in osteonal bone. J Mater Res. 2006;21(8):1913-21.
96. Burr DB, Turner CH, Naick P, Forwood MR, Ambrosius W, Sayeed Hasan M, Pidaparti R. Does microdamage accumulation affect the mechanical properties of bone? Journal of Biomechanics. 1998;31(4):337-45.
97. Koester KJ, Ager JW, Ritchie RO. The true toughness of human cortical bone measured with realistically short cracks. Nat Mater. 2008;7(8):672-7.
98. Nalla RK, Kruzic JJ, Kinney JH, Ritchie RO. Mechanistic aspects of fracture and R-curve behavior in human cortical bone. Biomaterials. 2005;26(2):217-31.

99. Jager I, Fratzl P. Mineralized collagen fibrils: a mechanical model with a staggered arrangement of mineral particles. Biophys J. 2000;79(4):1737-46.
100. Gao H, Ji B, Jäger IL, Arzt E, Fratzl P. Materials become insensitive to flaws at nanoscale: Lessons from nature. Proceedings of the National Academy of Sciences. 2003;100(10):5597-600.
101. Zioupos P, Currey JD. The extent of microcracking and the morphology of microcracks in damaged bone. Journal of Materials Science. 1994;29(4):978-86.
102. Zioupos P, Currey JD, Sedman AJ. An examination of the micromechanics of failure of bone and antler by acoustic emission tests and Laser Scanning Confocal Microscopy. Medical Engineering & Physics. 1994;16(3):203-12.
103. Braidotti P, Branca FP, Stagni L. Scanning electron microscopy of human cortical bone failure surfaces. Journal of Biomechanics. 1997;30(2):155-62.
104. Gupta HS, Messmer P, Roschger P, Bernstorff S, Klaushofer K, Fratzl P. Synchrotron diffraction study of deformation mechanisms in mineralized tendon. Phys Rev Lett. 2004;93(15):158101.
105. Akiva U, Wagner HD, Weiner S. Modelling the three-dimensional elastic constants of parallel-fibred and lamellar bone. Journal of Materials Science. 1998;33(6):1497-509.
106. Akkus O. Elastic deformation of mineralized collagen fibrils: An equivalent inclusion based composite model. J Biomech Eng-T Asme. 2005;127(3):383-90.
107. Gupta HS, Seto J, Wagermaier W, Zaslansky P, Boesecke P, Fratzl P. Cooperative deformation of mineral and collagen in bone at the nanoscale. Proc Natl Acad Sci U S A. 2006;103(47):17741-6.
108. Nikolov S, Raabe D. Hierarchical modeling of the elastic properties of bone at submicron scales: the role of extrafibrillar mineralization. Biophys J. 2008;94(11):4220-32.
109. Yuan F, Stock SR, Haeffner DR, Almer JD, Dunand DC, Brinson LC. A new model to simulate the elastic properties of mineralized collagen fibril. Biomech Model Mechanobiol. 2010.
110. Gao H. Application of fracture mechanics concepts to hierarchical biomechanics of bone and bone-like materials. International Journal of Fracture. 2006;138:37.
111. Almer JD, Stock SR. Probing the micro-mechanical behavior of bone via high-energy x-rays. 5th International Conference on Synchrotron Radiation Materials Science Chicago, IL: Proc., edited by A. Macrander, et al.; 2006.
112. Hull D, Clyne TW. An introduction to composite materials. 2nd edition ed. Cambridge, UK: Cambridge University Press; 1996.
113. Hellmich C, Ulm FJ. A unified continuum micromechanics approach to the ultrastructural elasticity of mineralized tissues. 15th ASCE Engineering Mechanics Conference; June 2-5; Columbia University, New York, NY2002.
114. Buehler MJ. Molecular nanomechanics of nascent bone: fibrillar toughening by mineralization. Nanotechnology. 2007;18(29).
115. Tadano S, Giri B, Sato T, Fujisaki K, Todoh M. Estimating nanoscale deformation in bone by X-ray diffraction imaging method. Journal of Biomechanics. 2008;41(5):945-52.
116. Zimmermann EA, Barth HD, Ritchie RO. The Multiscale Origins of Fracture Resistance in Human Bone and Its Biological Degradation. JOM. 2012;64:8.
117. Gautieri A, Buehler MJ, Redaelli A. Deformation rate controls elasticity and unfolding pathway of single tropocollagen molecules. Journal of the Mechanical Behavior of Biomedical Materials. 2009;2(2):130-7.
118. Ackbarow T, Chen X, Keten S, Buehler MJ. Hierarchies, multiple energy barriers, and robustness govern the fracture mechanics of alpha-helical and beta-sheet protein domains. Proc Natl Acad Sci U S A. 2007;104(42):16410-5.

119. Keten S, Buehler MJ. Asymptotic Strength Limit of Hydrogen-Bond Assemblies in Proteins at Vanishing Pulling Rates. Physical Review Letters. 2008;100(19):198301.
120. Launey ME, Buehler MJ, Ritchie RO. On the Mechanistic Origins of Toughness in Bone. Annual Review of Materials Research. 2010;40(1):25-53.
121. Buehler MJ, Keten S, Ackbarow T. Theoretical and computational hierarchical nanomechanics of protein materials: Deformation and fracture. Progress in Materials Science. 2008;53(8):1101-241.
122. Taylor D, Hazenberg JG, Lee TC. Living with cracks: Damage and repair in human bone. Nat Mater. 2007;6(4):263-8.
123. Fantner GE, Hassenkam T, Kindt JH, Weaver JC, Birkedal H, Pechenik L, Cutroni JA, Cidade GAG, Stucky GD, Morse DE, Hansma PK. Sacrificial bonds and hidden length dissipate energy as mineralized fibrils separate during bone fracture. Nat Mater. 2005;4(8):612-6.
124. Fantner GE, Oroudjev E, Schitter G, Golde LS, Thurner P, Finch MM, Turner P, Gutsmann T, Morse DE, Hansma H, Hansma PK. Sacrificial bonds and hidden length: Unraveling molecular mesostructures in tough materials. Biophysical Journal. 2006;90(4):1411-8.
125. Smith BL, Schaffer TE, Viani M, Thompson JB, Frederick NA, Kindt J, Belcher A, Stucky GD, Morse DE, Hansma PK. Molecular mechanistic origin of the toughness of natural adhesives, fibres and composites. Nature. 1999;399(6738):761-3.
126. Reilly GC, Currey JD. The development of microcracking and failure in bone depends on the loading mode to which it is adapted. Journal of Experimental Biology. 1999;202(5):543-52.
127. Krauss S, Fratzl P, Seto J, Currey JD, Estevez JA, Funari SS, Gupta HS. Inhomogeneous fibril stretching in antler starts after macroscopic yielding: indication for a nanoscale toughening mechanism. Bone. 2009;44(6):1105-10.
128. Tai K, Ulm F-J, Ortiz C. Nanogranular Origins of the Strength of Bone. Nano Letters. 2006;6(11):2520-5.
129. Gupta HS, Fratzl P, Kerschnitzki M, Benecke G, Wagermaier W, Kirchner HOK. Evidence for an elementary process in bone plasticity with an activation enthalpy of 1eV. Journal of The Royal Society Interface. 2007;4(13):277-82.
130. Peterlik H, Roschger P, Klaushofer K, Fratzl P. From brittle to ductile fracture of bone. Nat Mater. 2006;5(1):52-5.
131. Nalla RK, Kruzic JJ, Ritchie RO. On the origin of the toughness of mineralized tissue: microcracking or crack bridging? Bone. 2004;34(5):790-8.
132. Vashishth D, Behiri JC, Bonfield W. Crack growth resistance in cortical bone: Concept of microcrack toughening. Journal of Biomechanics. 1997;30(8):763-9.
133. Currey JD. Physical characteristics affecting the tensile failure properties of compact bone. Journal of Biomechanics. 1990;23(8):837-44.
134. Wang X, Puram S. The Toughness of Cortical Bone and Its Relationship with Age. Annals of Biomedical Engineering. 2004;32(1):123-35.
135. Carriero A, Zimmermann EA, Büsse B, Ager III JW, Ritchie RO, Shefelbine SJ. Fracture toughness in murine bone: a novel multiscale investigation. 18th Congress of the European Society of Biomechanics; 1-4 July, 2012; Lisbon, Portugal 2012.
136. Nalla RK, Kruzic JJ, Kinney JH, Balooch M, Ager JW, Ritchie RO. Role of microstructure in the aging-related deterioration of the toughness of human cortical bone. Mater Sci Eng. 2006;26:10.
137. Nalla RK, Kruzic JJ, Kinney JH, Ritchie RO. Effect of aging on the toughness of human cortical bone: evaluation by R-curves. Bone. 2004;35(6):1240-6.
138. Nalla RK, Stölken JS, Kinney JH, Ritchie RO. Fracture in human cortical bone: local fracture criteria and toughening mechanisms. Journal of Biomechanics. 2005;38(7):1517-25.

139. Ritchie RO. Mechanisms of fatigue-crack propagation in ductile and brittle solids. International Journal of Fracture. 1999;100(1):55-83.
140. Zimmermann EA, Launey ME, Barth HD, Ritchie RO. Mixed-mode fracture of human cortical bone. Biomaterials. 2009;30(29):5877-84.
141. He MY, Cao HC, Evans AG. Mixed-mode fracture: The four-point shear specimen. Acta Metallurgica et Materialia. 1990;38(5):839-46.
142. Zimmermann EA, Launey ME, Ritchie RO. The significance of crack-resistance curves to the mixed-mode fracture toughness of human cortical bone. Biomaterials. 2010;31(20):5297-305.
143. Parsamian GP, Norman TL. Diffuse damage accumulation in the fracture process zone of human cortical bone specimens and its influence on fracture toughness. Journal of Materials Science: Materials in Medicine. 2001;12(9):779-83.
144. Vashishth D, Tanner KE, Bonfield W. Contribution, development and morphology of microcracking in cortical bone during crack propagation. Journal of Biomechanics. 2000;33(9):1169-74.
145. Currey JD, Brear K, Zioupos P. The effects of ageing and changes in mineral content in degrading the toughness of human femora. Journal of Biomechanics. 1996;29(2):257-60.
146. Zioupos P. On microcracks, microcracking, in-vivo, in vitro, in-situ and other issues1999.
147. Sahar ND, Hong S-I, Kohn DH. Micro- and nano-structural analyses of damage in bone. Micron. 2005;36(7–8):617-29.
148. Fazzalari NL, Forwood MR, Manthey BA, Smith K, Kolesik P. Three-dimensional confocal images of microdamage in cancellous bone. Bone. 1998;23(4):373-8.
149. Norman TL, Wang Z. Microdamage of human cortical bone: Incidence and morphology in long bones. Bone. 1997;20(4):375-9.
150. Burr DB, Stafford T. Validity of the Bulk-Staining Technique to Separate Artifactual From In Vivo Bone Microdamage. Clinical Orthopaedics and Related Research. 1990;260:305-8.
151. Zioupos P. In vivo fatigue microcracks in human bone: material properties of the surrounding bone matrix. Eur J Morphol. 2005;42(1-2):31-41.
152. Boyce TM, Fyhrie DP, Glotkowski MC, Radin EL, Schaffler MB. Damage type and strain mode associations in human compact bone bending fatigue. Journal of Orthopaedic Research. 1998;16(3):322-9.
153. Carter DR, Hayes WC. Compact bone fatigue damage—I. Residual strength and stiffness. Journal of Biomechanics. 1977;10(5–6):325-37.
154. Reilly GC, Currey JD. The effects of damage and microcracking on the impact strength of bone. Journal of Biomechanics. 2000;33(3):337-43.
155. Sobelman OS, Gibeling JC, Stover SM, Hazelwood SJ, Yeh OC, Shelton DR, Martin R. Do microcracks decrease or increase fatigue resistance in cortical bone? Journal of Biomechanics. 2004;37:9.
156. Hiller LP, Stover SM, Gibson VA, Gibeling JC, Prater CS, Hazelwood SJ, Yeh OC, Martin RB. Osteon pullout in the equine third metacarpal bone: effects of ex vivo fatigue. Journal of Orthopaedic Research. 2003;21(3):481-8.
157. Malik CL, Stover SM, Martin RB, Gibeling JC. Equine cortical bone exhibits rising R-curve fracture mechanics. Journal of Biomechanics. 2003;36(2):191-8.
158. Launey ME, Chen PY, McKittrick J, Ritchie RO. Mechanistic aspects of the fracture toughness of elk antler bone. Acta Biomaterialia. 2010;6(4):1505-14.
159. Prince RL, Glendenning P. Disorders of bone and mineral other than osteoporosis. Med J Aust. 2004;180(7):354-9.

160. Klibanski A, Adams-Campbell L, Bassford T, Blair SN, Boden SD, Dickersin K, Gifford DR, Glasse L, Goldring SR, Hruska K, Johnson SR, McCauley LK, Russell WE, Osteopor NCDP. Osteoporosis prevention, diagnosis, and therapy. Jama-J Am Med Assoc. 2001;285(6):785-95.
161. Glaser DL, Kaplan FS. Osteoporosis. Definition and clinical presentation. Spine (Phila Pa 1976). 1997;22(24 Suppl):12S-6S.
162. Boskey AL, DiCarlo E, Paschalis E, West P, Mendelsohn R. Comparison of mineral quality and quantity in iliac crest biopsies from high- and low-turnover osteoporosis: an FT-IR microspectroscopic investigation. Osteoporos Int. 2005;16(12):2031-8.
163. Viguet-Carrin S, Garnero P, Delmas PD. The role of collagen in bone strength. Osteoporosis international : a journal established as result of cooperation between the European Foundation for Osteoporosis and the National Osteoporosis Foundation of the USA. 2006;17(3):319-36.
164. Bailey AJ. Changes in bone collagen with age and disease. J Musculoskel Neuron Interact. 2002;2(6):3.
165. Burr DB. Osteoporosis and fracture risk: bone matrix quality. J Musculoskel Neuron Interact. 2002;2((6)):2.
166. Mendelsohn R, Paschalis EP, Sherman PJ, Boskey AL. IR Microscopic Imaging of Pathological States and Fracture Healing of Bone. Appl Spectrosc. 2000;54(8):1183-91.
167. Boskey A. Assessment of bone mineral and matrix using backscatter electron imaging and FTIR imaging. Current Osteoporosis Reports. 2006;4(2):71-5.
168. Boskey A, Mendelsohn R. Infrared analysis of bone in health and disease. Journal of Biomedical Optics. 2005;10(3):031102-9.
169. Nih Consensus Development Panel on Osteoporosis Prevention D, Therapy. OSteoporosis prevention, diagnosis, and therapy. JAMA: The Journal of the American Medical Association. 2001;285(6):785-95.
170. Endres HG, Dasch B, Maier C, Lungenhausen M, Smektala R, Trampisch HJ, Pientka L. Diagnosis and treatment of osteoporosis in postmenopausal women with distal radius fracture in Germany. Curr Med Res Opin. 2007;23(9):2171-81.
171. Smals A. An atlas of osteoporosis: Edited by J.C. Stevenson and M.S. Marsh Published by The Parthenon Publishing Group. European Journal of Obstetrics & Gynecology and Reproductive Biology. 1993;48(2):153.
172. van Staa TP, Leufkens HGM, Abenhaim L, Begaud B, Zhang B, Cooper C. Use of oral corticosteroids in the United Kingdom. QJM. 2000;93(2):105-11.
173. Canalis E, Bilezikian JP, Angeli A, Giustina A. Perspectives on glucocorticoid-induced osteoporosis. Bone. 2004;34(4):593-8.
174. Reid DM, Hughes RA, Laan RFJM, Sacco-Gibson NA, Wenderoth DH, Adami S, Eusebio RA, Devogelaer J-P. Efficacy and Safety of Daily Risedronate in the Treatment of Corticosteroid-Induced Osteoporosis in Men and Women: A Randomized Trial. Journal of Bone and Mineral Research. 2000;15(6):1006-13.
175. Gu G, Mulari M, Peng Z, Hentunen TA, Väänänen HK. Death of osteocytes turns off the inhibition of osteoclasts and triggers local bone resorption. Biochemical and Biophysical Research Communications. 2005;335(4):1095-101.
176. Burr DB. Muscle Strength, Bone Mass, and Age-Related Bone Loss. Journal of Bone and Mineral Research. 1997;12(10):1547-51.
177. Balooch G, Yao W, Ager JW, Balooch M, Nalla RK, Porter AE, Ritchie RO, Lane NE. The aminobisphosphonate risedronate preserves localized mineral and material properties of bone in the presence of glucocorticoids. Arthritis & Rheumatism. 2007;56(11):3726-37.

178. Lane NE, Yao W, Balooch M, Nalla RK, Balooch G, Habelitz S, Kinney JH, Bonewald LF. Glucocorticoid-Treated Mice Have Localized Changes in Trabecular Bone Material Properties and Osteocyte Lacunar Size That Are Not Observed in Placebo-Treated or Estrogen-Deficient Mice. Journal of Bone and Mineral Research. 2006;21(3):466-76.
179. Weinstein RS. Glucocorticoid-Induced Bone Disease. New England Journal of Medicine. 2011;365(1):62-70.
180. Knott L, Whitehead CC, Fleming RH, Bailey AJ. Biochemical-Changes in the Collagenous Matrix of Osteoporotic Avian Bone. Biochem J. 1995;310:1045-51.
181. Dixon PH, Christie PT, Wooding C, Trump D, Grieff M, Holm I, Gertner JM, Schmidtke J, Shah B, Shaw N, Smith C, Tau C, Schlessinger D, Whyte MP, Thakker RV. Mutational analysis of PHEX gene in X-linked hypophosphatemia. J Clin Endocrinol Metab. 1998;83(10):3615-23.
182. Jan de Beur SM, Levine MA. Molecular pathogenesis of hypophosphatemic rickets. J Clin Endocrinol Metab. 2002;87(6):2467-73.
183. Berndt TJ, Schiavi S, Kumar R. "Phosphatonins" and the regulation of phosphorus homeostasis. Am J Physiol Renal Physiol. 2005;289(6):F1170-82.
184. Raeder H, Shaw N, Netelenbos C, Bjerknes R. A case of X-linked hypophosphatemic rickets: complications and the therapeutic use of cinacalcet. Eur J Endocrinol. 2008;159 Suppl 1:S101-5.
185. Chan GK, Duque G. Age-Related Bone Loss: Old Bone, New Facts. Gerontology. 2002;48(2):62-71.
186. Kanis JA. Diagnosis of osteoporosis and assessment of fracture risk. The Lancet. 2002;359(9321):1929-36.
187. Currey JD, Butler G. The mechanical properties of bone tissue in children. The Journal of Bone & Joint Surgery. 1975;57(6):810-4.
188. McCalden RW, McGeough JA, Barker MB, Court-Brown CM. Age-related changes in the tensile properties of cortical bone. The relative importance of changes in porosity, mineralization, and microstructure. The Journal of Bone & Joint Surgery. 1993;75(8):1193-205.
189. Tommasini SM, Nasser P, Jepsen KJ. Sexual dimorphism affects tibia size and shape but not tissue-level mechanical properties. Bone. 2007;40(2):498-505.
190. Schaffler MB, Choi K, Milgrom C. Aging and matrix microdamage accumulation in human compact bone. Bone. 1995;17(6):521-5.
191. Hirano T, Turner CH, Forwood MR, Johnston CC, Burr DB. Does suppression of bone turnover impair mechanical properties by allowing microdamage accumulation? Bone. 2000;27(1):13-20.
192. Vashishth D. Hierarchy of bone microdamage at multiple length scales. International Journal of Fatigue. 2007;29(6):1024-33.
193. Suzuki H, Amizuka N, Oda K, Li M, Yoshie H, Ohshima H, Noda M, Maeda T. Histological evidence of the altered distribution of osteocytes and bone matrix synthesis in klotho-deficient mice. Archives of Histology and Cytology. 2005;68(5):371-81.
194. Sell DR, Monnier VM. Structure elucidation of a senescence cross-link from human extracellular matrix. Implication of pentoses in the aging process. Journal of Biological Chemistry. 1989;264(36):21597-602.
195. Nyman JS, Roy A, Acuna RL, Gayle HJ, Reyes MJ, Tyler JH, Dean DD, Wang X. Age-related effect on the concentration of collagen crosslinks in human osteonal and interstitial bone tissue. Bone. 2006;39(6):1210-7.
196. Viguet-Carrin S, Follet H, Gineyts E, Roux JP, Munoz F, Chapurlat R, Delmas PD, Bouxsein ML. Association between collagen cross-links and trabecular microarchitecture properties of human vertebral bone. Bone. 2010;46(2):342-7.

197. Plantalech L, Guillaumont M, Vergnaud P, Leclercq M, Delmas PD. Impairment of gamma-carboxylation of circulating osteocalcin (bone gla protein) in elderly women. Journal of Bone and Mineral Research. 1991;6(11):1211-6.
198. Grynpas MD, Tupy JH, Sodek J. The distribution of soluble, mineral-bound, and matrix-bound proteins in osteoporotic and normal bones. Bone. 1994;15(5):505-13.
199. Handschin RG, Stern WB. X-ray diffraction studies on the lattice perfection of human bone apatite (Crista Iliaca). Bone. 1995;16(4, Supplement):S355-S63.
200. Denisov-Nikolskii YI, Zhilkin BA, Doktorov AA, Matveichuk IV. Ultrastructural organization of the human lamellar bone tissue mineral component in aged and elderly. Morfologiia. 2002;122(5):5.
201. Yerramshetty JS, Lind C, Akkus O. The compositional and physicochemical homogeneity of male femoral cortex increases after the sixth decade. Bone. 2006;39(6):1236-43.
202. Pellegrino ED, Biltz RM. Mineralization in the chick embryo. Calcified Tissue International. 1972;10(1):128-35.
203. Kanis JA, Borgstrom F, De Laet C, Johansson H, Johnell O, Jonsson B, Oden A, Zethraeus N, Pfleger B, Khaltaev N. Assessment of fracture risk. Osteoporosis International. 2005;16(6):581-9.
204. Sherman S, Hadley EC. Aging and bone quality: An underexplored frontier. Calcified Tissue International. 1993;53(0):S1-S.
205. Zimmermann EA, Schaible E, Bale H, Barth HD, Tang SY, Reichert P, Busse B, Alliston T, Ager JW, Ritchie RO. Age-related changes in the plasticity and toughness of human cortical bone at multiple length scales. Proceedings of the National Academy of Sciences. 2011.
206. Grabner B, Landis WJ, Roschger P, Rinnerthaler S, Peterlik H, Klaushofer K, Fratzl P. Age- and genotype-dependence of bone material properties in the osteogenesis imperfecta murine model (oim). Bone. 2001;29(5):453-7.
207. Arlot M, Meunier PJ, Boivin G, Haddock L, Tamayo J, Correa-Rotter R, Jasqui S, Donley DW, Dalsky GP, Martin JS, Eriksen EF. Differential Effects of Teriparatide and Alendronate on Bone Remodeling in Postmenopausal Women Assessed by Histomorphometric Parameters. Journal of Bone and Mineral Research. 2005;20(7):1244-53.
208. Martin RM, Correa PHS. Bone quality and osteoporosis therapy. Arquivos Brasileiros de Endocrinologia & Metabologia. 2010;54:186-99.
209. Lochmuller EM, Jung V, Weusten A, Wehr U, Wolf E, Eckstein F. Precision of high-resolution dual energy X-ray absorptiometry of bone mineral status and body composition in small animal models. European cells & materials. 2001;1:43-51.
210. Hernandez CJ, Keaveny TM. A biomechanical perspective on bone quality. Bone. 2006;39(6):1173-81.
211. Schuit SCE, van der Klift M, Weel AEAM, de Laet CEDH, Burger H, Seeman E, Hofman A, Uitterlinden AG, van Leeuwen JPTM, Pols HAP. Fracture incidence and association with bone mineral density in elderly men and women: the Rotterdam Study. Bone. 2004;34(1):195-202.
212. Whitmarsh T, Humbert L, De Craene M, Del Rio Barquero LM, Frangi AF. Reconstructing the 3D Shape and Bone Mineral Density Distribution of the Proximal Femur From Dual-Energy X-Ray Absorptiometry. Medical Imaging, IEEE Transactions on. 2011;30(12):2101-14.
213. Laet C, Kanis J, Odén A, Johanson H, Johnell O, Delmas P, Eisman J, Kroger H, Fujiwara S, Garnero P, McCloskey E, Mellstrom D, Melton L, Meunier P, Pols H, Reeve J, Silman A, Tenenhouse A. Body mass index as a predictor of fracture risk: A meta-analysis. Osteoporosis International. 2005;16(11):1330-8.
214. Silverman S, Calderon A. The Utility and Limitations of FRAX: A US Perspective. Current Osteoporosis Reports. 2010;8(4):192-7.

215. Siris Es CYATA, et al. BOne mineral density thresholds for pharmacological intervention to prevent fractures. Archives of Internal Medicine. 2004;164(10):1108-12.
216. Leslie WD, Lix LM, Johansson H, Oden A, McCloskey E, Kanis JA, for the Manitoba Bone Density P. Does osteoporosis therapy invalidate FRAX for fracture prediction? Journal of Bone and Mineral Research. 2012;27(6):1243-51.
217. Garvey CJ, Hanlon R. Computed tomography in clinical practice. BMJ. 2002;324(7345):1077-80.
218. Felsenberg D. New teschniques for assessing bone health. Medicographia. 2010;32(4):6.
219. Fratzl P, Paris O, Klaushofer K, Landis WJ. Bone mineralization in an osteogenesis imperfecta mouse model studied by small-angle x-ray scattering. J Clin Invest. 1996;97(2):396-402.
220. Xiong X, Qi X, Ge X, Gu P, Zhao J, Zhao Q, Gao X. A novel Phex mutation with defective glycosylation causes hypophosphatemia and rickets in mice. J Biomed Sci. 2008;15(1):47-59.
221. Boskey A, Frank A, Fujimoto Y, Spevak L, Verdelis K, Ellis B, Troiano N, Philbrick W, Carpenter T. The PHEX transgene corrects mineralization defects in 9-month-old hypophosphatemic mice. Calcif Tissue Int. 2009;84(2):126-37.
222. Cullity BD, Stock SR. Elements of X-Ray Diffraction. 3 ed: Prentice Hall; 2001.
223. Guinier A. X-ray diffraction in crystals, imperfect crystals, and amorphous bodies: Courier Dover Publications; 1994.
224. Wenk HR, Heidelbach F. Crystal alignment of carbonated apatite in bone and calcified tendon: Results from quantitative texture analysis. Bone. 1999;24(4):361-9.
225. Wess TJ. Collagen fibril form and function. Adv Protein Chem. 2005;70:341-74.
226. Wess TJ, Drakopoulos M, Snigirev A, Wouters J, Paris O, Fratzl P, Collins M, Hiller J, Nielsen K. The use of small-angle x-ray diffraction studies for the analysis of structural features in archaeological samples. Archaeometry. 2001;43:117-29.
227. Guinier A. Structure of Age-Hardened Aluminium-Copper Alloy. Nature. 1938;142:2.
228. Fratzl P, Jakob HF, Rinnerthaler S, Roschger P, Klaushofer K. Position-resolved small-angle X-ray scattering of complex biological materials. J Appl Crystallogr. 1997;30(2):765-9.
229. Fratzl P, Paris O, Zizak I, Lichtenegger H, Roschger P, Klaushofer K. Analysis of the hierarchical structure of biological tissues by scanning X-ray scattering using a micro-beam. Cell Mol Biol. 2000;46(5):993-1004.
230. Balta-Calleja FJ, Vonk CG. X-ray Scattering of Synthetic Polymers. Oxford: Elsevier Science Ltd; 1989.
231. Roschger P, Grabner BM, Rinnerthaler S, Tesch W, Kneissel M, Berzlanovich A, Klaushofer K, Fratzl P. Structural development of the mineralized tissue in the human L4 vertebral body. Journal of Structural Biology. 2001;136(2):126-36.
232. Hammersley AP. FIT2D: An Introduction and Overview. ESRF1997 Contract No.: ESRF97HA02T.
233. Rinnerthaler S, Roschger P, Jakob HF, Nader A, Klaushofer K, Fratzl P. Scanning small angle X-ray scattering analysis of human bone sections. Calcif Tissue Int. 1999;64(5):422-9.
234. Gourrier A, Li C, Siegel S, Paris O, Roschger P, Klaushofer K, Fratzl P. Scanning small-angle X-ray scattering analysis of the size and organization of the mineral nanoparticles in fluorotic bone using a stack of cards model. J Appl Crystallogr. 2010;43(6):1385-92.
235. Tesch W, Vandenbos T, Roschgr P, Fratzl-Zelman N, Klaushofer K, Beertsen W, Fratzl P. Orientation of mineral crystallites and mineral density during skeletal development in mice deficient in tissue nonspecific alkaline phosphatase. J Bone Miner Res. 2003;18(1):117-25.

236. Ballarre J, Manjubala I, Schreiner WH, Orellano JC, Fratzl P, Cere S. Improving the osteointegration and bone-implant interface by incorporation of bioactive particles in sol-gel coatings of stainless steel implants. Acta Biomater. 2010;6(4):1601-9.
237. Bunger M, Foss M, Erlaccher K, Li H, Zou X, Langdahl B, Bunger C, Birkedal H, Basenbacher F, Pedersen J. Bone nanostructure nean titanium and porous tantalum implants studied by scanning small angle x-ray scattering European Cells and Materials. 2006;12:11.
238. Janmey PA, McCulloch CA. Cell mechanics: Integrating cell responses to mechanical stimuli. Annu Rev Biomed Eng. 2007;9:1-34.
239. Vogel V, Sheetz M. Local force and geometry sensing regulate cell functions. Nat Rev Mol Cell Bio. 2006;7(4):265-75.
240. Hauge Bünger M, Foss M, Erlacher K, Bruun Hovgaard M, Chevallier J, Langdahl B, Bünger C, Birkedal H, Besenbacher F, Skov Pedersen J. Nanostructure of the neurocentral growth plate: Insight from scanning small angle X-ray scattering, atomic force microscopy and scanning electron microscopy. Bone. 2006;39(3):530-41.
241. Paris O, Aichmayer B, Al-Sawalmih A, Li C, Siegel S, Fratzl P. Mapping Lattice Spacing and Composition in Biological Materials by Means of Microbeam X-Ray Diffraction. Advanced Engineering Materials. 2011;9999:9.
242. Paris O. From diffraction to imaging: New avenues in studying hierarchical biological tissues with x-ray microbeams (Review). Biointerphases. 2008;3(2):Fb16-Fb26.
243. ESRF. What is a synchrotron? Grenoble2012 [updated 18-09-2012 13:57; cited 2012 07/11/2012].
244. Ltd DLS. How do synchrotrons work? Harwell2012 [updated 04/07/2012; cited 2012 07/11/2012].
245. Duke P. Synchrotron Radiation Production and Properties: Oxford University Press; 2009.
246. Bilderback DH, Elleaume P, Weckert E. Review of third and next generation synchrotron light sources. Journal of Physics B: Atomic, Molecular and Optical Physics. 2005;38:7.
247. Barth HD, Launey ME, MacDowell AA, Ager JW, Ritchie RO. On the effect of X-ray irradiation on the deformation and fracture behavior of human cortical bone. Bone. 2010;46(6):1475-85.
248. Barth HD, Zimmermann EA, Schaible E, Tang SY, Alliston T, Ritchie RO. Characterization of the effects of x-ray irradiation on the hierarchical structure and mechanical properties of human cortical bone. Biomaterials. 2011;32(34):8892-904.
249. Földváry CM, Takács E, Wojnárovits L. Effect of high-energy radiation and alkali treatment on the properties of cellulose. Radiation Physics and Chemistry. 2003;67(3–4):505-8.
250. Karunaratne A, Boyde A, Esapa CT, Hiller J, Terrill NJ, Brown SDM, Cox RD, Thakker RV, Gupta HS. Symmetrically reduced stiffness and increased extensibility in compression and tension at the mineralized fibrillar level in rachitic bone. Bone. 2012;(0).
251. Boyde A, Jones SJ. Backscattered Electron Imaging of Dental-Tissues. Anatomy and Embryology. 1983;168(2):211-26.
252. Boyde A, Jones SJ, Aerssens J, Dequeker J. Mineral density quantitation of the human cortical iliac crest by backscattered electron image analysis: variations with age, sex, and degree of osteoarthritis. Bone. 1995;16(6):619-27.
253. Boyde A, Travers R, Glorieux FH, Jones SJ. The Mineralization Density of Iliac Crest Bone from Children with Osteogenesis Imperfecta. Calcified Tissue International. 1999;64(3):185-90.
254. Ruffoni D, Fratzl P, Roschger P, Klaushofer K, Weinkamer R. The bone mineralization density distribution as a fingerprint of the mineralization process. Bone. 2007;40(5):1308-19.

255. Misof BM, Roschger P, Tesch W, Baldock PA, Valenta A, Messmer P, Eisman JA, Boskey AL, Gardiner EM, Fratzl P, Klaushofer K. Targeted Overexpression of Vitamin D Receptor in Osteoblasts Increases Calcium Concentration Without Affecting Structural Properties of Bone Mineral Crystals. Calcified Tissue International. 2003;73(3):251-7.
256. Zizak I, Roschger P, Paris O, Misof BM, Berzlanovich A, Bernstorff S, Amenitsch H, Klaushofer K, Fratzl P. Characteristics of mineral particles in the human bone/cartilage interface. J Struct Biol. 2003;141(3):208-17.
257. Basser PJ, Schneiderman R, Bank RA, Wachtel E, Maroudas A. Mechanical properties of the collagen network in human articular cartilage as measured by osmotic stress technique. Arch Biochem Biophys. 1998;351(2):207-19.
258. Elliott JC, Dover SD. X-ray microtomography. J Microsc. 1982;126(2):211-3.
259. Muller R, Ruegsegger P. Micro-tomographic imaging for the nondestructive evaluation of trabecular bone architecture. Stud Health Technol Inform. 1997;40:61-79.
260. Perilli E, Baruffaldi F, Visentin M, Bordini B, Traina F, Cappello A, Viceconti M. MicroCT examination of human bone specimens: effects of polymethylmethacrylate embedding on structural parameters. J Microsc. 2007;225(Pt 2):192-200.
261. Shefelbine SJ, Simon U, Claes L, Gold A, Gabet Y, Bab I, Muller R, Augat P. Prediction of fracture callus mechanical properties using micro-CT images and voxel-based finite element analysis. Bone. 2005;36(3):480-8.
262. Davis G, Evershed A, Elliott J, Mills D. Quantitative X-ray microtomography with a conventional source. Proc Spie. 2010;7804.
263. Kiessling F, Razansky D, Alves F. Anatomical and microstructural imaging of angiogenesis. Eur J Nucl Med Mol Imaging. 2010;37 Suppl 1:S4-19.
264. Nazarian A, Stauber M, Zurakowski D, Snyder BD, Muller R. The interaction of microstructure and volume fraction in predicting failure in cancellous bone. Bone. 2006;39(6):1196-202.
265. McErlain DD, Appleton CTG, Litchfield RB, Pitelka V, Henry JL, Bernier SM, Beier F, Holdsworth DW. Study of subchondral bone adaptations in a rodent surgical model of OA using in vivo micro-computed tomography. Osteoarthr Cartilage. 2008;16(4):458-69.
266. Jobke B, Burghardt AJ, Muche B, Hahn M, Semler J, Amling M, Majumdar S, Busse B. Trabecular Reorganization in Consecutive Iliac Crest Biopsies when Switching from Bisphosphonate to Strontium Ranelate Treatment. PLoS ONE. 2011;6(8):e23638.
267. Taylor M, Cotton J, Zioupos P. Finite element simulation of the fatigue behaviour of cancellous bone. Meccanica. 2002;37(4-5):419-29.
268. Verhulp E, van Rietbergen B, Huiskes R. Comparison of micro-level and continuum-level voxel models of the proximal femur. Journal of Biomechanics. 2006;39(16):2951-7.
269. Wansleeben C, van Gurp L, Feitsma H, Kroon C, Rieter E, Verberne M, Guryev V, Cuppen E, Meijlink F. An ENU-Mutagenesis Screen in the Mouse: Identification of Novel Developmental Gene Functions. PLoS ONE. 2011;6(4):e19357.
270. Hitotsumachi S, Carpenter DA, Russell WL. Dose-repetition increases the mutagenic effectiveness of N-ethyl-N-nitrosourea in mouse spermatogonia. Proceedings of the National Academy of Sciences of the United States of America. 1985;82(19):6619-21.
271. Bode VC. Ethylnitrosourea mutagenesis and the isolation of mutant alleles for specific genes located in the T region of mouse chromosome 17. Genetics. 1984;108(2):457-70.
272. Justice MJ, Noveroske JK, Weber JS, Zheng BH, Bradley A. Mouse ENU mutagenesis. Human molecular genetics. 1999;8(10):1955-63.

273. Lyon MF, Scriver CR, Baker LRI, Tenenhouse HS, Kronick J, Mandla S. The Gy Mutation - Another Cause of X-Linked Hypophosphatemia in Mouse. Proceedings of the National Academy of Sciences of the United States of America. 1986;83(13):4899-903.
274. Eicher EM, Southard JL, Scriver CR, Glorieux FH. Hypophosphatemia - Mouse Model for Human Familial Hypophosphatemic (Vitamin-D-Resistant) Rickets. Proceedings of the National Academy of Sciences of the United States of America. 1976;73(12):4667-71.
275. Storm TM, Francis F, Lorenz B, Boddrich A, J. EM, Lehrach H, Metinger T. Pex gene deletions in Gy and Hyp mice provide mouse models for X-linked hypophosphatemia. Human molecular genetics. 1997;6:7.
276. Carpinelli MR, Wicks IP, Sims NA, O'Donnell K, Hanzinikolas K, Burt R, Foote SJ, Bahlo M, Alexander WS, Hilton DJ. An ethyl-nitrosourea-induced point mutation in phex causes exon skipping, x-linked hypophosphatemia, and rickets. Am J Pathol. 2002;161(5):1925-33.
277. Boskey AL, Chiang P, Fermanis A, Brown J, Taleb H, David V, Rowe PS. MEPE's diverse effects on mineralization. Calcif Tissue Int. 2010;86(1):42-6.
278. Lane NE, Yao W. Glucocorticoid-induced bone fragility. Ann N Y Acad Sci. 2010;1192:81-3.
279. Dalle Carbonare L, Bertoldo F, Valenti MT, Zenari S, Zanatta M, Sella S, Giannini S, Cascio VL. Histomorphometric analysis of glucocorticoid-induced osteoporosis. Micron. 2005;36(7–8):645-52.
280. O'Brien CA, Jia D, Plotkin LI, Bellido T, Powers CC, Stewart SA, Manolagas SC, Weinstein RS. Glucocorticoids Act Directly on Osteoblasts and Osteocytes to Induce Their Apoptosis and Reduce Bone Formation and Strength. Endocrinology. 2004;145(4):1835-41.
281. Chappard D, Legrand E, Basle MF, Fromont P, Racineux JL, Rebel A, Audran M. Altered trabecular architecture induced by corticosteroids: a bone histomorphometric study. J Bone Miner Res. 1996;11(5):676-85.
282. Tritos NA, Biller BMK, Swearingen B. Management of Cushing disease. Nat Rev Endocrinol. 2011;7(5):279-89.
283. Hardy R, Cooper MS. Adrenal gland and bone. Archives of Biochemistry and Biophysics. 2010;503(1):137-45.
284. Bailey MA, Mullins JJ, Kenyon CJ. Mineralocorticoid and Glucocorticoid Receptors Stimulate Epithelial Sodium Channel Activity in a Mouse Model of Cushing Syndrome. Hypertension. 2009;54(4):890-6.
285. Sahut-Barnola I, de Joussineau C, Val P, Lambert-Langlais S, Damon C, Lefrançois-Martinez A-M, Pointud J-C, Marceau G, Sapin V, Tissier F, Ragazzon B, Bertherat J, Kirschner LS, Stratakis CA, Martinez A. Cushing's Syndrome and Fetal Features Resurgence in Adrenal Cortex–Specific <italic>Prkar1a</italic> Knockout Mice. PLoS Genet. 2010;6(6):e1000980.
286. Sarac MS, Zieske AW, Lindberg I. The lethal form of Cushing's in 7B2 null mice is caused by multiple metabolic and hormonal abnormalities. Endocrinology. 2002;143(6):2324-32.
287. Stenzel-Poore MP, Cameron VA, Vaughan J, Sawchenko PE, Vale W. Development of Cushing's syndrome in corticotropin-releasing factor transgenic mice. Endocrinology. 1992;130(6):3378-86.
288. Mazziotti G, Angeli A, Bilezikian JP, Canalis E, Giustina A. Glucocorticoid-induced osteoporosis: an update. Trends in Endocrinology & Metabolism. 2006;17(4):144-9.
289. Jilka RL, Weinstein RS, Takahashi K, Parfitt AM, Manolagas SC. Linkage of decreased bone mass with impaired osteoblastogenesis in a murine model of accelerated senescence. The Journal of clinical investigation. 1996;97(7):1732-40.
290. Kuro-o M, Matsumura Y, Aizawa H, Kawaguchi H, Suga T, Utsugi T, Ohyama Y, Kurabayashi M, Kaname T, Kume E, Iwasaki H, Iida A, Shiraki-Iida T, Nishikawa S, Nagai R,

Nabeshima Y-i. Mutation of the mouse klotho gene leads to a syndrome resembling ageing. Nature. 1997;390(6655):45-51.
291. Masuda H, Chikuda H, Suga T, Kawaguchi H, Kuro-o M. Regulation of multiple ageing-like phenotypes by inducible klotho gene expression in klotho mutant mice. Mechanisms of Ageing and Development. 2005;126(12):1274-83.
292. Kuro-o M. Klotho and aging. Biochimica et Biophysica Acta (BBA) - General Subjects. 2009;1790(10):1049-58.
293. Almeida M, Han L, Martin-Millan M, O'Brien CA, Manolagas SC. Oxidative stress antagonizes Wnt signaling in osteoblast precursors by diverting beta-catenin from T cell factor- to forkhead box O-mediated transcription. J Biol Chem. 2007;282(37):27298-305.
294. Reynolds RM, Dennison EM, Walker BR, Syddall HE, Wood PJ, Andrew R, Phillips DI, Cooper C. Cortisol secretion and rate of bone loss in a population-based cohort of elderly men and women. Calcified Tissue International. 2005;77(3):134-8.
295. Van Cauter E, Leproult R, Kupfer DJ. Effects of gender and age on the levels and circadian rhythmicity of plasma cortisol. The Journal of clinical endocrinology and metabolism. 1996;81(7):2468-73.
296. Ritchie RO, Barth HD, Launey ME, MacDowell AA, Ager JW. On the effect of X-ray irradiation on the deformation and fracture behavior of human cortical bone. Bone. 2010;46(6):1475-85.
297. Merchant SN, Burgess B, O'Malley J, Jones D, Adams JC. Polyester Wax: A New Embedding Medium for the Histopathologic Study of Human Temporal Bones. The Laryngoscope. 2006;116(2):245-9.
298. Lewis RA, Berry A, Hall CJ, Helsby WI, Parker BT. The RAPID detector system - first user data. Nucl Instrum Meth A. 2000;454(1):165-72.
299. Benecke G, Kerschnitzki M, Fratzl P, Gupta HS. Digital image correlation shows localized deformation bands in inelastic loading of fibrolamellar bone. J Mater Res. 2009;24:10.
300. Yuehuei H, Robert A. Mechanical Testing of Bone and the Bone-Implant Interface. 1999.
301. Gere JM, Timoshenko SP. Mechanics of materials. 3 ed: PWS-KENT Publishing company; 1990.
302. Boyde A, Firth EC. Musculoskeletal responses of two year old Thoroughbreds to training. 8. Quantitative backscattered electron scanning electron microscopy and confocal fluorescence microscopy of the epiphysis of the third metacarpal bone. New Zealand Veterinary Journal. 2005;53(2):10.
303. Doube M, Kłosowski MM, Arganda-Carreras I, Cordelières FP, Dougherty RP, Jackson JS, Schmid B, Hutchinson JR, Shefelbine SJ. BoneJ: Free and extensible bone image analysis in ImageJ. Bone. 2010;47(6):1076-9.
304. Currey JD. The effect of porosity and mineral content on the Young's modulus of elasticity of compact bone. J Biomech. 1988;21(2):131-9.
305. Clowes JA, Eastell R. The role of bone turnover markers and risk factors in the assessment of osteoporosis and fracture risk. Best Pract Res Cl En. 2000;14(2):213-32.
306. Bowe AE, Finnegan R, de Beur SMJ, Cho J, Levine MA, Kumar R, Schiavi SC. FGF-23 inhibits renal tubular phosphate transport and is a PHEX substrate. Biochemical and Biophysical Research Communications. 2001;284(4):977-81.
307. Fratzl P, Paris O, Klaushofer K, Landis WJ. Bone mineralization in an osteogenesis imperfecta mouse model studied by small-angle x-ray scattering. J Clin Invest. 1996;97(2):396-402.

308. Thurner PJ, Chen CG, Ionova-Martin S, Sun LL, Harman A, Porter A, Ager JW, Ritchie RO, Alliston T. Osteopontin deficiency increases bone fragility but preserves bone mass. Bone. 2010;46(6):1564-73.
309. Barbaric I, Perry MJ, Dear TN, Da Costa AR, Salopek D, Marusic A, Hough T, Wells S, Hunter AJ, Cheeseman M, Brown SDM. An ENU-induced mutation in the Ankrd11 gene results in an osteopenia-like phenotype in the mouse mutant Yoda. Physiol Genomics. 2008;32(3):311-21.
310. Boyde A, Knight PJ, Jones SJ. Further scanning electron microscope studies of the preparation of class II cavities. Br Dent J. 1972;132(11):447-57.
311. Tzaphlidou M, Berillis P. Collagen fibril diameter in relation to bone site. a quantitative ultrastructural study. Micron. 2005;36(7-8):703-5.
312. Currey JD. The design of mineralised hard tissues for their mechanical functions. J Exp Biol. 1999;202(Pt 23):3285-94.
313. Fritsch A, Hellmich C. 'Universal' microstructural patterns in cortical and trabecular, extracellular and extravascular bone materials: micromechanics-based prediction of anisotropic elasticity. J Theor Biol. 2007;244(4):597-620.
314. Kinney JH, Balooch M, Haupt DL, Jr., Marshall SJ, Marshall GW, Jr. Mineral distribution and dimensional changes in human dentin during demineralization. J Dent Res. 1995;74(5):1179-84.
315. Balooch M, Habelitz S, Kinney JH, Marshall SJ, Marshall GW. Mechanical properties of mineralized collagen fibrils as influenced by demineralization. J Struct Biol. 2008;162(3):404-10.
316. Ecarot B, Glorieux FH. Osteoblast Cultures - a Valuable Tool for the Study of Hypophosphatemic Vitamin-D-Resistant Rickets. Nestle Nutr Works Se. 1991;21:79-89

285.
317. Kindt JH, Thurner PJ, Lauer ME, Bosma BL, Schitter G, Fantner GE, Izumi M, Weaver JC, Morse DE, Hansma PK. In situ observation of fluoride-ion-induced hydroxyapatite-collagen detachment on bone fracture surfaces by atomic force microscopy. Nanotechnology. 2007;18(13).
318. Boyde A. Evidence against osteocytic osteolysis. Metabolic Bone Disease Related Research. 1980;2s:17.
319. Miao D, Liu H, Plut P, Niu M, Huo R, Goltzman D, Henderson JE. Impaired endochondral bone development and osteopenia in Gli2-deficient mice. Exp Cell Res. 2004;294(1):210-22.
320. Barak MM, Currey JD, Weiner S, Shahar R. Are tensile and compressive Young's moduli of compact bone different? Journal of the Mechanical Behavior of Biomedical Materials. 2009;2(1):51-60.
321. Kaneko TS, Bell JS, Pejcic MR, Tehranzadeh J, Keyak JH. Mechanical properties, density and quantitative CT scan data of trabecular bone with and without metastases. Journal of Biomechanics. 2004;37(4):523-30.
322. Vashishth D, Tanner KE, Bonfield W. Fatigue of cortical bone under combined axial-torsional loading. J Orthop Res. 2001;19(3):414-20.
323. Almer JD, Stock SR. Micromechanical response of mineral and collagen phases in bone. Journal of Structural Biology. 2007;157(2):365-70.
324. Demiaux I, Arlot ME, Chapuy MC, Meunier PC, Delmas PD. Serum osteocalcin is increased in patients with osteomalacia: correlations with biochemical and histomorphometric findings. The Journal of Clinical Endocrinology & Metabolism. 1992;74(5):6.
325. Marie P, Glorieux F. Relation between hypomineralized periosteocytic lesions and bone mineralization in vitamin D-resistant rickets. Calcified Tissue International. 1983;35(1):443-8.

326. Currey JD. The relationship between the stiffness and the mineral content of bone. Journal of Biomechanics. 1969;2(4):477-80.
327. Fritsch A, Hellmich C. 'Universal' microstructural patterns in cortical and trabecular, extracellular and extravascular bone materials: Micromechanics-based prediction of anisotropic elasticity. Journal of Theoretical Biology. 2007;244(4):597-620.
328. Steendijk R, Boyde A. Scanning electron microscopic observations on bone from patients with hypophosphataemic (vitamin D resistant) rickets. Calcified Tissue International. 1973;11(3):242-50.
329. Begley MR, Philips NR, Compton BG, Wilbrink DV, Ritchie RO, Utz M. Micromechanical models to guide the development of synthetic 'brick and mortar' composites. J Mech Phys Solids. 2012;60(8):1545-60.
330. Ji BH, Gao HJ. Mechanical properties of nanostructure of biological materials. J Mech Phys Solids. 2004;52(9):1963-90.
331. Bar-On B, Daniel Wagner H. Effective moduli of multi-scale composites. Composites Science and Technology. 2012;72(5):566-73.
332. Bar-On B, Wagner HD. Mechanical model for staggered bio-structure. J Mech Phys Solids. 2011;59(9):1685-701.
333. Balooch G, Balooch M, Nalla RK, Schilling S, Filvaroff EH, Marshall GW, Marshall SJ, Ritchie RO, Derynck R, Alliston T. TGF-β regulates the mechanical properties and composition of bone matrix. Proceedings of the National Academy of Sciences of the United States of America. 2005;102(52):18813-8.
334. Hang F, Barber AH. Nano-mechanical properties of individual mineralized collagen fibrils from bone tissue. Journal of the Royal Society, Interface / the Royal Society. 2011;8(57):500-5.
335. Reisinger AG, Pahr DH, Zysset PK. Principal stiffness orientation and degree of anisotropy of human osteons based on nanoindentation in three distinct planes. Journal of the mechanical behavior of biomedical materials. 2011;4(8):2113-27.
336. Bach-Gansmo FL, Brüel A, Thomsen JS, Birkedal H. Calcified Cartilage in mature rat cortical bone European Calcified Tissue Society 2012 39th Annual Congress; 05/2012; Stockholm, Sweden: Bone; 2012. p. S113.
337. Kaneko TS, Pejcic MR, Tehranzadeh J, Keyak JH. Relationships between material properties and CT scan data of cortical bone with and without metastatic lesions. Medical engineering & physics. 2003;25(6):445-54.
338. Reilly DT, Burstein AH, Frankel VH. The elastic modulus for bone. Journal of Biomechanics. 1974;7(3):271-5.
339. Yener NY, Dong XN, David PF, Clifford ML. The dependence between the strength and stiffness of cancellous and cortical bone tissue for tension and compression: Extension of a unifying principle. Bio-Medical Materials and Engineering. 2004;14(3):303-10.
340. Gupta S, van der Helm FCT. Load transfer across the scapula during humeral abduction. Journal of Biomechanics. 2004;37(7):1001-9.
341. Briggs AM, Greig AM, Wark JD, Fazzalari NL, Bennell KL. A review of anatomical and mechanical factors affecting vertebral body integrity. Int J Med Sci. 2004;1(3):170-80.
342. Ferretti JL, Cointry GR, Capozza RF, Frost HM. Bone mass, bone strength, muscle-bone interactions, osteopenias and osteoporoses. Mechanisms of Ageing and Development. 2003;124(3):269-79.
343. Kohrt WM, Barry DW, Schwartz RS. Muscle forces or gravity: what predominates mechanical loading on bone? Med Sci Sports Exerc. 2009;41(11):2050-5.
344. Thakker RV, O'Riordan JL. Inherited forms of rickets and osteomalacia. Baillieres Clin Endocrinol Metab. 1988;2(1):157-91.

345. Schott GD, Wills MR. Muscle Weakness in Osteomalacia. Lancet. 1976;1(7960):626-9.
346. Turner CH. Biomechanics of bone: determinants of skeletal fragility and bone quality. Osteoporos Int. 2002;13(2):97-104.
347. Bianchi ML, Morandi L, Andreucci E, Vai S, Frasunkiewicz J, Cottafava R. Low bone density and bone metabolism alterations in Duchenne muscular dystrophy: response to calcium and vitamin D treatment. Osteoporos Int. 2011;22(2):529-39.
348. Reid IR, Hardy DC, Murphy WA, Teitelbaum SL, Bergfeld MA, Whyte MP. X-linked hypophosphatemia: a clinical, biochemical, and histopathologic assessment of morbidity in adults. Medicine (Baltimore). 1989;68(6):336-52.
349. Rowe R, Goldspink G. Muscle fibre growth in five different muscles in both sexes of mice, i. Normal mice. J Anat. 1969;104(3):12.
350. Aono Y, Hasegawa H, Yamazaki Y, Shimada T, Fujita T, Yamashita T, Fukumoto S. Anti-FGF-23 neutralizing antibodies ameliorate muscle weakness and decreased spontaneous movement of Hyp mice. Journal of Bone and Mineral Research. 2011;26(4):803-10.
351. Sullivan W, Carpenter T, Glorieux F, Travers R, Insogna K. A prospective trial of phosphate and 1,25-dihydroxyvitamin D3 therapy in symptomatic adults with X-linked hypophosphatemic rickets. Journal of Clinical Endocrinology & Metabolism. 1992;75(3):879-85.
352. Bergwitz C, Roslin NM, Tieder M, Loredo-Osti JC, Bastepe M, Abu-Zahra H, Frappier D, Burkett K, Carpenter O, Anderson D, Garabedian M, Sermet I, Fujiwara TM, Morgan K, Tenenhouse HS, Juppner H. SLC34A3 mutations in patients with hereditary hypophosphatemic rickets with hypercalciuria predict a key role for the sodium-phosphate cotransporter NaPi-IIc in maintaining phosphate homeostasis. American Journal of Human Genetics. 2006;78(2):179-92.
353. Schönau E, Werhahn E, Schiedermaier U, Mokow E, Schiessl H, Scheidhauer K, Michalk D. Influence of Muscle Strength on Bone Strength during Childhood and Adolescence. Hormone Research in Paediatrics. 1996;45(Suppl. 1):63-6.
354. Nordström P, Thorsen K, Bergström E, Lorentzon R. High bone mass and altered relationships between bone mass, muscle strength, and body constitution in adolescent boys on a high level of physical activity. Bone. 1996;19(2):189-95.
355. Bauer DC, Browner WS, Cauley JA, Orwoll ES, Scott JC, Black DM, Tao JL, Cummings SR. Factors associated with appendicular bone mass in older women. The Study of Osteoporotic Fractures Research Group. Ann Intern Med. 1993;118(9):657-65.
356. Slemenda CW, Reister TK, Hui SL, Miller JZ, Christian JC, Johnston CC, Jr. Influences on skeletal mineralization in children and adolescents: evidence for varying effects of sexual maturation and physical activity. J Pediatr. 1994;125(2):201-7.
357. Smith JP, Hicks PS, Ortiz LR, Martinez MJ, Mandler RN. Quantitative measurement of muscle strength in the mouse. Journal of Neuroscience Methods. 1995;62(1–2):15-9.
358. Seeman E, Hopper JL, Young NR, Formica C, Goss P, Tsalamandris C. Do genetic factors explain associations between muscle strength, lean mass, and bone density? A twin study. American Journal of Physiology - Endocrinology And Metabolism. 1996;270(2):E320-E7.
359. Sherk VD, Palmer IJ, Bemben MG, Bemben DA. Relationships Between Body Composition, Muscular Strength, and Bone Mineral Density in Estrogen-Deficient Postmenopausal Women. Journal of Clinical Densitometry. 2009;12(3):292-8.
360. Taaffe DR, Cauley JA, Danielson M, Nevitt MC, Lang TF, Bauer DC, Harris TB. Race and Sex Effects on the Association Between Muscle Strength, Soft Tissue, and Bone Mineral Density in Healthy Elders: The Health, Aging, and Body Composition Study. Journal of Bone and Mineral Research. 2001;16(7):1343-52.
361. Frost HM. On Our Age-Related Bone Loss: Insights from a New Paradigm. Journal of Bone and Mineral Research. 1997;12(10):1539-46.

362. Vestergaard P, Mosekilde L. Hyperthyroidism, bone mineral, and fracture risk--a meta-analysis. Thyroid. 2003;13(6):585-93.
363. Sinaki M, Brey RH, Hughes CA, Larson DR, Kaufman KR. Balance disorder and increased risk of falls in osteoporosis and kyphosis: significance of kyphotic posture and muscle strength. Osteoporos Int. 2005;16(8):1004-10.
364. Smith R, Stern G. Myopathy, Osteomalacia and hyperparathyroidism. Brain. 1967;90(3):10.
365. Compston J. Management of glucocorticoid-induced osteoporosis. Nat Rev Rheumatol. 2010;6(2):82-8.
366. Van Staa TP, Laan RF, Barton IP, Cohen S, Reid DM, Cooper C. Bone density threshold and other predictors of vertebral fracture in patients receiving oral glucocorticoid therapy. Arthritis Rheum. 2003;48(11):3224-9.
367. Kalpakcioglu BB, Engelke K, Genant HK. Advanced imaging assessment of bone fragility in glucocorticoid-induced osteoporosis. Bone. 2011;48(6):1221-31.
368. Bouvard B, Audran M, Legrand E, Chappard D. Ultrastructural characteristics of glucocorticoid-induced osteoporosis. Osteoporosis International. 2009;20(6):1089-92.
369. Weinstein RS, Chen JR, Powers CC, Stewart SA, Landes RD, Bellido T, Jilka RL, Parfitt AM, Manolagas SC. Promotion of osteoclast survival and antagonism of bisphosphonate-induced osteoclast apoptosis by glucocorticoids. Journal of Clinical Investigation. 2002;109(8):1041-8.
370. Eastell R, Barton I, Hannon RA, Chines A, Garnero P, Delmas PD. Relationship of early changes in bone resorption to the reduction in fracture risk with risedronate. J Bone Miner Res. 2003;18(6):1051-6.
371. Saag KG, Emkey R, Schnitzer TJ, Brown JP, Hawkins F, Goemaere S, Thamsborg G, Liberman UA, Delmas PD, Malice MP, Czachur M, Daifotis AG, Interven G-IO. Alendronate for the prevention and treatment of glucocorticoid-induced osteoporosis. New England Journal of Medicine. 1998;339(5):292-9.
372. LoCascio V, Bonucci E, Imbimbo B, Ballanti P, Adami S, Milani S, Tartarotti D, DellaRocca C. Bone loss in response to long-term glucocorticoid therapy. Bone Miner. 1990;8(1):39-51.
373. Courtney AC, Hayes WC, Gibson LJ. Age-related differences in post-yield damage in human cortical bone. Experiment and model. Journal of Biomechanics. 1996;29(11):1463-71.
374. Gupta H, Wagermaier W, Zickler G, Hartmann J, Funari S, Roschger P, Wagner H, Fratzl P. Fibrillar level fracture in bone beyond the yield point. International Journal of Fracture. 2006;139(3):425-36.
375. Heuck F. Comparative investigations of the function of osteocytes in bone resorption. Calcif Tissue Res. 1970:Suppl:148-9.
376. Reilly GC. Observations of microdamage around osteocyte lacunae in bone. Journal of Biomechanics. 2000;33(9):1131-4.
377. Reilly GC, Currey JD. The effects of damage and microcracking on the impact strength of bone. J Biomech. 2000;33(3):337-43.
378. Koester KJ, Ager JW, 3rd, Ritchie RO. The true toughness of human cortical bone measured with realistically short cracks. Nat Mater. 2008;7(8):672-7.
379. Schneider P, Meier M, Wepf R, Muller R. Towards quantitative 3D imaging of the osteocyte lacuno-canalicular network. Bone. 2010;47(5):848-58.
380. Nicolella DP, Feng JQ, Moravits DE, Bonivitch AR, Wang Y, Dusecich V, Yao W, Lane N, Bonewald LF. Effects of nanomechanical bone tissue properties on bone tissue strain: implications for osteocyte mechanotransduction. J Musculoskelet Neuronal Interact. 2008;8(4):330-1.

381. Kerschnitzki M, Wagermaier W, Roschger P, Seto J, Shahar R, Duda GN, Mundlos S, Fratzl P. The organization of the osteocyte network mirrors the extracellular matrix orientation in bone. J Struct Biol. 2011;173(2):303-11.
382. Hui SL, Slemenda CW, Johnston CC. Age and bone mass as predictors of fracture in a prospective study. The Journal of Clinical Investigation. 1988;81(6):1804-9.
383. Burstein AH, Reilly DT, Martens M. Aging of bone tissue: mechanical properties. The Journal of Bone & Joint Surgery. 1976;58(1):82-6.
384. George WT, Vashishth D. Susceptibility of aging human bone to mixed-mode fracture increases bone fragility. Bone. 2006;38(1):105-11.
385. Ishii M, Yamaguchi Y, Yamamoto H, Hanaoka Y, Ouchi Y. Airspace enlargement with airway cell apoptosis in klotho mice: a model of aging lung. J Gerontol A Biol Sci Med Sci. 2008;63(12):1289-98.
386. Kawaguchi H, Manabe N, Miyaura C, Chikuda H, Nakamura K, Kuro-o M. Independent impairment of osteoblast and osteoclast differentiation in klotho mouse exhibiting low-turnover osteopenia. Journal of Clinical Investigation. 1999;104(3):229-37.
387. Boskey AL, Coleman R. Aging and Bone. Journal of Dental Research. 2010;89(12):1333-48.
388. Kuhn LT, Grynpas MD, Rey CC, Wu Y, Ackerman JL, Glimcher MJ. A comparison of the physical and chemical differences between cancellous and cortical bovine bone mineral at two ages. Calcified Tissue International. 2008;83(2):146-54.
389. Negri AL. The klotho gene: A gene predominantly expressed in the kidney is a fundamental regulator of aging and calcium/phosphorus metabolism. J Nephrol. 2005;18(6):654-8.
390. Cooper DML, Thomas CDL, Clement JG, Turinsky AL, Sensen CW, Hallgrímsson B. Age-dependent change in the 3D structure of cortical porosity at the human femoral midshaft. Bone. 2007;40(4):957-65.
391. Rochefort GY, Pallu S, Benhamou CL. Osteocyte: the unrecognized side of bone tissue. Osteoporosis International. 2010;21(9):1457-69.
392. Eyre DR, Dickson IR, Van Ness K. Collagen cross-linking in human bone and articular cartilage. Age-related changes in the content of mature hydroxypyridinium residues. The Biochemical journal. 1988;252(2):495-500.
393. Sell DR, Monnier VM. Structure Elucidation of a Senescence Cross-Link from Human Extracellular-Matrix - Implication of Pentoses in the Aging Process. Journal of Biological Chemistry. 1989;264(36):21597-602.
394. Boyde A, Hendel P, Hendel R, Maconnachie E, Jones SJ. Human cranial bone structure and the healing of cranial bone grafts: a study using backscattered electron imaging and confocal microscopy. Anatomy and Embryology. 1990;181(3):235-51.
395. Kingsmill VJ, Boyde A. Mineralisation density of human mandibular bone: quantitative backscattered electron image analysis. Journal of Anatomy. 1998;192(2):245-56.
396. MRC. Research Changes Lives - MRC Strategic Plan 2009-2014. 2009.
397. Beaupied H, Lespessailles E, Benhamou CL. Evaluation of macrostructural bone biomechanics. Joint Bone Spine. 2007;74(3):233-9.
398. Cummings SR, Karpf DB, Harris F, Genant HK, Ensrud K, LaCroix AZ, Black DM. Improvement in spine bone density and reduction in risk of vertebral fractures during treatment with antiresorptive drugs. The American Journal of Medicine. 2002;112(4):281-9.
399. Allen MR, Burr DB. Mineralization, microdamage, and matrix: How bisphosphonates influence material properties of bone. IBMS BoneKEy. 2007;4(2):49-60.

400. Garnero P, Bauer DC, Mareau E, Bilezikian JP, Greenspan SL, Rosen C, Black D. Effects of PTH and Alendronate on Type I Collagen Isomerization in Postmenopausal Women With Osteoporosis: The PaTH Study. Journal of Bone and Mineral Research. 2008;23(9):1442-8.
401. Paschalis EP, Glass EV, Donley DW, Eriksen EF. Bone Mineral and Collagen Quality in Iliac Crest Biopsies of Patients Given Teriparatide: New Results from the Fracture Prevention Trial. Journal of Clinical Endocrinology & Metabolism. 2005;90(8):4644-9.
402. Dobnig H, Stepan JJ, Burr DB, Li J, Michalská D, Sipos A, Petto H, Fahrleitner-Pammer A, Pavo I. Teriparatide Reduces Bone Microdamage Accumulation in Postmenopausal Women Previously Treated With Alendronate. Journal of Bone and Mineral Research. 2009;24(12):1998-2006.
403. Sarkar S, Mitlak BH, Wong M, Stock JL, Black DM, Harper KD. Relationships Between Bone Mineral Density and Incident Vertebral Fracture Risk with Raloxifene Therapy. Journal of Bone and Mineral Research. 2002;17(1):1-10.
404. Jimenez-Palomar I, Shipov A, Shahar R, Barber AH. Influence of SEM vacuum on bone micromechanics using in situ AFM. Journal of the Mechanical Behavior of Biomedical Materials. 2012;5(1):149-55.
405. Carden A, Morris MD. Application of vibrational spectroscopy to the study of mineralized tissues (review). Journal of Biomedical Optics. 2000;5(3):259-68.
406. Carden A, Rajachar RM, Morris MD, Kohn DH. Ultrastructural Changes Accompanying the Mechanical Deformation of Bone Tissue: A Raman Imaging Study. Calcified Tissue International. 2003;72(2):166-75.
407. Morris MD, Finney WF, Rajachar RM, Kohn DH. Bone tissue ultrastructural response to elastic deformation probed by Raman spectroscopy. Faraday Discuss. 2004;126:159-68; discussion 69-83.
408. Sergo V, Sbaizero O, Clarke DR. Mechanical and chemical consequences of the residual stresses in plasma sprayed hydroxyapatite coatings. Biomaterials. 1997;18(6):477-82.
409. Timlin JA, Carden A, Morris MD, Rajachar RM, Kohn DH. Raman spectroscopic imaging markers for fatigue-related microdamage in bovine bone. Anal Chem. 2000;72(10):2229-36.
410. Morris MD, Mandair GS. Raman Assessment of Bone Quality. Clinical Orthopaedics and Related Research. 2011;469(8):2160-9.
411. Yeni Y, Yerramshetty J, Akkus O, Pechey C, Les C. Effect of Fixation and Embedding on Raman Spectroscopic Analysis of Bone Tissue. Calcified Tissue International. 2006;78(6):363-71.
412. Pezzotti G. Raman piezo-spectroscopic analysis of natural and synthetic biomaterials. Analytical and Bioanalytical Chemistry. 2005;381(3):577-90.

Rickets induces significant deterioration in nanomechanical quality through incomplete extrafibrillar mineralization: evidence from in-situ synchrotron X-ray scattering and backscattered electron imaging

A Karunaratne[1], CT Esapa[2, 3], J Hiller[4], A Boyde[5], R Head[2, 3], JHD Bassett[6], NJ Terrill[4], GR Williams[6], MA Brown[7], P Croucher[8], SDM Brown[3], RD Cox[3], AH Barber[1], RV Thakker[2], HS Gupta[1]

1. School of Engineering and Material Sciences, Queen Mary University of London, Mile End Road, London, E1 4NS, UK 2. Academic Endocrine Unit, Nuffield Department of Clinical Medicine, Oxford Centre for Diabetes, Endocrinology and Metabolism, University of Oxford, Churchill Hospital, Headington, Oxford, OX3 7JL, UK 3. MRC Mammalian Genetics Unit and Mary Lyon Centre, MRC Harwell, Harwell Science and Innovation Campus, OX11 0RD, UK 4. Diamond Light Source Ltd., Diamond House, Harwell Science and Innovation Campus, Chilton, Didcot, Oxfordshire, OX11 0DE, United Kingdom 5. Queen Mary University of London, Oral Growth and Development, Institute of Dentistry, Bart's and The London School of Medicine, London E1 1BB, UK 6. Molecular Endocrinology Group, MRC Clinical Sciences Centre & Division of Investigative Sciences, Imperial College London, Hammersmith Campus, Du Cane Road, London W12 0NN, UK 7. University of Queensland Diamantina Institute, the University of Queensland, Princess Alexandra Hospital, Brisbane, QLD, 4102, Australia 8. The Mellanby Centre for Bone Research, Department of Human Metabolism, University of Sheffield, Sheffield, S10 2RX, UK

Aim and objectives

Metabolic bone disorders like rickets and osteoporosis cause significant reduction in both bone quantity and material quality, leading to dramatic reductions in mechanical parameters like fracture resistance.

Aim –
Demonstration of the ultrastructural functional link between altered bone quality (reduced mineralization) and abnormal fibrillar-level mechanics.

Objectives –
•Application of novel, real-time synchrotron X-ray nanomechanical imaging method on a ENU mutagenesis murine model (Elvis) exhibiting reduced extrafibrillar mineralization due to reduction in bone mineral density.

•Mineral content is estimated using quantitative backscattered electron imaging.

•Development of a simple, unifying model linking changes in nanoscale material properties of the mineralized fibrils to observed nano-mechanical behaviour, we combine the in-situ SAXS and qBSE results.

Comparison of in situ X-ray nanomechanical imaging with other assays of bone functional competence

Technique	Diagnostic level of the hierarchical organization of bone	In-situ mechanical testing	In-vivo/in-vitro	Monitoring of treatment effect	Relating structural and mechanical behaviour of same specimen
DEXA – BMD - mineral density per area	Micro level – Cortical and trebecular bone	No	In -vivo	Poor – Fails to separate measures for trabecular and cortical bone [10]	No
qCT/mCT – BMD - mineral density per volume	Micro level	Yes	In -vivo	Yes - Separates cortical and trabecular bone[10]	No, developing
qBSE – BMD Distribution	Micro level	No	In -vivo	Yes - only in 2D	No
In-situ mechanical testing with SAXS/WAXD – In-Vitro Nanomechanical Functional Imaging of bone	Nanolevel – mineralized collagen fibril	Yes	in-vitro	Yes –Measure the changes to the material and functionality of the bone at nano level	Yes

Experimental procedure

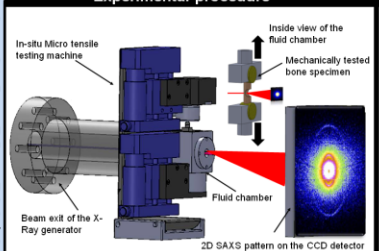

Data analysis

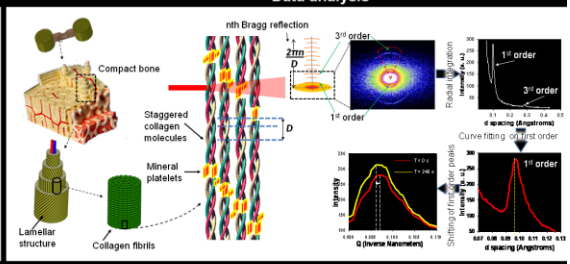

Results: In –situ Nanoscale Mechanical Testing

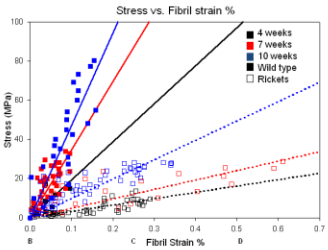

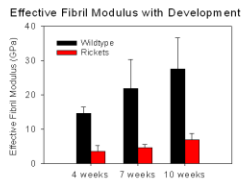

•The effective fibril modulus (σ/ε_{fb}) increased consistently with development. In the hierarchical staggered model[7,9] such a change may be due to an increased extrafibrillar matrix stiffness over this period.

•The effective modulus of the Elvis mice at every age was significantly less than their wild type counterparts. Possibly due to the reduced extrafibrillar mineralisation.

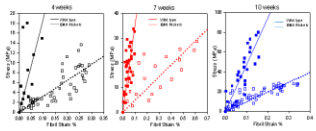

•The fibrils strain much more in the region of elastic deformation in rickets mice femora compared to wild-type mice of the same age due to the lowered lateral mineral straight-jacketing effect.

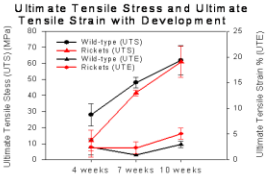

•Ultimate tensile stress increases with age in both wild type and rickets, but UTS of rickets was less than the normal mice. There was a greater failure strain in rickets compared to wild type.

Results : Quantitative Backscattered Electron Imaging

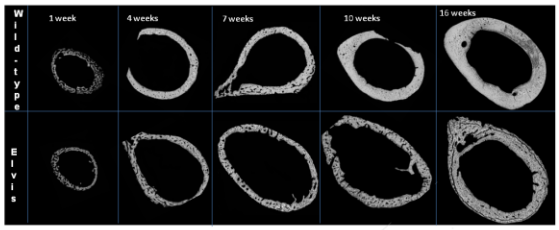

•A highly heterogeneous mineralized matrix at the microscale, with a large fraction of poorly mineralized cortex in Elvis mice.

•The reduced local (micro) primary mineralisation rate in rickets compared to wild type mice is most likely linked to the overall reduction in mineralization.

•The large reduction in heterogeneity between 1 week to 4 weeks – leading to more uniform mineralization – observed in wild type mice is completely absent in the Elvis mice.

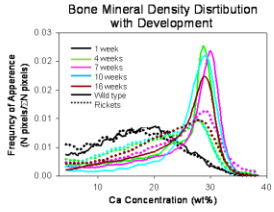

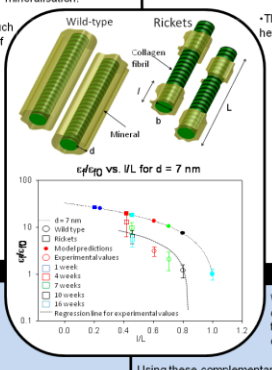

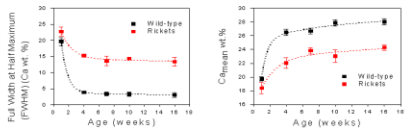

Model

We developed a simple model and we take collagen fibrils from mature wild type mice as fully covered with a mineral coating of probably uniform thickness (d), while in the fibrils of rickets mice they are only partly covered with mineral even in fully mature tissue.

The total % elongation of the partly mineralized and fully mineralized fibril – ε_f and $\varepsilon_{f,0}$
Elastic moduli of the mineral and collagen - E_m and E_f

$$\varepsilon_{f,0} = \frac{4F}{\pi b^2 E_f}\left[1/\sqrt{1+\frac{4\left(d^2+db\right)E_m}{b^2 E_f}}\right] \rightarrow eq.1 \qquad \varepsilon_{f,u} = \frac{4F}{\pi b^2 E_f} \rightarrow eq.2$$

The ratio of the fibril strain at intermediate mineralization (eq.1) ($0 < l < L$) to that of the fibril at full mineralization (eq.2) ($l = L$) is

$$\frac{\varepsilon_f}{\varepsilon_{f,0}} = \left[1+4\frac{d}{b}\left(\frac{d}{b}+1\right)\frac{E_m}{E_f}+\frac{l}{L}\left(1-4\frac{d}{b}\left(\frac{d}{b}+1\right)\frac{E_m}{E_f}\right)\right]$$

Conclusion

We have utilised the skeletal phenotype from a mouse model of XLHR (Elvis) to demonstrate the power of in-situ synchrotron SAXS combined with micromechanical testing to serve as an in-vitro functional imaging technique to measure the bone quality degradation in metabolic bone diseases.

Using these complementary methods and results we proposed a tentative nanoscale model of the mineralized collagen fibril in rickets, where incomplete extrafibrillar mineralization leads to a larger elongation and a lower effective fibril modulus.

Our approach clearly shows the power of synchrotron-based in-situ X-ray nanomechanical imaging as a diagnostic tool to identify functional alterations in bone quality at the nanoscale in metabolic bone disease conditions such as osteoporosis, osteoarthritis, and aging.

References

I. Barbaric et al., *Physiological Genomics 32, 311 (Feb 19, 2008)*. 2. H. S. Gupta et al., *Proceedings of the National Academy of Sciences of the United States of America 103, 17741 (Nov 21, 2006)*. 3. X. W. Xiong et al., *Journal of Biomedical Science 15, 47 (Jan, 2008)*. 4. N. P. Camacho, C. M. Rimnac, R. A. Meyer, S. Doty, A. L. Boskey, *Bone 17*, 271 (Sep, 1995). 5. X. Yao, L. F. Bonewald, J. D. Eick, Y. Wang, paper presented at the Materials Research Society Spring Meeting, Symposium KK, San Francisco, USA 2009. 6. Gourrier et al., *Journal of Applied Crystallography 40, 78 (2007)*. 7. Gupta, et al., *Proc Natl Acad Sci U S A*, 103, 17741-6 (2006). 8.

DISRUPTION IN FIBRILLAR LEVEL FRACTURE MECHANISMS IN RACHITIC MICE BONE: MEASURED USING IN-SITU CANTILEVER BENDING WITH MICROFOCUS SAXD

A Karunaratne[1], CT Esapa[2, 3], J Hiller[4], A Boyde[5], NJ Terrill[4], SDM Brown[3], RD Cox[3], RV Thakker[2], HS Gupta[1]

1. School of Engineering and Material Sciences, Queen Mary University of London, Mile End Road, London, E1 4NS, UK 2. Academic Endocrine Unit, Nuffield Department of Clinical Medicine, Oxford Centre for Diabetes, Endocrinology and Metabolism, University of Oxford, Churchill Hospital, Headington, Oxford, OX3 7JL, UK 3. MRC Mammalian Genetics Unit and Mary Lyon Centre, MRC Harwell, Harwell Science and Innovation Campus, OX11 0RD, UK 4. Diamond Light Source Ltd., Diamond House, Harwell Science and Innovation Campus, Chilton, Didcot, Oxfordshire, OX11 0DE, United Kingdom 5. Queen Mary University of London, Oral Growth and Development, Institute of Dentistry, Bart's and The London School of Medicine, London E1 1BB, UK

Motivation

Research Background:
Understanding how changes in the structure of the nanoscale bone matrix (*bone quality*) increase the risk of fracture is a key frontier area of clinical bone biomechanics. In the case of hypophosphatemic rickets, we have previously shown that reduced extrafibrillar mineralization (at the scale of 100 nm) leads to significantly enhanced fibrillar extensibility in tension (> 3x over controls) for only 20-30% reduction in mineral content[1]. Whether this mechanism is also relevant (beyond tension) for physiologically relevant loading like bending and compression is not known.

Objective:
To make the first simultaneous *in situ* measurement of compressive and tensile deformation at the fibrillar level in a prototypical bone disease (*ENU mutagenesis murine model*[2]) of low mineralization (hypophosphatemic rickets or *Hpr*). We use high brilliance microfocus synchrotron small-angle X-ray scattering (SAXS) combined with in situ cantilever bending to measure the (nanoscale) fibrillar strains developed in real time during (macroscale) deformation and fracture

Small Angle X-Ray Scattering

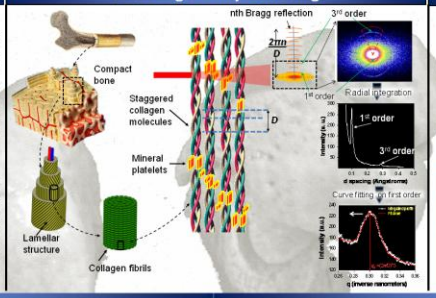

Experimental Procedure

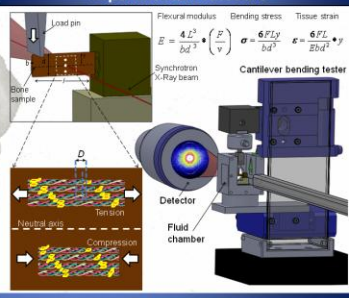

Results: *In-situ* Mechanical Testing

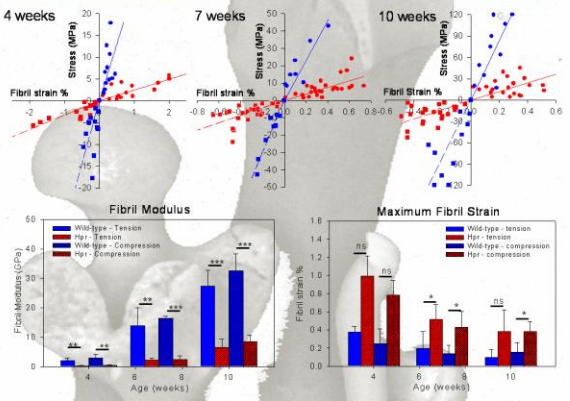

•The effective fibril modulus (σ/ε_f) increased consistently with development in the tensile and compression zones. In the hierarchical staggered model[3,4] such a change may be due to an increased extrafibrillar matrix stiffness over this period.

•The effective modulus of the *Hpr* mice at every age was significantly less than their wild type counterparts due to the reduced extrafibrillar mineralisation

.

•The maximum fibrils strain is much more in rickets mice humeri compared to wild-type mice of the same age due to the lowered lateral mineral straight-jacketing effect[1].

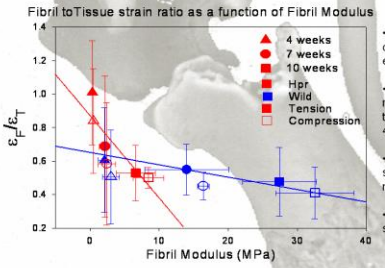

•Fibril to tissue strain ratio decreases with increasing effective fibril modulus.

•Due to the low effective fibril modulus in *Hpr* mice, fibril to tissue ratio is relatively higher at 4 and 7 weeks of age.

•In wild-type mice change in strain ratio with fibril modulus is not that significant.

•Fibril to tissue strain ratio stabilises at ratio of 0.5.

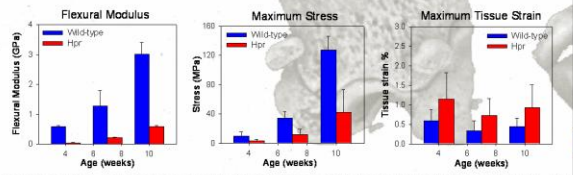

Flexural modulus and maximum bending stress increases with age in both wild type and rickets, but maximum stress of *Hpr* was less than the normal mice. There was a greater failure strain in *Hpr* compared to wild type

Results : Quantitative Backscattered Electron Imaging

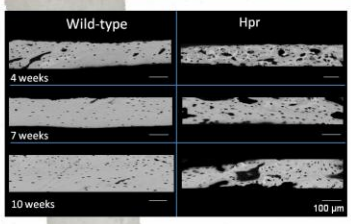

•A highly heterogeneous mineralized matrix at the microscale, with a large fraction of poorly mineralized cortex in *Hpr* mice.

•The *Hpr* cortical bone has hypomineralised periosteocytic lesions similar to previously reported osteomalacic patients [5].

•Osteocytic network in *Hpr* mice bone is randomly orientated compared to the wild-type indicating a disorganised collagen matrix deposited by *Hpr* osteoblasts.

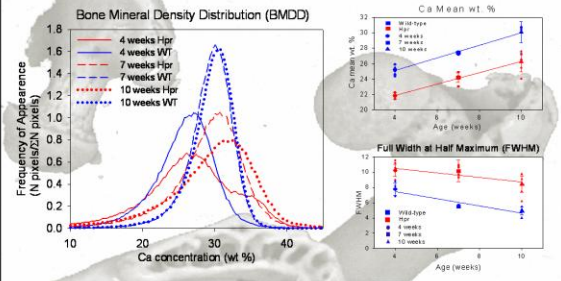

•The reduced local (micro) primary mineralisation rate in rickets compared to wild type mice is most likely linked to the overall reduction in mineralization.

•The overall reduction in heterogeneity between 4 weeks to 10 weeks – leading to more uniform mineralization – observed in wild type mice is less pronounced in the *Hpr* mice.

Conclusion

Here, we have shown that the same fibrillar nanoscale deformation mechanisms operate during physiologically relevant compressive loading showing the clinical relevance of our model[1] to understand causes of increased bone fragility in *Hpr*.

Our data are the first to directly quantify fibrillar-level compressive and bending deformation in a biochemically well-defined disease model.

This result is also interesting because at the macroscale, compressive stiffness and strength is usually higher than tension. Our results show that this difference is not reflected in a differential response between tension and compression at the nanoscale.

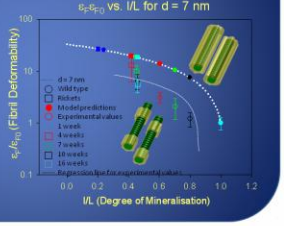

References

I. A. Karunaratne et al., *JMR 27, 876-890 (April 2012).* 2. Barbaric *et al., Physiological Genomics 32, 311 (Feb 19, 2008).* 3. H. S. Gupta *et al., Proceedings of the National Academy of Sciences of the United States of America 103, 17741 (Nov 21, 2006).* 4. Gupta, et al., *Proc Natl Acad Sci U S A* 103, 17741-6 (2006). 5. A. Boyde Metb Bone Dis Relat Res 2S (1980). 6. Gourrier *et al., Journal of Applied Crystallography 40, 78 (2007).* 8. Currey J. D. *J Exp Biol,* 202, 3285-94 (1999), 9. Fratzl et al., *Journal of Clinical Investigation* 97, 396-402 (1996)

Disruption of muscle stress-mediated mineral orientation at the nanoscale in the flat scapular bones of rickets mice with development

A Karunaratne, GR Davis, J Hiller, CT Esapa, NJ Terrill, RV Thakker, HS Gupta

Queen Mary University of London

diamond

Aim and Objectives

Metabolic and neuromuscular bone disorders like rickets and muscular dystrophy are also associated with altered *in-vivo* muscular force distributions on the skeletal system which can potentially alter the spatial and temporal dynamics of mineralized tissue formation.

Aim

Demonstration of the mechanism for the increased macroscopic fracture risk in rickets and muscular dystrophy is via a significant alteration in the mineral nanostructure, mediated by an altered spatial distribution of muscle forces.

Objectives

We use a mouse model for X-linked hypophosphataemic rickets, a disease that is associated with progressive weakness and wasting of skeletal muscle (1) as well as lowered bone mineral content

Quantification of the degree of orientation and the direction of mineral nanopatelet alignment over the entire width of the scapula bone using position – resolved scanning small angle X-ray scattering (sSAXS).

X-ray microtomography was used to obtain the tomographic images to provide qualitative surface structural information and idealised radiographs to calculate scapula bone thickness for SAXS intensity normalisation

Experimental setup and Data analysis

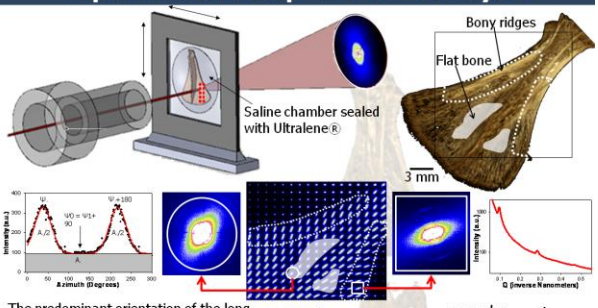

The predominant orientation of the long axis of the mineral crystals is along the direction defined by the angle (2)

$\psi_i = \psi_i + 90$

The degree of orientation ρ is defined by

$\rho = A_1 / (A_0 + A_1)$

$I = \int_{q\,min}^{q\,max} \int_{X_1}^{X_2} I(q, X)\, q^2\, dq\, dX$

$\tilde{I} = 2\pi\, \varphi_1 \varphi_2\, (\Delta\rho)^2$

φ_1 and φ_2 - volume fractions of the two phases (3)

$\Delta\rho$ – mean electro density between those two phases

Results - *Abnormal development in Hpr mice scapula*

3D rendered images and their 2D sSAXS composite maps combining predominant orientation and degree of orientation

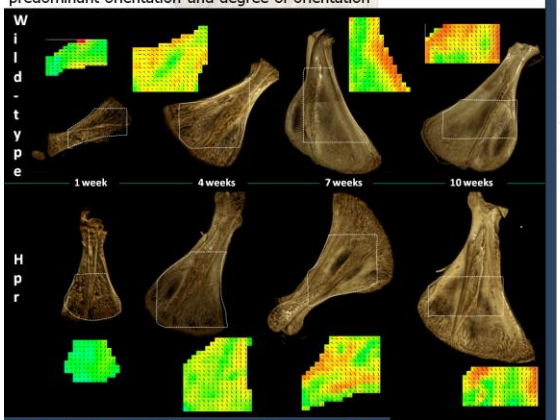

Quantitative Analysis nano structural parameters

Composite map of mineral particle orientation showing two anatomical regions lateral border (black box) and infraspinous fossa (white box) that subjected to different muscle forces, were selected to measure the degree of orientation, angle of mineral particles and SAXS intensity

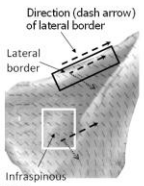

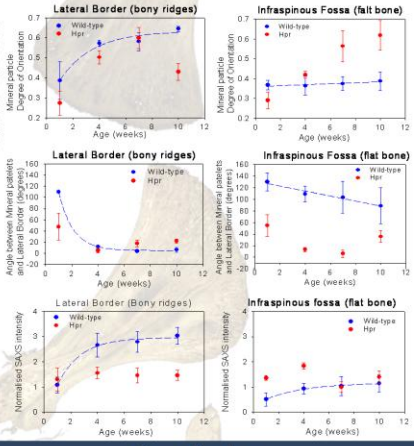

Correlation with altered muscular force distributions in Rickets bone

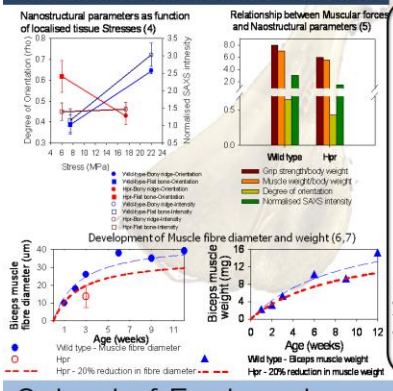

Model

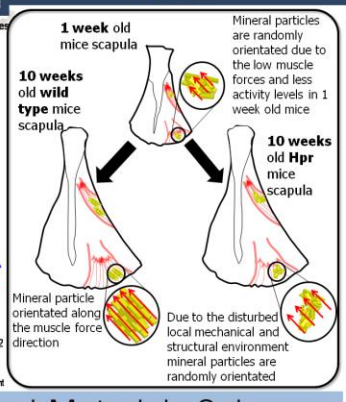

Conclusion

During skeletal development we find a much larger increase in mineral nanoplatelet alignment and amount of mineral in the bony ridges compared to the flat bony regions in normal mice.

Our results also show that alterations in nanostructural properties such as mineral particle degree of orientation and direction of mineral particles are mainly due to the combined effect of altered muscle forces and reduced mineralisation in the disease condition.

Therefore we conclude that nanostructural parameters play a vital role in controlling the fracture risk in the bone tissue. Also, the nanostructural parameters like the degree of orientation and mineral particle angle could potentially be used as a marker to estimate the fracture risk in bone in metabolic (rickets) and neuromuscular bone diseases (muscular dystrophy).

References

(1) Smith et al, 1967, Brain 90(3):10, (2) Rinnerthaler et al, 1998, Calcif Tissue Int;64(5):422-9, (3) Gourrier et al, 2007, J Appl Crystallogr 40:78-82, (4) Gupta et al, 2004, J Biomech;37(7):1001-9, (5) Aono et al, 2011, Journal of Bone and Mineral Research;26(4):803-10, (6) Rowe et al, 1969, J Anat;104(3):12. (7) Endo et al. 2003. Endocrinology; 144(12):5138-44.

School of Engineering and Materials Science

Mechanical tester for I22 - *in-situ* mechanical testing with synchrotron microfocus SAXS on biological tissues

A Karunaratne[1], CT Esapa[2, 3], J Hiller[4], A Boyde[5], NJ Terrill[4], SDM Brown[3], RD Cox[3], RV Thakker[2], HS Gupta[1]

1. School of Engineering and Material Sciences, Queen Mary University of London, UK 2. Academic Endocrine Unit, Nuffield Department of Clinical Medicine, Oxford Centre for Diabetes, Endocrinology and Metabolism, University of Oxford, Churchill Hospital, UK 3. MRC Mammalian Genetics Unit and Mary Lyon Centre, MRC Harwell, Harwell Science and Innovation Campus UK 4. Diamond Light Source Ltd., Diamond House, Harwell Science and Innovation Campus, UK, 5. Queen Mary University of London, Oral Growth and Development, Institute of Dentistry, Bart's and The London School of Medicine, UK

Motivation

Research Background:
Understanding how changes in the structure of the nanoscale bone matrix (*bone quality*) increase the risk of fracture is a key frontier area of clinical bone biomechanics. To investigate the alterations to the nanostructural and mechanical properties of bone during metabolic disease conditions such as rickets and osteoporosis, we proposed to use high brilliance microfocus synchrotron small-angle X-ray scattering (μSAXS) combined with in situ micromechanical testing.

This high resolution diagnostic technique is capable of measuring the (nanoscale) fibrillar strains developed in real time during (macroscale) deformation and fracture.

Objectives:
One of the main initial objectives of this multidisciplinary project was to design a specialized ***in-situ* micromechanical testing machine** for small-scale murine bone testing. Special challenges involve design of miniature sample holders and *in-situ* fluid chamber systems, to test irregular bone tissues in close to *in-vivo* states.
Development of assay to link ultra structural changes to altered mechanical properties such as increased fracture risk in Glucorcortucoid induced osteoporosis (GIOP).

Design and Development

Fluid chamber assembly

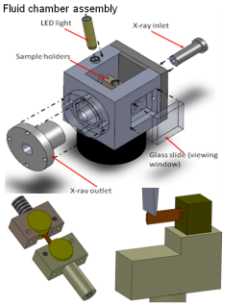

Sample holders for Tensile testing | Sample holders for Cantilever bending

Testing modes

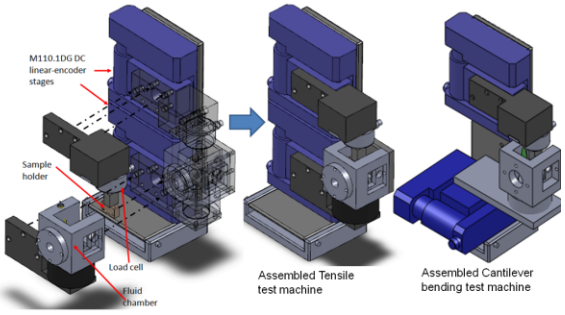

Bone hierarchical structure

The collagen molecules are staggered axially along the fibril, a periodic electron density profile exist along the fibril axis which result in series of Bragg reflections with period 2π/D in the SAXD pattern

Nano structural and mechanical parameters

Fibrillar deformation mechanisms

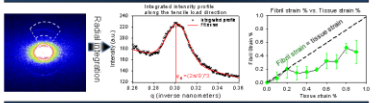

Fibrillar orientation

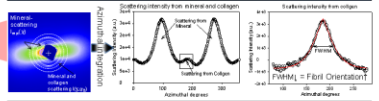

Mineral orientation

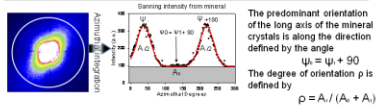

The predominant orientation of the long axis of the mineral crystals is along the direction defined by the angle

$\psi_h = \psi_i + 90$

The degree of orientation ρ is defined by

$\rho = A_v / (A_v + A_h)$

In-situ microtensile testing with μSAXS at the I22 beam line

Collagen fibril strain ε_f → tracking the shifts of the third order reflection peak position

Tissue strain ε_t → non contact video extensometry by imaging the separation of ink markers

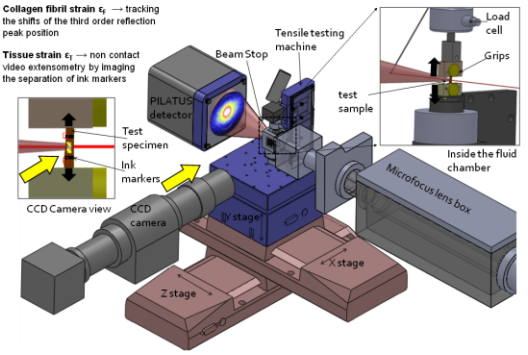

Synchrotron nano-mechanics

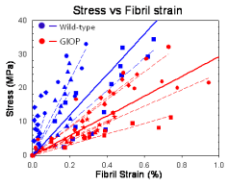

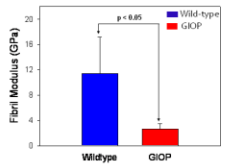

- Effective fibril modulus (s/ε_f) is significantly lower in GIOP mice compared to the wild-type mice
- Fibrils strain is larger in GIOP mice bone specimens compared to the wild-type mice

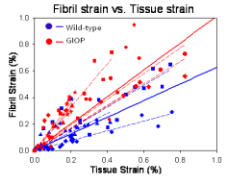

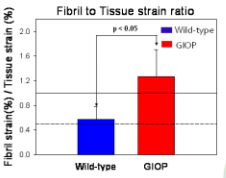

- For a given tissue strain, the mineralized collagen fibril strain of GIOP mice is much higher compared to the wild type mice

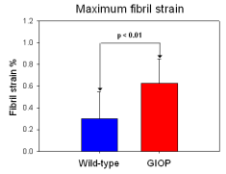

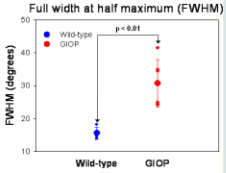

The FWHM for GIOP mice was significantly ($p<0.01$) higher compared to wild-type, indicating a lesser degree of fibrillar alignment relative to the tensile axis.

A. Karunaratne et al, JBMR, 27(4):876-90 (Apr, 2012) Karunaratne et al, 2012, Bone, (May 2012) May 15 H. S. Gupta et al, PNAS 103, 17741 (Nov, 2006). Gourrier et al., Journal of Appl Cryst 40, 78 (2007). Gupta, et al., Proc Natl Acad Sci U S A 103, 17741-6 (2006).

Synchrotron nano-structural parameters

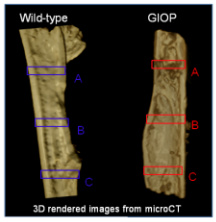

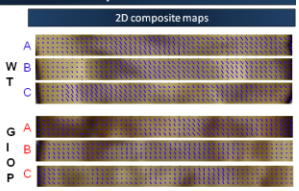

We quantified the degree (lengths of the lines) and direction (direction of the lines) of mineral particle alignment of the mice humerus at 3 different locations along the long axis.

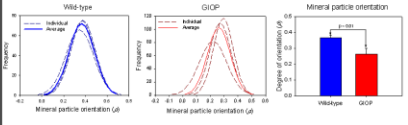

These measurements revealed a significant reduction in mineral nano-crystallite orientation in GIOP compared to wild-type mice.

Material Level Alterations

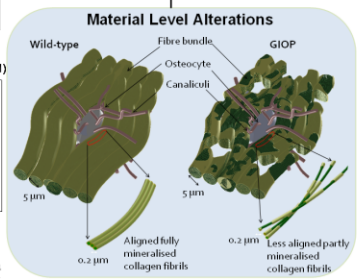

Conclusion

- A new micro-mechanical tester specialized for *in-situ* fibrillar level mechanics of biological tissues (size = ~100 μm width) was designed and successfully used at the I22 NCD beamline at Diamond.
- The micromechanical setup was used as an *in-vitro* functional imaging technique to understand (a) nanoscale origins of the mechanical and structural differences in a prototypical model for bone disease (rickets, GIOP and ageing) induced *via* ENU mutagenesis and (b) age-related development of the nanomechanics and structure in bones.
- Results presented here, proves glucocorticoid treatment has a direct effect on material level structural and mechanical properties.
- Our approach clearly shows the power of synchrotron-based *in-situ* X-ray nanomechanical imaging as a diagnostic tool to identify functional alterations in bone quality at the nanoscale in metabolic bone diseases.